

A MICROMACHINED FLOATING ELEMENT SHEAR STRESS SENSOR USING
MOIRÉ TRANSDUCTION FOR HARSH ENVIRONMENTS

By

TAI-AN CHEN

A DISSERTATION PRESENTED TO THE GRADUATE SCHOOL
OF THE UNIVERSITY OF FLORIDA IN PARTIAL FULFILLMENT
OF THE REQUIREMENTS FOR THE DEGREE OF
DOCTOR OF PHILOSOPHY

UNIVERSITY OF FLORIDA

2012

© 2012 Tai-An Chen

In loving memory of my father and to my family for their love and support

ACKNOWLEDGMENTS

Financial support for this project was provided by the Office of Naval Research (ONR). First and foremost, I would like to thank my advisor, Dr. Mark Sheplak, as well as Dr. Wei Shyy, for providing me the opportunity to perform research at the Interdisciplinary Microsystems Group (IMG) at the University of Florida. Dr. Sheplak is a significant influence in my life by enriching my life with guidance and insight over the years. I also would like to thank my committee members, Dr. Louis N. Cattafesta III, Dr. David Arnold, Dr. Henry Zmuda, Dr. Tony Schmitz and Dr. David Norton for their technical assistance on this project. The staff at the ECE department has been very helpful and I would like to personally thank Shannon Chillingworth for the help that she has given me over the years.

The environment at IMG is invaluable and although it would be difficult to list all of the help that I have received over the years, nevertheless, I would like to give special thanks to the following members of IMG. From day one, Dr. Stephen Horowitz has been a mentor to me and I would like to thank him for all of the years of friendship between our families. I am grateful for the help that Dr. Vijay Chandrasekharan provided during the microfabrication process at Georgia Tech. I am thankful for the numerous insights, both technical and otherwise, that Dr. Ben Griffin has provided over the years. Jeremy Sells deserves special thanks for all of his assistance with my research and friendship. I am especially grateful to Jess Meloy for her electrical engineering insight, circuitry help, sensor testing and debugging that she has provided. I am thankful for David Mills for his assistance with optical testing. Dylan Alexander, Nik Zawodny, Tiffany Reagan and Brandon Bertolucci deserve my thanks for their laboratory assistance that they have provided. Jason June and Casey Barnard

deserves my thanks for help during the final weeks leading up to my dissertation defense. I would like to thank Matt and Lisa Ordoñez for their friendship. In addition, I would like to thank Phillip Cunio, Talitha Cunio, Tessa Gebert and their families for their friendship and support. The staff at Georgia Tech are very courteous and I would like to particularly thank Vinh Nyugen for his help during the microfabrication process.

I could not have made it this far in life without the help of my friends and family. I would like to thank my brother, Tai-Jen Chen, and my mom, Lih-Ing-Lee Chen for their support from home. I cannot help but to thank Wellington Porto, Mestre Jelon and the members of his extended family. Their friendship and guidance not only help to grow me inside of the “Roda” but in life as well. Aimee Green and Oaklianna Caraballo also deserve my thanks for their friendship and support. I would like to express my thanks to Mr. Anjing Chen and his family for all of the help and support that he has provided. Mr. Anjing Chen has been instrumental in helping me develop my creative abilities. I would like to thank my wife, Yi-Hsuan (Amy) Lin, as well as my in-laws. I could not have asked for a better mother-in-law and father-in-law and I appreciate the love and support that they have given me these last few years. My wife has stood by my side during some of the most difficult periods in my life and I am forever grateful for her. My son, Lucas, has also been an inspirational factor in my life and I am proud to be his father.

Finally, I would like to thank my father, Dr. Tzong-Hsi Chen. He will forever be missed but more importantly, he will forever be remembered.

TABLE OF CONTENTS

	<u>page</u>
ACKNOWLEDGMENTS.....	4
LIST OF TABLES.....	10
LIST OF FIGURES.....	11
CHAPTER	
1 INTRODUCTION	20
1.1 Motivation	20
1.2 Fiber Optic Sensing Technology.....	22
1.3 Overview for Wall Shear Stress Measurement	24
1.4 Research Objectives.....	29
1.5 Dissertation Overview	30
2 BACKGROUND	33
2.1 Techniques for Measuring Shear Stress.....	33
2.2 Indirect Shear Stress Sensors	34
2.3 Direct Shear Stress Measurements	38
2.3.1 Conventional Direct Measurements	38
2.3.2 Direct, Floating Element Techniques	39
2.3.2.1 Capacitive detection techniques	43
2.3.2.2 Piezoresistive detection techniques.....	45
2.3.2.3 Optical detection techniques.....	46
2.4 Summary	49
3 MECHANICAL MODELING	66
3.1 Device Design.....	66
3.1.1 Lumped Element Representation.....	67
3.1.2 Linear Deflection	69
3.1.3 Nonlinear Deflection.....	72
3.2 Sensor Parameters	74
4 OPTICS	85
4.1 Optics Background.....	85
4.2 Motivation for Phase Modulation.....	85
4.2.1 Geometric Moiré Background	88
4.2.2 Modeling the Moiré fringe as a Sinusoid	90
4.3 Optical Non-idealities.....	93
4.3.1 Angular Errors	93

4.3.2	Grating Width Variations	94
4.3.3	Talbot Distance	95
4.3.4	Contrast and Material Selection	97
4.3.5	Out-of-Plane Sensitivity.....	100
4.4	“Ideal” Optical Fringe Estimation.....	102
4.4.1	Least Squares Curvefit.....	103
4.4.2	Fast Fourier Transform	105
4.4.3	Cross-Correlation	106
4.4.4	Spatial Phase Detection.....	107
4.5	Data Reduction	109
4.6	Summary	110
5	OPTOELECTRONICS AND OPTICAL PACKAGING	121
5.1	Optoelectronics.....	121
5.1.1	Light Sources	121
5.1.2	Fiber Optics.....	123
5.1.3	Optical Crosstalk.....	126
5.1.4	Photodiodes	127
5.1.5	Photodiode Noise.....	130
5.2	Optical Packaging Overview	131
5.2.1	LED Board	131
5.2.2	Optical Fiber Bundle.....	131
5.2.3	Optical Fiber to Sensor Adaptor	132
5.2.4	Photodiode Array Board.....	133
5.2.5	Data Acquisition System	134
5.2.6	Transimpedance Amplifier	134
5.3	Summary	136
6	MICROFABRICATION.....	151
6.1	Microfabrication Process.....	151
6.1.1	Cavity Etch.....	152
6.1.2	Aluminum Gratings.....	152
6.1.3	Anodic Bond Process.....	153
6.1.4	KOH Etch Process	154
6.1.5	Front-to-Back Align	155
6.1.6	Tethers Release.....	156
6.1.7	Dicing.....	156
6.2	Microfabrication Results.....	157
7	EXPERIMENTAL CHARACTERIZATION.....	161
7.1	Experimental Optical Calibration.....	161
7.1.1	Optic Fiber Bundle Calibration Setup	161
7.1.2	Optical Loss Budget	162
7.1.3	Fiber Bundle Calibration Results.....	163

7.1.4	Optical Test Bed Overview.....	163
7.1.5	Optical Test Bed Design	164
7.1.6	Optical Test Structures.....	165
7.1.7	Optical Test Bed Results.....	166
7.2	Experimental Optical Fringe Estimation Technique Comparison.....	167
7.3	Device Calibration.....	168
7.3.1	Device Characterization	169
7.3.2	Static Calibration Overview	169
7.3.3	Static Calibration Theory.....	169
7.3.4	Static Calibration Results Using Conventional Optics.....	170
7.3.5	Static Calibration Results Using the Fiber Bundle.....	171
7.3.6	Post Processing Algorithm for the Static Flowcell Measurements	171
7.3.7	Photodiode Measurement Corrections.....	171
7.3.7.1	RoMack fiber sorting.....	172
7.3.7.2	Uneven optical fiber spacing correction	172
7.3.7.3	Optical wafer calibration	173
7.3.7.4	External reference photodiode.....	175
7.3.8	Curvefit Section.....	175
7.3.8.1	Initial prefit for the optical fringe	176
7.3.8.2	Curvefitting flow data	177
7.3.9	Simulation of the Optical Fringe Estimation Techniques.....	177
7.3.10	Moiré Simulation Using Images	179
7.3.11	Static Sensitivity Calibration Results	181
7.3.12	Dynamic Calibration Overview	183
7.3.13	Dynamic Calibration Theory.....	184
7.3.13.1	AC sensitivity calibration.....	185
7.3.13.2	AC sensitivity results.....	186
7.3.13.3	Pressure sensitivity calibration.....	187
7.3.13.4	Pressure sensitivity calibration results	187
7.3.13.5	Frequency response calibration.....	188
7.3.13.6	Frequency response results.....	188
8	CONCLUSIONS AND FUTURE WORK	227
8.1	Conclusions	227
8.2	Research Contributions	228
8.3	Research Limitations	229
8.4	Recommendations for Future Work	231
8.4.1	Fiber Bundle Redesign.....	232
8.4.2	Sensor Redesign.....	232
8.5	Summary	233
APPENDIX		
A	MECHANICAL ANALYSIS.....	236
B	MICROFABRICATION PROCESS TRAVELER	252

C OPTICAL TESTBED SCHEMATICS.....	255
LIST OF REFERENCES	260
BIOGRAPHICAL SKETCH.....	268

LIST OF TABLES

<u>Table</u>		<u>page</u>
2-1	Shear stress measurement techniques.	52
3-1	Selected geometries for the second-generation optical Moiré shear stress sensor.....	81
5-1	Resistance and capacitance values for the Hamamatsu S4111-16Q photodiode array.....	137
7-1	Amount of light intensity loss at the various optic fiber interfaces.....	192
7-2	Correlation coefficients and slopes for various algorithms.....	192
7-3	Correlation coefficients for simulated photodiode data.	192
7-4	Correlation coefficients for simulated photodiode data with static spatial debris.....	192
7-5	Correlation coefficients for the various fringe estimation techniques using the optical fiber mask simulation.....	193

LIST OF FIGURES

<u>Figure</u>	<u>page</u>
1-1	Illustration of the velocity profiles in a boundary layer for a steady flow moving over a flat, solid body surface. 32
1-2	Turbulent boundary layer profile for mean velocities. 32
2-1	Illustration of some indirect shear stress measurement techniques.. 53
2-2	Illustration of a microfence structure for indirect shear stress measurement. 53
2-3	Thermal and velocity boundary layers from a hot-film shear stress sensor. 54
2-4	The first micromachined thermal shear stress sensor developed by Oudheusden et al. 54
2-5	Typical structure of a thermal shear stress sensor using a cavity for thermal isolation developed by Ho et al. 54
2-6	A micromachined thermal shear stress sensor developed by Kälvesten using polyimide filled trenches for thermal isolation. 55
2-7	Micromachined thermal shear stress sensor developed by Cain and Sheplak... 55
2-8	A schematic for the Doppler-based optical shear stress sensor. 56
2-9	A diagram of a micro-pillar structure for indirect shear measurement. 56
2-10	Experimental setup of a surface stress sensitive film for direct shear stress measurement..... 57
2-11	Diagram of an ionic-polymer shear stress sensor..... 57
2-12	Illustration of two types of floating elements. 57
2-13	Illustration of two types of floating element misalignment..... 58
2-14	Forces acting on the floating element from wall shear stress and pressure gradient induced forces (net lip force and shear stress in the cavity). 58
2-15	Schematic an interferometric shear stress sensor by Pulliam et al..... 59
2-16	Schematic of a capacitive shear stress sensor using a polymer floating element developed by Schmidt et al. 59
2-17	Examples of capacitive comb finger shear stress sensors. 60

2-18	Schematic of a cantilever-based, capacitive shear stress sensor by Zhe.	60
2-19	Schematic of a capacitive shear stress sensor by Chandrasekharan.....	61
2-20	Schematic of the capacitive sensor and inductor coil for wireless shear stress sensing by Sells [67].....	61
2-21	Schematic of a piezoresistive shear stress sensor for low flow applications by Ng and Goldberg.	62
2-22	Schematic of a piezoresistive shear stress sensor for underwater application by Barlian.	62
2-23	Schematic of a piezoresistive shear stress sensor by Li.	63
2-24	Schematic of the integrated photodiodes in the optical shutter shear stress sensor by Padmanabhan. Figure adapted from Padmanabhan [61].	63
2-25	Schematic of the 2D micro-pillar optical shear stress sensor by Tseng and Lin.....	64
2-26	Figure of an optical shear stress sensor using Moiré amplification developed by Horowitz et al.	64
2-27	Illustration of an optical Moiré shear stress sensor packaged in a laminar flowcell and observed using large, conventional optical packaging.	65
2-28	Schematic of an optical shear stress sensor using a microsphere resonator.	65
3-1	Illustration of the optical Moiré shear stress sensor.....	81
3-2	Diagram of the geometric features of the optical shear stress sensor.	82
3-3	Cross-section view of a shear stress sensor using mechanical representation.....	82
3-4	Diagram of a point load and distributed load on a clamped-clamped beam.	82
3-5	Coordinate plane system for determining the elevation and azimuth of a wafer.....	83
3-6	Illustration of the operating space for a mechanical sensor optimization.....	84
4-1	Illustration of various amplitude modulation techniques.	111
4-2	Illustration of various inteferometric techniques.	112
4-3	Amplitude modulation techniques for the micro-machined, floating-element flow application.	112

4-4	Phase modulation technique for micro-machined, floating-element flow applications.....	112
4-5	Drawings of Moiré fringe patterns.	113
4-6	Superposition of two grating sets with spatial pitches of g_1 and g_2 in parallel to form a Moiré fringe pattern with a Moiré spatial period G	113
4-7	Diagram illustrating a Moiré amplified shift of distance Δ for a given grating shift of distance δ	114
4-8	Illustration of sinusoids representing intensity profiles of the optical fringe.....	115
4-9	Graphical representation of a binary pulse train from Moiré gratings.	116
4-10	Illustration of an angular error α between two grating functions, ϕ_1 and ϕ_2	116
4-11	Moiré fringe sharpening due to non-equal grating gap to width ratio.....	116
4-12	Moiré fringe pattern when the grating width and gap are equal.....	117
4-13	Diagram illustrating virtual images from the gratings at successive Talbot distance intervals. Figure is adapted from Post et al [76].	117
4-14	Cross section of an optical Moiré shear stress sensor illustrating the reflectivity and transmissivity components of the various material interfaces...	118
4-15	Material property plots to determine contrast.	119
4-16	Illustration of a sinusoid representing a Moiré fringe pattern using intensities based off of material selection.....	119
4-17	Illustration of out-of-plane effects on the width of the Moiré fringe.....	120
4-18	Plot showing the percentage deviation in the phase curve-fits due to data reduction.....	120
5-1	A comparison of the space requirement between conventional optics and miniaturized optics for imaging the Moiré pattern on the shear stress sensor.	137
5-2	Prototype LED (Lumex SML-LX1610USBC) circuitry board for an optical fiber bundle array using FC connectors.....	138
5-3	Diagram of various optic fiber index profiles.....	138
5-4	Light reflecting and transmitting at the Interface between two media. [13]	139

5-5	Light angles between two optical medium with respect to the critical angle [13]	139
5-6	Illustration of the transmitting and receiving optical fiber pair.	140
5-7	A transmitting and receiving fiber with a reflecting mirror modeled in Optica. ..	140
5-8	Illustration of the source-receive optical fiber pairs in relation to the optical fringe.	141
5-9	Modeling light from the source fiber to multiple receiving optical fibers.	142
5-10	Optical fiber mapping between the source and receive fibers.	142
5-11	An estimation of the collected light intensities across the optical fiber bundle array.	143
5-12	Equivalent circuit for representing a photodiode.	143
5-13	Illustration of the p-n junction for a typical diode.	144
5-14	Formation of EHP in the P-N Junction of a photodiode.	144
5-15	A plot of the current voltage curve for a photodiode.	144
5-16	Graph representing the different regions of operation in a photodiode.	145
5-17	Illustration of noise contributions in a photodiode. [90]	145
5-18	Overview of the experimental optical packaging setup.	145
5-19	Optical fiber bundle manufactured by Romack Optics.	146
5-20	Schematic for the fiber plug adaptor to rigidly connect the Romack fiber bundle to the optical shear stress sensor.	146
5-21	Schematic of the Romack fiber plug attached to the photodiode array board circuitry.	147
5-22	Diagram of a Hamamatsu S4111-16Q photodiode array with 16 elements. Diagram is adapted from Hamamatsu [91].	147
5-23	Photosensitivity of a Hamamatsu S4111-16Q. Diagram is from Hamamatsu [91].	148
5-24	Equivalent circuit of the photodiode and the operational amplifier.	148
5-25	Transfer function of the photodiode circuitry measured by the spectrum analyzer.	149

5-26	Illustration of the photodiode array board with amplifiers in a Faraday cage for noise measurements.	149
5-27	Noise measurements from the photodiode array board in a Faraday cage.	150
6-1	A cross-sectional diagram illustrating the basic steps in the optical shear stress sensor device fabrication; drawing not to scale.	158
6-2	SEM image of a released floating element on a 50 Pa, 5 kHz device.	159
6-3	Photograph of a 5 Pa 1 kHz Moiré shear stress sensor.	159
6-4	Photograph of the wafer inside the dicing saw chamber.	160
6-5	Photograph of a 5 Pa, 1 kHz device with stiction.	160
7-1	Schematic of the optical fiber calibration experimental setup.	193
7-2	Photograph of the sensor plug of the Romack optical fiber bundle illustrating the following: incorrect input/output fiber mapping, random misalignment between source/receive fiber pairs and non-uniform spacing between adjacent optical fibers in the fiber bundle.	194
7-3	Diagram of the optical fiber scrambled mapping between the light source to the source fibers of the sensor plug and the receive fibers to the photodetectors for the Romack fiber bundle.	195
7-4	Measured light intensity levels indicating light loss from the Doric LED to the Ceramoptec fiber adapter to the Romack fiber bundle to the sensor and back through the Romack fiber bundle and recorded with a photodetector.	196
7-5	Light calibration between each optical pathway from the light source through the various optical fibers channels and to the optical detector.	197
7-6	Nanopositioner for optical calibration using Moiré test plates.	198
7-7	Photograph and illustration of the optical test structures.	199
7-8	Test structure data using the fiber bundle and the nanopositioner along with least squares curvefits.	199
7-9	Displacement of the Moiré fringe pattern versus the mechanical displacements of the floating element test structures.	200
7-10	The resulting sensitivities and error bars from the nanopositioner using various optical fringe estimation techniques.	201
7-11	Schematic illustrating the experimental setup for statically calibrating the shear stress sensor in a laminar flow cell.	202

7-12	A graph of the Moiré fringe pattern with a sinusoidal least-squares curve-fit superimposed.	202
7-13	The deflection of the 5 Pa, 2 kHz shear stress sensor over a 5 Pa range in a laminar flow cell.	203
7-14	Resulting image plots of the optical fiber centroid detection algorithm.	204
7-15	The relative fiber centroid locations are mapped to the image of the fiber bundle.	204
7-16	A plot showing the recorded photodiode intensities using simultaneous source fiber illumination.	205
7-17	Photodiode sensitivity calibration plots.	206
7-18	Comparison of the simultaneous source fiber illumination calibration vs. individual source fiber illumination calibration technique showing the amount of optical crosstalk.	207
7-19	Correction plots for light fluctuation compensation using a reference photodiode.	208
7-20	Simulated photodiode data for optical fringe estimation.	209
7-21	Performance of the spatial phase estimation using various fringe estimation techniques.	210
7-22	Simulated spatial debris superimposed on the simulated photodiode data.	211
7-23	Performance of the spatial phase estimation in the presence of spatial debris using various fringe estimation techniques.	212
7-24	A photograph of the fiber mask simulation using a imaged Moiré fringe.	213
7-25	Various fringe estimation of simulated optical fringe deflection using a fiber mask.	213
7-26	FFT fringe estimation of simulated optical fringe deflection using a fiber mask at a pixel deflection resolution.	214
7-27	Phase estimation on the photodiode data using the n-sines, least-squares curvefit.	215
7-28	Performance of the phase estimation techniques on a 5Pa, 5kHz sensor using the various fringe estimation techniques.	216
7-29	Static calibration results with error bounds generated from a Monte Carlo simulation using 95% confidence intervals.	217

7-30	Particle velocity profile of the acoustic waves at the wall due to the no-slip boundary condition.	217
7-31	Schematic illustrating the experimental setup for dynamically calibrating the shear stress sensor in a plane wave tube.	218
7-32	Dynamic calibration setup configuration for shear stress only in the PWT.	218
7-33	Ac sensitivity results of a 50 Pa, 5 kHz sensor placed at quarter-wavelength from a rigid termination at a frequency of 1.1 kHz.	219
7-34	Sensitivity due to pressure monitored at 2.2 kHz during the quarter-wavelength ac sensitivity testing at 1.1 kHz.	220
7-35	Dynamic calibration setup configuration for pressure only in the PWT.	220
7-36	The sensitivity of a 50 Pa, 5 kHz due to pressure at a half-wavelength.	221
7-37	Dynamic calibration setup configuration for frequency response calibration in the PWT.	221
7-38	Frequency response calibration of 50 Pa, 5 kHz sensor maintained at quarter-wavelength distance from a rigid termination.	222
7-39	Illustration of several potential lateral deflection sources due to pressure.	223
7-40	The measured sound pressure levels by the microphone at the rigid termination and the microphone at the sensor.	224
7-41	Ac sensitivity using individual optical fibers tested at 1.1 kHz.	225
7-42	FRF estimation using the results of a single optical fiber and the microphone at the wall.	226
8-1	Illustration of the proposed optic fiber configuration for future experiments.	235
A-1	Illustration of point and distributed forces for in-plane (shear stress) deflection.	251
A-2	Illustration of point and distributed forces for out-of-plane (pressure) deflection.	251
C-1	Schematic of the push structure for the optical testbed.	255
C-2	Schematic of the mount for securing the sensor plates of the optical testbed. .	256
C-3	Schematic of the base structure of the optical testbed.	257

C-4	Schematic of the sensor plates for securing the silicon and Pyrex test structures.....	258
C-5	Overall schematic for the optical testbed.....	259

Abstract of Dissertation Presented to the Graduate School
of the University of Florida in Partial Fulfillment of the
Requirements for the Degree of Doctor of Philosophy

A MICROMACHINED FLOATING ELEMENT SHEAR STRESS SENSOR USING
MOIRÉ TRANSDUCTION FOR HARSH ENVIRONMENTS

By

Tai-An Chen

December 2012

Chair: Mark Sheplak

Major: Electrical and Computer Engineering

A direct, micromachined shear stress sensor using a Moiré amplification technique is presented in this dissertation. Shear stress or skin friction measurements are useful in aerodynamic, flow control and biomedical applications. Conventional approaches to shear stress measurements typically either indirect measurements or lack the spatial or temporal resolution required for time-resolved direct measurements. Indirect shear stress measurements infer shear stress using other flow quantity and require prior knowledge of the flow, which limits its usefulness during application. Micromachined floating element shear stress sensors offers the ability for direct, time-resolved, shear stress measurements.

This research uses an optical Moiré transduction technique for micromachined floating element device. Optical fibers are used to significantly reduce the packaging size and improve robustness over conventional microscope imaging systems. The prototype optical fiber bundle system developed in this research is demonstrated on an optical test-bed. In addition, the optical fiber bundle is demonstrated to work with a Moiré sensor for mean and dynamic shear stress measurements.

CHAPTER 1 INTRODUCTION

The goal of this research is to develop a MEMS-based floating-element optical shear stress sensor using Moiré interferometry that can be used for a time-resolved, direct measurement of shear stress in a harsh environment. This research extends previous work [1] by transitioning the optical detection of Moiré fringe patterns from a benchtop microscope to a fully packaged sensor suitable for use in wind- or water-tunnel testing. A miniaturized optical package enables the device to be placed in an inhospitable environment, such as the surface of a submarine model in a water tunnel. Optical fibers are used as a waveguide to transmit light from a source to the floating-element and the reflected light from the floating element with the Moiré encoded light signal is then transmitted back towards the optoelectronics for signal processing. Water flow measurements and high temperature gas shear stress sensing are possible since the device itself can be exposed to the harshness of the sensing environment while the optoelectronic components can be safely shielded while observing the Moiré fringe patterns on the device through the fiber optics.

In this chapter, basic background information on shear stress and optical sensing is provided. Furthermore, the expected contributions of this research are listed. Finally, an overview guide for the rest of the dissertation is provided.

1.1 Motivation

The ability to measure shear stress or skin friction drag is an important asset for various research communities that include aerodynamic, biomedical and industrial process control applications. In aerodynamics, the performance of many vehicles is dominated by viscous effects and the drag attributed to skin friction can account for as

much as 50% of the total drag on the vehicle [2–4]. By observing the dissipative losses from the viscous effects, the vehicles may be designed to minimize the amount of drag experienced along the surface, thus improving the fuel efficiency. Skin friction measurements are also useful for fundamental aerodynamic research as well as applications such as flow control [3], [5]. Wall shear stress measurements can be used to determine the transition from laminar to turbulent flow and to find the location where the flow separates causing huge increases in drag [3], [6–8]. In biomedical research, applications that monitor blood flow in arteries also benefit from wall shear stress measurement. The shear measured in the arteries can help indicate abnormalities in the blood flow to detect arterial diseases such as atherosclerosis [9], [10].

Several techniques have been developed with the goal of measuring skin friction. However, currently few shear stress sensors have been developed possessing the necessary spatial and temporal resolution suitable for time-resolved shear stress measurements in turbulent flows [3]. Conventional shear stress measurement techniques, such as hot film probes and hot wire, have the potential for time-resolved measurements but do not meet the spatial requirements to measure the small turbulent structures and their bandwidth is insufficient to capture the spectrum in turbulent flows. For practical applications, overcoming harsh environmental challenges further increases the difficulty for complicates shear stress measurements [11]. Skin friction techniques using micromachined sensors have the potential to meet the temporal and scaling requirements and the various micromachined transduction techniques for shear measurement are described in more detail in Chapter 2.

The main focus of this research is the development of a miniaturized optical transduction scheme for use with a shear stress sensor with sufficient spatial resolution and bandwidth that can eventually be used for quantitative shear stress measurements in an underwater or moderately high-temperature environment. This research also has the potential for the device to be transitioned into high temperature environments using the same concepts but with high-temperature capable materials [12]. The motivation for selecting optical fibers for use with the shear stress sensor is discussed in the next section and is followed by a discussion of wall shear stress.

1.2 Fiber Optic Sensing Technology

One of the major challenges faced by conventional, free space optics is the issue of line of sight, which subjects the optical detection scheme to any changes in the medium surrounding optics [13]. By using a guiding medium, such as an optical fiber, difficulties with respect to the line of sight can be mitigated. The optical pathway achieved by using fiber optics allows communications signals to be transmitted hundreds of kilometers [14]. Light is maintained inside the core of the optical fiber using total internal reflection and the signal attenuation experience by the optical fiber per distance is much less than the losses seen by electrical cables [14].

In addition to benefits in the transmission of light in comparison to large scale optics, there are several key advantages using optical fibers as part of a transduction technique [15]. A desirable characteristic in any sensor is the ability to only detect the desired quantity of interest without gaining additional interference from the environment. Electromagnetic interference (EMI) is a common source of noise for sensors with electronics. However, optical systems are immune to EMI. Additionally, it is difficult to tap and intercept the light signal in optical fibers, which results in added security for data

transmission [16]. When compared to the large lenses used in conventional optics, fiber optics are often small and light in weight that enables a compact design. Optical fibers can be made out of transparent plastic or glass. Since these materials used in optical fibers are dielectric, this provides electrical isolation in the optical transduction. The material of the fiber optics can be replaced with high temperature capable materials, such as sapphire optical fibers [17]. Since the light transmission cannot generate a spark, it is safe to use in a flammable gas environment [18]. Furthermore, since rate of data transmission for optical fibers is based on the speed of light in a given medium, the bandwidth for opto-mechanical sensors is usually limited by the mechanical structure and not the opto-electronics.

The primary disadvantage when using optical fiber sensing technology is the cost and complexity in the packaging to achieve precision alignment [19]. Compared to electrical systems, optical fibers are often more expensive. Splicing optical fibers together are more difficult and costly than soldering electrical wires together. Optical transmitters and receiver components are more expensive than electrical components [20]. However, as optical communication technology improves, the cost continues to be reduced.

For miniaturization of the optical shear stress sensor, the small, light-weight features of optical fibers are beneficial in reducing the overall size of the packaging. With immunity from EMI and electrical isolation of the dielectric materials, the optical fibers do not introduce undesirable signals into the system. The ability to transmit high-speed signals over long distances allows the device and other opto-electronic

components to be shielded at a remote location away from the inhospitable shear sensing environment.

1.3 Overview for Wall Shear Stress Measurement

For a given flow over a solid boundary, two different forces occur at the surface; a force in the normal direction and a force in the tangential direction. The force per unit area in the normal direction is the flow quantity known as pressure. The force per unit area in the tangential direction to the wall is the flow quantity known as shear stress [21], [22].

In a viscous flow, the velocity of the fluid is zero at the surface of the solid boundary due to the no-slip boundary condition as illustrated in Figure 1-1. The profile of the velocity gradient is related to the viscosity of the fluid. The velocity of the fluid is zero at the surface of the stationary solid boundary due to the no-slip boundary condition. At some distance normal to the surface, the velocity asymptotes to the velocity of the free stream flow. This region where the velocity, u , transitions from the no-slip condition until the velocity reaches 99% of velocity in the free stream flow, U_∞ , is known as a boundary layer with thickness, δ [23]. When the velocity profile no longer changes, the flow has reached its free stream condition.

Wall shear stress is related to the viscosity of the fluid and velocity gradient normal to the surface. In a boundary layer, the expression to relate the viscosity and the velocity gradient to the wall shear stress, τ_w , for a Newtonian fluid is [21],

$$\tau_w = \mu \left. \frac{du}{dy} \right|_{y=0}, \quad (1-1)$$

where μ is the dynamic viscosity, u is the velocity of the fluid tangential to the surface, and y is the distance normal from the surface.

The skin-friction coefficient is the wall shear stress is often non-dimensionalized by the dynamic pressure [24],

$$C_f = \frac{\tau_w}{\frac{1}{2}\rho U_\infty^2}, \quad (1-2)$$

where ρ is the density.

In turbulent flow, wall shear stress can be decomposed into a mean component and fluctuating components. In turbulent flows, eddies are formed in the flow. For the smaller eddies, the effects from molecular diffusion and viscous effects becomes important. Characteristic length and time scales are used to resolve the turbulent structures. The non-dimensionalized viscous length scale is defined as the ratio between the kinematic viscosity of the fluid ν and the friction velocity u_τ and is expressed as,

$$l^+ = \frac{\nu}{u_\tau}, \quad (1-3)$$

The friction velocity is given by,

$$u_\tau = \sqrt{\frac{\tau_w}{\rho}}, \quad (1-4)$$

where τ_w is the wall shear stress and ρ is the density of the fluid. The wall length of the fluid is defined as,

$$y^+ = \frac{y}{l^+} = y \left(\frac{u_\tau}{\nu} \right). \quad (1-5)$$

In turbulent flows, the Kolmogorov microscales are a theoretical approach to estimate the smallest characteristic length scale and time scales [3], [5], [25] and are given by,

$$\frac{\eta}{\delta} \sim \left(\frac{u\delta}{\nu} \right)^{-3/4} = \text{Re}_\delta^{-3/4} \quad (1-6)$$

and

$$\frac{Tu}{\delta} \sim \left(\frac{u\delta}{\nu} \right)^{-1/2} = \text{Re}_\delta^{-1/2}, \quad (1-7)$$

where η is the Kolmogorov length scale, T is the Kolmogorov time scale, u is the typical eddy velocity, δ is the boundary layer thickness, ν is the kinematic viscosity, and Re is the Reynolds number. The ratio between eddy velocity and the free stream velocity, u/U_∞ , typically scale on the order of $\sim 10^{-2}$ for a wide range of Reynolds numbers [25].

An empirical study is performed by Hutchins et al. using hotwires to estimate the scaling requirements for a turbulent boundary layer [26]. The non-dimensionalized length and temporal scales used by Hutchins are,

$$L^+ = L \frac{u^*}{\nu} \quad (1-8)$$

and

$$t^+ = \frac{tu^{*2}}{\nu} \quad (1-9)$$

where u^* represents the friction velocity.

Based on the study, the non-dimensional length and time resolution should $L^+ < 20$ and $t^+ < 3$, to avoid spatial averaging and avoid low pass filtering the data due to insufficient bandwidth respectively. The maximum length scale for a sensor should be,

$$L_{\max} \leq 20 \frac{\nu}{u^*}, \quad (1-10)$$

and the minimum bandwidth of the sensor should be,

$$f_{\max} = \frac{1}{t_{\max}} \geq \frac{u^{*2}}{3\nu}. \quad (1-11)$$

Although the hotwire study is indirect comparison to shear stress measurement, the length and time scales are useful as an initial estimate for the spatial and temporal resolution requirements for measurement in a turbulent boundary layer. In order to accurately capture the fluctuating shear stress spectra, the sensor is estimated to have spatial resolution of $\sim 100 \mu m$ to avoid spatial averaging and a temporal resolution of at least ~ 1 kHz [3] for sufficient bandwidth.

In an equilibrium turbulent boundary layer, the mean velocity profile has several regions near the wall: the viscous region, the buffer region and the logarithmic region. A non-dimensional wall unit, y^+ , is used to describe the span of each region as shown in Figure 1-2.

In the viscous sublayer, which ranges from $y^+ = 0$ to $y^+ = 5$, is the region closest to the wall and has a linear mean velocity profile with respect to distance [25]. In this region, the viscous stress dominates when compared to Reynolds stress. The velocity profile of the viscous region is characterized by the following equation,

$$u^+ = \frac{U(y)}{u^*} = y^+. \quad (1-12)$$

The flow is not steady in the viscous region [25] and is appropriate for observing instantaneous wall shear stress.

The logarithmic region, or the inertial sublayer, is the region where the Reynolds stress dominates compared to viscous effects starting at $y^+ \approx 30$. The profile of the mean velocity is logarithmic and is characterized by the following equation,

$$u^+ = \frac{U(y)}{u^*} = \frac{1}{\kappa} \ln y^+ + C. \quad (1-13)$$

where κ is the Von Kármán constant and C is constant using empirical results [27].

The buffer region is the region between the viscous region and the logarithmic region. In this region, the mean velocity transitions from a linear profile to logarithmic profile and both the viscous and Reynolds stresses are important. The transition in the buffer region can be estimated using Spalding's law of the wall equation [24], [27],

$$y^+ = u^+ + e^{-\kappa C} \left[e^{\kappa u^+} - 1 - \kappa u^+ - \frac{(\kappa u^+)^2}{2} - \frac{(\kappa u^+)^3}{6} \right]. \quad (1-14)$$

The outer layer of the boundary layer past the logarithm region is considered to be the wake region. The wake region is dominated by large scale eddies with length scales on the order of the boundary layer thickness, δ [28].

Due to the spatial and temporal requirements, the microfabrication technology involved in manufacturing microelectromechanical systems (MEMS) are ideal to produce shear stress sensors that meet these requirements. The compliant, low mass, MEMS devices for shear measurements have superior bandwidth when compared to conventional techniques discussed in Chapter 2. A common micro-machined device structure for direct shear stress detection is a floating-element.

Several issues have to be addressed when using floating element structures. In a turbulent boundary layer, the magnitude of turbulent pressure fluctuations are larger than the wall shear stress fluctuations by an order of magnitude [29]. Specifically, the frequency dependent wall pressure fluctuations are shown to be on the order of 7 – 20 dB higher than the streamwise shear stress [30]. For the spanwise shear stress component, the wall pressure is found to 15 – 20 dB higher [30]. Inherent to floating-element structures are gaps which should be minimized to avoid disturbing the flow. If the gap widths are within the viscous sublayer ($y^+ = 5$), then the surface is considered to be hydraulically smooth [31].

The scaling advantages seen by MEMS devices enables minute force detection, negligible sensor alignment, small physical gap distances in the device while being hydraulically smooth, smaller pressure induced errors and cross axial sensitivities when compared to conventional techniques, and immunity to thermal expansion drift related issues [32]. The mechanical non-idealities are discussed in Chapter 3.

1.4 Research Objectives

An ideal shear stress sensor should have the necessary temporal and spatial resolution to measure the quantity of interest. External environmental effects such as temperature variations, pressure fluctuations and electromagnetic interference should not influence shear stress measurements and an ideal sensor should be immune to such effects. An ideal shear stress sensor should be able to be calibrated without requiring *a priori* knowledge of the flow and the measurements should not drift over time. The sensor should be robust and easily adapted into the experimental setup.

This research addresses the temporal and spatial resolution requirements with a micromachined floating element sensor to enable detection of small forces. An optical Moiré transduction technique is selected to gain immunity from temperature, pressure, and electromagnetic effects. The floating element sensor is a direct shear stress measurement technique and does not require prior knowledge of the flow. An optical fiber packaging system is used to improve the robustness of the overall sensor setup.

The emphasis of the research is to demonstrate a proof-of-concept, prototype optical Moiré shear stress sensor. Non-optimized sensors are used during the calibration of the optical fiber bundle. The goal is to have a functioning device with an optical package that independent of an optical benchtop in a laboratory for shear stress measurement.

The following is a list of contributions as a result of this research:

- Development of the first optical-based, micromachined, floating element sensing system suitable for wind and water tunnel measurements.
- Development of an optical test-bed to mechanically simulate floating-element deflection and optical fringe deflection for calibrating various optical setups.
- Static and dynamic characterization of the shear stress sensor using the miniaturized optical packaging.

1.5 Dissertation Overview

The proposal is organized is organized as follows. Chapter 1 described the motivation for using optical fibers and the motivation for measuring shear stress. In Chapter 2, previous shear stress sensors using various transduction techniques are described. Chapter 3 outlines the mechanical design and equations for calculating the response of the sensor in addition to a brief sensor redesign section. Chapter 4 describes the concept of Moiré amplification and introduces several techniques for

estimating the phase of Moiré fringe patterns. Background information for the optical components used in the transduction scheme as well as the packaging is presented in Chapter 5. In Chapter 6, the microfabrication process for constructing an optical Moiré shear stress device is described. The optical fiber bundle and optoelectronics In Chapter 7, non-idealities in optic fiber bundle are characterized and optical simulations are performed. The static and dynamic characterizations of the shear stress sensor using fiber optics are demonstrated as well. Recommendations for future work and a list of contributions are discussed in Chapter 8.

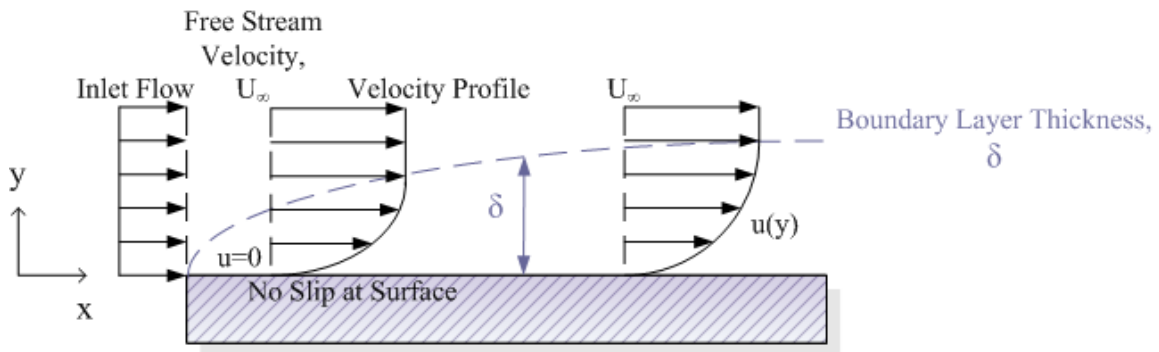


Figure 1-1. Illustration of the velocity profiles in a boundary layer for a steady flow moving over a flat, solid body surface.

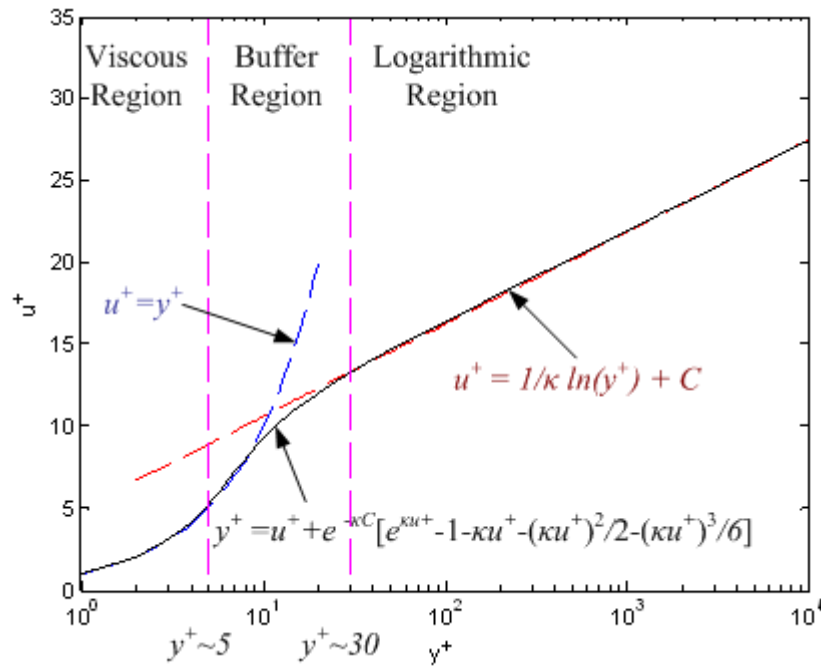


Figure 1-2. Turbulent boundary layer profile for mean velocities.

CHAPTER 2 BACKGROUND

In this chapter, previous existing shear stress measurement techniques are discussed, with an emphasis on MEMS-based, floating element shear stress sensors. The methodology and the overall performance of the various shear stress measurement devices, as well as the benefits and challenges that each transduction scheme encounters, are reviewed.

2.1 Techniques for Measuring Shear Stress

Existing shear stress sensor can be classified as either indirect or direct sensors [3] and as either macroscale (conventional) or microscale (micromachined) sensors and is summarized in Table 2-1. Indirect shear stress sensors measure other flow related quantities and infer a shear stress using correlation. As a result, the indirect sensors suffer from limitations in the accuracy of the method of correlation used to derive shear stress. Flow around surface obstacles, heat/mass transfer analogies, and velocity profile techniques are all examples of indirect shear stress measurement techniques [33].

Direct shear stress sensors measure the shear stress quantity directly. Conventional direct shear measurement techniques include liquid crystal coatings, oil film interferometry and shear stress sensitive coatings, which requires the use of optics to observe shear stress. However, for both the liquid crystal coating and oil film interferometry techniques, issues such as a shear conditions during start up and shutdown of a wind tunnel as well as deterioration limit the use of these techniques. Furthermore, these techniques do not provide time-resolved shear stress measurements. Microscale sensors typically have features on the order of microns and

have an overall size on the order of millimeters or less. Direct, microscale sensors are ideal for time-resolved shear stress measurements due to favorable scaling for turbulent flow. A common technique for direct shear stress measurement is to integrate the shear force over a floating element structure. The floating element has a compliant element to provide a restorative force during shear stress measurement. The deflection of the floating element is compared to the response of the transduction technique used for measuring shear force, such as capacitive, piezoresistive or optical techniques.

2.2 Indirect Shear Stress Sensors

Conventional, indirect shear stress sensors include surface obstacle sensors such as Preston tubes and Stanton tubes as illustrated in Figure 2-1. Their widespread usage is due to the simplicity in setup and ease of use [28]. Preston tubes are pitot tubes located on the wall surface and measure velocity at a known distance from the wall [33]. The range of the velocity profile for the Preston tube extends from the viscous sublayer and into the logarithmic region of the boundary layer. Stanton tubes/razor blades are a limiting case of the Preston tubes [28], operating in the viscous sublayer (linear) region of the velocity profile. Both the Preston tubes and Stanton tubes correlation methods use the law of the wall to indirectly relate flow to shear stress. Although these techniques are simple to use, the disadvantage of these techniques is that prior knowledge of the velocity profile is required for determining shear stress and the measurements are not time-resolved.

Microfences are cantilever surface obstruction devices that protrude into the viscous sublayer as shown in Figure 2-2. The height of the fence is restricted by the height of the viscous sublayer. The micromachined fences measures the pressure difference on either side of the fence to indirectly infer shear stress. Although relatively

simple to manufacture and the small geometry of the fence, calibration of the fence is difficult and requires prior knowledge of the flow. The flow constants, which relates differential pressure and shear stress, are necessary for calibration and determined empirically [34].

Micromachined thermal shear stress sensors are indirect temperature resistive sensors that convert temperature into voltage that is in turn correlated to wall shear stress. The typical thermal sensor generates a thermal boundary layer inside a velocity boundary layer by locally heating the fluid surrounding the thermal sensor to a temperature greater than the fluid temperature [3], [28], [33], [35] (Figure 2-3). Changes in the temperature are observed by monitoring the changes in a resistive sensing element.

Since the correlation between the temperature changes and wall shear stress depend on theoretical or empirical heat transfer analogies, the accuracy of the shear stress measurements is highly dependent on the accuracy on the heat transfer analogies. Repeatability in the calibration is an issue due to the unsteady heat conduction to the substrate and the dynamic response of the device is limited by the thermal inertia [3], [11].

Oudheusden et al. first developed a micromachined, thermal flow rate sensor [36]. The device uses a thermopile on a silicon chip for sensing as shown in Figure 2-4. Poor thermal isolation in the substrate added to the thermal mass, thereby increasing the thermal inertia and decreasing the frequency response. Due to the lack of thermal isolation, the micromachined thermal sensor did not mark an improvement over existing

conventional techniques at that time [3]. Subsequent micromachined thermal sensors developed attempted to address this issue using various thermal isolation techniques.

Ho et al. [37] developed several different micromachined thermal shear stress sensors using a vacuum cavity to reduce the substrate heat conduction to the thermal sensor as depicted in Figure 2-5. Their typical sensor consists of a polysilicon resistor, which is used as a heating element for the surrounding fluid, and is located on a silicon nitride membrane, which is replaced with a Parylene membrane in subsequent devices. The membrane forms a vacuum cavity over a base substrate to improve thermal isolation. These sensors are placed in an array to for shear stress mapping over a planar 2D surface as well as over a curved surface using flexible arrays.

Kälvesten [38] approached the substrate conduction heating effects by developing a thermal anemometer that includes KOH etched trenches filled with polyimide surrounding the sensor as illustrated in Figure 2-6. The polyimide surrounding the sensor acts to insulate the device from the substrate. The polysilicon resistor heats the flow and two temperature sensitive diodes located on the device measure the gas and sensor temperature.

Cain et al. [39] have developed thermal shear stress sensors using the vacuum cavity concept similar to Ho and Tai for thermal isolation as shown in Figure 2-7. The sensor improves on the earlier work by replacing the polysilicon resistor with a platinum sensing element to improve the thermal coefficient of resistance TCR, operating range, and to reduce $1/f$ noise.

The reliability of the various micromachined thermal sensors as discussed above is dependent on the accuracy of the empirical heat transfer correlations and the ability

to thermally isolate the device. Additional issues, such as measurement errors due to temperature drift, limit the usefulness of thermal sensors for shear stress measurement.

Another method for indirectly measuring shear stress is the use of the velocity profile to correlate to shear stress. Fourgnette et al. of VioSense Corporation designed an optical wall shear stress sensor based off the work started by Naqwi and Reynolds [40] that uses diffractive optics to obtain shear stress by measuring the near wall boundary layer as shown in Figure 2-8 [41]. The optical transduction for the device uses light from a input laser source, which diverges into a PMMA diffractive lens and into chrome parallel slits. The light is reflected off of the particles in the linear velocity region of the boundary layer and the reflected fringes are received by a photodetector. The measured Doppler frequency from the particles is multiplied by the dynamic viscosity of the fringe divergence to obtain the velocity gradient at the wall. The velocity profile of the boundary is used to determine the mean shear stress. Some of the drawbacks for this setup include difficulty seeding the near wall boundary layer with particles and low data rate due to the seeded particles.

Micro-pillars are micromachined, indirect shear stress sensors that are surface obstacles devices mounted on a wall as shown in Figure 2-9. The flexible pillars protrude from the surface of the wall into the viscous sublayer and the height of the micropillars is limited by the thickness of the viscous sublayer. The pillars are deflected in the direction of the flow and the deflections are optically observed and correlated to shear stress. An array of the micropillars can be used to map the shear stress distribution on the wall. However, neighboring pillars have to be separated at such a distance that local disturbances of the flow from each pillar does not interfere with each

other. An example of an existing micropillar device is the Micro-Pillar Shear Stress Sensor (MPS³) by Große et al. [42].

2.3 Direct Shear Stress Measurements

Several direct shear stress techniques are discussed in the following sections. While oil film and liquid crystal techniques are considered to be “quasi-direct” shear stress measurements, the focus is on micromachined floating elements for direct shear stress measurements.

2.3.1 Conventional Direct Measurements

Oil film interferometry and liquid crystal techniques are both classified as a “quasi-direct” method for skin-friction measurements [3]. Both techniques rely on the use of optics to obtain shear stress. Oil film techniques observe the thinning of oil on a surface when shear stress is applied. The imaging system for oil film techniques typically uses a light-source and an optical detector. The oil is applied to a model surface for observation and the oil thickness is determined using interferometry. The height of the oil film is correlated to the shear stress. For liquid crystal skin friction measurement, when shear stress is applied to a liquid crystal coating, the optical properties of the liquid crystal changes accordingly. The optical changes in the liquid crystal coating due to shear stress allow the liquid crystal technique to be used as a flow visualization tool. Several components are common among the various liquid crystal techniques. A liquid crystal coating is applied to a model surface, which should be ideally sensitive to shear stress and insensitive to temperature. Light is either reflected or transmitted. For the various liquid crystal techniques, either the light intensity or wavelength is observed. Although these methods are non-intrusive for shear stress measurements, the oil film

and liquid crystal techniques are limited to mean shear stress measurements and the spatial resolution is typically limited to the optics.

Surface stress sensitive films have also been developed as a means to detect shear stress as shown in Figure 2-10 [43]. The elastic film deforms under the applied shear stress and the continuous distribution of skin friction is observed using a light source and camera. The captured images are modeled using finite element analysis (FEA). The elastic film is sensitive to both skin friction and pressure gradients. Pressure gradients contribute to the generation of shear stress displacements on the film and the shear stress contribution due to pressure have to be removed using FEA [43].

Etebari et al. has developed a conventional, ionic polymer based, direct shear stress sensor [11]. The ionic polymer membrane is plated with conductive metal layers and exhibit piezoelectric-like behavior. Upon an applied mechanical deformation, the membrane generates an electric field and electrodes are used to acquire the signal from the sensor. The membrane is attached to a fixed plate, and a second plate attached to an electromagnetic shaker is used apply a mechanical shear stress [44] as shown in Figure 2-11. The sensor is reported to have unreliable steady measurement but due to the high capacitance of the ionic polymer, the sensor is reported to respond well to high frequencies [11]. The sensor was tested up to 5 kHz but sensitivity and noise floor results were not provided.

2.3.2 Direct, Floating Element Techniques

The typical floating element technique for direct shear stress measurement consists of a floating element for integrating shear stress and a restorative structure, such as tethers or cantilevers. The two main types of floating element support are the

parallel-linkage balance and the pivoted balance [33] as shown in Figure 2-12. The balances can either be a displacement or feedback balance. A displacement balance correlates the applied wall shear stress to the deflection of the floating element and a force feedback balance maintains a static position of the floating element by responding with an opposing force towards the applied shear stress [28]. The microscale dimensions of micromachined floating element devices are favorable for the spatial and temporal resolution requirements. Floating element sensors can use capacitive, piezoresistive or optical techniques for transduction.

Several limitations have to be addressed when using the floating element technique. Winters [3], [33] discusses the following the issues that may arise with the use of conventional floating elements for direct shear stress measurement:

- The ability to measure small forces vs. the spatial resolution of the sensor
- The effects of the gaps surrounding the floating element structure
- The effects of misalignments in the floating element
- The force contribution due to pressure gradients acting on the floating element

One possible source of flow disturbance may be generated by the existing gaps surrounding the floating element and the wall. In order for the gaps not to disturb the flow, the gap sizes have to be smaller than several viscous length scales. Such gap sizes is possible using micromachining technology.

Both protruding and recessed floating element misalignments can generate forces and moments on the floating element [33], [45] as shown in Figure 2-13. Generally, micromachined floating elements do not require alignment on the floating element structure. Instead, the primary source of misalignment errors in micromachined floating elements is in the packaging and installation of the device.

The forces applied on the floating element due to shear stress and the forces induced by pressure gradient in a 2-D channel flow can be seen in Figure 2-14. The shear stress across the top surface and the bottom surface of the floating element are defined as τ_w and τ_g respectively. The wall shear stress on the top surface of the floating element for a Poiseuille flow in a channel and the gap shear stress on the bottom surface are defined as,

$$\tau_w = \frac{h}{2} \frac{dP}{dx}, \quad (2-1)$$

and

$$\tau_g = \frac{g}{2} \frac{dP}{dx}, \quad (2-2)$$

where h is the height of the channel, dP/dx is the differential pressure drop across the length of the floating element and g is height of the recessed gap under the floating element. The pressures acting on the sides of the floating element are defined as P_2 and P_1 . The difference between the two pressures can be expressed as [46],

$$P_2 - P_1 = \left(\frac{dP}{dx} \right) W_e, \quad (2-3)$$

where W_e is the width of the floating element. The sum of the forces F_x acting across the floating element is [46],

$$\sum F_x = \tau_w (L_e W_e) + \tau_g (L_e W_e) + \underbrace{(P_2 - P_1)}_{\frac{dP}{dx} L_e} (T_e W_e), \quad (2-4)$$

where L_e is the length of the floating element and T_e is the thickness of the floating element. Using the definition of shear stress in a channel, pressure differential and the sum of the forces, it can be shown that the effective shear stress is given by [46],

$$\tau_{eff} = \tau_w \left(1 + \frac{g}{h} + \frac{2T_e}{h} \right). \quad (2-5)$$

While the measurement errors induced by pressure gradients are dependent on the geometry of the experimental setup and the floating element, micromachined floating element typically have three order of magnitude reduction of pressure gradient induced errors over convention floating elements [3].

The shear stress due acceleration can be approximated by the following equation,

$$\tau_a = \frac{Force}{Area} = \frac{ma}{A} = \frac{\left(\frac{\rho L_e W_e T_e}{mass} \right) a}{\underset{area}{L_e W_e}} = \rho T_e a, \quad (2-6)$$

where m , ρ , L_e , W_e , T_e , A , is the mass, density, length, width, thickness and area of the floating element, and a is the acceleration. The low-mass MEMS floating element sensors offer favorable scaling over conventional floating elements. MEMS floating element sensors offer several orders of magnitude improvement over conventional floating elements since MEMS floating element thickness are typically scale on the order of $\sim 10 \mu m$ whereas conventional sensors scale on the order of $\sim 1 mm$ [3].

An example of a conventional, direct floating element sensor is an interferometric optical strain gauge developed by Pulliam et al. for shear stress measurements. The optical strain gauge consists of an optical fiber and a floating element head as shown in Figure 2-15 [11], [47]. The strain gauge design was based off of the previous designs

from Schetz et al [47], [48]. As the 1/4" cantilevered floating element moves as a result of shear force, the strain in the cantilever is measured by the change interferometric region between the floating element and the optical fiber. The light is transmitted through the optical fiber and received using the same fiber. The calibration between the deflection of the floating element head and shear stress was not provided. However, wind tunnel testing showed that the skin friction gauge measured a coefficient of friction is $C_f \approx 0.0012$ at Mach 3 [47].

A review of existing micromachined floating element sensors is presented the following paragraphs and is organized by transduction technique.

2.3.2.1 Capacitive detection techniques

The first reported micromachined floating-element sensor for shear stress sensor was developed by Schmidt et al. [46], [49]. The device used a differential capacitive transduction scheme for detecting shear, which incorporated P-MOS transistors that are built into the sensor to detect the change in capacitance (Figure 2-16). The device was experimentally calibrated in air and is reported to have a sensitivity of $52 \mu V/Pa$. Since the device was manufactured using a polyimide/aluminum microfabrication technique, the polyimide layer is susceptible to moisture absorption in-plane, which resulted in a drift in the mechanical sensitivity due to the moisture dependent stress. Due to the high impedance of the sensor, the device is also susceptible to electromagnetic interference (EMI). In addition, the device used front-side wire bonds. Although this device faced a number of challenges, the significance of this device is that it demonstrated the potential for shear stress measurements using micromachined floating-elements.

Pan et al. [50] and Hyman et al. [51] have developed capacitive floating element shear stress sensors using comb fingers; the former device is based on differential capacitive, and the latter is based on a capacitive force-feedback and are shown in Figure 2-17. The devices have a sensitivity of approximately 1 V/Pa . Some of the drawbacks of the devices are that the sensors were not flush-mounted and the sensors used front-side wire bonds. The dynamic response of the sensors was not reported.

Zhe et al. have developed a capacitive floating element using a cantilever as the restorative, supporting element instead of tethers for support (Figure 2-18) [52]. The cantilevered floating element structure along with two neighboring beams is used to form differential capacitors. The reported sensitivity of the device is 337 mV/Pa and the lowest detectable shear stress is 0.04 Pa . A dynamic response was not reported. The device on calibration has a large 13% uncertainty due to misalignments in the test channel width and the test channel height. As a capacitive a technique, the device is susceptible to EMI.

Chandrasekharan et al. have developed a capacitive shear stress sensor with interdigitated, asymmetric comb fingers (Figure 2-19) [53]. A simple 2-mask fabrication process is used to define the features of the device and the surface of the device is metal plated with nickel. Bond pads are situated towards the sides of the device for electrical contact. A printed circuit board (PCB) with voltage amplifiers are used to detect the differential output voltage. The device has a sensitivity of 7.66 mV/Pa and a bandwidth of 6.2 kHz . Currently, the performance of this sensor has the highest reported dynamic range ($> 102 \text{ dB}$) as well as the lowest reported noise floor per

minimum detectable signal ($14.9\mu Pa$) [54]. Since this sensor is susceptible to humidity, this sensor is only capable of fluctuating shear stress measurements.

Following Chandrasekharan's design approach, Sells introduced a wireless detection scheme to the capacitive sensor [55]. An inductor coil is added to the capacitive sensor to form a LC tank circuit and the resonance is monitored by a spectrum analyzer and is shown in Figure 2-20. Furthermore, Sells reduced the humidity sensitivity of Chandrasekharan's sensor by the introduction an additional passivation layer coating to the surface of the device. Although Sells is able to achieve a mean shear stress calibration, a dynamic shear stress calibration is not obtained due to the measurement setup.

Meloy subsequently developed an alternate capacitive sensing approach based off of the shear stress sensors developed in Sells's research [56]. Meloy employed a modulation/demodulation technique for sensing capacitance. A static and dynamic calibration is obtained using Meloy's capacitive sensing technique and the reported sensitivity is 6.5 mV/Pa and the bandwidth is 4.7 kHz.

2.3.2.2 Piezoresistive detection techniques

Ng [57] and Goldberg [58] designed a piezoresistive shear stress sensor for high shear stress measurements up to 100 kPa (Figure 2-21). Top-side implanted piezoresistors are arranged in a Wheatstone bridge configuration to detect axial motion in the floating-element. A significant contribution of the device is that the electrical contacts are on the back-side, which allowed the sensor to be flushed mounted while protecting the wire bonds from the flow environment. However, the device possessed a

low sensitivity and was not designed for turbulence measurements due to the target high shear stress application.

Barlian et al. has developed a piezoresistive shear stress sensor for underwater measurement (Figure 2-22) [59]. The piezoresistors are implanted on both the top and sides of the tethers for pressure and shear stress detection, respectively. The device was mechanically calibrated using a benchtop vibrometer and has a reported in-plane sensitivity of $50 \text{ mV}/\mu\text{N}$. The dynamic data was not reported.

Li et al. has developed a piezoresistive shear stress sensor using Boron diffused, side-implanted piezoresistors at the end cap of the tethers (Figure 2-23) [60]. The four side implanted resistors are used to form a Wheatstone bridge for monitoring changes in resistance. The experimental calibration of the device yielded a sensitivity of $4.24 \mu\text{V}/\text{Pa}$ up to 2 Pa . The noise floor is reported to be $48 \text{ nV}/\sqrt{\text{Hz}}$ ($11.4 \text{ mPa}/\sqrt{\text{Hz}}$) at 1 kHz and a flat frequency response up to 6.7 kHz . The drawback of this device is that piezoresistors are sensitive to temperature and susceptible to thermal drift. The complexities in the microfabrication resulted in a mismatch between the active and dummy Wheatstone bridge configuration, which hampers temperature compensation during calibration.

2.3.2.3 Optical detection techniques

Padmanabhan et al. developed an optical floating-element shear stress sensor with on-chip photodetectors [61]. An external light source is used and the floating element acts like optical shutters over the integrated photodiodes to sense the floating element displacement (Figure 2-24). The sensor offers immunity from EMI and is insensitive to pressure fluctuations. However, the optical transduction relies on an

external light source in the experimental setup. Fluctuations in the incident light relative to the mechanical motion of the sensor affects the calibration of the device.

Furthermore, the device used front-side bonds, which adds disturbances to the flow.

Since the optoelectronics are embedded next to the floating element, this configuration does not allow for shear stress measurements in a high temperature environment due to the proximity of the photodiodes and the excessive heat.

Tseng and Lin have developed an optical shear stress sensor using micro-Fabry–Perot interferometry (Figure 2-25) [62]. Optical fibers are used to detect a flexible, reflective micro-pillar structure that serves as the floating element as well as a micro-mirror. The perpendicular position of the two optical fibers with respect to the micro-mirror allows 2D shear stress measurement. For the micro-pillar sensor, the experimental sensitivity is expressed in terms of the shear stress per spectral shift and is reported to be 0.65 Pa/nm with a sensor resolution of 0.065 Pa . Shear measurements in 2D and the frequency response of the sensor are not reported. The drawback of the sensor is that it has a high temperature sensitivity, which is reported to be 3.4 nm/K and a large noise-floor of $2\text{--}3 \text{ nm}$, which corresponds to a shear stress of $1.3 \text{ Pa} \sim 1.95 \text{ Pa}$.

Horowitz et al. introduced a micromachined floating-element sensor using Moiré amplification for shear detection (Figure 2-26) [63]. The device consists of a silicon floating element with tethers that are bonded to a Pyrex base structure. Aluminum gratings on the silicon and Pyrex structures produced the optical Moiré fringe patterns. A microscope is used to observe the fringe patterns and a line-scan charge-coupled device (CCD) camera is used to record the images. The benefits of using the optical

Moiré sensor is that this transduction technique offers increased mechanical sensitivity using the Moiré amplification, immunity from EMI and pressure insensitivity, since variations in the light intensity theoretically does not affect the phase extraction. However, some of the challenges faced using the optical Moiré sensor is that the bulky packaging is rather cumbersome and moving the experimental setup to a non-optical benchtop environment is difficult. For the static calibration, the optical shear stress sensor was tested up to 1.3 Pa in a laminar flow cell and the sensitivity of device was $0.26 \text{ } \mu\text{m}/\text{Pa}$. For the dynamic calibration, the resonant frequency of the device was found to be 1.7 kHz and the noise floor was $1.6 \text{ nm}/\sqrt{\text{Hz}}$ using 1 Hz bins centered at 1 kHz . This corresponds to a minimum detectable shear stress is $6.2 \text{ mPa}/\sqrt{\text{Hz}}$. The use of a CCD for data acquisition adds unnecessary limitations on the overall performance of the device. The large size of the CCD requires optical magnification, such as a laboratory microscope, in order to observe the Moiré fringe patterns which significantly increases the overall packaging size and is shown in Figure 2-27. The large amount of pixel data recorded by the CCD and the CCD sampling rate can also limit the bandwidth during data acquisition. Although the results from the proof-of-concept Moiré device are promising, the use of bulky optics offers room for improvement.

Ayaz et al. introduced an optical shear stress sensor based on whisper gallery mode resonator [64]. A silica beam attached to a pivot is used to support a flat plate that is serves as a sensing surface. When the sensing surface deflects, the silica beam deforms a PMDS based microsphere. The configuration of this device is shown in Figure 2-28. The microsphere is also attached to a tapered section of optical fiber. A

tunable laser coupled to the optical is used to excite the optical modes of the sphere and a photodiode monitors the optical resonance over the range of laser frequencies. The minimum detectable shear stress can be adjusted (from mPa to μ Pa) by changing the mixing ratio of the PDMS but as the MDS improves, the bandwidth decreases.

2.4 Summary

In this chapter, several indirect and direct shear stress measurement techniques are reviewed with an emphasis on micromachined, floating element techniques. Floating element shear stress sensors can be categorized by their transduction techniques into three main types: capacitive, piezoresistive and optical. The capacitive shear stress sensors typically use either comb fingers or the floating element with a base substrate to form the parallel plates necessary for capacitive measurements. Some of the benefits of capacitive shear stress sensors include straight-forward manufacturing processes, simplified packaging, and insensitivity to fluctuations in temperature. However, the capacitive technique is subject to parasitic capacitance and the capacitive measurements are inherently sensitive to EMI. For operation in a conductive fluid such as water, substantial packaging is required to isolate the capacitive comb fingers or plates and electrodes from the surrounding medium. Piezoresistive shear stress sensors typically have piezoresistors implanted on the tethers. A Wheatstone bridge is typically used to monitor changes in the resistance. The piezoresistive shear stress sensors can drift due to temperature and may require compensation. Optical shear stress sensors typically require the use of a light source, a photodetector and some sort of guide for the optical pathway, such as fiber optics or lenses, for transduction. Optical shear stress sensors are highly sensitive to optical misalignments and are difficult to package. However, optical shear stress sensors are

immune to EMI and have the potential to operate in a conducting fluid medium and some optical sensors have the potential for high temperature measurements. The performances of notable floating-element devices can be seen in the following Table 2-2.

This research capitalizes on the benefits of optical shear stress sensors, in particular, using optical Moiré fringes as the transduction technique. The micromachining technology used to manufacture the sensor allows for sufficient spatial resolution and bandwidth to accurately measure turbulent structures in a flow, enabling time-resolved, direct shear stress measurements. The Moiré pattern on the floating element amplifies the deflection due to the applied shear stress which increases the sensitivity of the device. Optical fibers are used to reduce the complexity of the overall packaging and to connect the sensor and the optoelectronic components used for imaging fringe patterns. The optical Moiré transduction technique using optical fibers enables direct shear stress measurements in harsh environments that might not be realized with the other transduction techniques.

The proposed device for this research uses aluminum gratings patterned on a silicon floating element and a Pyrex base structure to generate a Moiré fringe pattern. The size consideration of the Moiré fringe is determined by the desired amplification, the performance of the sensor, microfabrication limits of the optical gratings and by the manufacturing limits of the optical fiber bundle. The fiber bundle consists of 16 source/receive pairs of fibers to illuminate the Moiré pattern and output the discretized fringe pattern to photodiodes. The combination of the optic fiber bundle and

photodiodes removes the unnecessary performance limitations and size restrictions imposed by a CCD camera.

Table 2-1. Shear stress measurement techniques.

	Indirect	Direct
Conventional (Macro)	Surface obstacle sensors, Thermal, Mass Transfer	Oil film, Liquid crystal coatings, Shear stress sensitive coatings
Micromachined (Micro)	Thermal, Micropillars, Microfences	Floating element

Table 2-2. Summary of various floating element shear stress sensors performance and characteristics.

Author	Type	Dyn Range	Sensitivity	BW	Remarks
Schmidt 1988	Floating Element, Capacitive	0.01-1 Pa	52 uV/Pa	10 kHz	First MEMS shear stress sensor
Ng/Goldberg 1991/1994	Floating Element, Piezoresistive	1 kPa-100 kPa			Backside wire bonds, low sensitivity
Padmanabhan 1995	Floating Element, Optical	1.4 mPa - 10 Pa	0.4 mV/Pa	10 kHz	Optical shutter; frontside bond
Pan/Hyman 1995	Floating Element, Capacitive	0.5-3.8 Pa	1 V/Pa	n/a	Pan: Differential capacitive, Hyman: Force feedback
Zhe/Modi 2001	Floating Element, Capacitive	0.04 Pa	337 mV/Pa	n/a	Large sensitivity, large uncertainty, high NF
Tseng/Lin 2003	Micro Pillar, Optical	0.065 Pa	0.65 Pa/nm		
Horowitz 2004	Floating Element, Optical	6.2 mPa-1.3 Pa	13 um/Pa	1.7 kHz	Bulky packaging
Barlian 2005	Floating Element, Piezoresistive		50 mV/uN		
Li 2006	Floating Element, Piezoresistive	11.4 mPa - 2 Pa	4.24 uV/Pa	6.7 kHz	Thermal drift
Chandrasekharan 2009	Floating Element, Capacitive	102 dB	7.66 mV/ Pa	6.2 kHz	Highest reported dynamic range, lowest MDS; susceptible to EMI and humidity

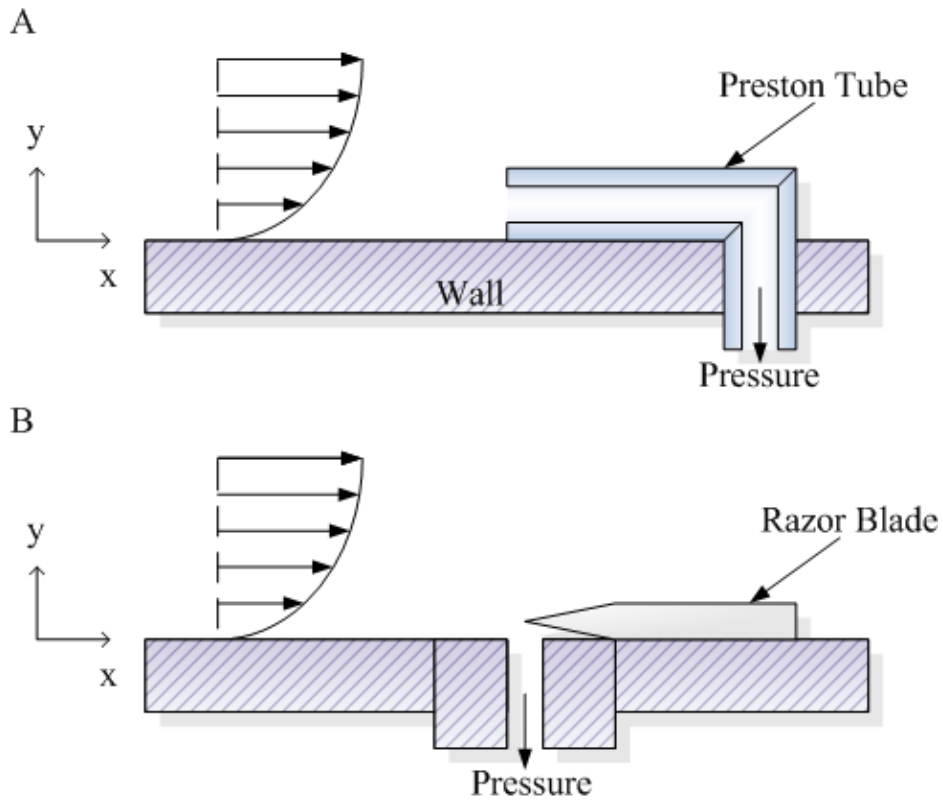


Figure 2-1. Illustration of some indirect shear stress measurement techniques. A) Preston tube. B) Stanton tube/Razor blade.

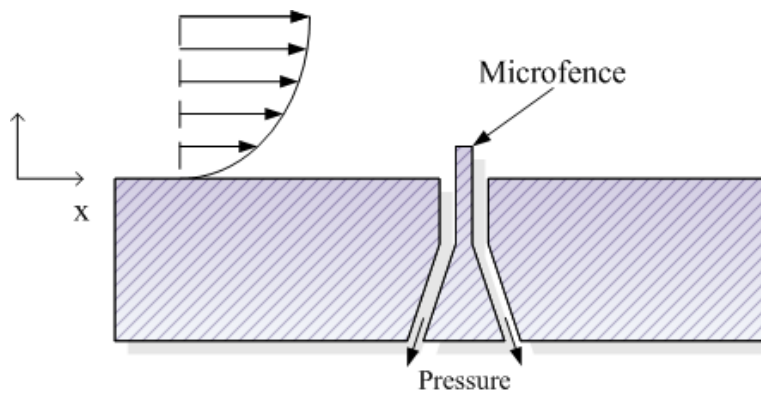


Figure 2-2. Illustration of a microfence structure for indirect shear stress measurement.

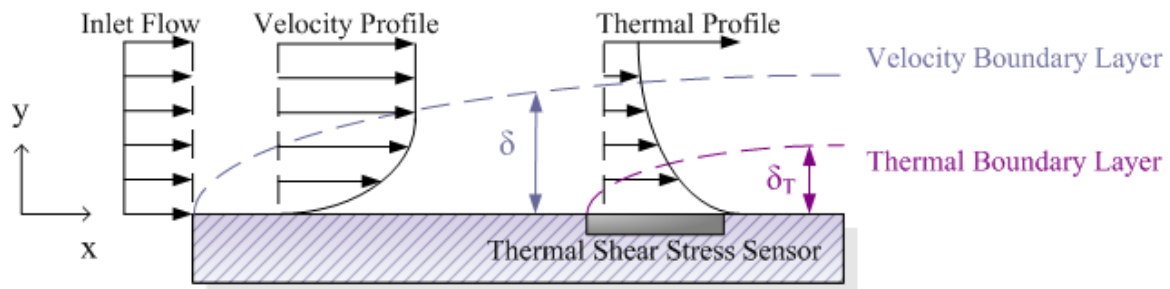


Figure 2-3. Thermal and velocity boundary layers from a hot-film shear stress sensor. Figure is adapted from Naughton and Sheplak [3].

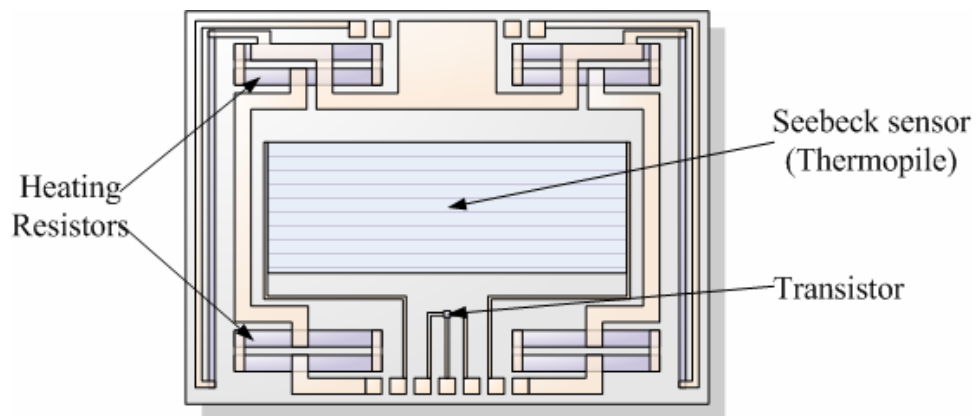


Figure 2-4. The first micromachined thermal shear stress sensor developed by Oudheusden et al. Figure adapted from Oudheusden [36].

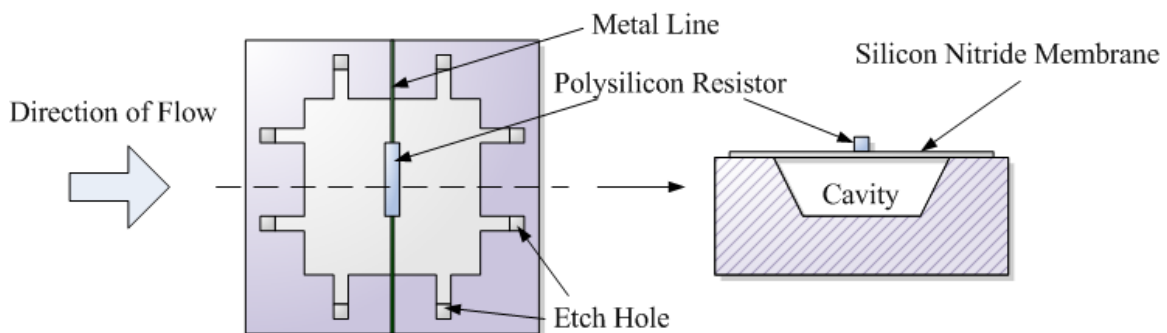


Figure 2-5. Typical structure of a thermal shear stress sensor using a cavity for thermal isolation developed by Ho et al. Figure adapted from Liu et al [65].

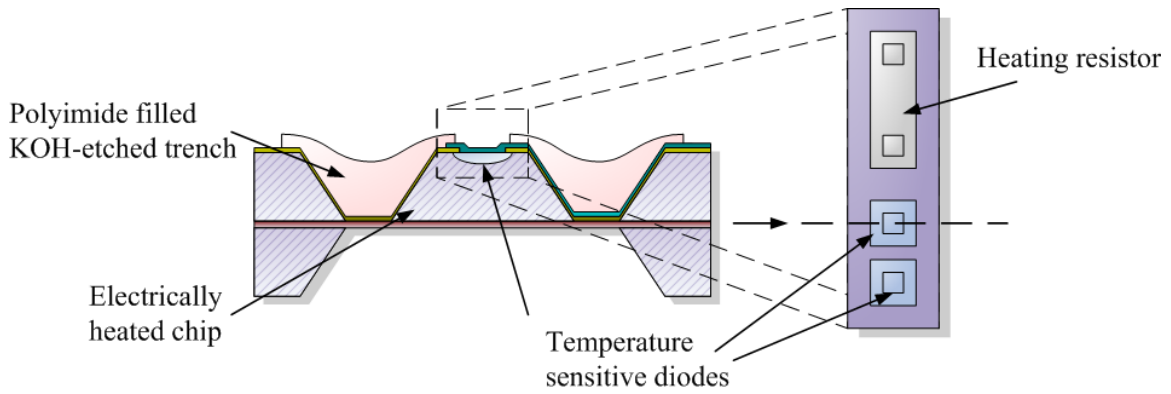


Figure 2-6. A micromachined thermal shear stress sensor developed by Kälvesten using polyimide filled trenches for thermal isolation. Figure adapted from Kälvesten [66].

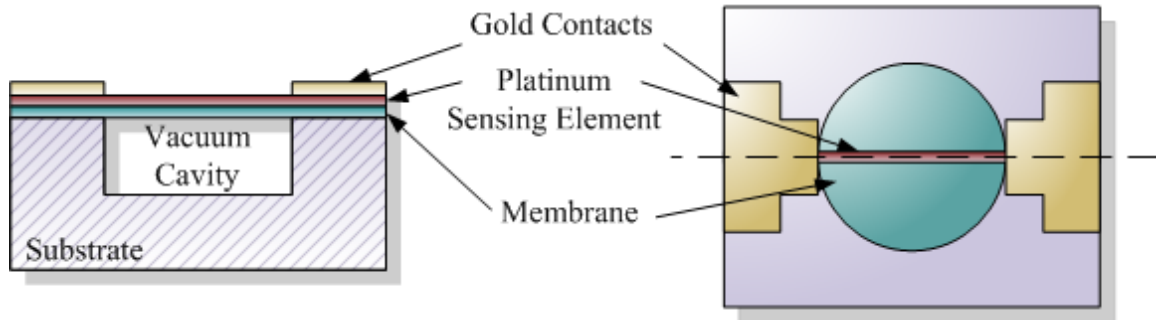


Figure 2-7. Micromachined thermal shear stress sensor developed by Cain and Sheplak. Figure adapted from Cain and Sheplak [39].

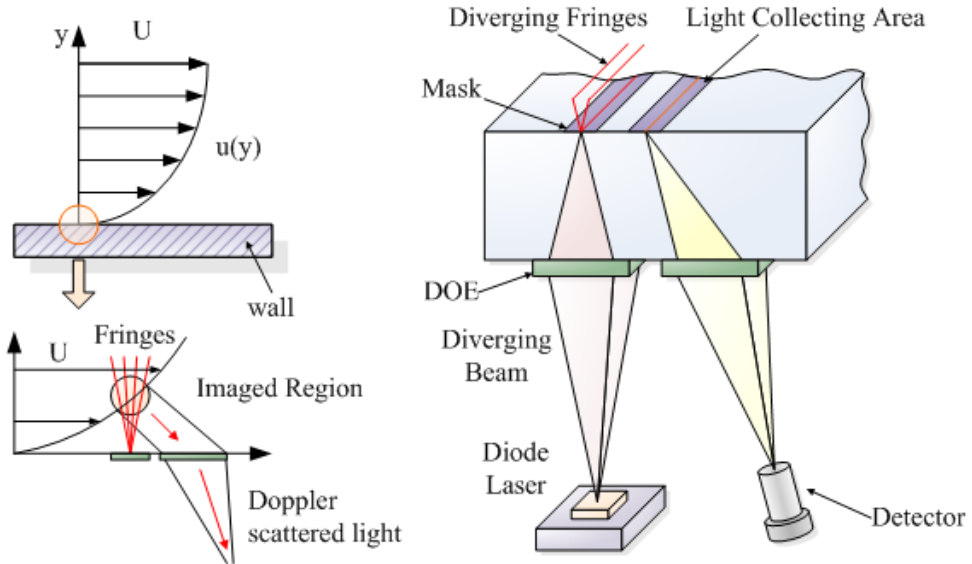


Figure 2-8. A schematic for the Doppler-based optical shear stress sensor. Figure adapted from Viosense [67].

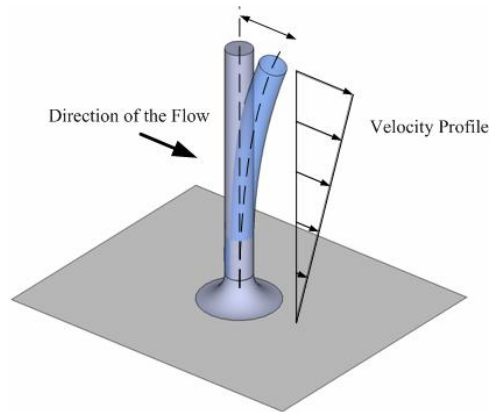


Figure 2-9. A diagram of a micro-pillar structure for indirect shear measurement.

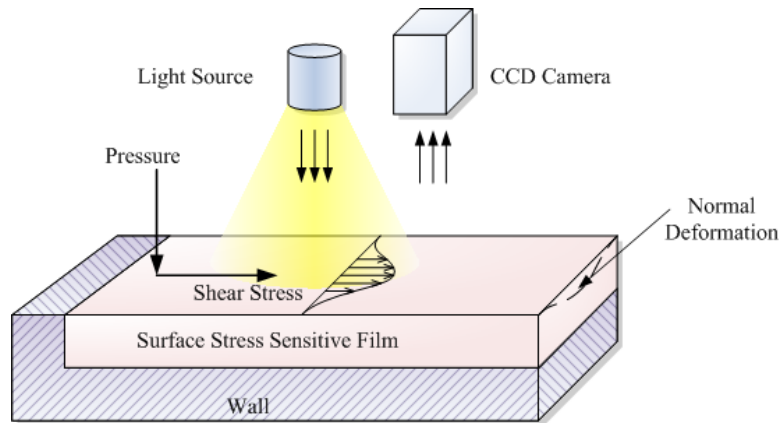


Figure 2-10. Experimental setup of a surface stress sensitive film for direct shear stress measurement. Figure adapted from Crafton [43].

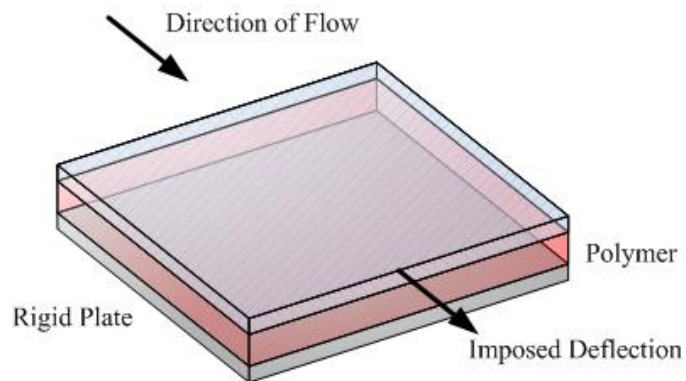


Figure 2-11. Diagram of an ionic-polymer shear stress sensor.

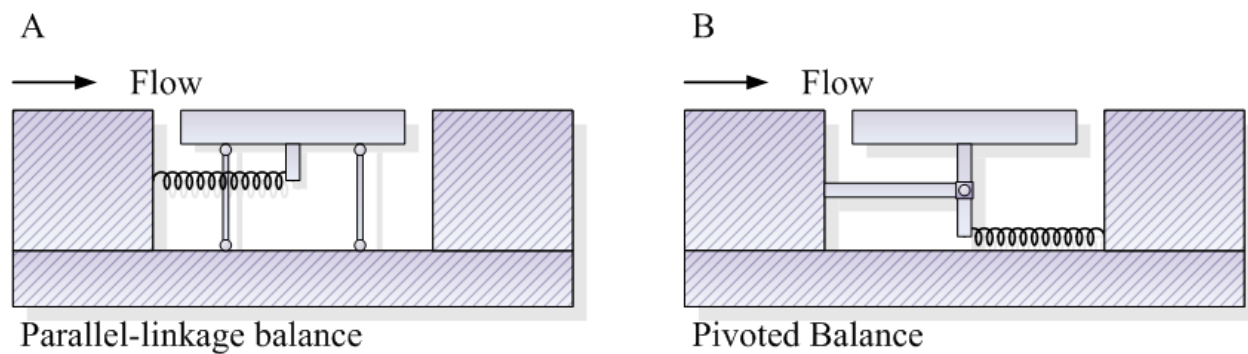


Figure 2-12. Illustration of two types of floating elements. A) Parallel-linkage balance. B) Pivoted balance.

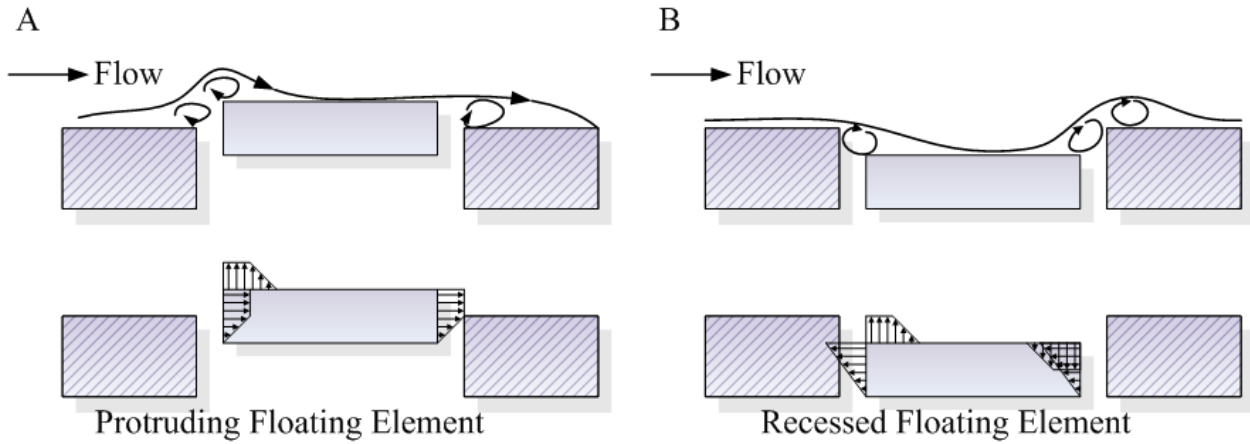


Figure 2-13. Illustration of two types of floating element misalignment. A) Protruding floating element. B) Recessed floating element.

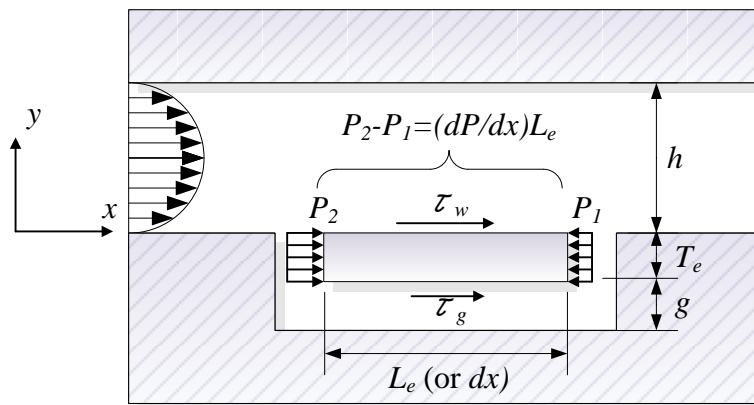


Figure 2-14. Forces acting on the floating element from wall shear stress and pressure gradient induced forces (net lip force and shear stress in the cavity).

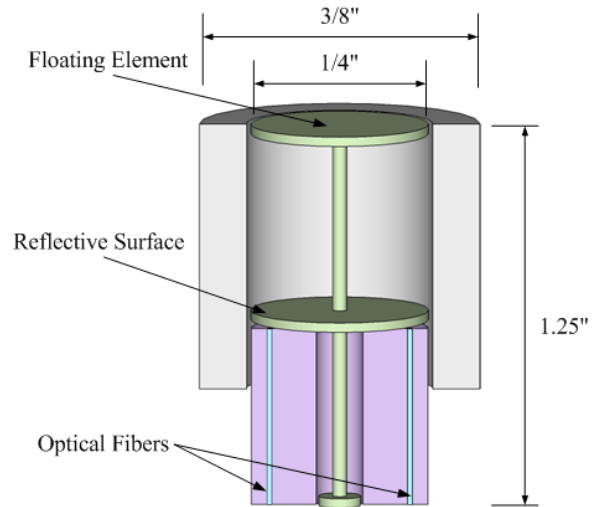


Figure 2-15. Schematic an interferometric shear stress sensor by Pulliam et al. Figure adapted from Pulliam [47].

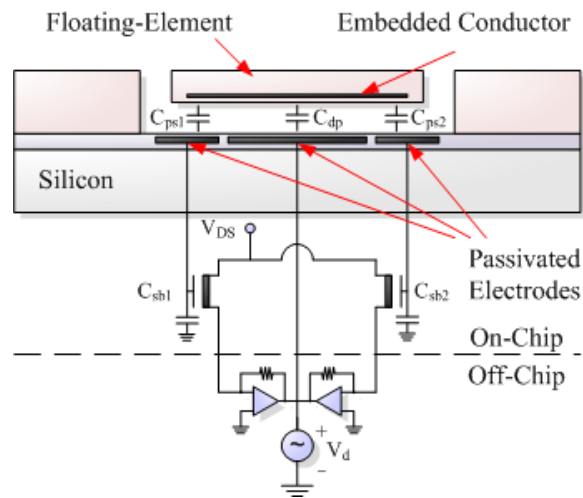


Figure 2-16. Schematic of a capacitive shear stress sensor using a polymer floating element developed by Schmidt et al. Figure adapted from Schmidt [46].

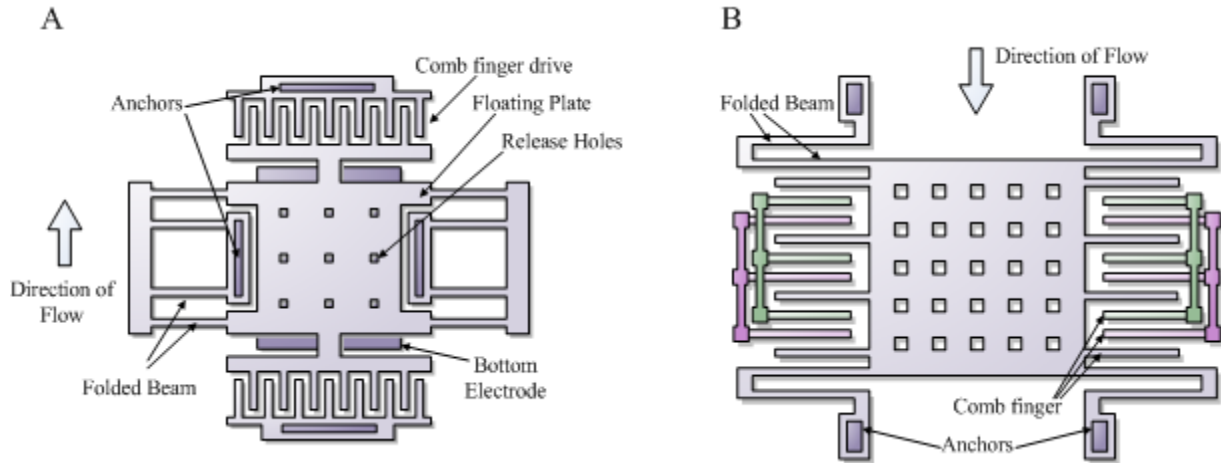


Figure 2-17. Examples of capacitive comb finger shear stress sensors A) Capacitive comb finger developed by Pan. B) Capacitive comb finger developed by Hyman. Figure from adapted Pan [50] and Hyman [51].

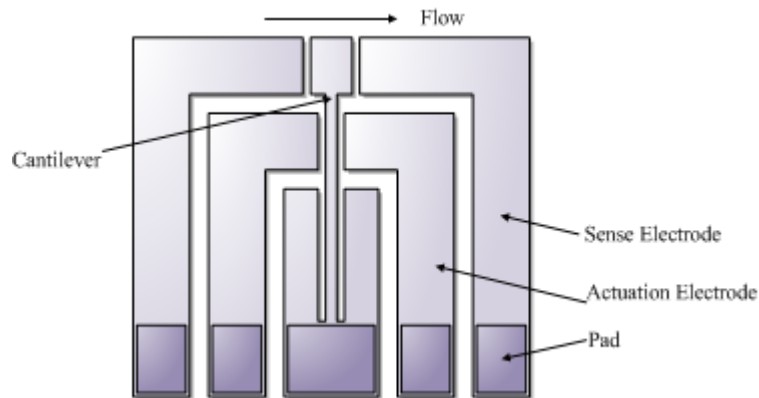


Figure 2-18. Schematic of a cantilever-based, capacitive shear stress sensor by Zhe. Figure adapted from Zhe [52].

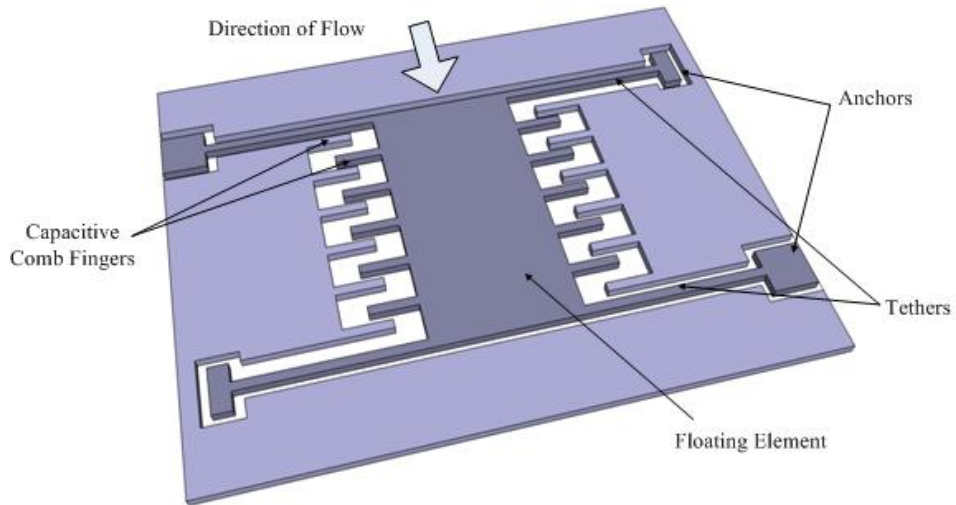


Figure 2-19. Schematic of a capacitive shear stress sensor by Chandrasekharan. Figure adapted from Chandrasekharan [54].

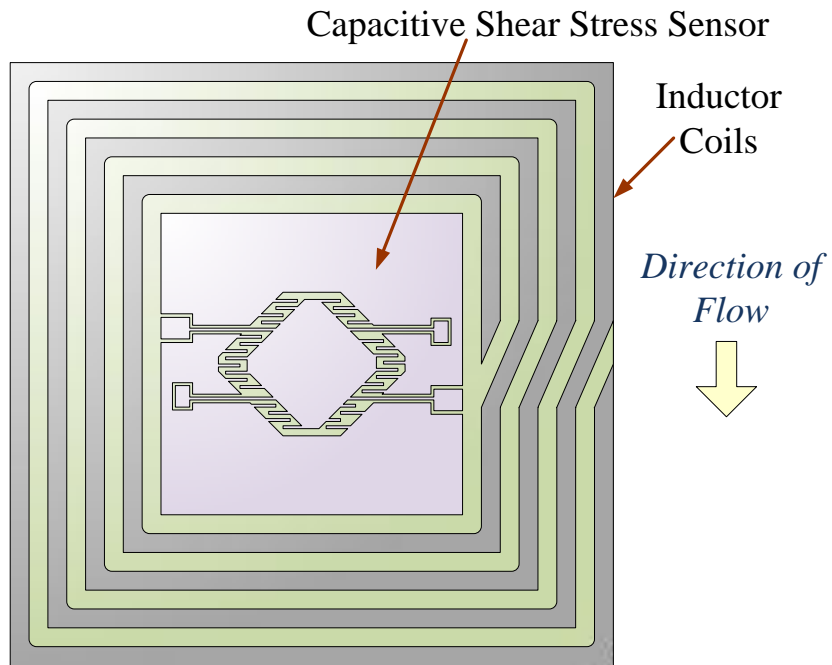


Figure 2-20. Schematic of the capacitive sensor and inductor coil for wireless shear stress sensing by Sells [68].

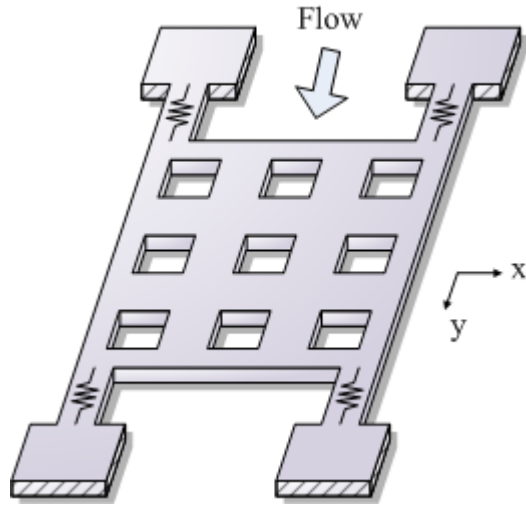


Figure 2-21. Schematic of a piezoresistive shear stress sensor for low flow applications by Ng and Goldberg. Figure adapted from Ng [57].

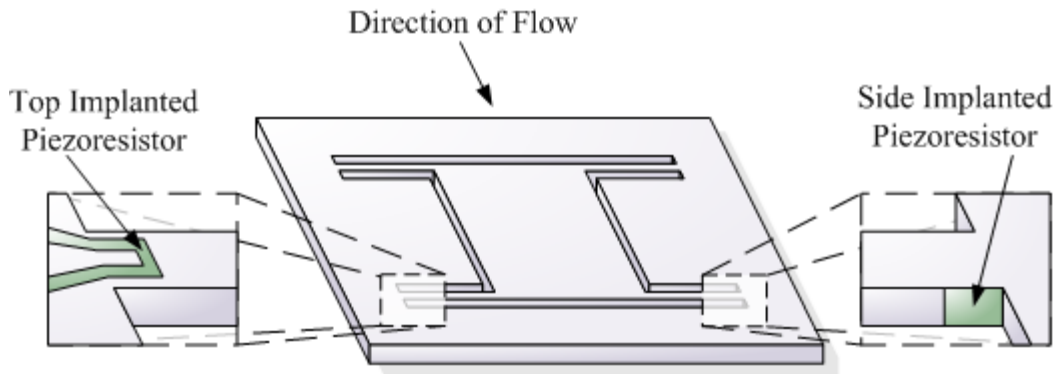


Figure 2-22. Schematic of a piezoresistive shear stress sensor for underwater application by Barlian. Figure adapted from Barlian [59].

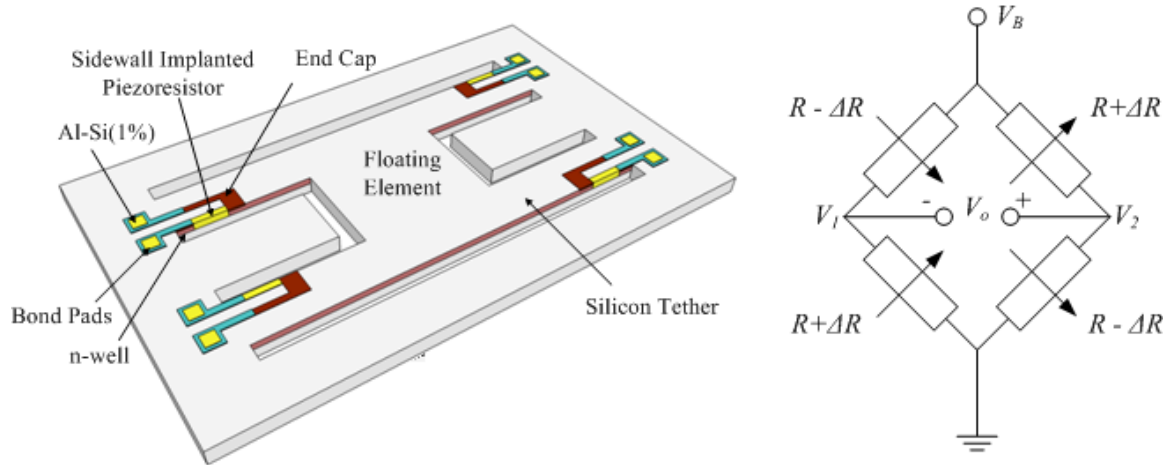


Figure 2-23. Schematic of a piezoresistive shear stress sensor by Li. Figure adapted from Li [69].

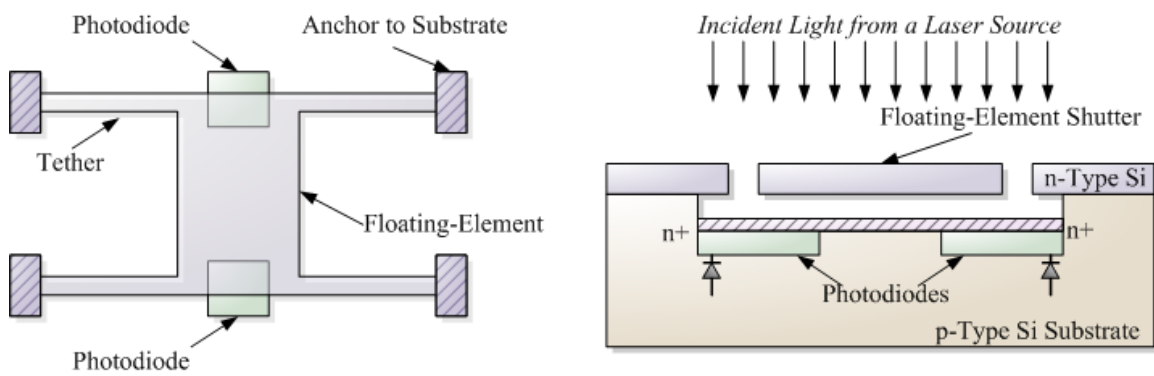


Figure 2-24. Schematic of the integrated photodiodes in the optical shutter shear stress sensor by Padmanabhan. Figure adapted from Padmanabhan [61].

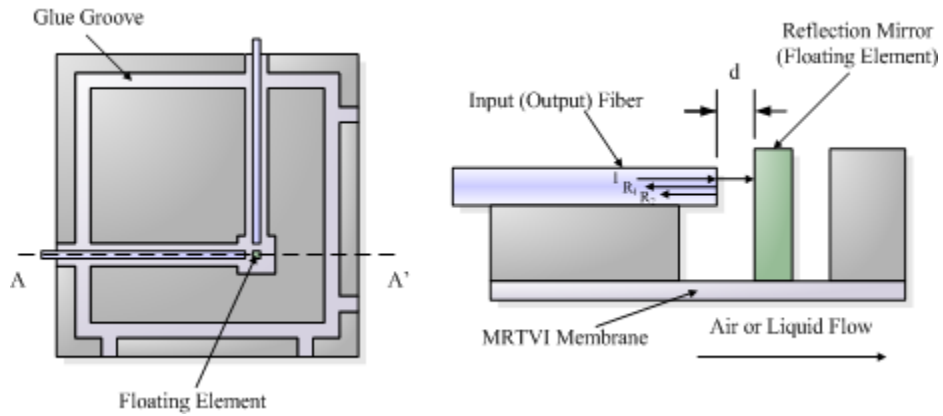


Figure 2-25. Schematic of the 2D micro-pillar optical shear stress sensor by Tseng and Lin. Figure adapted from Tseng and Lin [62].

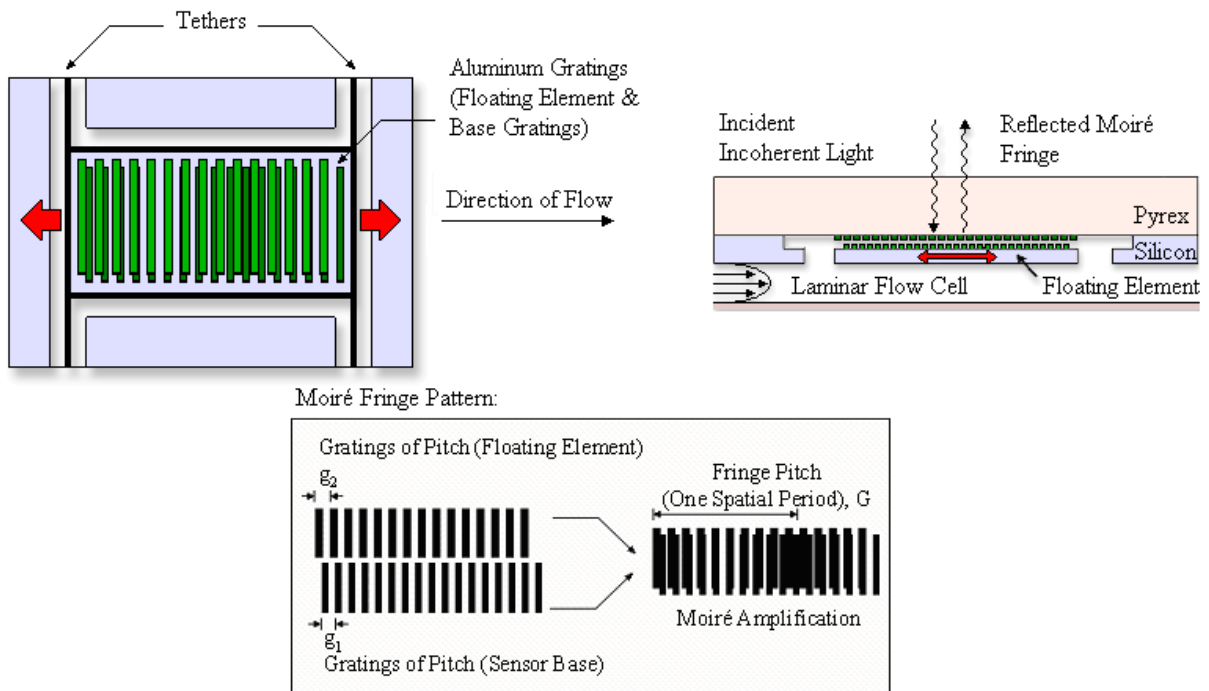


Figure 2-26. Figure of an optical shear stress sensor using Moiré amplification developed by Horowitz et al. Figure from Horowitz et al. and is used with permission [63].

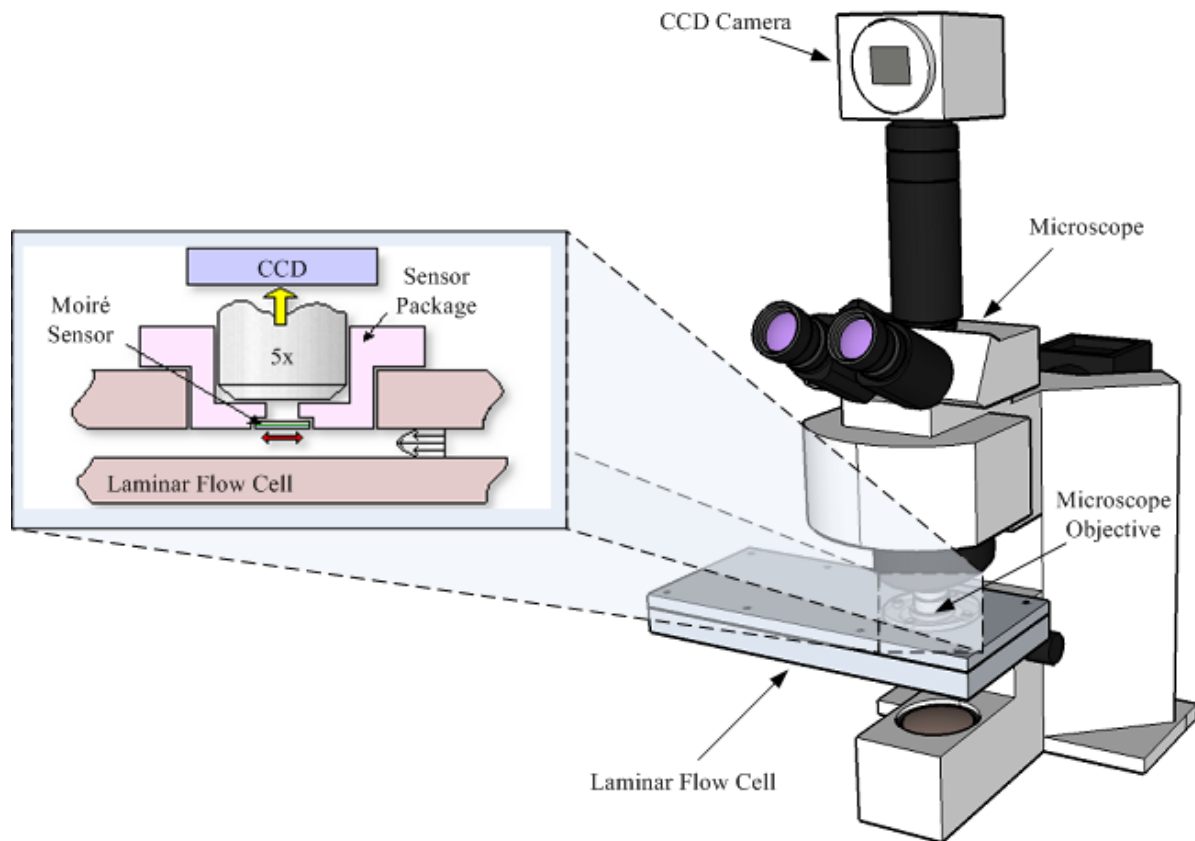


Figure 2-27. Illustration of an optical Moiré shear stress sensor packaged in a laminar flowcell and observed using large, conventional optical packaging.

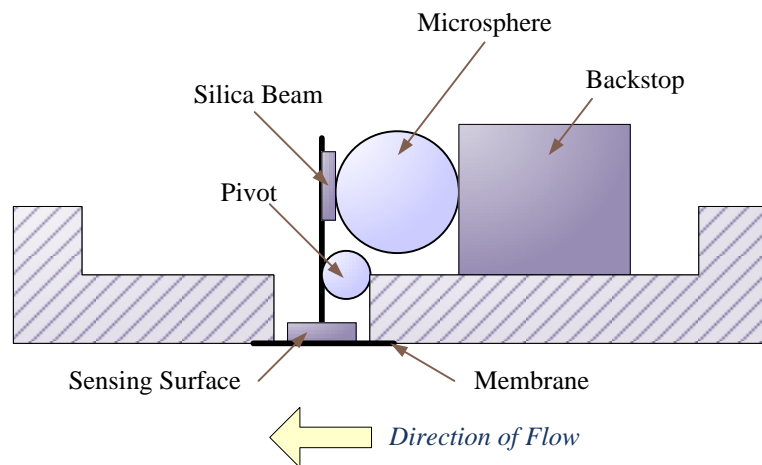


Figure 2-28. Schematic of an optical shear stress sensor using a microsphere resonator.

CHAPTER 3 MECHANICAL MODELING

In this chapter, the mechanical modeling and design of a second-generation optical shear stress sensor using Moiré interferometry is discussed. The mechanics of the floating element determine the mechanical sensitivity, bandwidth and linearity of the sensor. The previous optical Moiré shear stress sensor used conventional optics for imaging, such as a microscope. The Moiré shear stress sensor in this research is designed specifically for use with an optical fiber bundle package for imaging which impose geometric constraints on the element.

The equations for modeling a floating element shear stress sensor are described in this chapter. A simplified mechanical representation for the device as a clamped-clamped beam is used to obtain the floating element deflection due to an applied shear. The deflection of the floating element results in an amplified Moiré fringe shift and the details of the Moiré optical transduction technique are discussed in Chapter 4.

3.1 Device Design

The basic structure of the optical shear stress sensor consists of a silicon floating element that is suspended by two pairs of silicon tethers over a Pyrex base structure as shown in Figure 3-1. The optical Moiré fringe pattern is generated from two sets of aluminum gratings that are located on the silicon floating element and the Pyrex structure. The transparent Pyrex layer serves as a backside optical pathway to Moiré pattern. The deflections in the silicon floating element result in an amplified shift in the Moiré pattern.

The notation used for defining the structures is as follows: the length, width and thickness of the silicon floating element are given by L_e , W_e and T_e while the length,

width and thickness of the tethers are denoted by L_t , W_t and T_t , respectively as shown in Figure 3-2. The pitch of the aluminum gratings on the silicon floating element is defined as g_1 and the pitch of the aluminum gratings on the Pyrex base structure is g_2 . For each of the grating sets, the actual width of the individual gratings is half of the pitch distance.

This device can be modeled using a mass-spring-damper system. The pair of tethers on both sides of the floating element act as a set of springs and the floating element serves as the mass as illustrated in Figure 3-3. When a shear force acts upon the floating element, the floating element deflects and the optical fringe pattern generated by the optical gratings changes proportionally. In the absence of a shear force, the tethers restore the floating element to its initial position. The effective mass and the effective compliance are important for calculating the resonance of the device.

3.1.1 Lumped Element Representation

The mechanical mass-spring-damper system of the device can be modeled using a lumped equivalent circuit representation [1], [69], [70]. The lumped element modeling is valid assuming that the length scale of interest, such as the feature size of the sensing device, is much smaller than the characteristic length scale of the phenomena being measured, in this case, turbulent structures. From a fluid mechanics perspective, the validity of the lumped element assumption means the avoidance of spatial averaging.

The governing equation for a second-order mechanical system is given by the following differential equation,

$$F = m \frac{d^2 x}{dt^2} + b \frac{dx}{dt} + kx, \quad (3-1)$$

where F is the forcing term or the effort variable, x is the distance or displacement variable, m is the mass or inertance, b is the damping coefficient, and k is the spring constant or stiffness. The force in this case, is related to the wall shear stress and the distance is the mechanical deflection.

The frequency response of the mechanical system can be written in terms of angular frequency ω using a Fourier transform,

$$\frac{x(j\omega)}{F(j\omega)} = \frac{\left(\frac{1}{m}\right)}{(j\omega)^2 + \left(\frac{b}{m}\right)(j\omega) + \left(\frac{k}{m}\right)}. \quad (3-2)$$

The contribution to the frequency response due to damping is assumed to be negligible. Since the angular frequency ω is equal to $2\pi f$, where f is the cyclic frequency, the resonant frequency of undamped, spring-mass system is,

$$f = \frac{1}{2\pi} \sqrt{\frac{k}{m}}. \quad (3-3)$$

The stiffness k of the spring is inversely proportional to the compliance C and is given by,

$$k = \frac{1}{C}. \quad (3-4)$$

Substituting the effective mass M_{me} and the effective compliance C_{me} , the resonant frequency becomes,

$$f = \frac{1}{2\pi} \sqrt{\frac{1}{M_{me} C_{me}}}. \quad (3-5)$$

The effective mass and effective compliance of the device can be obtained by mechanically modeling the tethers as a clamped-clamped beam and the floating element as a mass [69]. The combination of the clamped-clamped beam and the

floating element results in a deflection equation which can then be used in energy equations to solve for the effective mass and effective compliance.

3.1.2 Linear Deflection

The assumption used in calculating the deflection equation is that the small deflections are linear, which enables the use of superposition for the contributions from the floating element and the tethers. Furthermore, if the floating-element is assumed to be rigid and homogeneous, the shear stress acting on the floating-element structure can be treated as a point load while the tethers are treated as a distributed shear stress across a clamp-clamped beam as shown in Figure 3-4.

Since there are two tethers supporting the floating element, the total length of the clamped-clamped beam is defined as,

$$x = 2 \cdot L_t. \quad (3-6)$$

The distributed load q , which represents the shear force distributed across the tethers is given by,

$$q = \tau_w W_t \quad (3-7)$$

where τ_w is the wall shear stress. The point load p , which represents the point force acting on the mass of the floating element is given by,

$$p = \frac{\tau_w W_e L_e}{2}. \quad (3-8)$$

The reason why the point load is divided by two is because there are two sets of tethers, supporting the floating element. If the thickness of the floating element and the thickness of the tethers are the same, the thickness of the tethers is denoted by T_t . The

resulting deflection δ using the superposition of a distributed load and a point load becomes,

$$\delta(x) = \frac{\tau_w}{2ET_i W_t^3} \left[W_e L_e \left(\frac{3}{2} L_e x^2 - x^3 \right) + W_t (x^4 - 4L_e x^3 + 4L_e^2 x^2) \right], \quad (3-9)$$

where x is the distance along the beam, and E is the Young's Modulus.

For the different orientations of silicon wafers, Young's modulus can be determined using stress and strain relationships. Normal stress σ is related to normal strain ε using stiffness coefficients C_{ij} and the compact matrix form is given by [71],

$$\sigma_i = \sum_j C_{ij} \varepsilon_j. \quad (3-10)$$

The inverse of the stiffness coefficient is the compliance coefficient, S_{ij} , which relates shear stress τ to pure shear γ and is expressed as [71],

$$\varepsilon_i = \sum_j S_{ij} \sigma_j. \quad (3-11)$$

The matrix for the stiffness coefficients of silicon C_{ij} is written as,

$$\begin{pmatrix} \sigma_x \\ \sigma_y \\ \sigma_z \\ \tau_{yz} \\ \tau_{zx} \\ \tau_{xy} \end{pmatrix} = \begin{pmatrix} C_{11} & C_{12} & C_{12} & 0 & 0 & 0 \\ C_{12} & C_{11} & C_{12} & 0 & 0 & 0 \\ C_{12} & C_{12} & C_{11} & 0 & 0 & 0 \\ 0 & 0 & 0 & C_{44} & 0 & 0 \\ 0 & 0 & 0 & 0 & C_{44} & 0 \\ 0 & 0 & 0 & 0 & 0 & C_{44} \end{pmatrix} \begin{pmatrix} \varepsilon_x \\ \varepsilon_y \\ \varepsilon_z \\ \gamma_{yz} \\ \gamma_{zx} \\ \gamma_{xy} \end{pmatrix} \quad (3-12)$$

where $C_{11} = 196 \text{ GPa}$, $C_{12} = 64 \text{ GPa}$ and $C_{44} = 80 \text{ GPa}$ for silicon [71]. The Young's modulus is related to the compliance coefficients given by [71], [72],

$$\frac{1}{E} = S_{11} - 2 \left(S_{11} - S_{12} - \frac{1}{2} S_{44} \right) (l_1^2 l_2^2 + l_2^2 l_3^2 + l_1^2 l_3^2) \quad (3-13)$$

where $l_1 = \cos \phi \cos \theta$, $l_2 = -\sin \phi$ and $l_3 = \cos \phi \sin \theta$. The angle θ defines the elevation in the z-direction and the angle ϕ defines the azimuth with respect to x-y plane of the wafer as shown in Figure 3-5.

The direction of the tethers are aligned in the $\langle 110 \rangle$ direction of a (100) silicon wafer, which results in $\theta = 0^\circ$ and $\phi = 45^\circ$. The compliance coefficients for a (100) silicon wafer are given as $S_{11} = 7.68 \times 10^{-12} Pa^{-1}$, $S_{12} = -2.14 \times 10^{-12} Pa^{-1}$ and $S_{44} = 12.6 \times 10^{-12} Pa^{-1}$ [72] which results in a Young's modulus of $E = 168.9 GPa$.

Since the maximum deflection of the tethers occurs at $x = L_t$, the deflection equation becomes the Euler-Bernoulli equation for small deflections,

$$\delta = \tau_w \frac{L_e W_e}{4ET_t} \left(\frac{L_t}{W_t} \right)^3 \left\{ 1 + 2 \frac{L_t W_t}{L_e W_e} \right\}. \quad (3-14)$$

The mechanical sensitivity for the device is proportional to the deflection of the floating element for a given shear stress,

$$S_m = \frac{\delta}{\tau_w}. \quad (3-15)$$

The effective compliance and the effective mass are computed by using the Euler-Bernoulli deflection equation into the work energy equations.

$$W_{PE} = \int dW_{PE}^* = \int_0^{q_0} e dq = \frac{1}{2} \left(\frac{1}{C_{me}} \right) \delta^2(L_t). \quad (3-16)$$

The effective compliance of the device is,

$$C_{me} = \frac{1}{4ET_t} \left(\frac{L_t}{W_t} \right)^3 \frac{\left(1 + 2 \cdot \left(\frac{W_t L_t}{W_e L_e} \right) \right)^2}{\left(1 + 4 \left(\frac{W_t L_t}{W_e L_e} \right) + \frac{64}{15} \left(\frac{W_t L_t}{W_e L_e} \right)^2 \right)}. \quad (3-17)$$

The effective mass of the system is found by relating the kinetic co-energy of the beam to the kinetic co-energy of the lumped system by,

$$W_{KE}^* = \int dW_{KE}^* = \int_0^f p df = \frac{1}{2} M_{me} f^2, \quad (3-18)$$

where p is momentum and f is a flow variable. The total effective mass of the device, including the contributions from the tethers and the mass of the floating element, is found to be,

$$M_{me} = \underbrace{\rho T_t (W_e L_e) \frac{\left(\frac{2048}{315} \left(\frac{W_t L_t}{W_e L_e} \right)^3 + \frac{652}{105} \left(\frac{W_t L_t}{W_e L_e} \right)^2 + \frac{52}{35} \left(\frac{W_t L_t}{W_e L_e} \right) \right)}_{M_{tethers_effective}} \frac{1}{\left(1 + 2 \left(\frac{W_t L_t}{W_e L_e} \right) \right)^2} + \underbrace{\rho T_e (W_e L_e)}_{M_{element}}, \quad (3-19)$$

where ρ_{Si} is the density of silicon and $\rho_{Si} = 2330 \frac{kg}{m^3}$.

The mechanical resonant frequency of the device can be found by substituting C_{me} and M_{me} into,

$$f = \frac{1}{2\pi} \sqrt{\frac{1}{M_{me} \cdot C_{me}}}. \quad (3-20)$$

3.1.3 Nonlinear Deflection

For a large deflection due to shear stress, the contribution from strain at the ends of the clamped-clamped beams needs to be accounted for and results in more unknown

variables than boundary conditions. The nonlinear deflection is approximated by using an energy-based solution given by [69],

$$\delta \left(1 + \left(\frac{3}{4} \right) \left(\frac{\delta}{W_t} \right)^2 \right) = \tau_w \frac{L_e W_e}{4ET_t} \left(\frac{L_t^3}{W_t^3} \right) \left\{ 1 + 2 \frac{L_t W_t}{L_e W_e} \right\}. \quad (3-21)$$

A solution for the deflection is found by using the known dimensions of the device and iteratively incrementing the shear stress level to solve for δ . The deflection in the device is considered to be nonlinear if the deflection using the nonlinear equation deviates 3% from the deflection using the Euler-Bernoulli equation. If the deflections in

the nonlinear deflection equation are small enough such that $\frac{3}{4} \left(\frac{\delta}{W_t} \right)^2 \ll 1$, then the

$\left(\frac{3}{4} \right) \left(\frac{\delta}{W_t} \right)^2$ term is considered to be negligible. As a result the equation for nonlinear deflection reduces to the Euler-Bernoulli equation for small deflections.

The bending stress distribution through the tethers is given by [69],

$$\sigma_x(x, y) = \frac{\tau_w W_e L_e L_t}{W_t^2 T} \left(1 - \frac{2y}{W_t} \right) \left(\left(\frac{3}{4} + 2 \frac{W_t L_t}{W_e L_e} \right) - \left(\frac{3}{2} + 6 \frac{W_t L_t}{W_e L_e} \right) \left(\frac{x}{L_t} \right) - \left(3 \frac{W_t L_t}{W_e L_e} \right) \left(\frac{x}{L_t} \right)^2 \right), \quad (3-22)$$

where x is the location along the length of the tether and y is the location along the width of the tether. The maximum shear stress is located at $x=0$ (edge) and $y=0$ (surface) of the tether [69].

The nonlinear deflection equation and bending stress distribution equation are useful to determine the upper end of the dynamic range. For large deflections, the

tethers typically exhibit nonlinearity before they fail from the from excessive stress for the geometries of interest

3.2 Sensor Parameters

The performance of a device can be attributed to several variables, such as the dimensions of the transducer, aspect ratios and material properties. Device manufacturing limitations, packaging and size requirements as well as target performance specifications limit the design of the sensor. The goal is to manufacture a redesigned floating element sensor that accommodates the prototype optic fiber bundle to observe a Moiré fringe pattern.

In order for the device to adequately measure shear stress, the sensor must have sufficient temporal and spatial resolution. For typical low speed applications, the spatial and temporal resolution can be estimated using the Kolmogorov length and time scales. Assuming a 10 Pa flow, the sensor should have a spatial resolution of $\sim 10 \text{ }\mu\text{m}$ and a temporal resolution of $\sim 10 \text{ kHz}$ to avoid spatial and low pass filtering the data due to insufficient bandwidth. Other considerations such as undesirable cross-axis vibration and pressure fluctuation contributions, fabrication limitations and optical components are observed when designing the geometries of the device.

A mechanical optimization can be used to maximize the sensor performance in terms of dynamic range and bandwidth. The goal is to optimize the in-plane response of the sensor due to shear stress while rejecting the out-of-plane response due to pressure [73]. The operating space for the out-of-plane pressure response can be replaced with constraints to allow for a single objective optimization. An illustration of the operation space is shown in Figure 3-6.

In order to improve the dynamic range of the sensor, it is desirable to minimize the noise floor and maximize the sensitivity. The noise floor and the sensitivity of the device can be related by the minimum detectable signal MDS. The MDS is defined as the smallest measurable signal in a device is the ratio between the noise floor and the sensitivity. The MDS for the Moiré sensor is a function of the noise the optoelectronics fringe estimation techniques, and the size of the sensor. However, the MDS for the optical shear stress sensor is currently not well defined due to the significant optical cross-talk issues inherent to the source-receive optical fiber pair of the optoelectronics as discussed in Chapter 4. Instead of performing a formal optimization, design variables based of previous floating element shear stress sensors are selected for a prototype Moiré sensor for use with fiber optics.

Design variables affect the target performance of the device, such as the resonance of the device, maximum shear stress due to nonlinearities and the minimum detectable signal of the device. The geometric design variables are L_e , W_e and T_e for the floating element, L_t , W_t and T_t for the tethers, and g_1 and g_2 for the pitch of the aluminum gratings on silicon and Pyrex layers, respectively.

The gratings determine the spatial period and amplification of the Moiré fringe pattern, which affect the overall sensitivity of the device. The dimensions of the floating element contributes significantly towards the total effective mass of the device while the tether dimensions affects the effective compliance in addition to some contribution towards the effective mass of the device.

Constraints are restrictions placed on design variables. Some of the constraints are based off of fabrication limitations, packaging requirements or performance

specifications. Other restrictions placed on design variables are bound, such as physical bounds. Upper bound (LB) and lower bounds (LB) restriction are placed on each of the design variables in order to prevent obtaining undesirable values.

$$\{LB\} < \{L_e, W_e, T_e, L_t, W_t, T_t\} < \{UB\}. \quad (3-23)$$

For the geometric constraints, the following values were used for a lower and upper bound per design variable,

- Tether Length: $100\mu m \leq L_t \leq 2000\mu m$
- Tether Width: $10\mu m \leq W_t \leq 30\mu m$
- Tether Thickness: $20\mu m \leq T_t \leq 50\mu m$
- Element Width: $1000\mu m \leq W_e \leq 3000\mu m$
- Element Length: $500\mu m \leq L_e \leq 2000\mu m$
- Element Thickness: $20\mu m \leq T_e \leq 50\mu m$
- Grating Pitch: $9\mu m \leq g_1, g_2 \leq 20\mu m$

Conservative values were selected for the dimensions of the floating element, tethers and gratings. The goal is to design a sensor that accommodates a prototype optic fiber bundle. The large width and length of the floating element is selected to ensure that the Moiré fringe pattern is easily positioned for the fiber bundle.

Furthermore, these dimensions are also selected to improve the microfabrication success rate of the devices.

The manufactured optical fiber bundle used to observe the Moiré fringe pattern has 16 fibers spread across a distance of approximately 1 mm. Photodiode arrays with 16 elements are readily available and the number of optical fibers are selected to match the photodiode elements. The detection of a full Moiré period is desired and so the minimum width of the floating element is set to be 1 mm to match the optical detection package. Furthermore, due to the current limitations in fabrication, the spatial pitch of

the gratings g_1 and g_2 are selected to be $9.9 \mu m$ and $10 \mu m$, which yields a resulting Moiré period of $990 \mu m$.

Shear stress contribution due to acceleration sensitivity, τ_a , in the floating element can be estimated from equation (2-6) and so acceleration is a function of shear stress, density and thickness of the floating element,

$$a = \frac{\tau_a}{\rho \cdot T_e} . \quad (3-24)$$

For an acceleration of 1 g, the shear stress contribution from acceleration on a silicon floating element with a thickness of $45 \mu m$ is $1.03 Pa$, where the density of silicon is $\rho_{Si} = 2330 kg/m^3$ and gravity is $g = 9.81 m/s^2$. Compared with a conventional floating of a thickness $1 mm$ or greater, the shear stress due to acceleration for $1 mm$ thick conventional floating element is $22.8 Pa$ or more.

To reduce the cross-axis pressure contribution on the floating element, an aspect ratio of the tether width to tether thickness has been selected to be at least 1:3. The larger tether thickness is to increase the stiffness of the tethers in the normal direction to reduce the deflections caused by pressure when detecting shear stress. Due to microfabrication restrictions, the width of the tethers was selected to be at least $10 \mu m$.

Using small deflection theory, if the area of the tethers are much smaller than the area of the floating element such that $L_t W_t \ll L_e W_e$, then the stream-wise compliance C_x (x-direction shown in figure Figure 3-3) of the floating element can be approximated using the following equation,

$$C_x = \frac{1}{k} = \frac{\delta}{F} \approx \frac{1}{4ET_t} \left(\frac{L_t}{W_t} \right)^3 . \quad (3-25)$$

Likewise, the cross-axis compliance in the y-direction, C_y , can be approximated using,

$$C_y \approx \frac{L_t^3}{EW_t T^3}. \quad (3-26)$$

The ratio between the transverse compliance of C_x and C_y is approximated as,

$$\frac{C_y}{C_x} \approx \left(\frac{W_t}{T}\right)^2. \quad (3-27)$$

An increase in the tether thickness results in a squared factor over the compliance in the y-direction. For a tether thickness of $45\mu m$ and a tether width of $10\mu m$, the 4.5 aspect ratio yields a $20.25\times$ less cross-axis compliance C_y than the stream-wise compliance, C_x .

The target specifications for the shear stress sensor are as follows: $5 Pa$ and $50 Pa$ for the shear stress and $1 kHz$, $2 kHz$ and $5 kHz$ for the resonant frequency. The desired parameters of interest are the resonant frequency, sensitivity, maximum deflection ΔL_{max} of the device. Table 3-1 shows the expected resonant frequency, sensitivity and maximum deflection, ΔL_{max} , as well as the deflection, ΔL , for a $5 Pa$ input.

Some useful trends and performance tradeoffs can be observed from the design of the sensor. Certain geometries influence certain performance characteristics more than others. For example, while the effective compliance in the stream-wise flow direction is inversely proportional to both the thickness and width of the tethers, a change in the width of the tethers is more significant than a change in the thickness of the tethers since the tether width term is to the third power and the tether thickness term is to the

first power. Furthermore, various performance characteristics are dependent on other characteristics, such as the relationship between compliance, sensitivity and resonance. For example, the sensitivity is proportional to compliance and hence, inversely proportional to stiffness. A large sensitivity is desired to minimize the MDS and hence, an increase in the compliance is desired. However, having smaller tether widths, which increases the compliance of the device, results in a reduction in the overall resonant frequency for the device and a decrease in the bandwidth. The compromise between the gain of the device due to its sensitivity and the frequency range where the device has constant sensitivity is known as the gain-bandwidth tradeoff. Additionally, as the maximum shear stress is increased, the sensitivity also decreases.

The aspect ratio between the tether width and the tether thickness results in a large thickness in the tethers and a large thickness in the floating element. As a result, the resonant frequency of the device is very low due to the size of the floating element. The optic requirements make the width of the floating element quite large and so the effective mass is large. Reducing the mass of the floating element to increase the resonant frequency by decreasing the thickness from either the cavity or flow surface side is not an option. Reducing the thickness of the floating element from the cavity side increases the gap distance between the optical gratings and reducing the floating element from the flow surface makes the surface of the floating element not flush.

In summary, the second-generation optical Moiré shear stress sensor is redesigned to accommodate a fiber optic package to capture the optical fringe pattern. The equations used to mechanically modeling the floating element sensor are described

and values for the design variables are listed. Also, a brief discussion of the performance tradeoffs is covered.

Table 3-1. Selected geometries for the second-generation optical Moiré shear stress sensor.

Device Design, Parameters	5Pa,1kHz	5Pa,2kHz	5Pa,5kHz	50Pa,5kHz
L_t (μm)	1400	1250	1100	800
W_t (μm)	10	10	20	20
T_t (μm)	43	43	43	43
L_e (μm)	1500	1000	1500	1500
W_e (μm)	1800	1500	2500	1500
T_e (μm)	43	43	43	43
f (kHz)	1.0	1.59	3.44	7.16
Sensitivity ($\frac{nm}{Pa}$)	257.52	102.47	21.72	5.02
ΔL_{max} (μm)	2.0	2.0	4.0	4.1
τ_{max} (Pa)	8	20	189	828
ΔL_{max} @ 5Pa (μm)	1.28	0.51	0.11	0.025

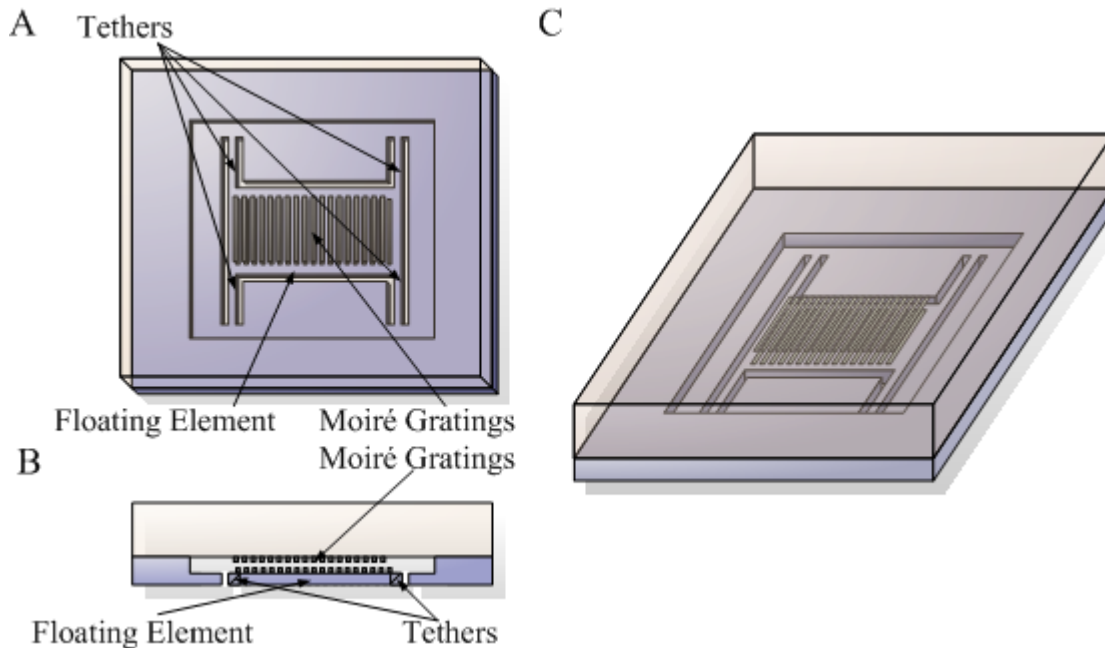


Figure 3-1. Illustration of the optical Moiré shear stress sensor. A) Top view. B) Side cross-sectional view. C) 3D oblique projection.

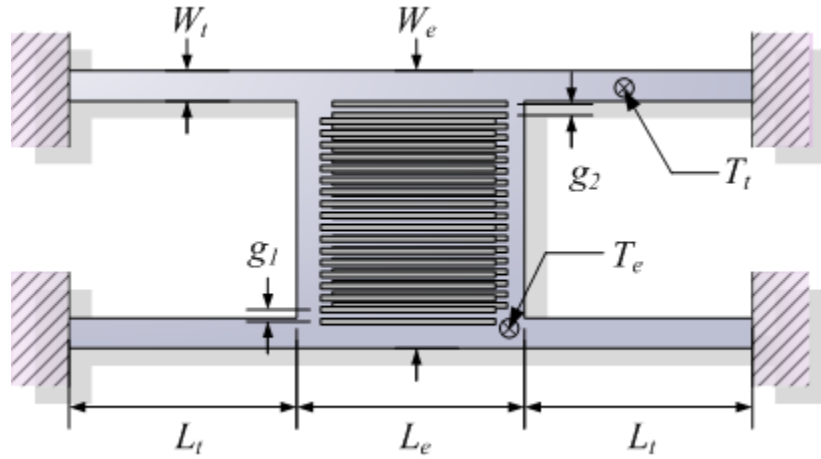


Figure 3-2. Diagram of the geometric features of the optical shear stress sensor.

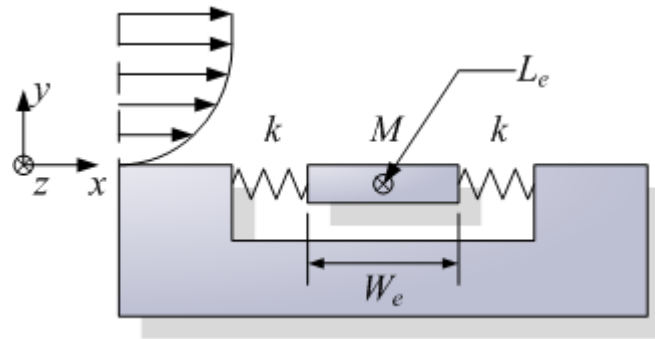


Figure 3-3. Cross-section view of a shear stress sensor using mechanical representation.

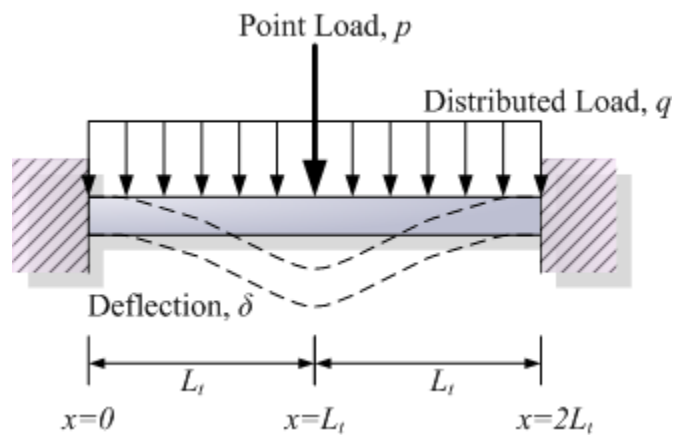


Figure 3-4. Diagram of a point load and distributed load on a clamped-clamped beam.

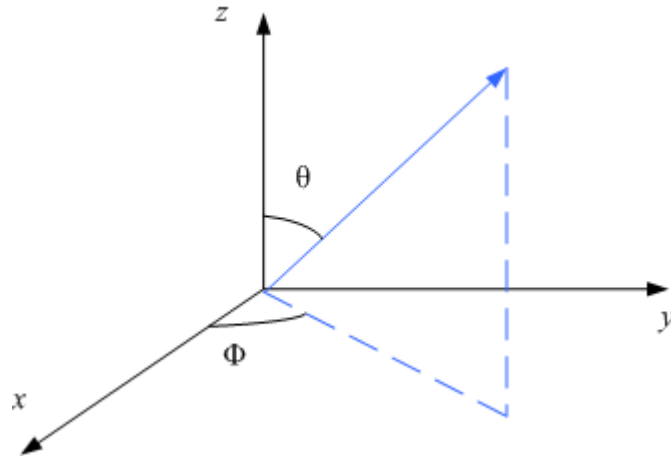


Figure 3-5. Coordinate plane system for determining the elevation and azimuth of a wafer.

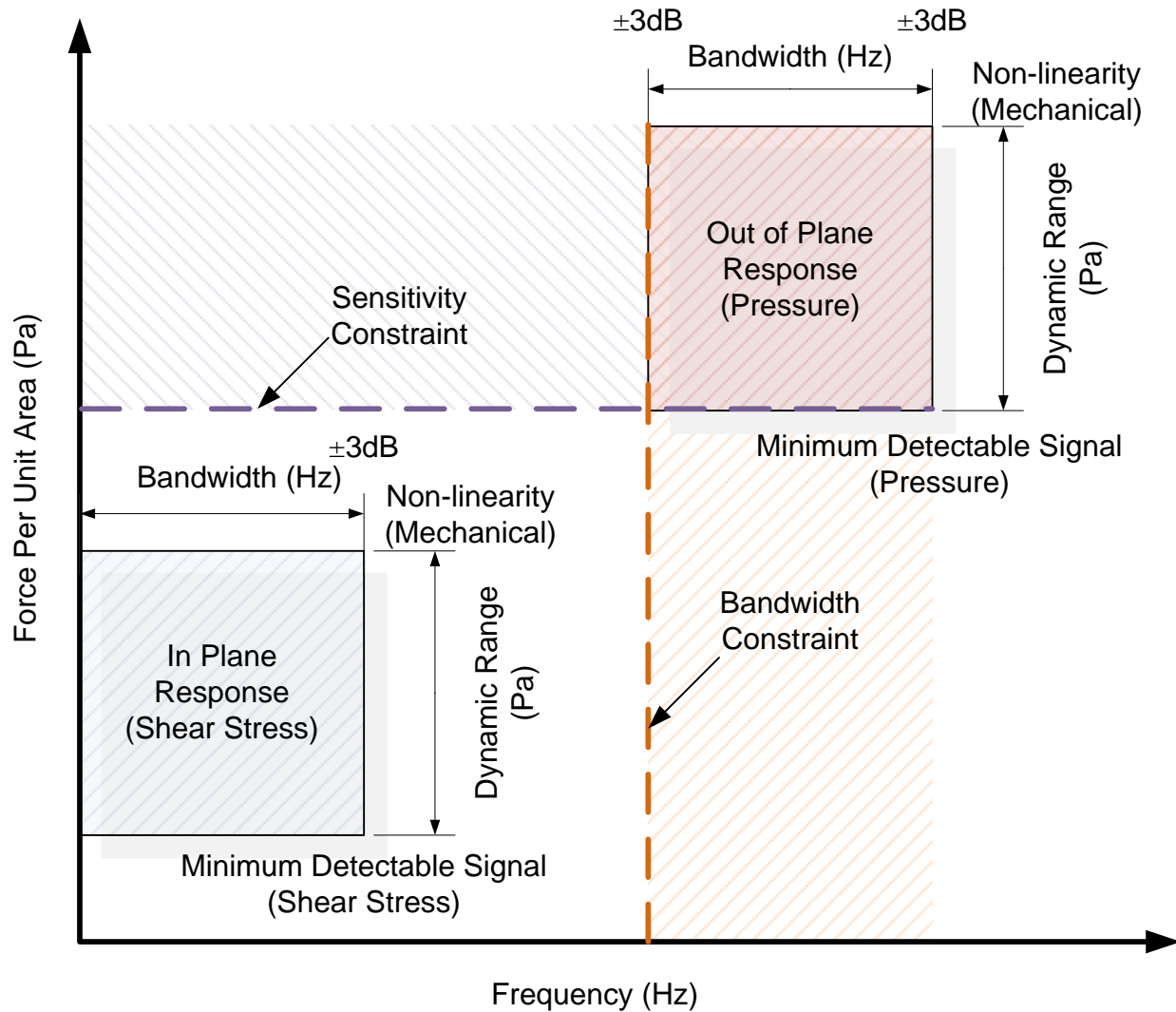


Figure 3-6. Illustration of the operating space for a mechanical sensor optimization.

CHAPTER 4 OPTICS

This chapter describes the background information regarding the optical transduction technique for the Moiré amplification as well as the optical packaging of the shear stress sensor. The first section provides details about generating Moiré fringes for optical amplification, followed by a discussion about the non-idealities of Moiré fringe that occur in applications. Several phase tracking techniques for Moiré fringe estimation as well as the motivation for data reduction algorithm are presented.

4.1 Optics Background

The optical transduction for the shear stress sensor uses a Moiré amplification technique. The benefit of using Moiré fringe patterns is that the small mechanical deflections in the floating element result in an optically amplified Moiré fringe shift, which increases the sensitivity of the sensor. The theory for computing the Moiré fringe patterns is discussed as well as curve-fitting the patterns. The motivation of reducing the overhead data for Moiré fringe estimation is also discussed in the following sections.

4.2 Motivation for Phase Modulation

In order to detect an optical fringe pattern, the fringe pattern must somehow be encoded and transmitted by light. Light modulation can be achieved by varying light properties such as amplitude, phase/frequency and to a lesser extent, polarization [74]. Since photodetectors respond to light intensity, these techniques are converted to intensity for measurement. In a review paper on optical microphones by Bilaniuk, several examples of each optical modulation techniques are summarized below [74].

Amplitude modulation is the variation of intensity of light in an optical path and can be classified as a radiated wave method or an evanescent wave method [74]. Radiated

methods modify the radiated energy in an optical path and evanescent methods uses mode coupling or absorption of the evanescent field. Several common amplitude modulation techniques that use the radiated wave method are the optical cantilever, lever, macrobend, moving gate [74] and the whispering gallery mode using microspheres [75] are shown in Figure 4-1. The most common intensity modulation technique is the optical lever, which uses a source-receive pair of waveguides to illuminate and collect varying intensities of reflected light from a moving surface. The cantilever technique varies the position of the receiving waveguide with respect to the source waveguide, which changes the amount of light collected by the receiving waveguide. The macrobend technique changes the curvature of the waveguide, thus altering the critical angle and varies the amount of light that remains in the medium. The moving gate is an optical shutter technique that blocks the amount of light transmitted or received by the position of the optical gratings. Examples of evanescent wave modulation are the microbend and coupled waveguide technique. The microbend technique scatters the optical modes of the propagating wave and the coupled waveguide uses wavevector matching for modulation.

Phase modulation is the combination of a reference light signal and a light signal with changes in distance or the refractive index in the optical path [74]. Two types of phase modulation are used: interferometric techniques and phase gratings. The interferometric techniques include Fabry-Perot, Michelson, and Mach-Zehnder as illustrated in Figure 4-2. The phase grating technique uses optical gratings to modulate the index of refraction of the optical pathway.

Although polarization modulation is not as common as amplitude or phase modulation, two types of light polarization techniques are used: liquid crystal and differential index shifter [74]. A polarizer is used to detect changes in polarization in a liquid crystal layer caused by vibrations [74]. For the differential index shifter, interaction between a glass plate and a waveguide film is excited by transverse electric and transverse magnetic modes, resulting in changes in the refractive index in the two modes and the phase difference is observed by a polarizer [74].

For the micro-machined, floating element in a flow application, the amplitude and phase modulation techniques are considered. Examples of floating elements using amplitude modulation technique are the optical shutter and optical lever as shown in Figure 4-3.

Optical shutter measurements are susceptible to light fluctuations in the optical path. Intensity fluctuations in the light source interfere with the desired signal collected by photodetectors. For flow applications, the location of the light source needs to be considered. Issues, such as vibration between the incident light source and optical shutter photodetectors, interferes with the overall measurement. For floating elements using the optical lever technique, the size and location of the optical fiber are important. Typically, the micro-machined, floating element are designed to be hydraulically smooth and in the flow. Introducing an optical fiber lever in the setup necessitates the fiber to be flushed and observe the hydraulically smoothness requirements to prevent disruption of the flow. Micro-machined floating elements may have thickness on the order of 10 and the diameter of the optical fiber need to be selected based on the requirement. In addition, the roughness of the sidewall of the floating element needs to be taken into

consideration for optical lever techniques. The ability to achieve a smooth sidewall for the floating is often dependent on the surface roughness generated by the microfabrication techniques.

For micro-machined floating elements using phase measurements in a flow application, a phase grating technique is selected. The periodic Moiré fringe pattern is a phase modulation technique for detecting lateral measurements as shown in Figure 4-4. Deflection of the Moiré gratings causes a shift in the phase of the spatial pattern. The spatial phase shift is insensitive to global amplitude fluctuations in the Moiré fringe [76].

4.2.1 Geometric Moiré Background

An ideal Moiré fringe pattern is a geometric optical phenomenon that occurs when two sets of gratings are superimposed together to form a periodic optical fringe pattern consisting of light and dark regions [77]. The two sets of gratings can have either identical or non-identical grating pitches, as shown in Figure 4-5. For identical sets of gratings, if the gratings of equal width and pitch are superimposed together at an angle and not parallel with each other, a Moiré fringe pattern can be observed. If the first set of gratings and the second set of gratings are almost identical in pitch but not equal, a Moiré pattern can be observed as long as the two grating sets are not perpendicular to each other. The latter case is sometimes referred to as Vernier fringe formation [78]; however, such a distinction is not made here. The parallel gratings with a slightly different pitch forms the Moiré fringe pattern used for the optical amplification in the device.

A useful characteristic of the Moiré pattern is that superimposed gratings have periodic regions of light and dark bands in the fringe pattern due to constructive and destructive interference. The spatial periodicity of the bands can be calculated from the

pitch of the two sets of gratings. Furthermore, upon a physical spatial displacement in one of the grating sets, the overall period results in an amplified optical shift in the bands.

The grating pitches, or line spacing between gratings, can be defined g_1 and g_2 , where the width of the gratings is half the distance of the pitch as shown in Figure 4-6. Since the pitch of g_1 and g_2 are not equal, the number of finer gratings is one more than the number of coarser gratings in a Moiré fringe period.

The spatial Moiré period, defined as G with units in length (mm), can be calculated from the sets of gratings using the following equation,

$$G = ng_2 = (n+1)g_1, \quad (4-1)$$

where n is the number of coarse pitch gratings in a period and $n+1$ is the number of fine pitch gratings in a period. The equation for the Moiré period can be rewritten as,

$$G = \frac{g_1 g_2}{g_2 - g_1}. \quad (4-2)$$

In terms of spatial frequency, denoted by f with units of inverse length ($1/mm$), the period is the inverse of frequency. The Moiré spatial period can be rearranged as,

$$\frac{1}{G} = \frac{1}{g_1} - \frac{1}{g_2}. \quad (4-3)$$

Alternatively, the spatial frequency of the Moiré fringe pattern can be expressed as the difference between the spatial grating frequencies,

$$f = f_1 - f_2 = \frac{1}{G}. \quad (4-4)$$

When a set of gratings is displaced by a distance denoted by δ , the optically amplified Moiré fringe displacement Δ can be calculated by the following equation,

$$\Delta = \delta \left(\frac{G}{g_2} \right), \quad (4-5)$$

where G/g_2 is the amplification factor of the Moiré shift. The effect of the Moiré amplification can be seen in Figure 4-7,

4.2.2 Modeling the Moiré fringe as a Sinusoid

Since the Moiré fringe pattern is periodic, the alternating light and dark bands of the Moiré fringe pattern can be modeled by a sinusoidal curve. In order to determine the optical spatial displacement in the Moiré fringe pattern, various curve-fitting techniques can be used for the optical fringe estimation and is discussed in a later section of this chapter. A general spatial sinusoidal function y , shown in Figure 4-8, is given by,

$$y(x) = I_0 + I \sin(2\pi fx + \phi), \quad (4-6)$$

where y is the intensity profile of the fringe pattern, I_0 is the DC offset of the sinusoidal curve, I is the amplitude or intensity, f is the spatial frequency of the Moiré fringe and is the inverse of the Moiré period ($f = 1/G$), x is the independent spatial position, and ϕ is the phase.

As the Moiré fringe pattern is displaced, the corresponding phase ϕ in the sinusoidal function also changes. The extracted phase ϕ from the curve-fits is used to obtain the displacement of the Moiré fringe shift and ultimately, the displacement of the floating element.

A physical set of Moiré gratings can be modeled as a binary pulse train. A periodic function of a two-sided Fourier series, Γ , can be represented as [79],

$$\Gamma(x) = \sum_{n=-\infty}^{\infty} a_n \cos(2\pi nx/T) + \sum_{n=-\infty}^{\infty} b_n \sin(2\pi nx/T), \quad (4-7)$$

where x is the spatial position, n is the number of samples in the function, T is the period of the function, and a_n and b_n are Fourier coefficients that describe the grating profile. For a binary square wave, the coefficients are given as [79],

$$a_n = \frac{1}{n\pi} \sin\left(\frac{\pi n\tau}{T}\right) = \frac{\tau}{n\pi} \operatorname{sinc}\left(\frac{n\tau}{T}\right), \quad (4-8)$$

and

$$b_n = 0. \quad (4-9)$$

where τ represents the width of the square wave shown in Figure 4-9. As n is increased, the number of overshoot oscillations on the square wave is reduced and the grating pattern converges towards a square wave function. Using the binary square wave coefficients, the periodic function can be reduced to,

$$\Gamma(x) = \sum_{n=-\infty}^{\infty} a_n \cos\left(\underbrace{2\pi nx/T}_{\gamma_1(x)}\right) = \sum_{n=-\infty}^{\infty} a_n \cos(\gamma_1(x)) \quad (4-10)$$

With an addition of a DC background intensity, denoted as d , the intensity transmission functions of the two individual gratings are written as,

$$\Gamma_1(x, y) = d_1 + \sum_{n=1}^{\infty} a_{1n} \cos(n\gamma_1(x, y)), \quad (4-11)$$

and

$$\Gamma_2(x, y) = d_2 + \sum_{m=1}^{\infty} a_{2m} \cos(m\gamma_2(x, y)). \quad (4-12)$$

Combining grating functions Γ_1 and Γ_2 yields [80],

$$\Gamma_1(x, y) \cdot \Gamma_2(x, y) = \left(\begin{array}{l} d_1 d_2 + d_1 \sum_{m=1}^{\infty} a_{2m} \cos[m\gamma_2(x, y)] \\ + d_2 \sum_{n=1}^{\infty} a_{1n} \cos[n\gamma_1(x, y)] \\ + \sum_{m=1}^{\infty} \sum_{n=1}^{\infty} a_{1n} a_{2m} \cos[n\gamma_1(x, y)] \cos[m\gamma_2(x, y)] \end{array} \right) \quad (4-13)$$

The first term terms in equation (4-13) describe the individual grating functions.

The last term, which describes the sum and difference between the two sets of gratings, can be rearranged using the product-to-sum trigonometric identity,

$$\cos(\alpha) \cdot \cos(\beta) = \frac{\cos(\alpha - \beta) + \cos(\alpha + \beta)}{2}. \quad (4-14)$$

The last term from equation (4-13) using the trigonometric identity from equation (4-14) yields [80],

$$\sum_{m=1}^{\infty} \sum_{n=1}^{\infty} \left(\begin{array}{l} a_{1n} \cdot a_{2m} \\ \times \cos[n\gamma_1(x, y)] \\ \times \cos[m\gamma_2(x, y)] \end{array} \right) = \left(\begin{array}{l} \frac{1}{2} \sum_{m=1}^{\infty} \sum_{n=1}^{\infty} a_{1n} a_{2m} \cos \left[\begin{array}{l} n\gamma_1(x, y) \\ -m\gamma_2(x, y) \end{array} \right] \\ + \frac{1}{2} \sum_{m=1}^{\infty} \sum_{n=1}^{\infty} a_{1n} a_{2m} \cos \left[\begin{array}{l} n\gamma_1(x, y) \\ +m\gamma_2(x, y) \end{array} \right] \end{array} \right). \quad (4-15)$$

The sum and difference between the two sets of gratings can be seen in equation (4-15). The term where $n=1$ and $m=1$, which contains the fundamental Moiré pattern [80] is written as,

$$\sum_{n=1}^1 a_{1n} \cos[\gamma_1(x, y)] \sum_{m=1}^1 a_{2m} \cos[\gamma_2(x, y)] = a_{11} a_{21} \frac{\cos[\gamma_1(x, y) - \gamma_2(x, y)]}{2}. \quad (4-16)$$

By introducing a DC intensity and observing a cosine to sine shift, equation (4-16) can be rearranged to match the format of a general sinusoid,

$$y(x) = \frac{1}{2} \underbrace{a_{11} a_{21}}_I \cos[\gamma_1(x, y) - \gamma_2(x, y)] + \underset{I_0}{DC} \quad (4-17)$$

$$\rightarrow y(x) = I \underset{\cos \rightarrow \sin}{\sin} \left(2\pi \left(\underbrace{f_1 - f_2}_{1/G} \right) x + \phi \right) + I_0$$

From equation (4-17), it can be observed that the difference between the grating frequencies is related to the overall Moiré period as previously defined in equation (4-4).

4.3 Optical Non-idealities

In the previous section, the geometries and calculations for the Moiré fringe pattern presented are for an ideal case. Non-idealities, such as angular misalignments, separation gaps between gratings sets, contrast from material selection and out-of-plane sensitivity, introduce errors to the overall fringe pattern and are discussed in this section.

4.3.1 Angular Errors

If angular errors are present in aligning the two grating sets together, the equation to calculate the relationship of angles to grating spacing can be derived using the following grating functions [80],

$$\gamma_1(x, y) = \frac{2\pi}{g_1} (x \cos \alpha + y \sin \alpha) \quad (4-18)$$

and

$$\gamma_2(x, y) = \frac{2\pi}{g_2} (x \cos \alpha - y \sin \alpha), \quad (4-19)$$

where γ_1 and γ_2 are the grating functions, shown in Figure 4-10, that describe the g_1 and g_2 gratings in the Cartesian coordinate system and α is the angle between the two sets of gratings.

By differencing the two grating functions, the equation can be reorganized into the following form,

$$\gamma_1(x, y) - \gamma_2(x, y) = \frac{2\pi}{G_{period}} x \cos \alpha + \frac{4\pi}{G_{average}} y \sin \alpha, \quad (4-20)$$

where $G_{average}$ is the average line spacing between the two grating sets and G_{period} is the period of the Moiré fringe pattern given by equation (4-2). The difference between the two grating functions is related to an integer fringe order number, M and is given by,

$$M 2\pi = \gamma_1(x, y) - \gamma_2(x, y). \quad (4-21)$$

Two special cases that can be derived from equation (4-20) are of particular interest. If the grating pitches are equal, that is, if $g_1 = g_2 = g$, then equation (4-20) can be reduced to,

$$M \cdot g = 2y \sin \alpha. \quad (4-22)$$

However, if the gratings are parallel and the angle α between the gratings is zero, the equation (4-20) can be simplified to,

$$M \cdot G_{period} = M \left(\frac{g_1 g_2}{g_1 - g_2} \right) = x. \quad (4-23)$$

A general expression relating the line space and angle between the two sets of gratings is given by,

$$M \cdot G_{average} = \frac{G_{average}}{G_{period}} x \cos \alpha + 2y \sin \alpha. \quad (4-24)$$

4.3.2 Grating Width Variations

Manufacturing errors may be present when generating the optical gratings. The difficulties associated with patterning and etching aluminum gratings using wet

processes can result an increase or decrease in the widths of the gratings. The accuracy in the pitch of the gratings is determined by the tolerance in the photomask and the pitch of the gratings should remain constant despite width variations in the gratings. The width variation in the optical gratings represents a duty cycle of grating width and gap spacing per grating pitch.

The grating pitch can be decomposed into the grating width w^+ and gap spacing w^- and is represented by the following equation,

$$g = w^+ + w^- . \quad (4-25)$$

For the case where $w^+ = w^-$, this represents a ratio of 1:1 duty cycle between the grating width and gap spacing and is the ideal case. If the ratio between the grating gap and width are is not 1:1, the shape of the optical fringe is determined by

$$\frac{h}{G} = \frac{1}{R_1 + 1} , \quad (4-26)$$

where G is the period of the optical fringe, h is the width of the dark fringe at the half intensity level and R1 is the ratio between the grating gap and width [77]. The optical fringe profile due to non-equal grating width to gap ratio ($w^+ \neq w^-$ and hence $R_1 \neq 1$) is illustrated in Figure 4-11. For the case where the grating width to gap ratio is 1:1 such that $R_1=1$, then the ratio between h:G is 1:2 and the result is shown in Figure 4-12. When the grating gap and width ratio is 1:1, this reveals the triangular pattern of an ideal Moiré period.

4.3.3 Talbot Distance

For the Moiré floating-element sensor, a recessed gap exists between the two sets of optical gratings. The gap distance between the two sets of gratings can affect the

overall contrast for the Moiré fringe. When a monochromatic collimated light source is used, the Talbot distance can be used to determine contrast.

At regularly spaced, interval distances normal from the Moiré fringe pattern, virtual images of the Moiré fringe pattern are reproduced, as shown in Figure 4-13. The distance where the self-imaging phenomenon occurs is known as the Talbot distance or the Fourier distance [77]. The Talbot distance, D_T , is defined as,

$$D_T = \frac{g^2}{\lambda} = \frac{1}{\lambda f^2}, \quad (4-27)$$

where g is the pitch, f is the frequency and λ is the wavelength of the light source.

The successive interval distance z where the virtual images occur is defined as,

$$z = nD_T, \quad (4-28)$$

where n is an integer. In order to obtain a reasonable contrast, the distance between the gratings should be within 5% of D_T . Thus, the optical gratings do not have to be in physical contact to produce Moiré fringes but it is recommended that the gratings should not be further than 5% of D_T to prevent the Moiré fringe from loss of contrast [77].

For example, the widths of the gratings used for the Moiré fringe pattern are on the order of $10 \mu m$. If the wavelengths of the light source are between $700 nm$ and $1000 nm$, then the gap distance between the gratings to remain within 5% of the Talbot distance is approximately between $5 \mu m$ and $7 \mu m$. If a monochromatic collimated light source is used, the gap spacing between the two sets of optical gratings, as determined by the Talbot distance, becomes a device fabrication constraint.

4.3.4 Contrast and Material Selection

The Moiré fringe pattern is represented by a periodic cycle of light and dark bands. If the contrast between the crest and trough of a sinusoid is insufficient, then the fringe estimation algorithm may not be able to distinguish and curve-fit the fringe pattern properly. Some factors that affect the contrast of a Moiré fringe are the material selection for the optical gratings and the incident light intensity.

Ideally, the materials selected for the Moiré gratings should reflect as much incident light from the gratings as possible to couple back to the receiving optical fibers. Furthermore, the structures that the Moiré gratings are mounted on should allow light to pass. The combination of reflective and transmitting light affects the contrast of the Moiré fringe pattern.

While incident light intensity contributes to the DC offset of the Moiré fringe, the incident light also contributes to the Moiré amplitude. If the incident light intensity is zero, then light is not reflected from gratings, resulting in a zero amplitude in the sinusoidal pattern and zero DC offset. Ideally, the incident light should not be too intense such that the DC offset dominates the fringe pattern.

The materials used in the optical Moiré shear stress sensor are silicon, Pyrex (Corning 7740) and aluminum as shown in Figure 4-14. Silicon is widely used in MEMS micromachining since silicon possess a high Young's Modulus and silicon is readily available. Aluminum is selected for its high reflectance value, typically 90% or higher and unlike silver, it does not oxidize as easily. Pyrex is essentially transparent and can be anodic bonded to silicon.

Using reference graphs [81–83] containing the reflectivity of silicon, $R_{Si}(\lambda)$, and aluminum, $R_{Al}(\lambda)$, and the transmissivity of Pyrex, $T_{Py}(\lambda)$, the graphs were combined to show the overall reflectance value of the aluminum and silicon shown in Figure 4-15. The line in the graph that shows reflection contribution of aluminum through Pyrex is used to represent the peak of the bright band in the Moiré fringe pattern. The line that shows reflection contribution of silicon through Pyrex is to represent the trough of the dark band in the Moiré fringe pattern. The range of wavelengths that the total reflectance was observed was between 300 nm to 1400 nm approximately.

The intensity representing the maximum peak of the Moiré fringe is the reflection contribution from aluminum through Pyrex at a given wavelength and can be calculated using the following equation,

$$I_{Al}(\lambda) = y_{\max}(x) = 1 - \underbrace{(1 - T_{Py}(\lambda))}_{R_{Py}(\lambda)} (R_{Al}(\lambda)). \quad (4-29)$$

where R_{Py} is the resulting reflectivity from Pyrex and is considered the light loss through Pyrex. Likewise, the intensity representing the minimum peak of the Moiré is the reflection contribution from silicon through Pyrex and is determined by,

$$I_{Si}(\lambda) = y_{\min}(x) = 1 - \underbrace{(1 - T_{Py}(\lambda))}_{R_{Py}(\lambda)} (R_{Si}(\lambda)). \quad (4-30)$$

The intensity I_{Al} represents the maximum peak of a sinusoidal curve and I_{Si} represents the minimum trough of the curve. The average intensity between I_{Al} and I_{Si} is denoted by $I_{50:50}$ and is calculated by,

$$I_{50:50}(\lambda) = 1 - \underbrace{(1 - T_{Py}(\lambda))}_{R_{Py}(\lambda)} \left(\frac{R_{Al}(\lambda) + R_{Si}(\lambda)}{2} \right). \quad (4-31)$$

The majority total reflectance of aluminum through Pyrex is 0.8 or higher from the ultraviolet through the infrared wavelengths. Between 800 *nm* and 825 *nm*, the reflectivity of aluminum through Pyrex approaches a reflectance value of 0.8. The reflectance value of silicon through Pyrex widely varies between the ultraviolet and infrared range with reflectivity values between 0.3 and 0.6. In the wavelength range of 600 *nm* and 1000 *nm*, the reflectivity of silicon through Pyrex approaches 0.3 or less.

The significance of the reflectivity values is to be able to determine the light source that provides the best contrast. A light source with a wavelength of 1000 *nm* or a light source with wavelengths between 600 *nm* to 700 *nm* would be ideal since these ranges would provide the most contrast between the aluminum and silicon reflectivity values through Pyrex.

Using the reflectivity values from the material graphs, the intensity and amplitudes of general sinusoid can be determined to model the Moiré fringe pattern (Figure 4-16). The 100% aluminum reflectance value through Pyrex for a given wavelength, denoted by I_{Al} , represents the maximum intensity value of a sinusoidal curve for a given spatial period, G , and the 100% silicon reflection through Pyrex, denoted by I_{Si} , represents the minimum intensity value. The difference between I_{Al} and I_{Si} is the peak-to-peak intensity range of a sinusoidal curve and the amplitude, $I_{50:50}$, is half of the intensity range. The calculated reflectivity values for the 50%-50% aluminum/silicon curve is the average intensity between I_{Al} and I_{Si} . The intensity value, $I_{50:50}$, is the DC offset for the

reflected sinusoidal fringe pattern and does not represent the total intensity value of the incoming light.

The generalized sinusoidal equation can be rewritten using the material parameters and is given by,

$$y(x) = I_{50:50}(\lambda) + \left(\frac{I_{At}(\lambda) - I_{St}(\lambda)}{2} \right) (\sin 2\pi fx + \phi). \quad (4-32)$$

The material data information is useful for determining the amplitude and the background intensity of the fringe pattern.

4.3.5 Out-of-Plane Sensitivity

The parameter of interest in the Moiré fringe estimation is the phase. Ideally, the frequency content in the Moiré fringe is constant. Fluctuations in the amplitude of the Moiré fringe or background light intensity should not affect the phase estimation. A source of the fluctuations in the amplitude and DC light is attributed to the incident light source.

Since the optical gratings are attached to a floating element, pressure gradients can cause out of plane deflections in the floating element (Figure 4-17). Ideally, the phase estimation should be insensitive to the fluctuations in the amplitude and DC light components. However, angular deflections in the floating element may cause changes in the frequency and inverse changes in the Moiré period, which distort the estimation of the phase.

The deviation of the Moiré period due to out of plane effects can be solved using a number of methods. By either using sinusoidal trigonometric identities or Pythagorean

theorem, the distorted Moiré width W_e' across the rotated width of the floating element is given by,

$$W_e' = \sqrt{W_e^2 - h^2}, \quad (4-33)$$

where h is the displacement of one end of the floating element in the normal direction.

This translates into a distortion on one set of the optical gratings on floating element.

The distorted grating can be derived from the original grating width by a ratio between the distorted width of the floating element and original width of the floating element,

$$g_1' = g_1 \frac{W_e'}{W_e}. \quad (4-34)$$

The distorted grating on the floating element results in a distorted Moiré period given by,

$$G' = \frac{g_1 g_2}{\left(\frac{W_e}{\sqrt{W_e^2 - h^2}} \right) g_2 - g_1}. \quad (4-35)$$

The percent deviation between the distorted Moiré period and the original Moiré period is given by,

$$\text{Percent Deviation} = \left| \frac{g_2 - g_1}{\left(\frac{W_e}{\sqrt{W_e^2 - h^2}} \right) g_2 - g_1} - 1 \right| \times 100\%. \quad (4-36)$$

Consider the out of plane deflection for a 5 Pa 2 kHz shear stress sensor. The floating element width is 1500 μm and the cavity depth is 2 μm . If the normal pressure applied deflects one end of the floating element such that the floating element reaches the bottom of the cavity, then the width of the floating element as observed by imaging

optics parallel to the sensor is $1499.9987 \mu m$. The change in percentage in the width of floating element due to out of plane rotation is less than 0.0001%.

For the given gratings widths of $9.9 \mu m$ and $10 \mu m$, the calculated Moiré fringe period is $990 \mu m$. Applying the percentage change in width to the $10 \mu m$ grating, the resulting Moiré period is found to be 990.098 , which represents less than 0.01% change in the period. For a 1% error shift to occur, the floating element of the $5 Pa 2 kHz$ sensor have to tilt at one end at a normal distance of $21 \mu m$ while the other end remains stationary.

4.4 “Ideal” Optical Fringe Estimation

In this research, the primary fringe estimation technique used for Moiré fringe estimation is the least squares curve-fit algorithm in MATLAB. The phase from the curve-fits are computed to indicate spatial displacement in the Moiré fringe pattern. Other algorithms that can potentially be used for fringe estimation are cross correlation, Fast Fourier Transforms (FFT), spatial phase detection and a quadrature method. The cross correlation technique compares a spatial fringe pattern with a shifted fringe pattern to track phase via convolution. However, this method is not as accurate when compared to the other algorithms when using a single Moiré fringe period and it is computationally demanding. The FFT is computationally efficient method of computing frequency and phase. However, this technique is susceptible to power leakage in adjacent frequency bins and the samples should be in the power of 2. The spatial phase detection (SPD) method uses a sine and cosine component of the given fringe pattern to produce a phase. Although the SPD is a fast and easy technique to use, errors may be introduced if the phase gradients are large over a grating interval [84].

An alternate technique for the fringe estimation is the quadrature method. In this method, four points of a full Moiré period are sampled at 90° out of phase. The four points are differenced and divided to obtain an overall phase. This method is a potential implementation for future generations of optical shear stress sensors using Moiré fringes. In this research, the four different techniques evaluated for fringe estimation are the least squares curvefit, fast Fourier transform, cross-correlation and spatial phase detection.

4.4.1 Least Squares Curvefit

The least squares curve-fitting is a method of data fitting by minimizing the error from a desired curve. The residuals are the errors between the predicted values and the measured values. The solution for the sinusoidal function is solved by iteratively comparing the experimental data to the predicted values until the sum of the square of the residuals is minimized [85]. A mathematical description for a least squares curvefit for a general sinusoid representing the optical fringe is described in the following section.

As previously discussed in this chapter, a Moiré fringe pattern can be modeled as a sinusoid. The generalized sinusoidal from equation (4-6) can be linearized by the following angle-sum trigonometric identity,

$$\sin(A + B) = \cos A \sin B + \sin A \cos B . \quad (4-37)$$

Applying the trigonometric identity to the sinusoidal equation equation (4-6) yields,

$$y = I_0 + I [\sin 2\pi fx \cos \phi + \cos 2\pi fx \sin \phi] . \quad (4-38)$$

Since the phase ϕ is constant, the $\sin \phi$ and $\cos \phi$ terms in equation (4-38) are collected with I as shown,

$$y = I_0 + \underbrace{I \cos \phi}_{I_1} \sin 2\pi fx + \underbrace{I \sin \phi}_{I_2} \cos 2\pi fx, \quad (4-39)$$

which simplifies to,

$$y = I_0 + I_1 \sin 2\pi fx + I_2 \cos 2\pi fx. \quad (4-40)$$

In order to convert the sinusoidal equation into a form of a linear least squares model to which sampled data can be compared to, equation (4-40) can be written as polynomials,

$$y = a_0 z_0 + a_1 z_1 + \dots + a_m z_m + e. \quad (4-41)$$

Equation (4-41) can be written in matrix form,

$$\{y\} = [Z]\{a\} + \{e\}. \quad (4-42)$$

The terms $\{a\}$ and $[Z]$ from the matrix are expressed as,

$$\{a\} = \begin{bmatrix} I_0 \\ I_1 \\ I_2 \end{bmatrix}, \quad (4-43)$$

and

$$[Z] = \begin{bmatrix} 1 & \sin 2\pi fx_1 & \cos 2\pi fx_1 \\ 1 & \sin 2\pi fx_2 & \cos 2\pi fx_2 \\ \vdots & \vdots & \vdots \\ 1 & \sin 2\pi fx_n & \cos 2\pi fx_n \end{bmatrix}, \quad (4-44)$$

where n is the number of data points sampled, which corresponds to the number of photodetectors in an array used to capture the optical fringe pattern. The sum of the square of the residuals is defined as,

$$S_r = \sum_{i=1}^n e^2 = \sum_{i=1}^n \left(y_i - \sum_{j=0}^2 a_j Z_{ji} \right)^2. \quad (4-45)$$

The sum of the square of the residuals, S_r , can be arranged into a matrix equation by taking the partial derivative with respect to a and is expressed as [85],

$$\left[[Z]^T [Z] \right] \{a\} = \left\{ [Z]^T \{y\} \right\}. \quad (4-46)$$

In order to obtain a phase angle, I_1 and I_2 can be related to the intensity I using equation (4-39), and is given by,

$$I = \frac{I_1}{\cos \phi} = \frac{I_2}{\sin \phi}. \quad (4-47)$$

Rearranging equation (4-47), the ratio between I_1 and I_2 is used to form a tangent,

$$\frac{I_2}{I_1} = \frac{\sin \phi}{\cos \phi} = \tan \phi. \quad (4-48)$$

The phase for a given Moiré fringe is calculated by the following equation,

$$\phi = \tan^{-1} \left(\frac{I_2}{I_1} \right). \quad (4-49)$$

The difference in spatial phase between an initial Moiré fringe at rest and a spatially displaced fringe pattern is proportional to the displacement of the floating element.

4.4.2 Fast Fourier Transform

The Fast Fourier Transform (FFT) can be used as a method to track the phase of a sinusoidal function. The FFT is a computationally efficient version of the Discrete Fourier Transform (DFT), which can be used to convert signals from the spatial domain into the frequency domain. Using discrete frequencies, the Fourier transform can be expressed as [86],

$$Y_k = \sum_{n=0}^{N-1} y_n e^{-j \frac{2\pi kn}{N}} \quad (4-50)$$

where $k = 0, 1, 2, \dots, N-1$.

The phase angle for each FFT can be obtained by the arctangent between the complex and the real components given by,

$$\phi_k = \tan^{-1} \frac{\text{Im}(Y_k)}{\text{Re}(Y_k)} \quad (4-51)$$

For an sinusoidal fringe at an initial position denoted by y_1 , the phase is ϕ_1 and displaced fringe patterns denoted by y_2 , the phase is ϕ_2 . The phase difference between ϕ_1 and ϕ_2 is the phase displacement ϕ and represents the spatial shift in the optical fringe.

In order for the FFT algorithm to work ideally, the number of samples should be a power of 2. Furthermore, the sampled data should ideally be integer multiples of an exact signal period to avoid leakage to the adjacent frequency bins in the power spectrum. The effects of leakage can be reduced through the use of weighting functions, such as a Hanning window.

4.4.3 Cross-Correlation

The cross-correlation method tracks the current optical fringe by comparing the subsequent fringe shifts with an initial zero phase fringe. Respectively, the equations for the initial phase fringe and displaced fringes is expressed as [86],

$$y_1 = I_{01} + I_1 \sin(2\pi fx), \quad (4-52)$$

and

$$y_2 = I_{02} + I_2 \sin(2\pi fx + \phi). \quad (4-53)$$

The cross-correlation is defined as,

$$R_{y_1 y_2}(\delta) = E[y_1(x) y_2(x + \delta)] \quad (4-54)$$

where $E[\]$ is an expectation operator and δ is the spatial lag. The initial phase fringe y_1 and displaced fringes y_2 are convolved to observe peak values in the cross-correlation. The cross-correlation between y_1 and y_2 is given by,

$$R_{y_1 y_2}(\delta) = \lim_{N \rightarrow \infty} \frac{1}{T} \int_{-T}^T y_1(x) y_2(x + \delta) d\delta, \quad (4-55)$$

where T is the record length. The discretized cross-correlation can be expressed as,

$$R_{y_1 y_2}(\Delta) = \frac{1}{N} \sum_{n=0}^{N-\Delta} y_1(n) y_2(n + \Delta), \quad (4-56)$$

where Δ is the discretized spatial lag. The phase shift is determined by observing the spatial shift between the peak values from the cross correlation,

$$\phi = \Delta_2 - \Delta_1 \quad (4-57)$$

where Δ_2 is the spatial lag at the maximum value from the cross-correlation of $R_{y_1 y_2}(\Delta)$ and Δ_1 is the spatial lag from the auto-correlation at $R_{y_1 y_1}(\Delta)$.

4.4.4 Spatial Phase Detection

The spatial phase detection method is a phase extraction technique based on an approach by Toyooka and Iwaasa in 1986 [87] and Sajan et al. in 1989 [84]. In order to use this technique, the general sinusoid form should be modified to a cosine by introducing a $\pi/2$ phase shift, which results in the following expression,

$$y = I_0 + I \cos(2\pi fx + \phi - \pi/2). \quad (4-58)$$

The Fourier cosine and sine integrals can be obtained and expressed as,

$$C = \int_{-\infty}^{\infty} y \cos(2\pi f_0 x) dx \quad (4-59)$$

and

$$S = \int_{-\infty}^{\infty} y \sin(2\pi f_0 x) dx. \quad (4-60)$$

The phase gradient β_i in the i th interval can be obtained by combining (4-59) and (4-60) is given by,

$$\frac{S}{C} = \frac{2\pi f}{2\pi f + \beta} \tan \phi. \quad (4-61)$$

If the phase gradient is large over a grating interval, errors are introduced. The cosine and sine integrals can be discretized and expressed as,

$$C = \sum_{i=1}^n y_i \cos(2\pi f x) \Delta x, \quad (4-62)$$

and

$$S = \sum_{i=1}^n y_i \sin(2\pi f x) \Delta x. \quad (4-63)$$

The phase, ϕ_i , at the midpoint over the i th interval is obtained by calculating the arctangent of C and S and is given by,

$$\phi_i = \tan^{-1} \left(\frac{S}{C} \right). \quad (4-64)$$

This research initially selected the least squares curvefitting algorithm for fringe estimation. The other fringe estimation algorithms are introduced to assess the validity of the least squares fringe estimation technique. An experimental evaluation the various fringe estimation algorithm is performed in the optical testbed section of Chapter

7. The next section discusses the motivation for reducing the number of data points sampled across an optical fringe.

4.5 Data Reduction

Initial least squares curve-fits using MATLAB were performed on image data containing 512 *pixels* from a line scan CCD array. The 512 *pixels* were sampled at a rate of 11.4 *kHz* and averaged 600 times to obtain a static mean measurement. A sinusoidal waveform was used to model the Moiré fringe pattern and a phase was extracted from the curve-fit.

In order to reduce the amount of data overhead, the Moiré fringe pattern was spatially down-sampled to represent a reduced pixel dataset. The pixel-binning of the Moiré fringe pattern simulates a reduced dataset for curve-fitting purposes.

Theoretically, as long as the spatial sampling satisfies the Nyquist Criteria for signal processing, a Moiré fringe pattern can be reconstructed and a phase from the least-squares curve-fit can be predicted. The predicted trend is as the number of pixels is down-sampled, the error in the extracted phase curve-fit increases. Figure 4-18

illustrates that as the number of pixels is reduced to the order of 10 *pixels*

$\sim O(\sim 10 \text{ pixels})$, the phase deviation from the rest of the extracted phases is 10% or less than the nominal phase values.

By reducing the necessary data points taken, this requires less data to be taken, allows faster data processing speeds and enables the ability to use a reasonable number individual optical fibers to individual photodiodes.

4.6 Summary

In summary, a discussion of geometrical Moiré is provided in this chapter. Two sets of optical gratings are used to generate a periodic fringe, which can be modeled as a general sinusoid. Upon a spatial shift in one set of gratings, the Moiré fringe pattern is proportionally shifted by an amplified distance. The shift in the sinusoidal fringe pattern can be monitored using various phase tracking techniques, such as the least squares curvefit, FFT, cross-correlation and spatial phase detection. The reduction of data sampled across an optical fringe reduces the complexity of the number optical fibers and photodetectors used to observe the Moiré fringe.

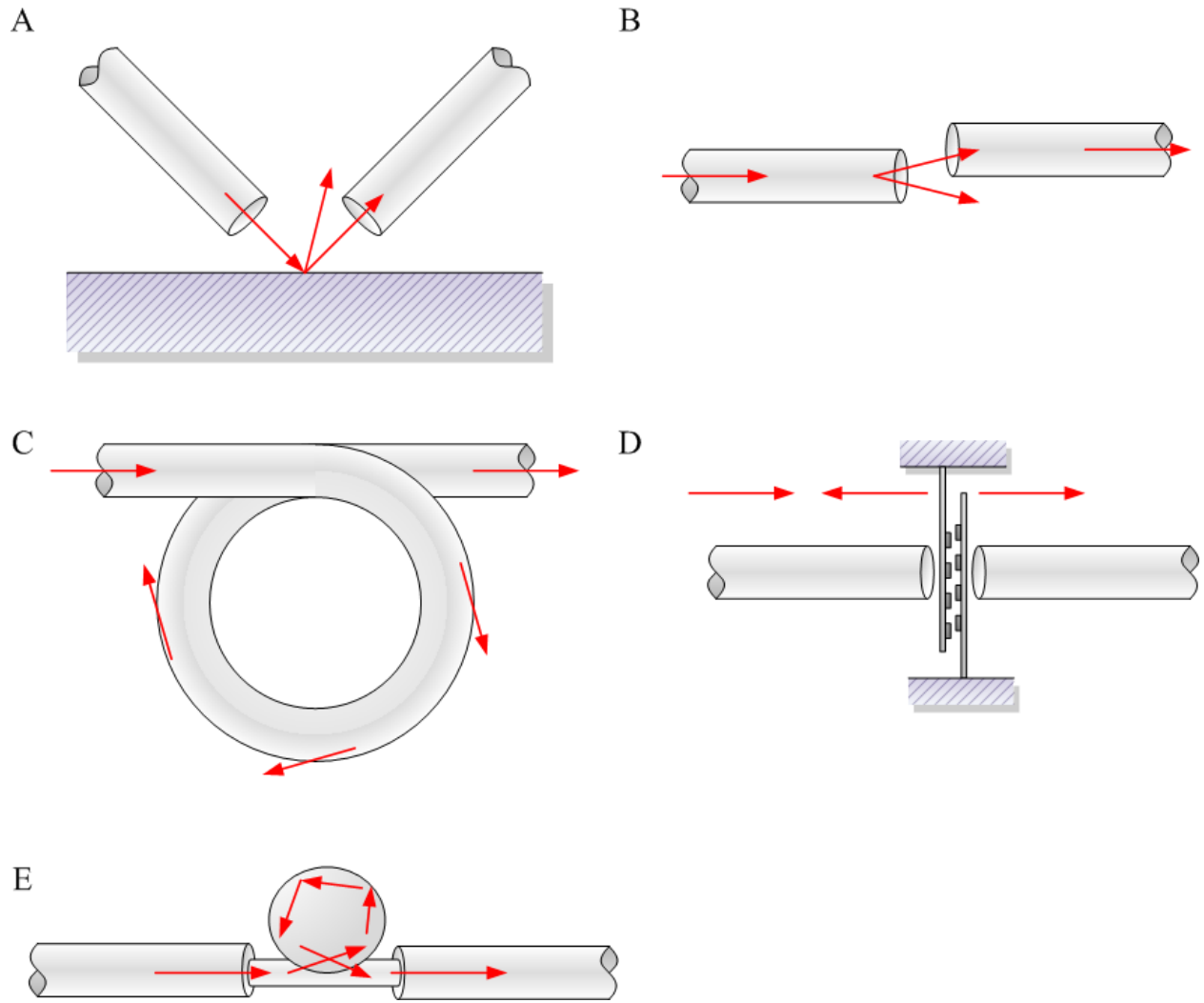


Figure 4-1. Illustration of various amplitude modulation techniques. A) Optical cantilever. B) Lever. C) Macrobend. D) Moving gate. E) Whispering gallery mode.

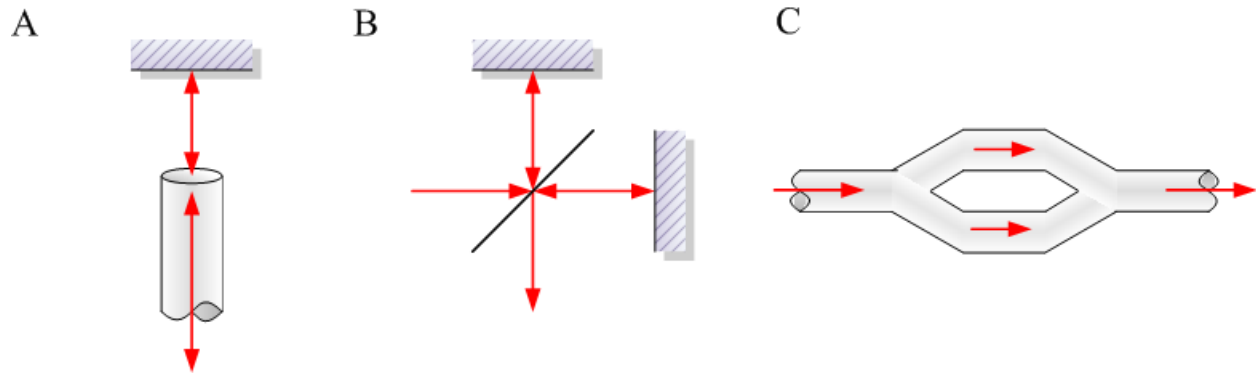


Figure 4-2. Illustration of various interferometric techniques. A) Fabry-Perot. B) Michelson. C) Mach-Zehnder.

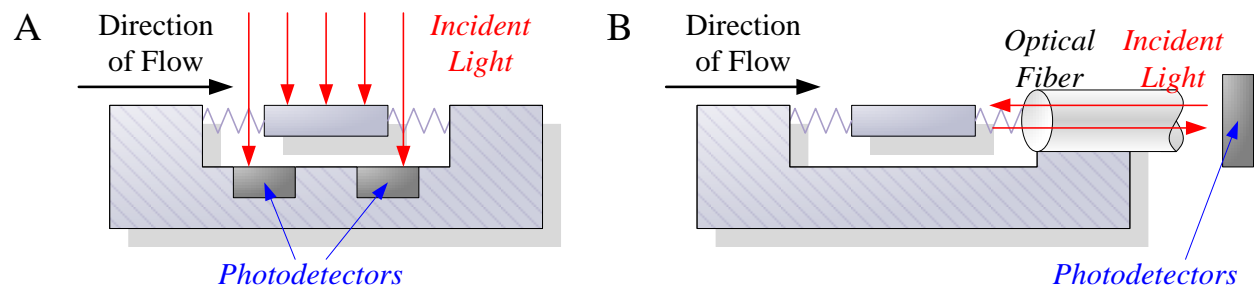


Figure 4-3. Amplitude modulation techniques for the micro-machined, floating-element flow application. A) Optical shutter. B) Optical lever.

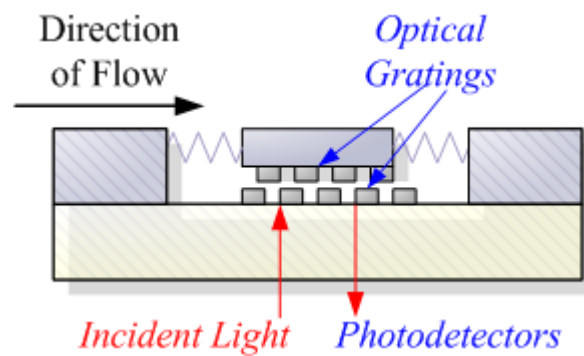


Figure 4-4. Phase modulation technique for micro-machined, floating-element flow applications.

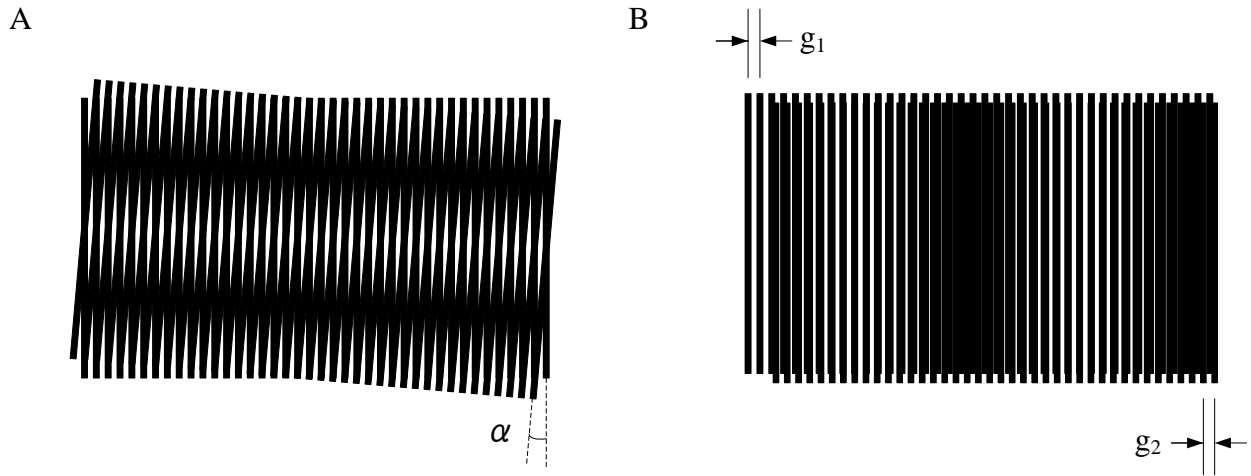


Figure 4-5. Drawings of Moiré fringe patterns. A) Equal grating pitch at an angle α . B) Similar grating sets with pitch g_1 and g_2 in parallel.

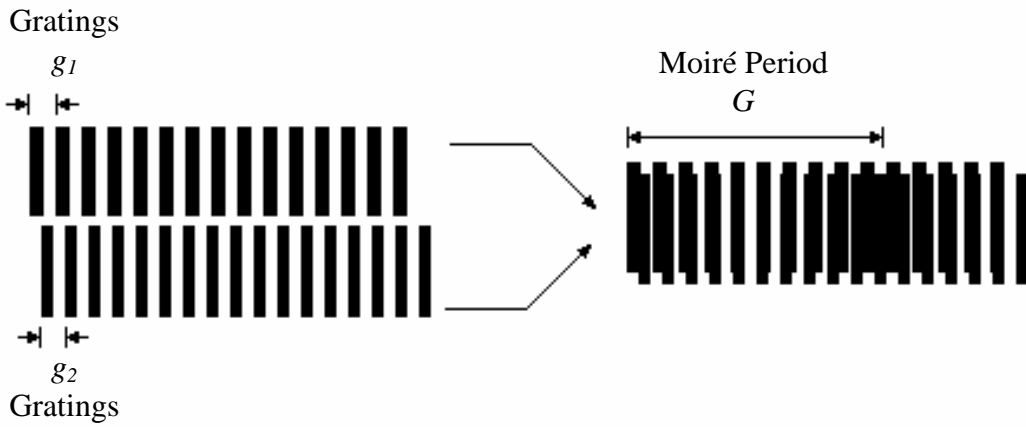


Figure 4-6. Superposition of two grating sets with spatial pitches of g_1 and g_2 in parallel to form a Moiré fringe pattern with a Moiré spatial period G .

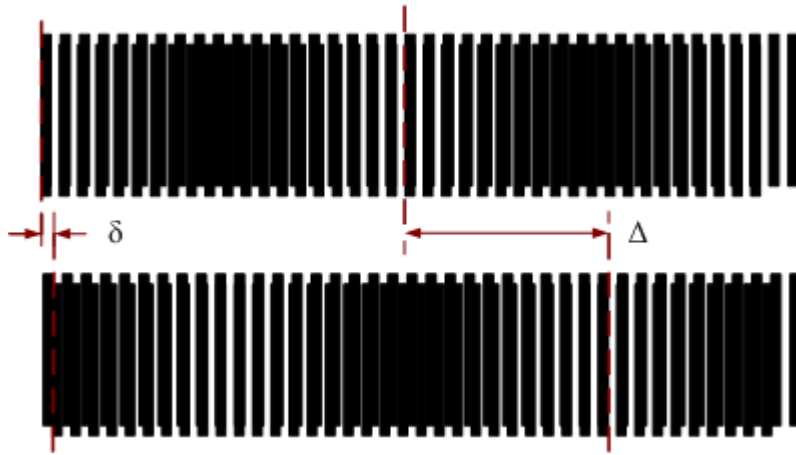


Figure 4-7. Diagram illustrating a Moiré amplified shift of distance Δ for a given grating shift of distance δ .

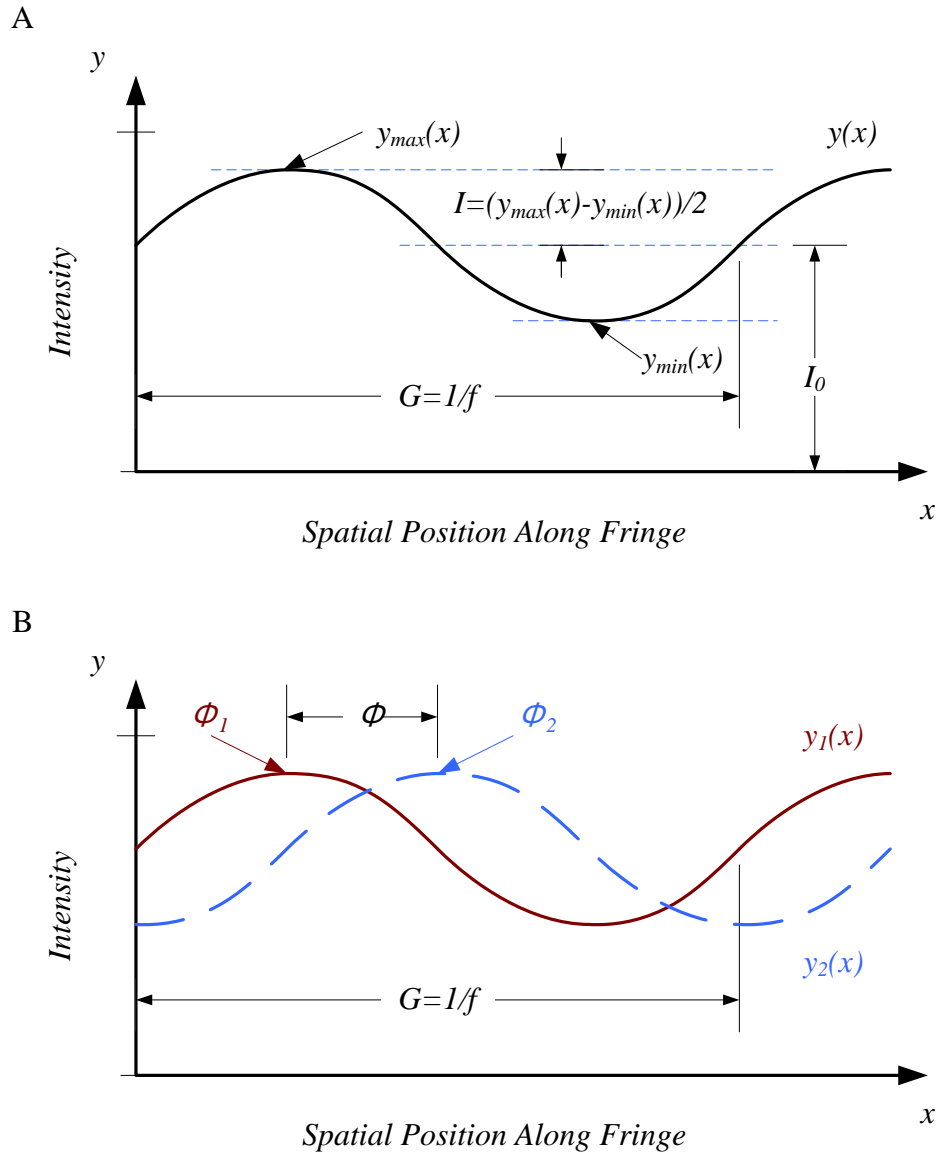


Figure 4-8. Illustration of sinusoids representing intensity profiles of the optical fringe. A) Sinusoidal intensity profile $y(x)$ showing amplitude I , frequency f and DC offset I_0 . B) Two sinusoidal intensity profiles, $y_1(x)$ and $y_2(x)$, with phase difference ϕ .

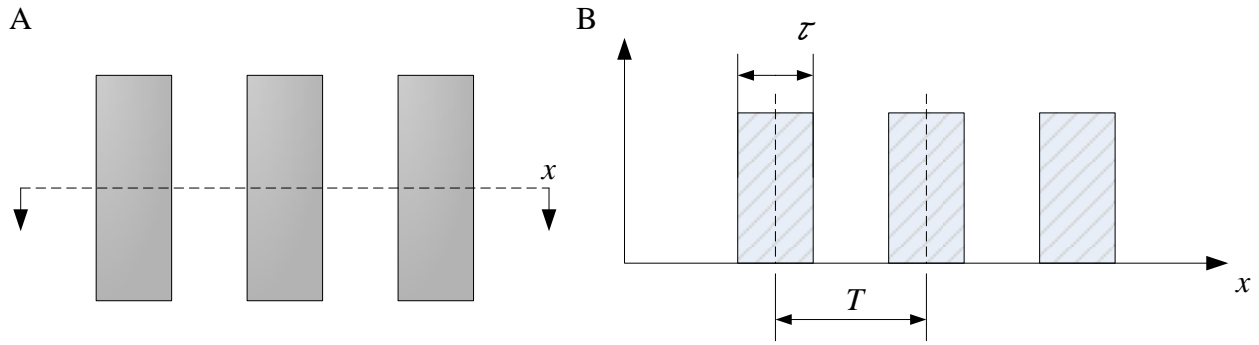


Figure 4-9. Graphical representation of a binary pulse train from Moiré gratings. A) Cross section of one set of Moiré gratings. B) Binary square-wave representation of the Moiré gratings.

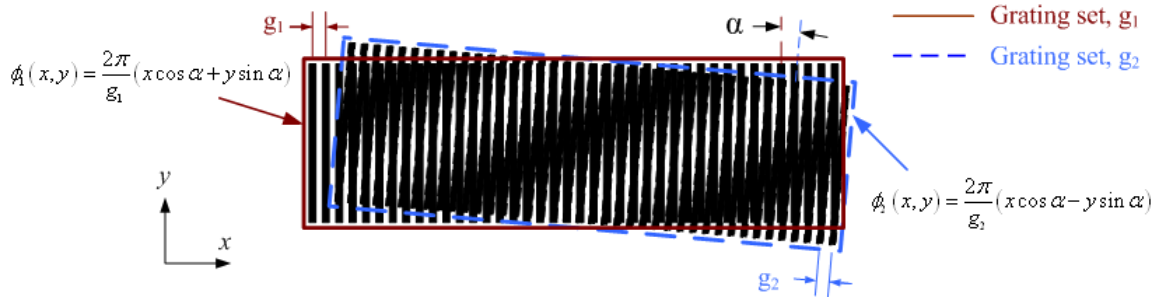


Figure 4-10. Illustration of an angular error α between two grating functions, ϕ_1 and ϕ_2 .

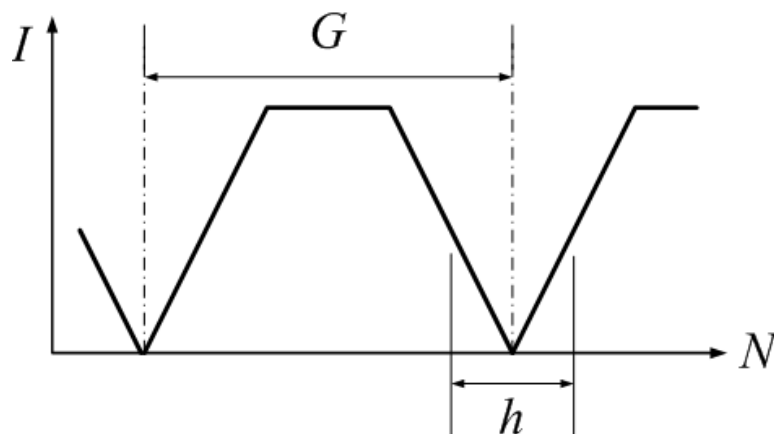


Figure 4-11. Moiré fringe sharpening due to non-equal grating gap to width ratio.

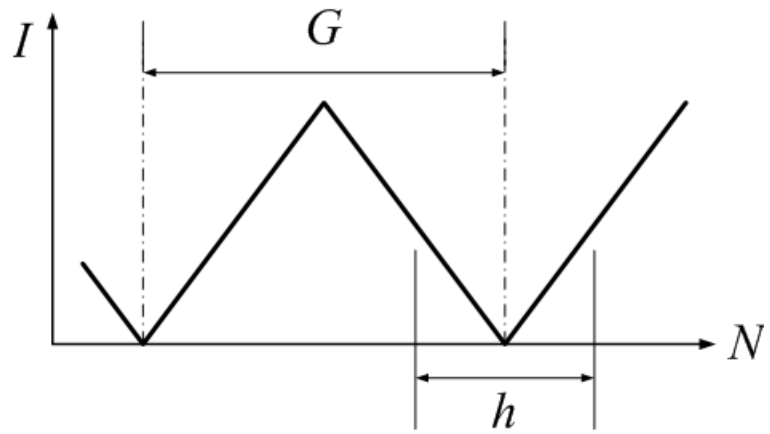


Figure 4-12. Moiré fringe pattern when the grating width and gap are equal.

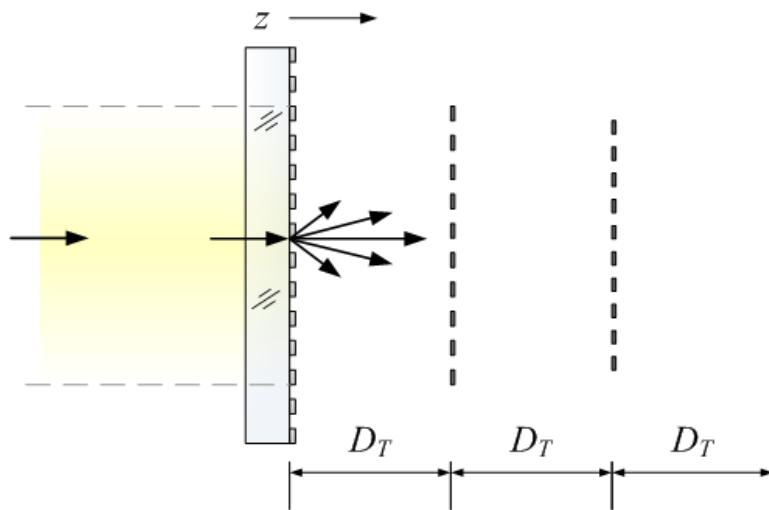


Figure 4-13. Diagram illustrating virtual images from the gratings at successive Talbot distance intervals. Figure is adapted from Post et al [77].

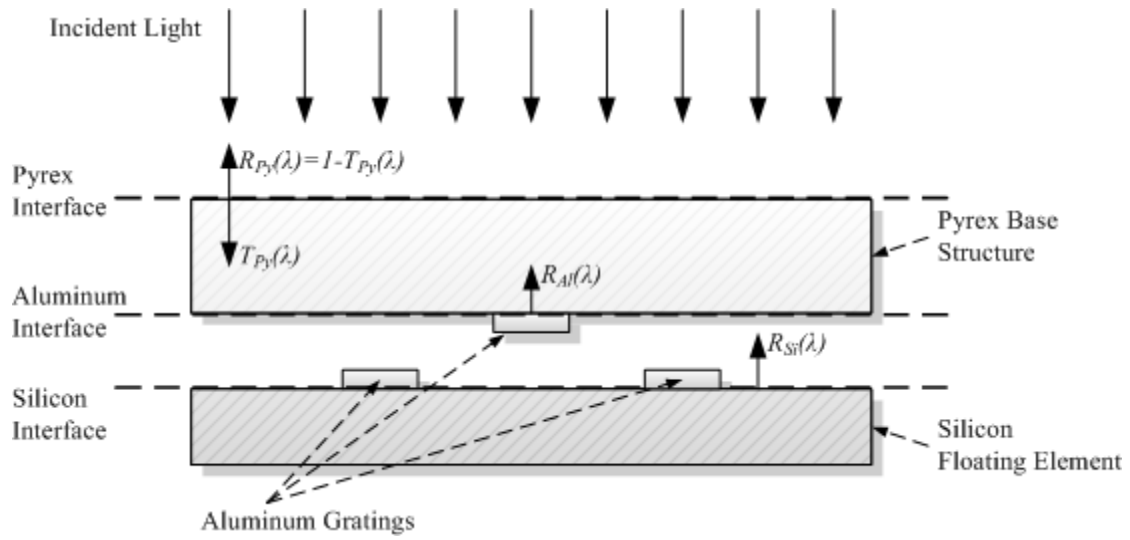


Figure 4-14. Cross section of an optical Moiré shear stress sensor illustrating the reflectivity and transmissivity components of the various material interfaces.

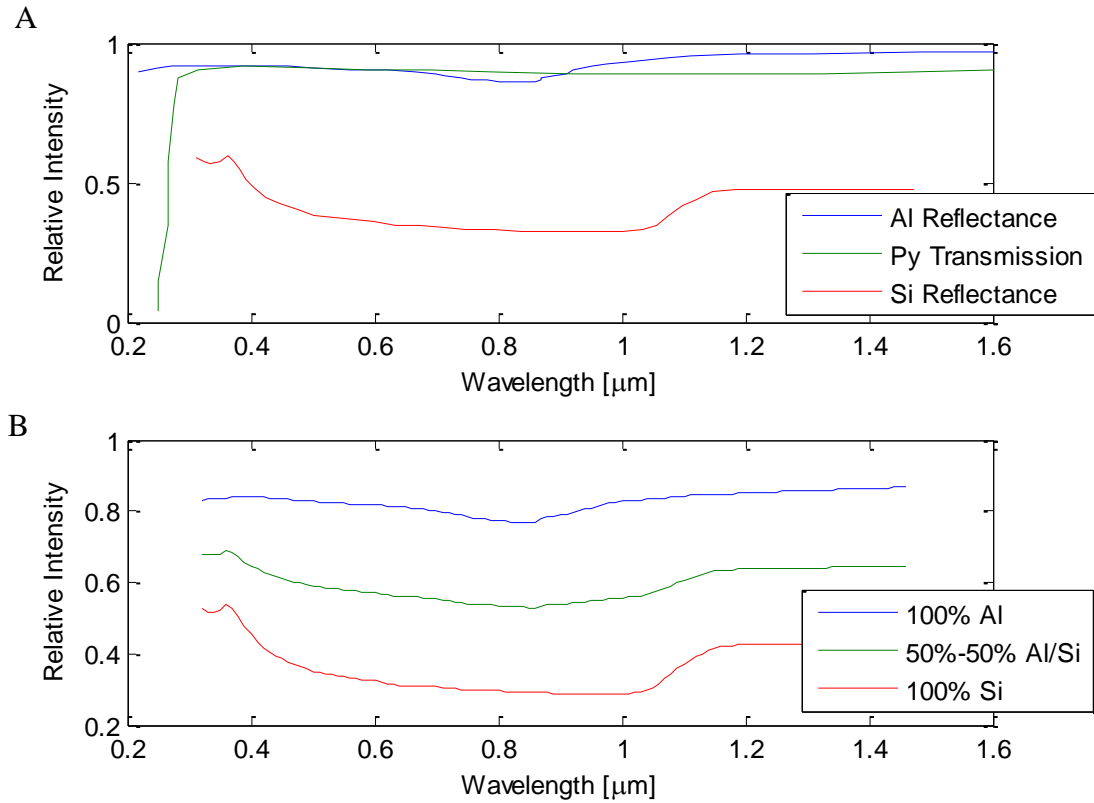


Figure 4-15. Material property plots to determine contrast. A) Graph of reflectance and transmittance of aluminum, silicon and Pyrex. B) The calculated reflectance of aluminum and silicon through Pyrex.

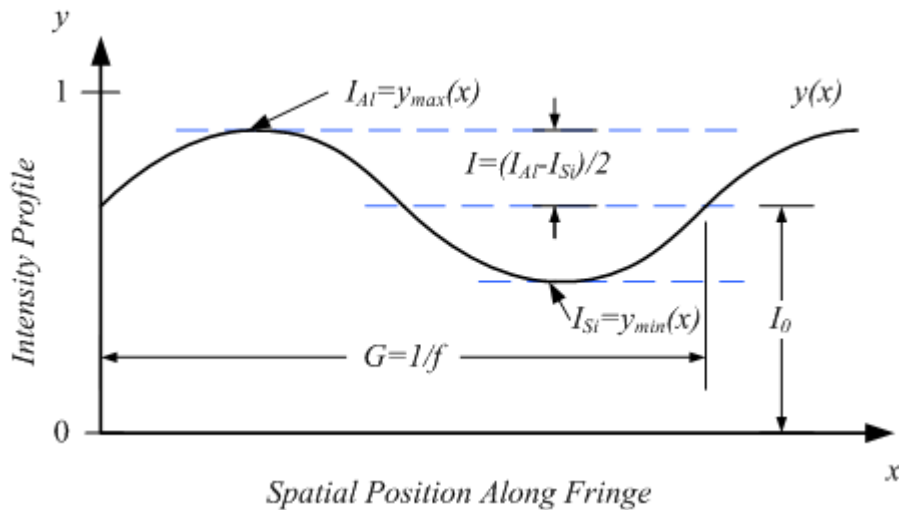


Figure 4-16. Illustration of a sinusoid representing a Moiré fringe pattern using intensities based off of material selection.

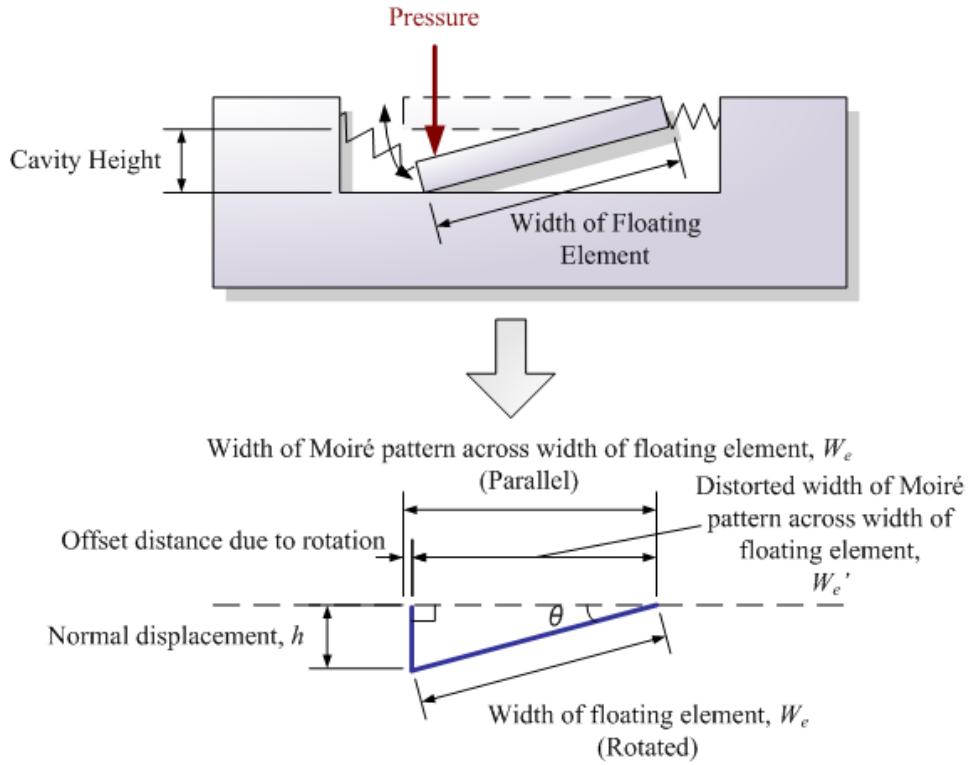


Figure 4-17. Illustration of out-of-plane effects on the width of the Moiré fringe.

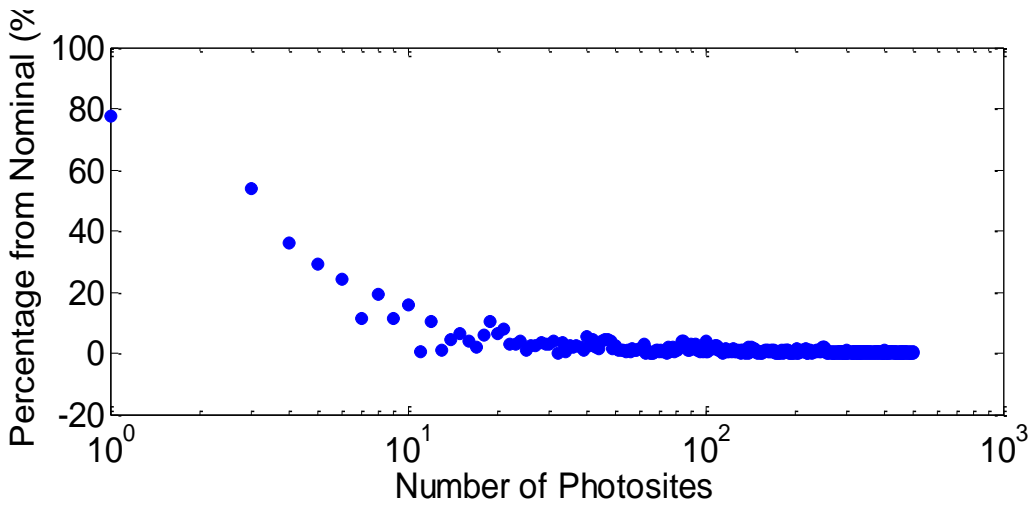


Figure 4-18. Plot showing the percentage deviation in the phase curve-fits due to data reduction.

CHAPTER 5 OPTOELECTRONICS AND OPTICAL PACKAGING

In order for a data acquisition system to record the Moiré pattern on the shear stress sensor, an optical pathway has to be established to transmit light to illuminate the fringe pattern and routed to a photodetection system. Conventional approaches to acquiring a Moiré signal relied on macro-scale, freespace, lens system, such as a laboratory microscope, to scale the Moiré fringe image to a CCD camera. This research uses a line array of optical fibers as waveguides to illuminate and route the signal towards the photodetectors.

In this chapter, the optoelectronics and packaging used to observe the Moiré patterns are discussed. Background information about fiber optics and photodiodes are presented as well as noise modeling for the photodiodes. Noise characterization of the photodiodes using a Faraday cage for electronic shielding is also presented.

5.1 Optoelectronics

The optoelectronics are the components used to optically detect the Moiré fringe patterns. Some of the key components are the light source, transmitting and receiving optical fiber pairs and the photodiode array. The difference between the conventional optics and optical fiber bundle approach is illustrated in Figure 5-1.

5.1.1 Light Sources

The illumination source is used to enable the photodiodes to detect the Moiré fringe pattern. The wavelength of the light source should be selected to maximize the contrast for the Moiré fringe pattern as well as match the peak response of the photodetector.

Some possibilities for light sources that can be used are white light sources, laser diodes or Light Emitting Diodes (LEDs). White light sources have broad wavelengths that encompass the visible spectrum. There are a few drawbacks for using the white light source. The different wavelengths in the white light produce different grating contrasts at the various wavelengths due to the material properties as discussed in Chapter 4. The light reflection and transmission varies for each of the material at different wavelengths and certain wavelengths produce better contrast than others. Integrating all the wavelengths mitigates the benefits seen from a high contrast wavelength. Furthermore, the intensity of the light is spread across the broad spectrum. Laser diode light sources have a narrow spectrum and are coherent. Typically, the laser diodes are usually higher powered than LEDs but the lasers produce phase interference patterns in multimode optical fiber due to the coherence of the laser.

In the initial experimental testing, multiple individual light emitting diodes LEDs (Lumex, SML-LX1610USBC) are used to illuminate the Moiré fringe pattern. The light source is incoherent and uncollimated. The peak wavelength for this LED is at 470 *nm* and has an output of 5 *lumens* . An array of 16 LED light sources are soldered on a prototype circuit board and the light sources are coupled to optical fibers using FC connectors as shown in Figure 5-2. However, using the multiple Lumex LEDs on a single board results in varying light intensities due to the coupling of each LED to the corresponding optical fibers.

A single LED (Doric Lenses) with a pigtailed FC connector is used to replace the Lumex LEDs while a fiber adapter bundle (Ceramoptec) is used to split the LED light source into multiple fibers for the optical fiber bundle (Romack).

5.1.2 Fiber Optics

The basic structure of a cylindrical optical fiber waveguide consists of a core region that is used for light transmission and an outer protective cladding. The cladding layer is used to provide a lower refractive index than the index of the core. Several common types of optical fibers include single mode, step-index multimode and the graded-index multimode fibers [13] and are shown in Figure 5-3. The different fiber configurations determine the profile of the refractive index inside the fiber and the number of modes allowed. In general, the high refractive index in the core region compared to the cladding of the fiber allows for light to be contained in the fiber using total internal reflection.

For an interface between two optical media with different indices, the relationship between the incident light and the reflected and transmitted light at an angle can be determined using Snell's law. Since the angle for the incident light and the reflected light are the same, $\theta_i = \theta_r$, Snell's law can be written as [13], [88],

$$\frac{\sin \theta_i}{\sin \theta_t} = \frac{n_2}{n_1}, \quad (5-1)$$

where θ_t is the angle for the transmitted light and n_1 and n_2 are the two indices of refraction representing the optical media. Figure 5-4 shows the relation between the reflected and transmitted angles, as well as the optical media.

For total internal reflection to occur, a critical angle θ_c is used to determine the angle where the light remains reflected inside the optical medium. The critical angle is defined as,

$$\theta_c = \sin^{-1} \frac{n_2}{n_1}. \quad (5-2)$$

The effect of the critical angle can be seen in Figure 5-5.

A transmitting and receiving optical fiber are used to reflect input light from a fiber connected to a light source to the device and back towards the fiber connected to a photodetector. The configuration of the fibers is shown in Figure 5-6. The optical fibers are placed adjacent to each other and the surface of the device is placed $500 \mu\text{m}$ away from the ends of the fiber to simulate a gap distance that is due to a $500 \mu\text{m}$ Pyrex layer. The equation for a numerical aperture NA of a fiber is given by [13],

$$NA = \sin \theta, \quad (5-3)$$

where θ is the acceptance angle. The coupling efficiency η_c is given by [13],

$$\eta_c = \frac{(NA)^2}{n_0^2}, \quad (5-4)$$

where n_0 is the index of refraction of the medium at the fiber interface, such as air.

The transmitting and receiving optical fibers used have a numerical aperture of 0.22 which corresponds to an acceptance angle of 12.7° . The core of the fibers is $50 \mu\text{m}$ in diameter and the cladding diameter is $65 \mu\text{m}$ for each fiber. The reflecting plane is set $500 \mu\text{m}$ from the transmitting and receiving fibers. Using basic geometry, the light from the transmitting fiber spreads a radius of $112.7 \mu\text{m}$ from the center of the fiber. When the light is reflected from the mirror surface, the distance is doubled. The significance of this result is that the transmitting and receiving fiber pairs are adjacent to neighboring fiber pairs. The light exiting from one pair of fibers can influence other fibers. Crosstalk results from light intensity in one fiber spilling into neighboring fibers and interferes with the actual signal of the encoded Moiré pattern. Such distortion affects the fringe estimation of the signal.

Ideally, the light intensity from each of the light source fibers should be equal so the incident light intensity is evenly distributed across the Moiré fringe pattern. Multiple light sources and fiber misalignment results in an uneven distribution of incident light. The cladding of the optical fibers should be thick enough such that crosstalk does not occur between parallel fibers.

An optical simulation is performed on a single set of transmitting and receiving fiber pairs. The optical software used is Optica 3, which is an add-on program to the computational software, Mathematica. Optical rays are traced in the fiber pair and a reflecting medium as shown in Figure 5-7. Energy intensities are measured at certain interfaces, such as the exit plane of the transmitting fiber, the plane surface of the reflecting mirror and the entrance plane of the receiving fiber.

For the simulation, the optical fibers are modeled as a PVF fiber with a core diameter of 0.05 mm and a cladding of 0.065 mm . At the input end of the transmitting fiber, a light source is generated and modeled using a Gaussian beam. Due to the computationally intensive nature of the simulation, the number of rays generated from the light source is 10 to obtain initial ray trace values. At the end of the transmitting fibers, a mirror is placed as a reflective surface representing the Moiré optic fringes. The distance between the fiber and mirror is 0.5 mm in order to model the thickness of a Pyrex base substrate of the Moiré shear stress sensor. The goal of this optical simulation is to observe the amount of light reflected from the mirror surface to the entrance plane of the receiving fiber in order to estimate the light lost from the fiber to the Moiré fringe. At the entrance plane of the receiving fiber, the energy profile was reduced to approximately 30% of the original light intensity, using the aforementioned

core and cladding diameters. However, the results of the Optica 3 fiber simulation highly varies with the number of discrete rays coupling into the receiving fiber and so further simulation are not pursued in favor of fiber simulation in optical cross-talk studies.

5.1.3 Optical Crosstalk

For a source-receive optical fiber bundle setup, shown in Figure 5-8, optical crosstalk can be a source of noise. When a signal is transmitted using a source-receive optic fiber pairs, a single source fiber may affect multiple receiving fibers. The amount of signal that the adjacent fibers may receive is dependent on a number of factors: the gap distance between the source and receive fibers, numerical aperture of the fibers, mode shape of the light signal and the medium of the gap.

The source and receive optical fibers are separate adjacent fibers and uses the reflection of the optical fringe to reconstruct a Moiré signal. The method of images can be used to represent the spacing between the source and receive fibers and is illustrated in Figure 5-8.

The optical fibers used in the setup are multi-mode silica based fibers with a numerical aperture of 0.22. An air gap and a Pyrex layer are present in between the source-receive fibers and the optical gratings. The index of reflection of the different mediums affects the spread of the light from the source fiber.

The light exiting the source optical fiber is modeled as a Gaussian beam [89]. The equation for a 2D Gaussian beam profile is,

$$I(x, y) = I_0 e^{-\left(\frac{(x-x_0)^2}{2\sigma_x^2} + \frac{(y-y_0)^2}{2\sigma_y^2} \right)}, \quad (5-5)$$

where x_0 and y_0 are the center coordinates of the Gaussian beam and σ_x and σ_y determines the width of the beam.

A simulation is performed to obtain an initial estimate of the amount of optical crosstalk that the neighboring fibers will receive as illustrated in Figure 5-9. The light generated by the source fiber is modeled by a Gaussian beam. The width Gaussian distribution is determined by the gap distance between the source-fiber pairs and the numerical aperture of the fibers. For a gap distance of 1 mm, the calculated width of the Gaussian beam covers approximately 7 optical fibers. Figure 5-10 illustrates the source-source and source-receive mapping and the resulting normalized intensity distribution for the source-source fibers and source-receive fibers is shown in Figure 5-11. The source fibers are denoted as S_n , where n represents the fiber number. The receive fibers are denoted as R_n .

Since the distance between the S1-R1 and S1-S2 are the same, the light intensity observed by R1 and S2 are expected to be the same and is shown in Figure 5-11. The percentage of the total intensity observed by R1 and S2 is estimated to around 2.7%. The receive fiber R2 is adjacent to R1 and is receiving an estimated 2.4% of the normalized intensity which indicates that a significant amount source light intended for R1 (89% of R1) is also observed by the neighboring fiber R2. At receive fiber R7, the received light is less than 0.1% of the total Gaussian beam.

5.1.4 Photodiodes

In general, a photodiode is an optical sensing device that converts an incident light into an electrical parameter, such as a current or voltage. There are two common modes of operation for a photodiode: photovoltaic and photoconductive. The

photovoltaic mode is useful for precision applications whereas the photoconductive mode is useful for high speed applications [90]. A less common mode of operation is the photoamperic mode, which is operated with very low resistance at output of the photodiode [13].

In the photovoltaic mode, a large external resistor is placed at the output of the photodiode equivalent circuit and no bias voltage is applied (zero bias). The large external resistor allows the output current to be relatively small when compared to the input photo-generated current [13]. In this mode of operation, high precision in linearity is obtained but the switching speed is reduced [90]. Also, in the photovoltaic mode, the noise consists primarily of thermal noise and does not have any dark current contribution [90]. Dark current is the current generated when the photodiode is not under any illumination. In the photoconductive mode, a bias voltage is applied at the output of the photodiode equivalent circuit. Reverse bias is typically used in the photoconductive mode, which results in higher switching speeds but the response becomes less linear and the noise is increased due to a presence of dark current [90].

The equivalent circuit for a typical photodiode in the photovoltaic mode and photoconductive mode are shown in Figure 5-12 [13]. The typical parameters used to model the photodiode are: the current generated from incident light i_{λ} , the ideal diode current i_d , junction or shunt capacitance C_j , the shunt resistance R_{sh} , and the series resistance R_s . The applied bias voltage is denoted by V_a .

Typically, a photodiode is made up of a p-n junction as shown in Figure 5-13. Between the p-layer and the n-layer, there is a charge neutral region known as the

depletion layer, or space charge region. The width of the depletion layer is based off of an applied voltage. The energy of a photon is given by,

$$E_{\text{photon}} = h\nu , \quad (5-6)$$

where h is Planck's constant ($h = 6.63 \times 10^{-34} \text{ J} \cdot \text{s}$) and ν is the frequency of the photon.

When an incident photon enters the depletion region with an energy greater than the band-gap energy, E_G , such that $h\nu > E_G$, this results in the formation of an electron-hole pair [15], EHP as illustrated in Figure 5-14. During the formation of an EHP, electrons are moved towards the conduction band which results in holes in the valence band. The amount of electron-hole pairs generated is proportional to the amount of incident light and when the photodiode is connected in a circuit, the generation of EHPs results in a photocurrent flow.

The current-voltage response of a typical photodiode is given by the ideal diode equation [71],

$$i_d = i_0 \left(e^{\frac{qV}{kT}} - 1 \right) - i_p , \quad (5-7)$$

where q is the elementary charge, V is the voltage across the diode, k is Boltzmann's constant, T is the temperature i_0 is the saturation current and i_p is the photocurrent due to incident light. The current to voltage relationship for the photodiode can be seen in Figure 5-15.

There are several regions of operation in a photodiode as shown in Figure 5-16. Depending on the polarity of the external applied voltage, the photodiode may be forward biased or reverse biased. However, if a sufficiently large amount of reverse

bias is applied to the photodiode, the region of operation is considered to be in the breakdown region and the photodiode is usually damaged as a result.

5.1.5 Photodiode Noise

The noise in the photodiode is composed of several noise components: thermal noise, shot noise, generation-recombination noise and flicker noise as shown in Figure 5-17. Thermal noise or Johnson noise can be attributed to the random thermal motion of electrons. Shot noise is the noise related to electrons and holes crossing the p/n junction of a photodiode. Flicker noise, or 1/f noise, is the frequency dependent noise related to charge carriers. Generation-recombination noise is the result of fluctuations in the generation and recombination of carriers [91]. At lower frequencies, the noise contributions from flicker noise dominates and at higher frequencies, the thermal noise dominates.

A typical quantity of interest for photodiodes is the noise equivalent power, which is the ratio of noise current and the current responsivity of a photodiode at a peak wavelength λ_p and is given by,

$$NEP = \frac{\text{Noise current} \left[A / \sqrt{Hz} \right]}{\text{Current responsivity at } \lambda_p \left[A / W \right]} \quad (5-8)$$

The NEP is the minimal detectable signal MDS of a photodiode. The MDS is defined as the ratio of noise per sensitivity. A lower NEP is desirable since a decrease in the NEP results in a higher signal-to-noise ratio for the photodiode.

In summary, the overall performance of the opto-electronic system is affected by the initial light intensity and profile, the ability to couple light into the optical fiber bundle, the ability to receive the light from the optical fringes of the sensor and the ability couple

light into the photodiode array. Other factors include the responsivity and noise in the photodiodes, as well as the fringe estimation technique.

5.2 Optical Packaging Overview

The miniaturized optical package can be categorized into three major components: the optoelectronics, the optical fiber bundle and the package for shear stress sensor (Figure 5-18). The optoelectronics consists of the light source and the photodetectors, along with the data acquisition system. The optical fiber bundle connects the optoelectronics to the shear stress sensor. The optical fiber bundle offers flexibility to the experimental setup and the optoelectronics benefit from the ability to be far removed from the harshness of the testing environment.

5.2.1 LED Board

The prototype light-source used for the optoelectronics are light emitting diodes (LEDs). An array of 16 individual LEDs are mounted onto a circuit board and each of the LEDs is surrounded by a FC connector mount. The FC connectors are used to attach the input end of the fiber bundle array for coupling. The Lumex LEDs, part number SML-LX1610USBC, have a 470 nm wavelength, operating voltage of 3.5 V , an intensity of 5 lumens and a view angle of 70° . Potentiometers are connected in series with resistors to each of the blue LED for individual gain adjustment. A subsequent LED board is planned to replace the prototype LED board with a wavelength that corresponds to the optimal wavelength region of photodetector to yield the most gain.

5.2.2 Optical Fiber Bundle

The optical fiber bundle consists of two rows of 16 multimode silica fibers. One row of the 16 fibers is used to transmit light from the light source towards the shear stress sensor and the other row of 16 fibers is used to receive light from the Moiré

pattern from the sensor towards the photodetectors. The optical fiber bundle is manufactured by Romack Optics, Inc. as shown in Figure 5-19.

At the input end of the light transmitting row of fibers, standard FC connectors are used to connect the input fiber to a light source with a matching FC connection. The other end of the transmitting row of fibers is packaged in a 0.25" x 0.25" x 1.5" aluminum optical housing plug, which is referred to as the sensor plug. The core diameter of each of the fibers is $50\ \mu\text{m}$ and the outer fiber cladding diameter is $65\ \mu\text{m}$. The optical fibers from the transmitting row are placed in a line and spaced roughly at $65\ \mu\text{m}$ apart from the center of each fiber. The optical fibers from the light receiving row are also spaced at $65\ \mu\text{m}$ from center-to-center and the center points of the receiving row of fibers are spaced $65\ \mu\text{m}$ from the transmitting row. The numerical aperture of all the fibers are 0.22, which corresponds to an acceptance angle of 12.7° for each fiber. The other end of the receiving row of fibers is terminated by a 0.313" x 0.75" x 1.5" aluminum optical housing plug, which is referred to as the photodetector plug, that is used to mount the plug to the photodiode array. The fibers in this aluminum plug are spaced $1\ \text{mm}$ to match the pitch spacing of each of the photodiode element.

5.2.3 Optical Fiber to Sensor Adaptor

The sensor interface of the Romack fiber bundle requires a connector to rigidly attach the optical shear stress sensor to the fiber bundle. An adaptor made out of aluminum is designed to connect the optical fiber bundle to the sensor and is shown in Figure 5-20. The optical shear stress sensors are bonded to a low-cost, interchangeable sensor chip mount made of aluminum using epoxy. The thickness of the interchangeable chip mount is $1\ \text{mm}$ and an aperture in the chip allows optical

access from the fibers to the Moiré fringe. Multiple set screws are used to rigidly fix the optical fiber bundle to the adaptor. The goal is to mitigate vibration between the optics and the sensor.

Due to the interchangeable sensor chip mounts, the total gap distance between the fiber and Moiré fringe is 1 *mm*. The gap distance affects the amount of light coupled between the source and receive fibers as well as the amount optical cross talk.

5.2.4 Photodiode Array Board

A Hamamatsu 16 element photodiode array (S4111-16Q) is used to detect the Moiré fringe pattern from the 16 optical fibers. The photodiode array is mounted on a circuit board, shown in Figure 5-21, and a reverse bias voltage is applied to the photodiode array. The breakdown region for the photodiode occurs approximately around 15V. Each individual photodiode element has an active area of 1.45 *mm* by 0.9 *mm* and each element is evenly spaced 1 *mm* apart shown in Figure 5-22. An optical fiber bundle is connected to photodiode array using an aluminum optical mount and the optical mount is fastened to the photodiode circuit board. The output from each of the photodiode array element is connected to transimpedance operational amplifiers (OPA129). The signals from the amplifiers are routed to BNC connectors, which are read simultaneously by a 16 channel external data acquisition system.

The spectral response of the photodiode array is shown in Figure 5-23. The region with the highest photosensitivity, or responsivity, occurs in the infrared wavelengths. For the S4111-16Q photodiode array, the responsivity is between 0.5 *A/W* and 0.58 *A/W* for the input light wavelengths between 800 *nm* to 950 *nm* [92].

Prior to testing with the photodiode array circuitry, several prototype photodiode boards are constructed. One of the boards is constructed with the optical holder and the pre-amplifiers but the photodiode array is not reverse-biased. The other prototype board is constructed with the optical holder but the pre-amplifiers are not included. However, the board without the pre-amplifiers has the photodiode array reverse-biased. The motivation for construction separate boards initially is to test the individual electronic characteristics. Eventually, a final board with both the pre-amplifiers and an applied reversed-bias on the photodiode array is planned to be manufactured for experimental testing. The distinction between the two prototype boards are identified in the following sections.

5.2.5 Data Acquisition System

The 16 signals from the photodiode array were sampled simultaneously using eight 2-channel dynamic signal acquisition modules from National Instruments, NI PXI-4472. These modules are mounted in a National Instruments chassis, NI PXI 1045. Additional acquisition modules on the PXI chassis are used to sample other signals, such as pressure readings from a Heise Pressure meter or control nanopositioner displacements.

5.2.6 Transimpedance Amplifier

The equivalent circuit of a photodiode element with an operational amplifier is illustrated in Figure 5-24. The transfer function for the photodiode and op amp is given by [93],

$$H(s) = \frac{Z_f}{1 + \frac{1}{A_{OL}(s)\beta(s)}} \quad (5-9)$$

where Z_f represents the selected feedback resistor and feedback capacitor, A_{oL} is the open loop gain and feedback factor, β . The feedback impedance is given by,

$$Z_f = R_f \parallel C_f . \quad (5-10)$$

and the feedback factor, which is a voltage divider between the feedback impedance and the impedance of the photodiode [93], is given by,

$$\beta(s) = \frac{Z_i}{Z_i + Z_f} \quad (5-11)$$

where Z_i is the input impedance of the photodiode.

When a reverse bias voltage is applied to the photodiode array, the shunt resistance value is $250 \text{ G}\Omega$ and the junction capacitance is 50 pF according to the Hamamatsu S4111-16Q photodiode datasheet and is shown in Table 5-1. Hamamatsu considers the series resistance to be negligible. The value for the selected feedback resistor is $3 \text{ M}\Omega$ and selected feedback capacitor is adjustable around 7 pF . A spectrum analyzer SR-785 is used to measure the transfer function of the photodiode circuitry and the result is shown in Figure 5-25.

To estimate the noise from the photodiode circuitry, an SR785 spectrum analyzer was used to measure the noise of the photodiode board. A double Faraday cage was used to shield the circuitry and minimize the amount of external noise as shown in Figure 5-26. The photodiode array was covered such that the photodiode only generates dark current. The result of the noise measurement is shown in Figure 5-27.

5.3 Summary

The optical fiber system developed in this research includes non-idealities that are characterized and discussed in experimental characterization section of chapter 7. Some non-idealities include the varying sensitivities and offsets among the photodiode channels in the array. The Romack fiber also has manufacturing issues which include uneven fiber spacing among the individual fibers and scrambled mapping between the source and receive fiber pairs. Intensity fluctuations attributed to the light source are monitored by introducing a second optic fiber bundle with an additional reference fiber. The configuration between the two optic fiber bundles is also discussed in chapter 7. The optic coupling to each of the fibers in the bundle varies. These issues with the optic fibers affect the fringe estimation process and optical characterization techniques are developed in this research to compensate for the issues with the optical fibers.

Table 5-1. Resistance and capacitance values for the Hamamatsu S4111-16Q photodiode array.

	R_{sh}	$C_j (V_R = 0V)$	$C_j (V_R = 10V)$	R_s
S4111-16Q	250 G Ω	200 pF	50 pF	10 Ω

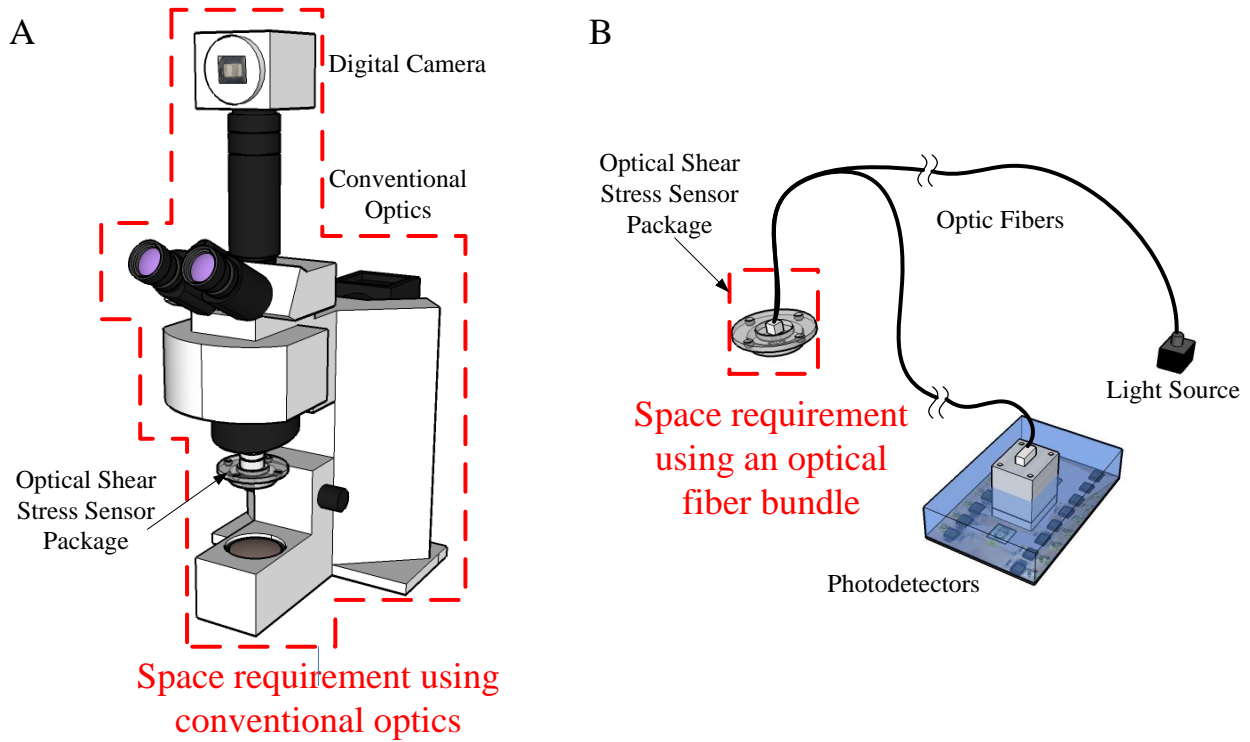


Figure 5-1. A comparison of the space requirement between conventional optics and miniaturized optics for imaging the Moiré pattern on the shear stress sensor. A) Conventional optic approach. B) Optical fiber bundle approach.

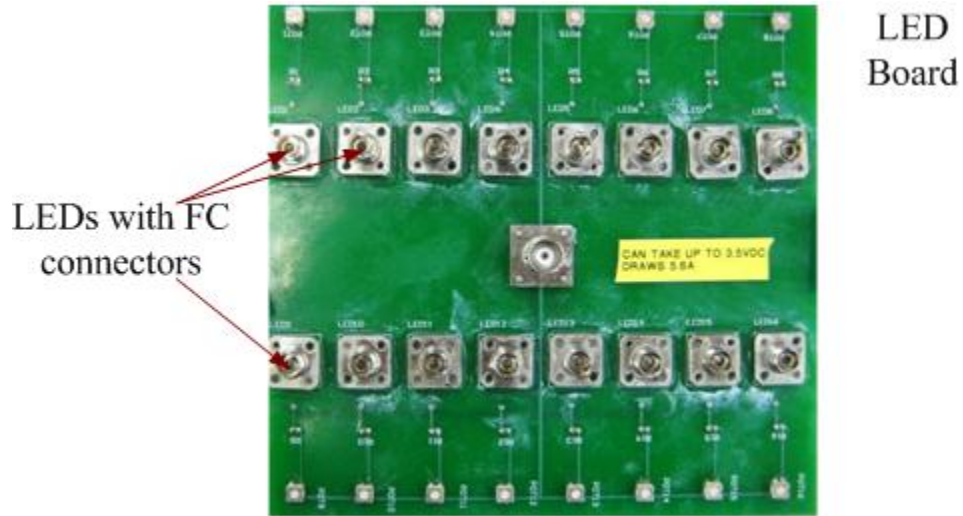


Figure 5-2. Prototype LED (Lumex SML-LX1610USBC) circuitry board for an optical fiber bundle array using FC connectors.

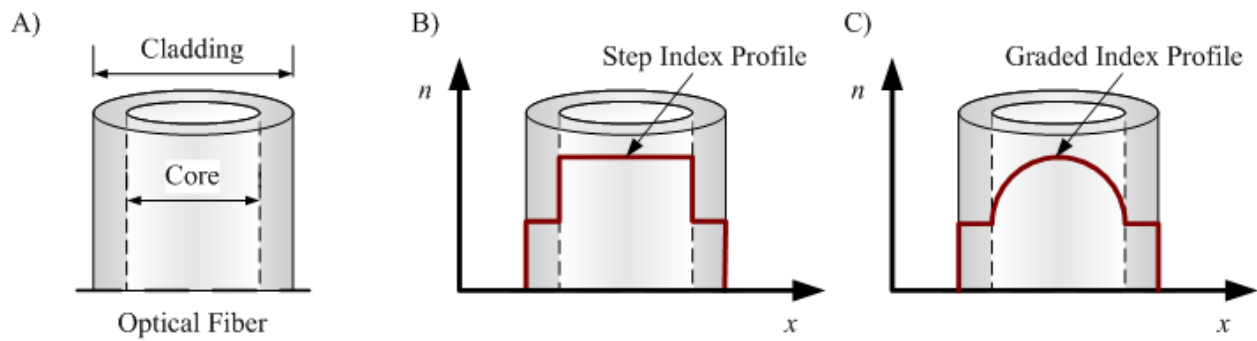


Figure 5-3. Diagram of various optic fiber index profiles. A) Single mode fiber. B) Step index multimode. C) Graded-index multimode fibers.

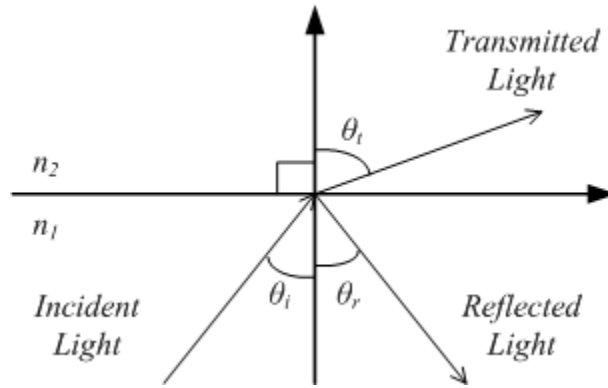


Figure 5-4. Light reflecting and transmitting at the Interface between two media. [13]

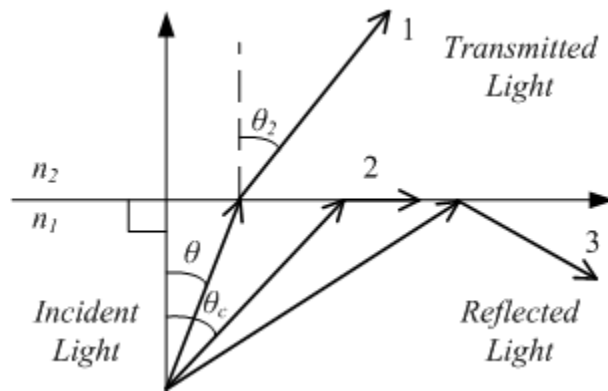


Figure 5-5. Light angles between two optical medium with respect to the critical angle [13]

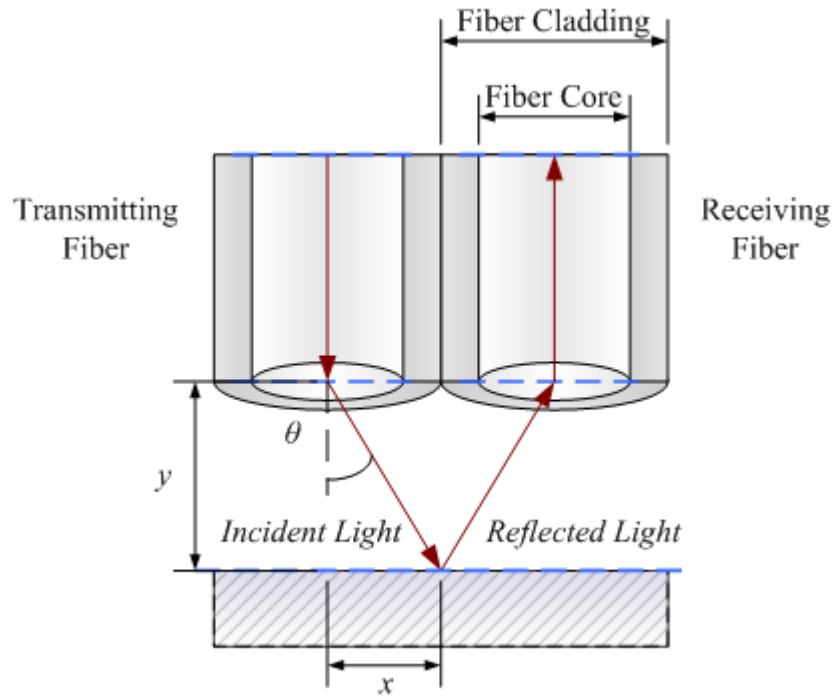


Figure 5-6. Illustration of the transmitting and receiving optical fiber pair.

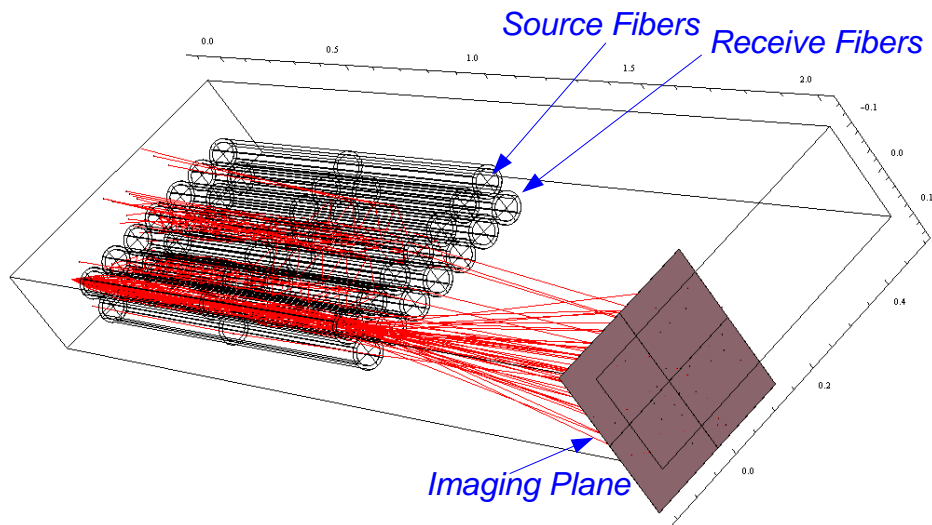


Figure 5-7. A transmitting and receiving fiber with a reflecting mirror modeled in Optica.

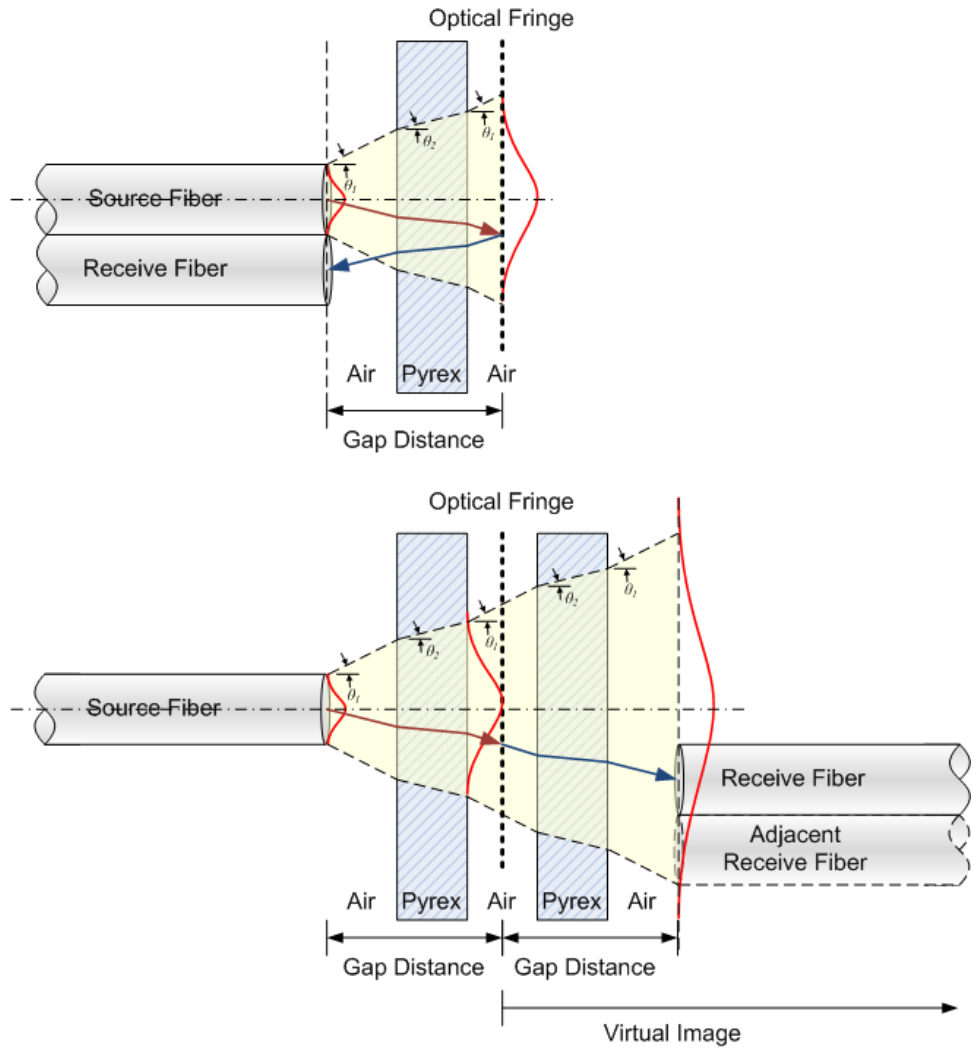


Figure 5-8. Illustration of the source-receive optical fiber pairs in relation to the optical fringe.

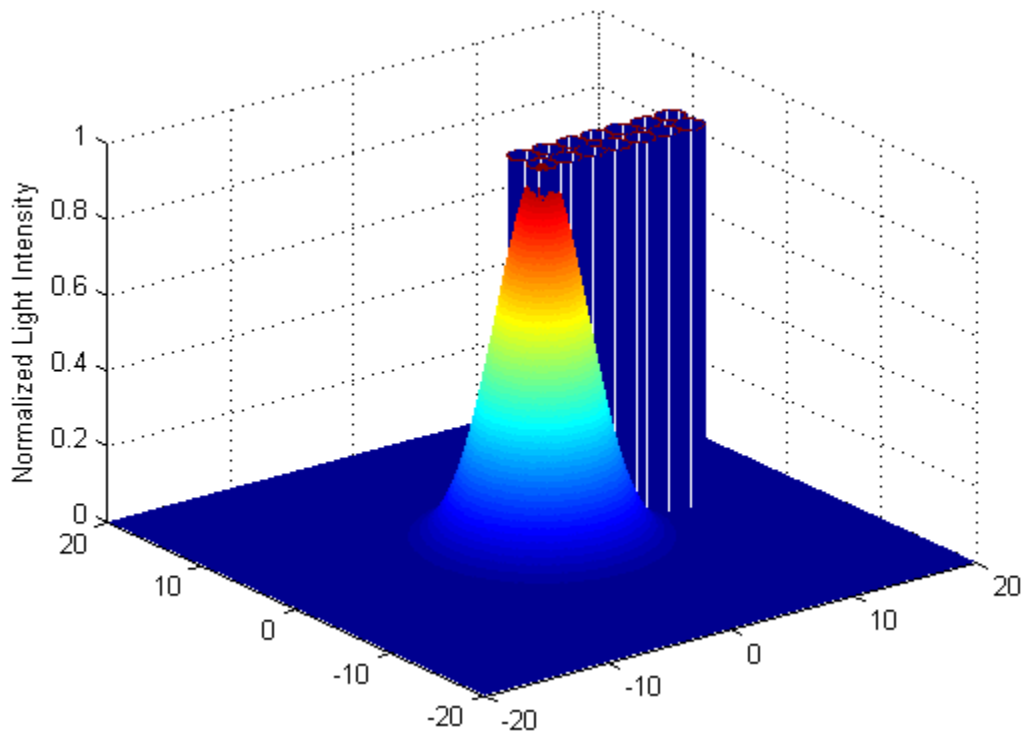


Figure 5-9. Modeling light from the source fiber to multiple receiving optical fibers.

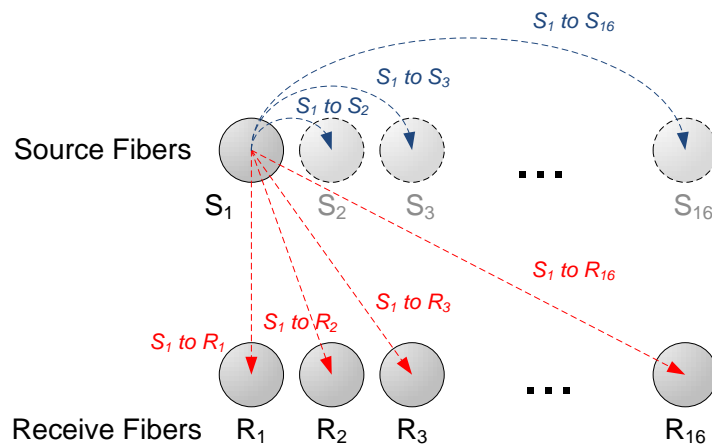


Figure 5-10. Optical fiber mapping between the source and receive fibers.

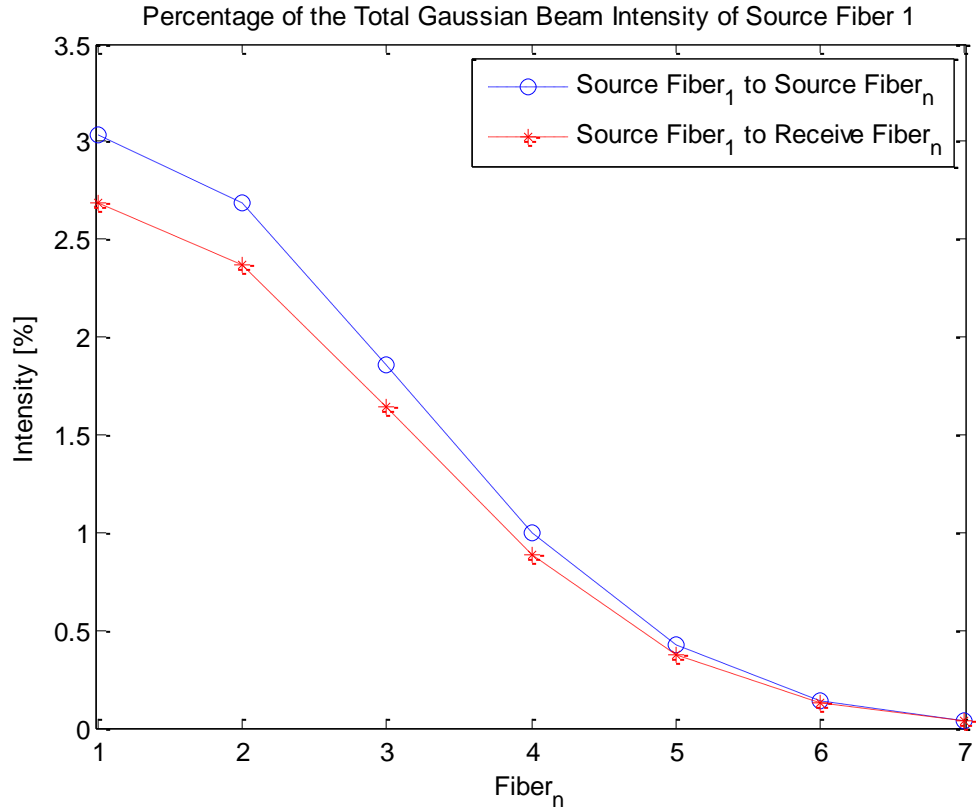


Figure 5-11. An estimation of the collected light intensities across the optical fiber bundle array.

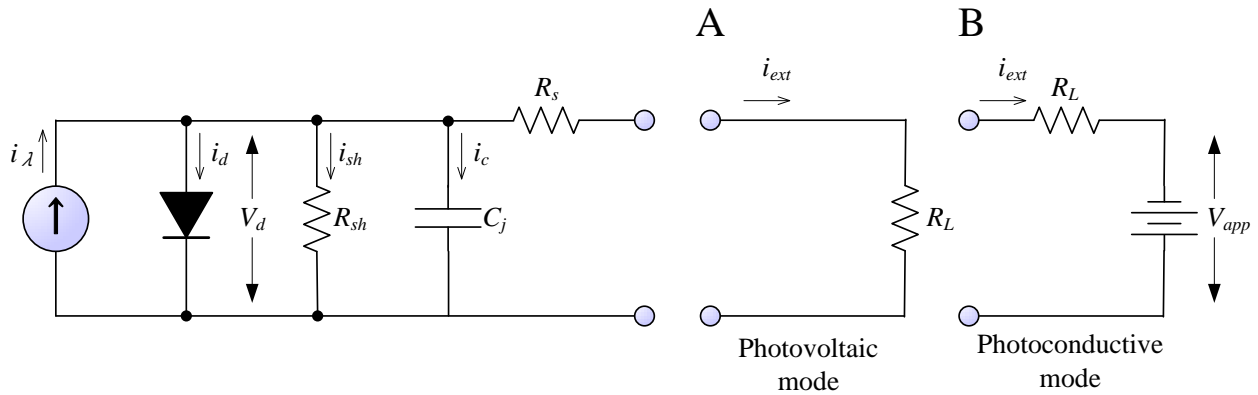


Figure 5-12. Equivalent circuit for representing a photodiode. A) Photovoltaic mode. B) Photoconductive mode.

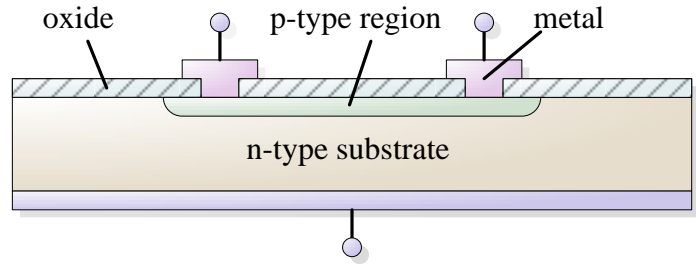


Figure 5-13. Illustration of the p-n junction for a typical diode.

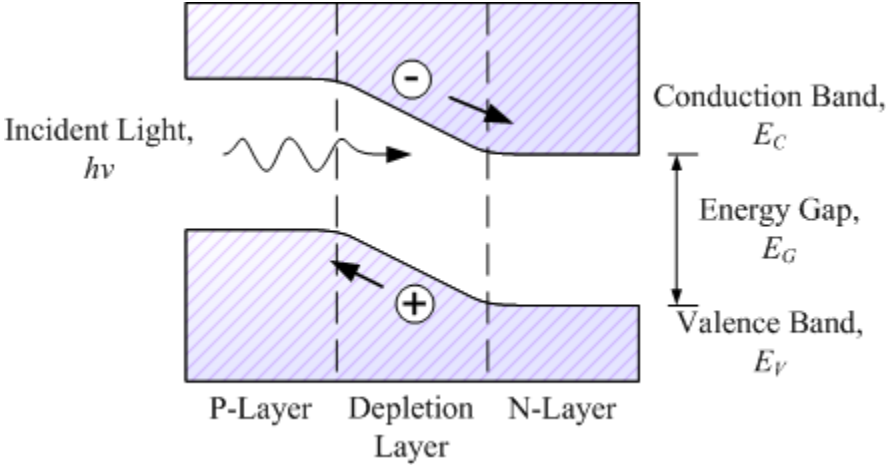


Figure 5-14. Formation of EHP in the P-N Junction of a photodiode.

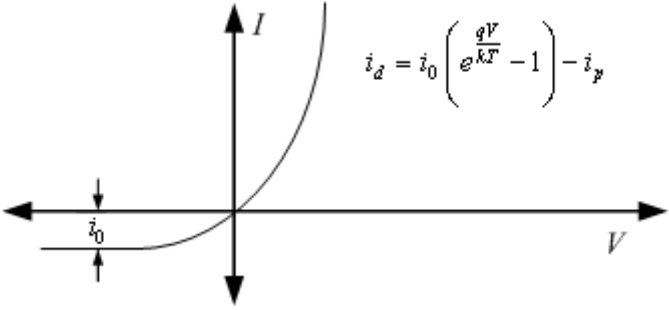


Figure 5-15. A plot of the current voltage curve for a photodiode.

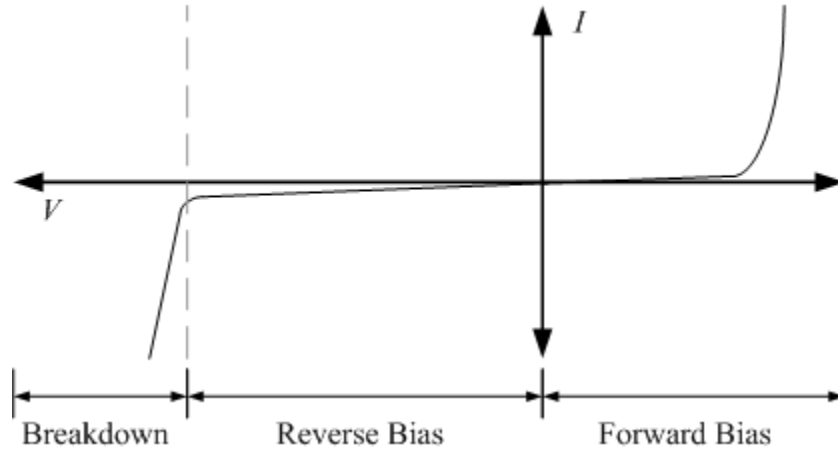


Figure 5-16. Graph representing the different regions of operation in a photodiode.

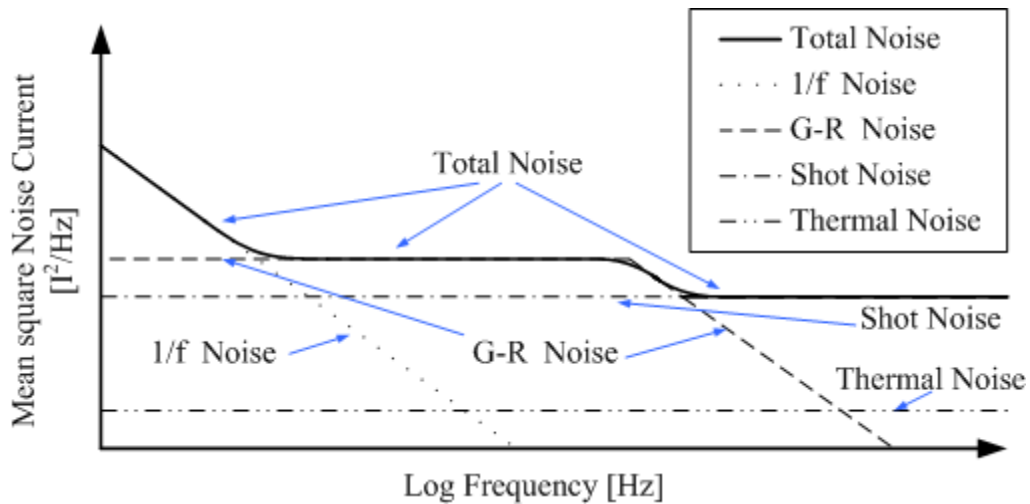


Figure 5-17. Illustration of noise contributions in a photodiode. [91]

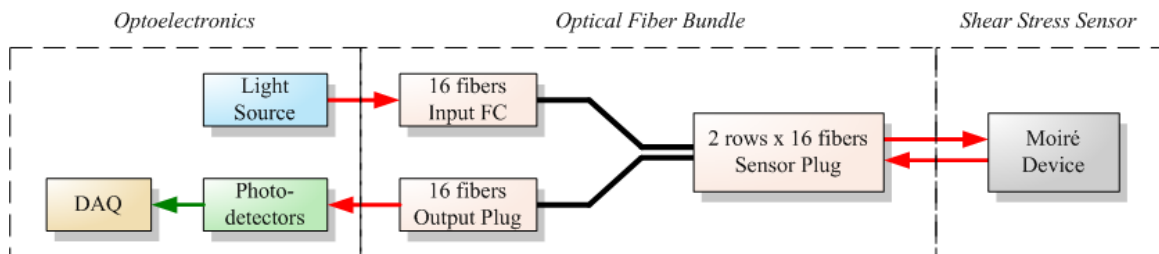


Figure 5-18. Overview of the experimental optical packaging setup.

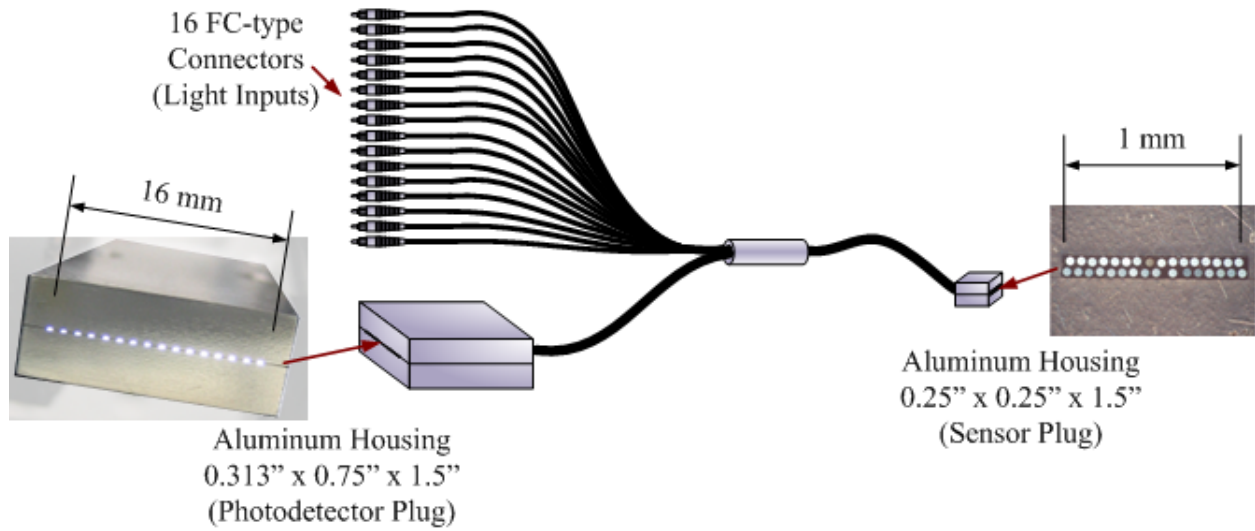


Figure 5-19. Optical fiber bundle manufactured by Romack Optics.

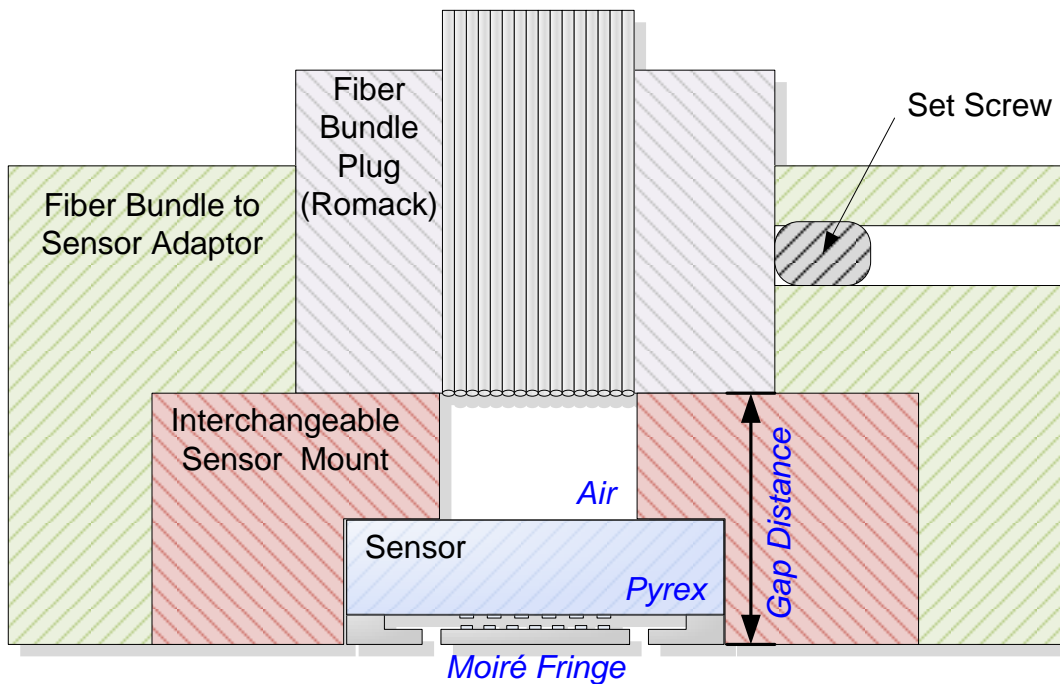


Figure 5-20. Schematic for the fiber plug adaptor to rigidly connect the Romack fiber bundle to the optical shear stress sensor.

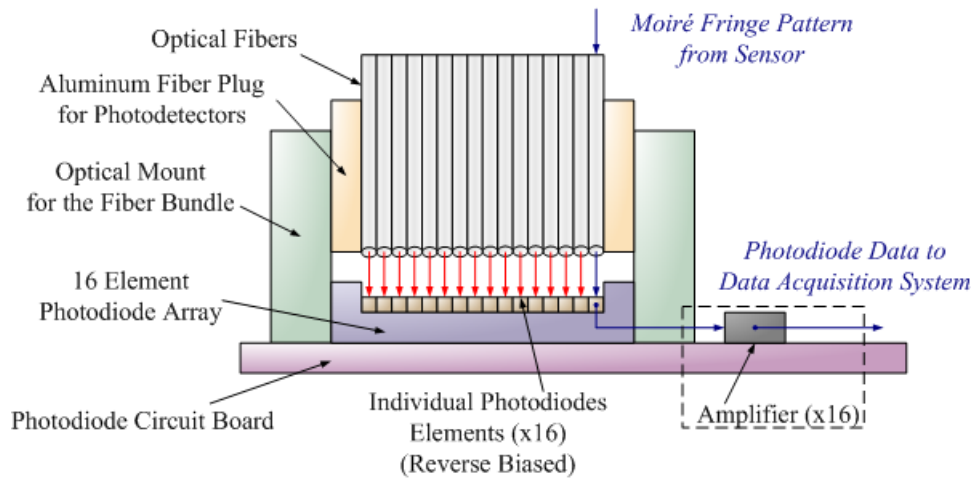


Figure 5-21. Schematic of the Romack fiber plug attached to the photodiode array board circuitry.

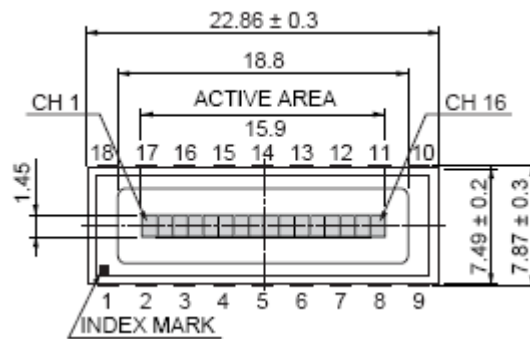


Figure 5-22. Diagram of a Hamamatsu S4111-16Q photodiode array with 16 elements. Diagram is adapted from Hamamatsu [92].

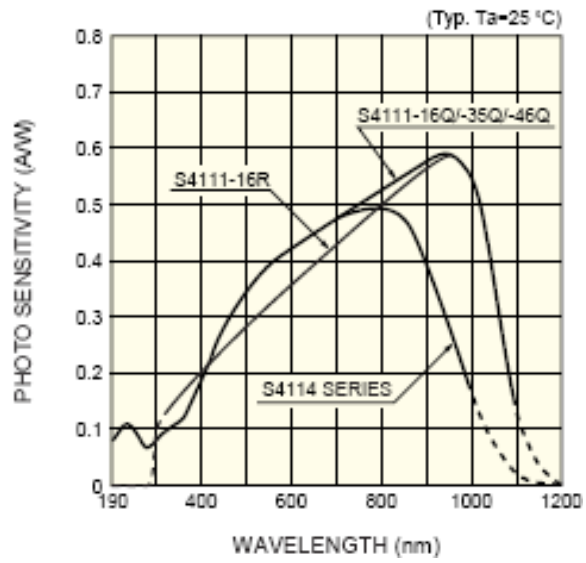


Figure 5-23. Photosensitivity of a Hamamatsu S4111-16Q. Diagram is from Hamamatsu [92].

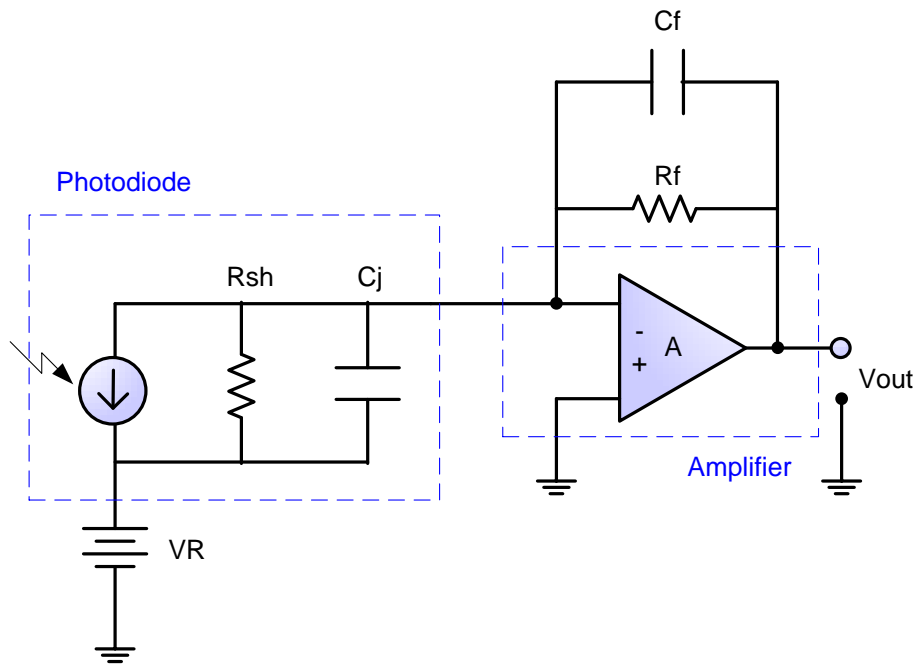


Figure 5-24. Equivalent circuit of the photodiode and the operational amplifier.

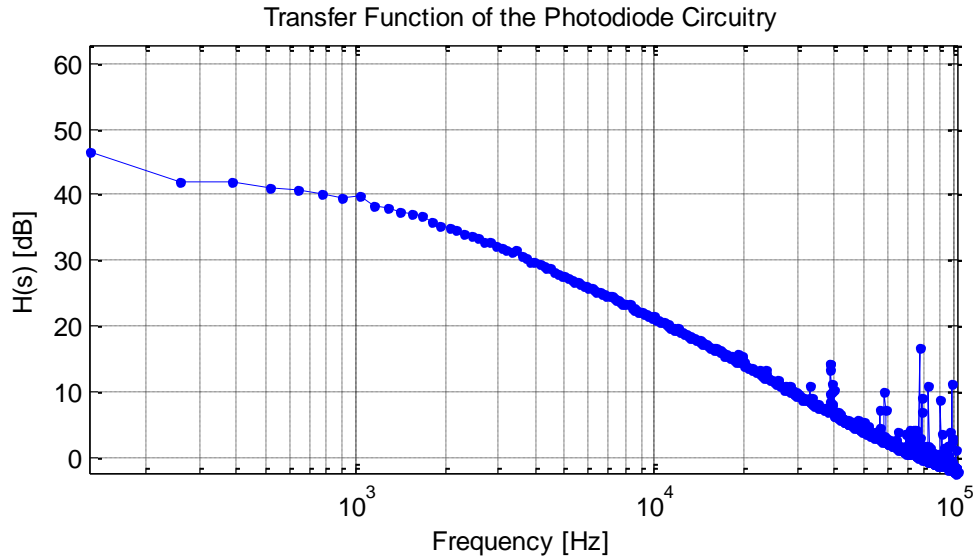


Figure 5-25. Transfer function of the photodiode circuitry measured by the spectrum analyzer.

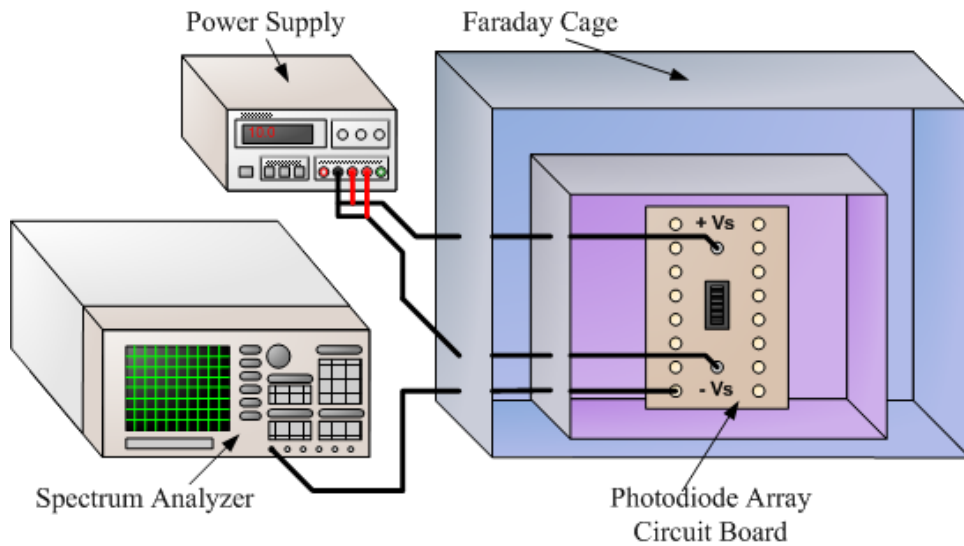


Figure 5-26. Illustration of the photodiode array board with amplifiers in a Faraday cage for noise measurements.

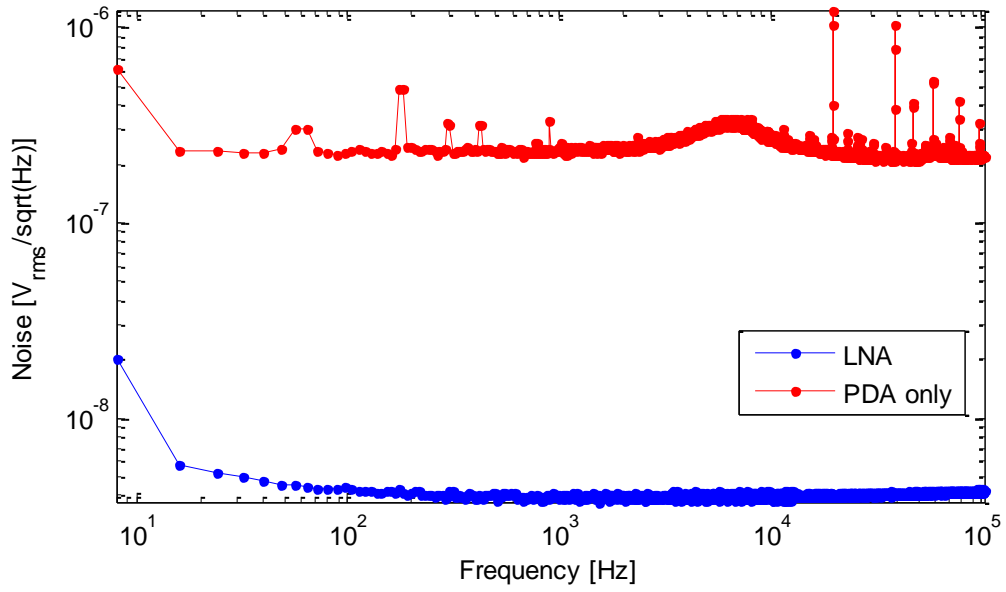


Figure 5-27. Noise measurements from the photodiode array board in a Faraday cage.

CHAPTER 6 MICROFABRICATION

In this chapter, the microfabrication process flow for a floating-element optical Moiré shear stress sensor is discussed. The process uses a 4 mask, bulk silicon-on-insulator (SOI) micro-machining process to create a silicon floating element with metal optical gratings supported by a Pyrex base structure. The next section provides a high-level overview of the process followed by a detailed discussion of the key steps. This chapter concludes with some results from the microfabrication.

The device fabrication process starts with a p-type, 100 mm diameter (100) silicon-on-insulator (SOI) wafer. The 45 μm silicon device layer of the SOI wafer is used to create the floating element structure, while the 1 μm buried oxide layer (BOX) serves as an etch stop for a subsequent thin-back process. A 100 mm Pyrex (Corning 7740) wafer serves as a transparent base structure for the device. Aluminium gratings are patterned on SOI and the Pyrex structure and an anodic bond is used to bond the wafers. The 500 μm bulk silicon and the BOX layer of the SOI are removed using KOH and a Buffered Oxide Etch (BOE), respectively. The floating element and tethers patterns are defined front-to-back wafer alignment are subsequently released using a deep reactive ion etching (DRIE) process. The majority of the microfabrication steps were performed at the Microelectronics Research Center at the Georgia Institute of Technology while the floating element release was performed at the University of Florida.

6.1 Microfabrication Process

An outline of the microfabrication steps is illustrated in Figure 6-1. A cavity is first etched into the thin side of the SOI wafer using a Deep Reactive Ion Etcher (DRIE).

Once the cavity is etched, a thin aluminum layer is deposited, patterned and then wet etched to form the first set of optical gratings. Similarly, aluminum is deposited, patterned and etched on a Pyrex wafer for the second set of gratings. The Pyrex wafer and SOI wafer are then anodic bonded to seal the cavity with the gratings in between. The thick silicon side of the SOI is then etched using a KOH solution until it reaches the buried oxide layer (BOX), which acts as an etch stop. The BOX layer is then removed using a BOE dip. A front to back alignment is used to pattern the tethers and the floating element. These features are then released using a DRIE etch. A brief plasma ashing is used to remove the remaining photoresist.

6.1.1 Cavity Etch

For the device layer of the SOI, DRIE is used to create a $2 \mu m$ cavity. This cavity serves as a recess for the aluminum gratings and the surface of the cavity should be smooth to deposit reflective gratings in a subsequent step. The $2 \mu m$ cavity was selected to minimize the distance between the gratings. The cavity distance should be within 5% of Talbot distance, D_T , which is discussed previously in Chapter 4 using equation (4-27) in order obtain a reasonable contrast.

6.1.2 Aluminum Gratings

Aluminum is deposited on the both the Pyrex and on the thin silicon side of the SOI wafer. Previous research has documented the reflectivity of $>50 \text{ nm}$ thick, aluminum films from wavelengths of 220 nm to 1000 nm [82]. The aluminum film is deposited $0.25 \mu m$ thick to allow enough light to reflect back from the surface of the aluminum. Aluminum has a 95% reflectance at infrared [94]. The aluminum was etched using an aluminum etchant (Transene, Type A). The temperature was set to

between 45~60°C , and the etch time was around 10 seconds. A brief Piranha etch was used to clean the surface of the device wafer prior to bonding.

6.1.3 Anodic Bond Process

Once the aluminum gratings for both SOI and Pyrex wafer are patterned, the next step is to bond the wafers together. The bond procedure requires a relatively low temperature to prevent the aluminum gratings from melting during the bond. The melting point of aluminum is 660°C [95]. An anodic bond is ideal for low temperature bond since the bond between Pyrex and silicon is electrochemical. A voltage is applied through an electrode on the Pyrex and through the SOI. The sodium ions are pulled towards the negative electrode, thus creating a sodium depletion region at the Pyrex-silicon interface, which allows the oxygen rich Pyrex region at the interface to bond with the silicon, forming a SiO_2 bond between the Pyrex and silicon [96].

Prior to bonding, the device wafer and Pyrex wafer have to be aligned. The Karl Suss MA6 Mask Aligner was reconfigured so a bond chuck can be used during wafer alignment. Mechanical flags are inserted between the wafers such to space the wafers evenly apart. During the bonding process, a piston evenly pushes down the Pyrex wafer down on to the device wafer to avoid the formation of air pocket gaps between the wafers.

Once the wafers are aligned, the bonding chuck is then transferred to the Karl Suss bonder. The temperature for the top and bottom side of the Pyrex and device wafer is set to 400°C . The voltage was set to ramp from 0 V to -750V and set for 4 minutes. Following that, the voltage was then switched to -1500 V for 15 minutes. The bond pressure applied by the electrode was 1837 mbar (183.7 kPa). Typically, the

pressure in the chamber of the bonder is in a state of vacuum to assist with the bonding, however, the device wafers were bonded at atmospheric pressure to reduce the formation air pockets. The wafers were allowed to cool down for several hours before they were removed from the bonder.

6.1.4 KOH Etch Process

The bulk silicon from the SOI were removed using a Potassium Hydroxide (KOH) wet etch process. A KOH 45% solution from J.T. Baker was prepared in a bath at 70°C. The temperature for the KOH bath was controlled by a Microtemp Model C16 controller module by Modutek Corp. For a <100> silicon wafer, the etch rate using the JTBaker KOH 45% solution at 70°C is 31 $\mu\text{m/hr}$ [97].

Prior to immersing the device wafer in the prepared KOH solution, the Pyrex side of the device wafer is protected from the KOH etchant. The procedure to protect the backside of the device wafer is to mount the device wafer to a mask reticle, such as a blank transparent photolithography mask or an additional Pyrex wafer, using Carnauba wax (Strahl & Pitsch Inc., SP 200, Batch #22903). The Carnauba wax flakes are spread around the edge of the device wafer and then melted on a hotplate at 85°C to form a wax seal. The KOH bath temperature was selected to be 70°C in order to increase the silicon consumption rate while maintaining a low enough temperature away from the melting point of the Carnauba wax, which is approximately 83°C [98]. The wax seal is then removed by reheating the glass substrate and device on a hotplate at 85°C. While the wax leaves a thin residue on the Pyrex wafer, the residue is removed via a Piranha etch.

A wafer boat was used to simultaneously process several wafers at one time to reduce the amount of time and KOH solution used. For the silicon 45 μm SOI wafer, the etch time was approximately 14.5 hours with an experimental etch rate of 24 $\mu\text{m}/\text{hr}$ while the 25 μm SOI wafer etched in 23 hours with an etch rate of 21.7 $\mu\text{m}/\text{hr}$. During the KOH etch process, the bulk silicon layer appeared to be rough and gray until the oxide layer is reached. The bulk silicon is considered to be completely etched when the surface of the device layer appears to be glossy and have a purplish hue due to the oxide layer.

A brief Piranha etch was used to clean off the Carnauba wax residue. This step is used to remove the Carnauba wax that might be covering the Moiré gratings. Following the Piranha etch, a brief BOE dip was performed to remove the 1 μm oxide etch stop in the SOI wafer. The purplish hue that is typical of an oxide should be not present on the surface of the silicon when finished with the HF dip.

6.1.5 Front-to-Back Align

The photoresist used for patterning the tethers is the Shipley S-1827 positive photoresist. The spin recipe for the initial phase is 500 rpm/s for the ramp acceleration and 4000 rpm for the speed for a duration of 30 seconds. The ramp down recipe was a speed of 0 rpm and 500 rpm/s for the ramp down. The device wafer with the S-1827 photoresist was soft baked on a hotplate at 115 C for 90 seconds.

A Karl Suss mask aligner with a front to back aligning capability is used to align the tethers mask to the device wafer. The exposure recipe for the alignment is to use the Channel 2 light with an intensity of 20 mW/cm^2 for 18 seconds. The S-1827

photoresist was developed using the MF AZ 319 developer for 60 seconds. The photoresist was placed on a hotplate and baked for a period of 5 minutes.

6.1.6 Tethers Release

The floating element and tethers were anisotropically etched using the deep reactive ion etcher (DRIE). The number of etch cycles for the 45 μm thick floating element wafers is approximately 32 cycles with a 12 second etch cycle and 7 second passivation cycle. This recipe etched approximately 1.4 μm per cycle.

The remaining photoresist on the floating element and tethers were removed using a plasma asher. Wet solvents are avoided to avoid stiction between the floating element and the Pyrex wafer. The etch rate for the Shipley photoresist is approximately 400 $\text{\AA}/\text{min}$. The device wafer is ashed approximately for 25 minutes.

6.1.7 Dicing

The wafer with the released tethers is diced using a dicing saw. The device wafer is carefully placed with the floating element face down on a handle wafer. A layer of plastic wrap is used to cover the floating element and the device wafer is attached to the handle wafer using double sided tape such that the Pyrex side is exposed and the sensitive tethers are protected. This is to prevent damage to the tethers as well as preventing liquids and debris from entering the tether gaps during the dicing process. The Pyrex side of the device wafer is scribed approximately two-thirds of the thickness into the Pyrex using the dicing saw. After the scribe lines were finished, the device wafer is then separated from the handle wafer and carefully cleaved to separate each individual die.

6.2 Microfabrication Results

After separating the individual devices using the dicing saw, the devices were carefully examined under a microscope. An SEM image of the sensor is shown in Figure 6-2 and a photograph of the sensor is shown in Figure 6-3. The yield of the device was reduced to less than 5% due to microfabrication and the combination of one or more defective tethers or poor definition in the Moiré fringe pattern. During the DRIE process, the individual devices were released at different times on different regions of the wafer. Subsequent etch and passivation to release the remaining devices resulted in trapezoidal tethers in the devices that were already released. The top surface of the tether width is optically measured using a microscope to be $17.5 \mu m$ and the bottom of the tether width is measured to be $11 \mu m$, resulting in a trapezoidal cross-section of the tether instead of the intended rectangular design. The trapezoidal tether geometry affects the compliance, resonance and pressure rejection of the device.

During the wafer dicing process, several devices are lost in the dicing saw chamber. A medium tact tape is adhere to the wafer as a base support but some devices lost contact from the tape once released while still inside the dicing chamber. The lost devices lowered the total yield and is shown in Figure 6-4. The wafer from the dicing saw also caused the floating elements in some devices to clamp down to the base structure due to stiction and is shown in Figure 6-5.

The mean and dynamic characterization results of these devices are discussed in the following experimental chapter.

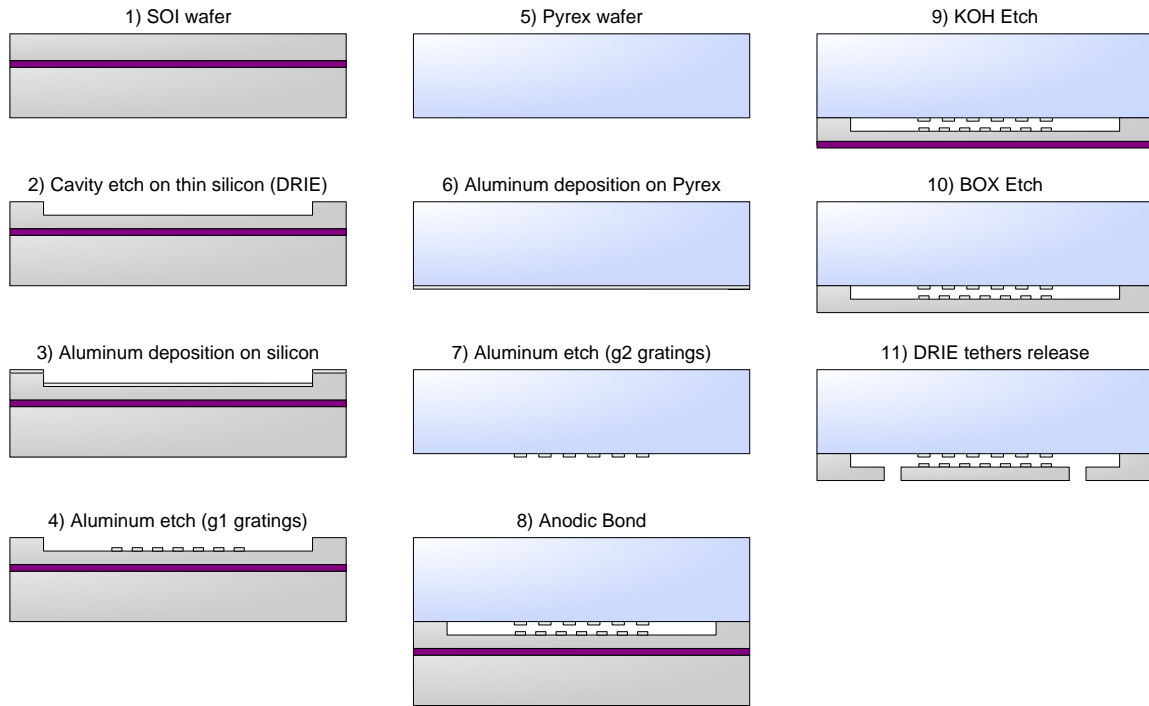


Figure 6-1. A cross-sectional diagram illustrating the basic steps in the optical shear stress sensor device fabrication; drawing not to scale.

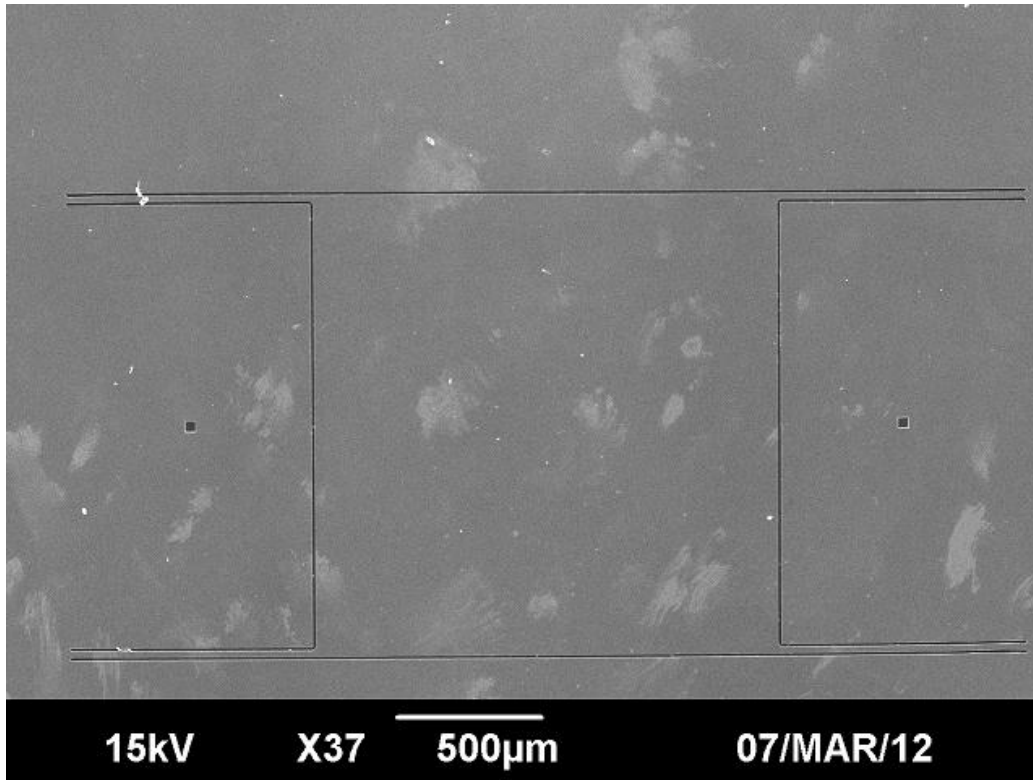


Figure 6-2. SEM image of a released floating element on a 50 Pa, 5 kHz device. Photo courtesy of Tai-An Chen.

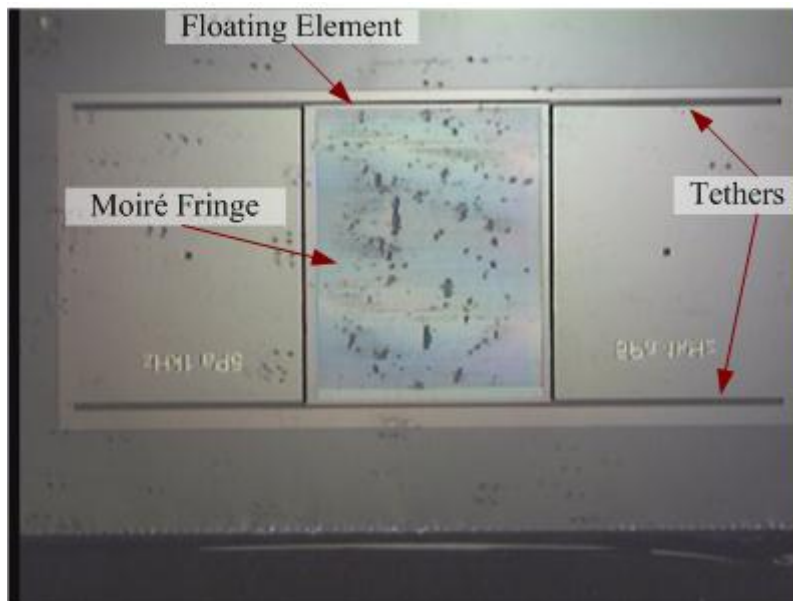


Figure 6-3. Photograph of a 5 Pa 1 kHz Moiré shear stress sensor. Photo courtesy of Tai-An Chen.

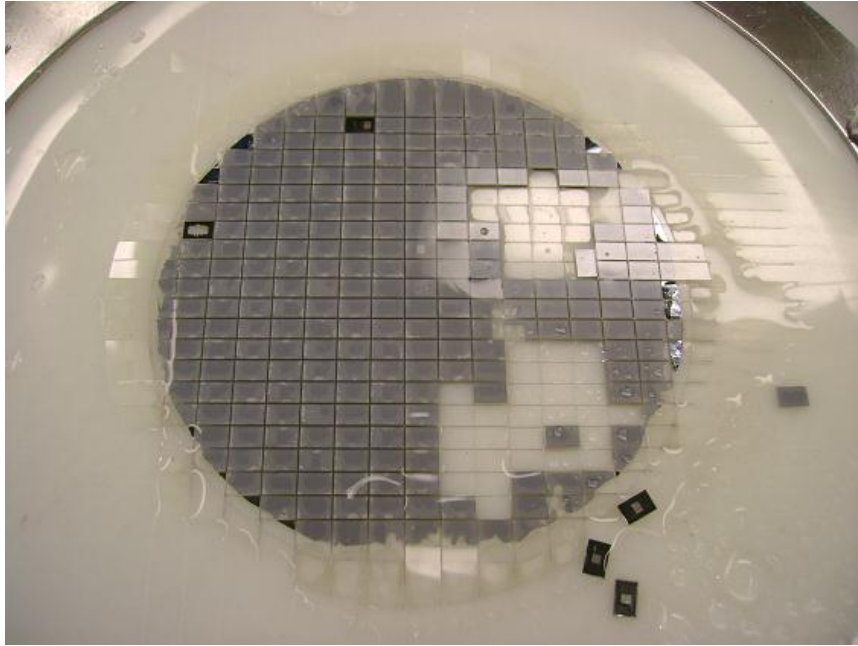


Figure 6-4. Photograph of the wafer inside the dicing saw chamber. Photo courtesy of Tai-An Chen.



Figure 6-5. Photograph of a 5 Pa, 1 kHz device with stiction. Photo courtesy of Tai-An Chen.

CHAPTER 7 EXPERIMENTAL CHARACTERIZATION

In this chapter, the experimental setups for calibrating the optical components as well as the optical shear stress sensor are discussed. The response of the optical setup is observed using a simulated microfabricated optical shear stress sensor that is mechanically controlled by a nano-positioner. The testing procedure for obtaining static and dynamic calibrations of the device is also discussed.

7.1 Experimental Optical Calibration

The optical fiber bundle manufactured by Romack Inc. is tested for variations between each fiber, misalignment issues and coupling losses for transmitting and receiving light. The Moiré fringe pattern generated by a simulated floating-element is mounted on a testbed and controlled by a mechanical nano-positioner. The mechanical deflections simulate the wall shear stress action upon the floating-element.

7.1.1 Optic Fiber Bundle Calibration Setup

The goal of an optical fiber calibration is to determine the different sensitivities between each fiber. The varying sensitivities and offsets between each optical fiber are undesirable and interfere with optical fringe measurements. The differences in sensitivity between fibers may be due to differences in fiber coupling and manufacturing misalignment. From the optical calibration results, a normalization algorithm is used to adjust the difference sensitivities between optical fibers to produce a uniform sensitivity. The adjustments from the normalization algorithm are applied to a measured signal to remove the sensitivity interference on the fringe measurements.

For the optical calibration setup, a single-channel, adjustable high brightness LED (Doric Lenses) is used as a light source for the optic fibers. An optical fiber bundle

adapter (Ceramoptec) is used to channel the LED light into an optical fiber bundle (Romack) for the shear stress sensor. For optical calibration purposes, the Moiré shear stress sensor is modeled by a Pyrex wafer (500 μm) with a thin film of aluminum to represent the maximum reflected intensity of the Moiré pattern while a Pyrex and silicon wafer is used to represent the minimum reflected intensity. The overall experimental setup is shown in Figure 7-1.

After purchasing the Romack optical fiber bundle, the following performance limiting issues were discovered: positioning, input/output fiber mapping, and alignment and is shown in Figure 7-2. The fiber center to center distances vary from fiber to fiber. Such misalignment affects the coupling from the fiber bundle to the light source and the photodiode array. The deviations in distance among the fibers are mapped. The fibers are tested on the optical testbed with the misalignment compensated via post processing prior to using the fiber bundle with the actual device. The incorrect fiber mapping between the input and output fibers are decoded and is shown in Figure 7-3.

7.1.2 Optical Loss Budget

The goal of the optical loss budget is to determine the light intensity losses at each optical component interface. The coupling between fiber bundles, coupling to the optical sensor, and manufacturing variances can result in optical losses. An estimate of the losses at each optical interface is obtained by introducing each optical component one at a time to observe the overall light intensity loss for the system as a result of each new component.

The maximum input current for the Doric Lenses LED is 700 mA which will determine the maximum sensitivity value for the optical calibration. The quoted power for the LED is 19 mW. Using a Newport Optical Power Meter (1830-C), the measured

optical output power at the pig-tailed fiber connection for the LED at 700 mA is 0.4 mW. If the light intensity directly from the Doric Lenses LED is considered to be at full intensity, then the intensity reduction at each optical fiber interface is graphically shown in Figure 7-4 and summarized in Table 7-1.

For the given optical fiber setup, a 62 dB reduction in light intensity level is observed from the input LED to the receiving photodiode array. For an input light intensity of 0.4 mW, a 62 dB reduction through the optic fibers results in the fiber output intensity on the order of 10 nW. The significant intensity loss through the current optical setup requires a high intensity light source and photodetectors capable of small measurements.

7.1.3 Fiber Bundle Calibration Results

The experimental setup for obtaining an optical light calibration is discussed this section. The Doric Lenses LED light source for the optical fiber bundle is controlled by a Keithley Sourcemeter 2400. Optic fibers from the Ceramoptec fiber adapter are connected to the light source and Romack fiber bundle and are tested individually. A Pyrex wafer with aluminum deposited on the backside represents the maximum peak reflection of the Moiré fringe. For this single channel calibration, a Newport optical power meter (1830-C) is used to record the light reflected from the Moiré fringe through the various optic fiber bundles. The result of this calibration is shown in Figure 7-5.

7.1.4 Optical Test Bed Overview

The purpose of the optical test bed is to simulate static deflections in the floating element using a motorized nano-positioner for optical transduction characterization. The floating element test structures have aluminum gratings that match the gratings on the optical shear stress sensors to generate Moiré fringe patterns that optically amplifies

mechanical deflections in the floating element. A custom made optical holder is interchanged with an alternate configuration to allow various optics to observe the Moiré fringes.

7.1.5 Optical Test Bed Design

The experimental optical test-bed assembly consists of several primary components: the base structure, the nano-positioner, a push structure, two sensor plates, a sensor plate mount, and an optics holder as illustrated in Figure 7-6. The aluminum gratings that are used to generate the Moiré fringe pattern are deposited on silicon and Pyrex test structures. The silicon test structure has a floating element and the aluminum gratings are recessed in a cavity 3 to 4 μm from the aluminum gratings on the Pyrex test structure. The individual test structures are mounted into the two sensor plates and clamped together in a sensor plate mount, forming the Moiré fringe pattern. Rubber gaskets between the test structures and the sensor plates are used to clamp the test structures together. The silicon test structure is designed such that the floating element extrudes past the Pyrex test structure when clamped together, allowing for an external mechanical device to deflect just the floating element. The sensor plate mount is fixed to a base structure, as is the motorized nano-positioner. A push structure that is mounted on the nano-positioner, is slowly traversed across the nano-positioner stage until the push structure comes in contact with the silicon floating element. An optical holder is placed over the Pyrex test structure to allow optical components, such as a fiber bundle, to be rigidly fixed over the Moiré fringe pattern for observation.

The Newport nano-positioner linear translation stage, model UMR8.51A, is controlled by Newport 850G linear stage actuator, capable of 51 *nm* resolution shifts. Input commands to the linear stage actuator are transmitted from a computer controlling a Newport ESP100 Motion Controller/Driver via a RS-232 serial connection.

7.1.6 Optical Test Structures

The optical test structures (Figure 7-7) are designed to sustain a mechanical deflection in the floating element while generating Moiré fringe patterns to model the fringe patterns on the actual shear stress sensor devices. The first test structure is made from a 0.5 *mm* thick silicon wafer and this structure contains the floating element and one set of aluminum gratings. The second test structure is made from Pyrex and contains the second set of aluminum gratings. The dimension of the floating element has a length of 10 *mm* and a width of 13 *mm*. The floating element is suspended by eight tethers to the rest of the silicon structure, each tether with a length of 1 *mm* and a width of 0.1 *mm*. The rest of the silicon structure is designed such that one side of the floating element is mechanically accessible by a push structure. A separation gap between the sets of aluminum grating pairs is generated by etching a 3 ~ 4 μm cavity into the floating element. Multiple sets of aluminum gratings are deposited on the floating element, each with a g_1 pitch of 9.9 μm . The other matching sets of aluminum gratings, with a g_2 pitch of 10 μm , are placed on a Pyrex test structure to form the Moiré fringe patterns. In total, five Moiré fringe patterns are generated on the test structures. Four of the Moiré patterns model the size and dimensions of the various shear stress sensors fabricated (5 *Pa* -1 *kHz*, 5 *Pa* -2 *kHz*, 5 *Pa* -5 *kHz*, 50 *Pa* -5 *kHz* device) and a fifth

Moiré pattern is generated for convenience in aligning an optical package to the test structure.

When the silicon and Pyrex structures are matched together, the floating element on the exposed side extends 1 *mm* past the Pyrex test structure, allowing an external mechanical deflection until the edge of the Pyrex is reached. The microfabrication process of the test structures is similar to the process of the actual device.

According to the Newport 850G linear stage actuator datasheet, the actuator is able to support a maximum axial load of 18 *lb-force*, which is equivalent to 4.448 *N*. The tethers supporting the floating-element were designed to account for the axial load. For a 1 μm deflection using the 100 μm wide, 500 μm thick and 1000 μm long tethers, the force for such a deflection is calculated to be 0.6 *N*.

7.1.7 Optical Test Bed Results

The resulting discretized Moiré fringe patterns from using the optical fibers were observed at several incremental displacements. Each of the channels from the photodiodes is sampled simultaneously via a 16 channel data acquisition system. For each displacement, the sampling rate is 20,000 *samples/s* and 1000 samples of the Moiré pattern were recorded and averaged. An alternate photodiode array board was constructed to primarily focus on the performance of the photodiodes without the use of the instrumentation amplifier. A reverse bias of 12 *V* was applied to the photodiode circuitry.

Due to the misalignments from the Romack Optics, Inc. manufactured fiber bundle as well as varying input light intensities from a 16 element LED board and coupling losses, a normalization routine was implemented to compensate for the different

maximum and minimum intensity ranges of each photodiode channel. Furthermore, the mean component of each channel was removed and so each channel ranged from -1 to 1. A least squares curvefit was performed to extract a phase component at each nanopositioner displacement shown in Figure 7-8. The phase from the curvefit is then be converted to a floating-element displacement.

In the initial optical calibration, the simulated floating-element test structures are deflected such that the Moiré fringe pattern phase wraps with the subsequent spatial Moiré period. The g_1 grating $9.9 \mu m$ and g_2 grating is $10 \mu m$, the resulting theoretical Moiré period is $990 mm$ and the calculated Moiré amplification is 100. As a result, the floating-element on the nanopositioner has to deflect $10 \mu m$ for the Moiré fringe to shift by a full period. The slope of the line for Figure 7-9 is 0.937 and the correlation coefficient for the line fit is 0.9972. The slope of the line fit corresponds to an experimental Moiré amplification of 93.7.

7.2 Experimental Optical Fringe Estimation Technique Comparison

In addition to the least squares fringe estimation technique, other estimation techniques were performed for comparison over a full Moiré period shift. At each displacement, the error in the measurement for each technique is calculated using 1000 data samples. A linear fit is performed over the phase shifts and the resulting correlation coefficients are observed. The performance of the various fringe estimation algorithms is shown in Figure 7-10.

The correlation coefficients for the least squares curvefit, FFT, cross-correlation and spatial phase detection algorithms are listed in Table 7-2. With the exception of the cross-correlation technique, each of the algorithms offers reasonable phase estimation.

Although the accuracy of various fringe estimation techniques can be improved by increasing the number of periods in the fringes, the limitations due to current manufacturing, packaging and device dimension constraints does not allow for this option. The least squares curvefit, FFT and cross-correlation have very high correlation coefficients. The resulting slopes from the least squares, FFT and cross correlation line fits range between 91 and 93, which corresponds to a Moiré magnification around 91 to 93. The theoretical Moiré magnification is 100. While the cross-correlation line fit has a slope of 101, the correlation coefficient is lower than the other fringe estimation techniques. While the least-squares curvefit, FFT and spatial phase detection methods show promising results, more work is needed to evaluate these techniques.

The initial optical calibration shows promise for the use of an optical fiber bundle to acquire Moiré fringe patterns. The Moiré pattern is shifted by a full period on the optical test-bed, which provides the range and mean for each photodiode channel. The range and mean allows each of the channels to be normalized, which is necessary for a good curve-fit. For an actual device, the Moiré fringe pattern is unable to shift by a full period before the deflections become nonlinear and so the photodiodes and light source have to be calibrated before testing to eliminate the variations between each channel.

7.3 Device Calibration

The optical shear stress sensor is characterized to obtain a static and dynamic response of the device. The response of the sensor is observed in a flow environment with known shear stress levels. The static calibration of the device is useful to determine the sensitivity of the device while the dynamic calibration is useful for finding the frequency response of the device.

7.3.1 Device Characterization

The characterization of the Moiré shear stress sensor is conducted in conjunction with the optical fiber bundles. The photodiode array detects shifts in the optical fringe pattern via the fiber bundles and all 16 elements is sampled simultaneously by a data acquisition system. Furthermore, a reference photodiode is used to monitor fluctuations in the intensities of the input light source to assist in normalizing the Moiré pattern for fringe estimation. The static and dynamic response of the shear stress sensor is observed.

7.3.2 Static Calibration Overview

The goal of a static calibration is to observe the response of the Moiré device in a known mean, steady shear stress environment. The optical Moiré sensor is placed in a 2-D laminar flow cell capable of mean shear stress flow. The sensor is mounted in an optical plug such that the optical fiber bundle has access to the Moiré fringe pattern. The spatial shift in the Moiré fringe pattern is detected by the photodiode array via the optical fiber bundle. The shift in the fringe pattern is correlated to the floating element deflection to obtain a mechanical shift. The mechanical shift of the sensor is compared to the various shear stress measurements, which is proportional to the pressure drop at a given distance and the height of the channel. The ratio between the mechanical shift and the shear stress is the sensitivity of the Moiré shear stress sensor.

7.3.3 Static Calibration Theory

For the static calibration of the device, the shear stress sensor is flush-mounted into a 2-D laminar flow cell. The flow cell provides a mean flow and the flow can be modeled as a Poiseuille flow between two semi-infinite parallel plates. Two pressure taps along the direction of the flow are connected to a pressure meter to obtain a

differential pressure. Assuming that the flow is steady, fully-developed and incompressible, the wall shear stress can then be calculated by [21],

$$\tau = \frac{h}{2} \frac{dP}{dx} \quad (7-1)$$

where dP is the differential pressure between the two pressure taps, h is the height of the channel, and dx is the distance across the differential pressure. The internal channel length of the flow cell is 13 inches and the internal height and width of the flow cell are 0.010 inches by 4 inches respectively. The shifts in the Moiré fringe patterns as observed by the optics are converted into a floating-element displacement. The floating-element displacements are then compared to the mean shear stress levels to obtain an overall sensitivity for the device.

7.3.4 Static Calibration Results Using Conventional Optics

For the initial calibration of a shear stress sensor, a 5 Pa, 2 kHz sensor was selected for testing. An adjustable microscope (Olympus SZX-12) along with an area-scan microscope camera (Olympus DP-11) was used to observe the Moiré fringe shift as a result from the given mean flow. The distance between the two pressure taps is 3 inches and a Heise pressure meter with a 50 in. of H_2O module is used to obtain differential pressure measurements. The mean flow was generated for a range of 0~5 Pa of shear stress. The schematic of the experimental setup is shown in Figure 7-11.

For each shear stress level, 20 images from the microscope camera were averaged to obtain a mean Moiré fringe pattern and the corresponding error bars at pixel. In Figure 7-12, the plot shows a least-squares curvefit using MATLAB across 800 pixels from an averaged Moiré fringe pattern to obtain a phase measurement, which is

converted into a floating-element deflection. During the experiment, vibrations between the floating-element and the microscope camera were observed. In order to filter the undesirable shifts in the image, a reference point at the edge of the floating-element was used to correct the Moiré fringe pattern and compensate for the vibrations.

From the preliminary static calibration, the 5 Pa, 2 kHz shear stress sensor yielded a sensitivity of 59 nm/Pa as shown in Figure 7-13. The correlation coefficient of the slope for the line fit is 0.9822.

7.3.5 Static Calibration Results Using the Fiber Bundle

For the static flow calibration of a shear stress sensor using the optical fiber bundle setup, a 50 Pa, 5 kHz sensor was selected. An optical calibration of the fiber bundle is first performed to account for the different sensitivities and offset of each photodiode channel in the array. A post-processing algorithm is used to adjust each photodiode channel and apply fringe estimation techniques to estimate deflections in the optical fringe.

7.3.6 Post Processing Algorithm for the Static Flowcell Measurements

For the static flow calibration of a shear stress sensor using the optical fiber bundle setup, a 50 Pa, 5 kHz sensor was selected. An optical calibration of the fiber bundle is first performed to account for the different sensitivities and offset of each photodiode channel in the array. A post processing algorithm is used to adjust each photodiode channel and apply fringe estimation techniques to estimate deflections in the optical fringe.

7.3.7 Photodiode Measurement Corrections

Before the measured intensities from the photodiodes array can be used the model the optical fringe, the data must be adjusted to correct for the different

sensitivities and offset of each photodiode and misalignments due to the uneven fiber spacing in the RoMack optical fiber.

7.3.7.1 RoMack fiber sorting

The optical fiber bundle was improperly manufactured by RoMack, Inc. (company is now acquired by LEONI Fiber Optics) and so a sorting algorithm is used to descramble the content of the fiber bundle. The corrected optical pathway was mapped by illuminating a single fiber at a time to determine the sorting order. The decoded optical pathway is shown in Figure 7-3. A look-up table based on the decoded pathway is used to sort the data collected the optical fiber bundle in order to properly reconstruct the optical fringe pattern.

7.3.7.2 Uneven optical fiber spacing correction

Another issue with the optical fiber bundle manufactured by RoMack, Inc. is the uneven gap spacing between the optical fibers. The original intended design was to have 16 fibers spread evenly across 1 mm. However, the manufactured fibers are not spaced properly as shown in Figure 7-2.

An optical detection algorithm was developed to detect and account for the uneven spacing of the fibers. The algorithm first estimates the approximate position of each of the fibers. The positions are used to generate a square mask to capture an image of each of the circular fibers as shown in Figure 7-14. In each of the localized fiber optic masks, an intensity threshold algorithm and a centroid function was used to resolve the center location of each optical fiber. The relative center locations of each fiber are mapped onto the overall fiber image to determine the uneven spacing between fibers and are shown in Figure 7-15. The locations of the optical fibers are in units of pixels. The end face of the fiber bundle array is measured under a microscope to obtain a pixel

to distance scaling. The width of the fiber array is measured to be 1.066 mm and the positions of the optical fibers are scaled accordingly.

7.3.7.3 Optical wafer calibration

The optical fiber bundle connected to the photodiode array is calibrated by determining the sensitivity and offset for each of the fiber to photodiode connection. An optical calibrating wafer is used to model materials used in the optical fringe. The calibrating wafer consists of a Pyrex wafer with an aluminum coating. The optical fiber bundle is mounted at the same gap distance between the bundle end face to the wafer surface as the optical fringe of an actual device. As the intensity of the light source of the fiber bundle is increased, the photodiode array should ideally increase at the same rate. Each of the measurements in the photodiode array is linearly curvefitted to yield the sensitivity and offset for each photodiode channel which is shown in equation (7-2),

$$I_n(x) = m_n \cdot x + b_n, \quad (7-2)$$

where n is the photodiode channel number, m is the slope or sensitivity of the photodiode and b is the offset.

In order to maintain a uniform sensitivity and offset for all of the photodiode channels in the array, one of the channels is designated as the reference channel and the sensitivity and offset of the referring channel is given by,

$$I_{ref}(x) = m_{ref} \cdot x + b_{ref}. \quad (7-3)$$

By combining equations (7-2) and (7-3), each of the n channels of the photodiode array can be corrected to match the referring channel and the equation is given by,

$$I_{ref}(x) = \frac{m_{ref}}{m_n} (I_n(x) - b_n) + b_{ref} \quad (7-4)$$

When the sensitivities and offsets of each of the photodiode array are collapsed into a uniform slope and offset, the photodiode data representing the optical fringe can now be used for a curvefit.

Two types of optical wafer calibrations are performed. The first is to illuminate all of the source fibers in the fiber bundle simultaneously and the second is to illuminate a single source fiber individually. The simultaneous illumination of all of the source fibers reveals the sensitivities and offset with crosstalk information and the single source fiber illumination test illustrates the contribution of crosstalk to each of the channels.

For the optical wafer test when the source fibers are illuminated simultaneously, the sensitivities and offsets measured are shown in Figure 7-16. The resulting line fit to the different photodiode channels and the adjusted uniform sensitivities and offsets are shown in Figure 7-17.

The amount of crosstalk contribution can be observed from using the individual fiber illumination calibration. As shown in Figure 7-18, the amount of light received by the photodiode from the simultaneous source fiber array illumination is significantly higher than the optical wafer calibration using individual source fibers. For the individual source fiber calibration, there are two types of intensities that are collected by the photodiode array which are: 1) direct light intensity from the primary source fiber to the primary receive fiber and 2) indirect light intensity from the primary source fiber to neighboring receive fibers due to the numerical aperture of the optical fibers. In some of the source-receive fiber pairs, the light coupled into the direct fiber pair are the dominant contribution to the maximum sensitivity while other source-receive fiber pairs, the light

from neighboring source fiber is the dominant light source. In the case where the neighboring source fiber is the dominant source, this may suggest that there is an obstruction in the optical pathway of the direct source fiber.

7.3.7.4 External reference photodiode

The purpose of an external reference photodiode separate from the photodiode array is to monitor any fluctuations in light intensity of the source light. The intensity measurements from the reference photodiode are used to adjust the intensity levels of the photodiode array.

The 16 photodiode channels in the Hamamatsu array are referenced to an external Newport photodiode connected to the Doric LED via the Ceramoptec fiber bundle splitter. Light intensity fluctuations in the LED can be monitored using the reference photodiode and the percentage change in the light intensity can be applied to the recorded intensities in the photodiode array.

An initial light intensity is recorded from the LED using a single Newport photodiode. Subsequent light intensity measurements from the Newport reference photodiode are calculated as a percentage change from the initial measurement as shown in Figure 7-19. The percentage change is used as a multiplicative factor to adjust the optical fringe measurements measured by the Hamamatsu photodiode array. Ideally, any light intensity fluctuation in the LED should be compensated for in the photodiode array data using this technique.

7.3.8 Curvefit Section

This section describes the curvefitting process for tracking the displacement of the Moiré optical fringe. As the floating element of the shear stress sensor is displaced, the periodic Moiré fringe is spatially displaced by an amplified distance. The shape of the

Moiré fringe is modeled by an n -number of sinusoids for curvefitting using a least-squares curvefit algorithm. The motivation for using a number of Fourier sinusoids for the curvefit is to better capture the ‘triangular’ characteristic of the Moiré pattern.

7.3.8.1 Initial prefit for the optical fringe

The purpose of an initial prefit is to establish the shape of the Moiré optical fringe and maintain the shape of the Moiré pattern during subsequent curvefits. There are two parts to the prefit: 1) determine the period of the Moiré pattern and 2) obtain the offset amplitude, and phase coefficients for curvefitting to the intensity of the photodiode data.

The spatial periodicity of the optical fringe is first established by using performing a least squares curvefit on a single sinusoid. The overall frequency of the Moiré pattern is initially determined from f_1 which should match the measured period of the Moiré period of 0.99 mm.

$$y(x) = I_0 + I_1 \cdot \sin(2\pi \cdot f_1 \cdot x + \phi_1) \quad (7-5)$$

The desired initial frequency is the fundamental spatial period of the Moiré pattern. The curvefitting bounds are set at $\pm 10\%$ of the fundamental frequency to account for possible misalignment or rotational issues with the device packaging. The x values used in the curvefit is based off of uneven spacing of the fibers in the RoMack fiber bundle.

A second curvefit is then performed while keeping the value fundamental spatial frequency of the Moiré fringe fixed. The remaining dc, amplitude, frequency and phase values are obtained are selected to determining the prefit Moiré pattern as shown in equation (7-6).

$$y(x) = I_0 + I_1 \cdot \sin \left(\underbrace{2\pi \cdot f_1 \cdot x + \phi_1}_{\text{fixed value}} \right) + \underbrace{\sum_2^n I_n \cdot \sin(2\pi \cdot f_n \cdot x + \phi_n)}_{\text{Additional Sinusoids}}, \quad (7-6)$$

where f_1 is the fundamental frequency of the optical fringe obtained by the curvefit to a single sinusoid.

7.3.8.2 Curvefitting flow data

For determining the optical fringe shift of the Moiré pattern, the sinusoidal coefficients from the prefit are fixed while an additional overall phase for the sinusoids is introduced to represent the spatial deflection of the optical fringe. The equation for the subsequent curvefits of the optical fringe is given by,

$$y(x) = I_0 + I_1 \cdot \sin \left(\underbrace{2\pi \cdot f_1 \cdot x + \phi_1 + \theta}_{\text{Overall Phase}} \right) + \underbrace{\sum_2^n I_n \cdot \sin \left(\underbrace{2\pi \cdot f_n \cdot x + \phi_n + \theta}_{\text{Overall Phase}} \right)}_{\text{Additional Sinusoids}}, \quad (7-7)$$

where θ represents the overall phase deflection of the Moiré pattern. The dc offset, amplitude, frequency and the individual sinusoidal phase coefficients are fixed based off of the values determined from the optical fringe pre-fit. Ideally, as the floating element is deflected due to a change in a given flow, only the overall phase of the Moiré pattern should change. The overall phase shift should be the same value for each of the fitted sinusoids.

7.3.9 Simulation of the Optical Fringe Estimation Techniques

The optical fringe data collected by the photodiode array is simulated to assess the performance of the different optical fringe estimation techniques. Furthermore, a study of the influence of stationary spatial debris on the fringe estimation algorithm is performed.

The optical fringe is modeled by a sinusoid with a dc offset, amplitude, spatial frequency and phase. The simulated photodiode data is also normalized to unity with the dc offset removed to see the effects it has on the curvefits as shown in Figure 7-20. The sinusoid is spatially sampled at 16 points to model the 16 channels of the photodiode array. The phase of the sinusoid is shifted an entire period. The resulting phase estimation on the simulated data from the least squares curvefit (LSQ), fast-fourier transform (FFT), spatial phase detection (SPD) and cross correlation (XCorr) are shown in Figure 7-21.

The metric used in this research for assessing the performance of the fringe estimation technique is the coefficient of determination, R^2 , where R is the correlation coefficient. The correlation coefficient can be computed by [85],

$$r = \frac{n \sum (x_i y_i) - (\sum x_i)(\sum y_i)}{\sqrt{n \sum x_i^2 - (\sum x_i)^2} \sqrt{n \sum y_i^2 - (\sum y_i)^2}} \quad (7-8)$$

where x_i and y_i are sample data points and n is the number of samples. Although the R^2 value is a convenient metric for measuring the “goodness-of-fit”, it is possible for some datasets to obtain high R^2 values despite the appearance of scattered data [85].

For the LSQ, FFT and SPD techniques, the sensitivity of the phase estimation is consistent between the photodiode data with an offset and the data without an offset. However, the dc offset in the photodiode data adversely affects the phase estimation in the cross correlation technique. The R^2 values for these techniques are listed in Table 7-3. Since the dc offset is constant, the correlation is still high between the initial fringe and the shifted fringe. When the offset is removed, the phase estimation using the cross correlation technique approaches the predicted spatial phase deflection of the

optical fringe. However, the cross correlation technique also suffers from resolution in the sampling of the optical fringe that results in a discretized, stair-step phase estimation. A potential solution to artificially increase the resolution of the cross-correlation technique is to pad the data in between the 16 photodiode channels with redundant intensity levels from the photodiode array.

Static spatial debris is modeled by selecting several photodiode channels while maintaining the intensity values constant during the spatial phase shift. The resulting photodiode data from the spatial debris modeling is illustrated in Figure 7-22. Several characteristics from the spatial debris on the curvefits are observed and the results are shown in Figure 7-23. The spatial debris affects the linearity of the phase estimation for various fringe estimation techniques and reduces the R^2 values depending on the amount of spatial debris. The R^2 values for these techniques in the presence of spatial debris are listed in Table 7-4. Furthermore, the spatial debris skews the stair-step phase estimation regions of the cross-correlation technique when the dc offset is removed from the photodiode data.

7.3.10 Moiré Simulation Using Images

A simulation of acquiring the Moiré fringe using the optical fiber bundle is performed to model the conditions of the curvefit algorithm using n Fourier n -sines. The optical fringe on the floating element is imaged using a Microscope. An image mask of the optical fiber bundle is generated and superimposed on the floating element photo. The deflection of the floating element is simulated by moving the fiber bundle mask laterally across the optical fringe.

The fiber mask is created by imaging the end face of receiving fibers and converting the image into a black and white image as shown in Figure 7-24. A

threshold value is used to determine which pixels are black or white in the fiber mask. The black and white values in the mask allow for binary operations to be performed. The fiber mask is scaled, adjusted for rotation, and then superimposed on the Moiré image. The region of light collected in the fiber mask is individually summed in each optical fiber and normalized by the area of the fiber to result in an intensity value for each fiber. The dc offset of simulated photodiode array data is removed and normalized to determine if the fringe estimation techniques improves without the dc component.

The results of the simulated Moiré fringe estimate using a fiber mask are shown in Figure 7-25. As predicted from the previous fringe estimation techniques section, the LSQ, SPD, and FFT have high R^2 values while the discretization from the XCorr technique lowers the R^2 value. The R^2 values are listed in Table 7-5. Due to the spatial frequency assumptions of the least squares and the spatial phase detection and the discretization issues of the cross-correlation techniques, the FFT method is preferred.

An additional simulation using fiber mask and FFT fringe estimation is performed. The input Moiré pattern is deflected a pixel resolution and the result is shown in Figure 7-26. For a 100 μm Moiré fringe deflection, the sensitivity between the input shift and the predicted FFT deflection is 0.953. The R^2 value for the FFT estimation is 0.997. Several non-idealities are present in the Moiré pattern photograph. The photograph of the optical fringe has an optical vignette effect and the darker regions of the photograph around the edges causes the FFT estimation to drift towards the edge of the photograph. For a 50 μm Moiré fringe deflection instead of a 100 μm deflection, the sensitivity improves between the input and predict shift to 0.997, where the fiber mask does not approach the edge of the photograph. A spatial beating effect is observed

along the sensitivity of the FFT estimation. This effect is attributed to both sets of gratings shifted simultaneously in the photograph. In real Moiré applications, only one set of the optical gratings is moving and the other set remains stationary. Since the simulated Moiré fringe deflection includes both sets of gratings moving, the spatial beating occurs approximately every $10\ \mu\text{m}$, which is the pitch of the optical grating. Even with the highly idealized image of the optical fringe pattern, the fringe estimation technique does not produce an exact fit. Additional non-idealities are present in the fringe estimation of an actual Moiré pattern. Varying sensitivities between photodiodes, optical crosstalk between optical fibers, source light intensity drifts increase the error of the fringe estimation.

7.3.11 Static Sensitivity Calibration Results

The spatial phase of the adjusted data is initially estimated using a least-squares curvefit with 3 Fourier sinusoids. At a given shear stress level, the 50 photodiode data measurements are taken to obtain a mean photodiode intensity level, which yields spatial phase. An example of the phase estimation using the least squares fringe estimation technique is shown in Figure 7-27. Furthermore, the 50 blocks of phase estimations are sampled to obtain an overall mean phase for a given flow.

The least squared curvefit relies on an initial estimate for the offset, amplitude, frequency and phase values. Ideally, the curvefit should be able to fit the coefficients close to the predicted values. A set of upper and lower bounds are used for the coefficients to keep the fits within the predicted value range. Optical non-idealities such as the static debris on the optical fringe, photodiode intensity corrections and optical crosstalk affect the performance of the least square curvefits.

Additional optical fringe estimation algorithms are performed, namely, the FFT, Spatial Phase Detection and Cross Correlation estimation techniques. For the spatial phase detection and cross correlation technique, an initial estimate for the spatial frequency is required to perform these estimates. Additionally, an initial optical fringe pattern is retained so the cross correlation can perform the comparisons between optical fringe in the zero flow case and the deflected optical fringe in subsequent flows. The results of the different phase estimation techniques are shown in Figure 7-28. The predicted sensitivity from the trapezoidal tethers theoretical model is 13.2 nm/Pa.

Ideally, the sensitivity of the optical fringe should be the same for all of the fringe estimation techniques whether the photodiode data has a dc offset or not. However, each estimation techniques have various assumptions which can cause inconsistencies in the results. The least-squares approach requires an initial spatial frequency estimation and initial bounds for the sinusoidal coefficients. The spatial phase detection requires an initial spatial frequency estimation as well. The spatial frequency estimation for the SPD technique is determined by the sinusoidal prefit in the least-squares approach. The cross-correlation technique did not show a phase deflection but the results can be attributed to the stair-step discretization as previously seen in the cross-correlation simulations. The width of the stair-step can be increased due to spatial debris on the optical fringe and the cross-correlation technique may have insufficient resolution to overcome the discretization. A line-fit for the FFT technique results in a sensor sensitivity of 15.0 nm/Pa. The R^2 value of the FFT line fit is 0.873.

A Monte Carlo simulation is performed to determine the error bounds of the static flow cell calibration. The 95% confidence intervals (2σ) generated from the data are

used to determine both the error bounds in both the shear stress calculation and the fringe estimation. The results are illustrated in Figure 7-29. The variability of the shim height in the flow cell is a major contributing factor in the measurement errors for the static calibration test [73], [99].

7.3.12 Dynamic Calibration Overview

The goal of a dynamic calibration is to observe the dynamic response of the sensor over a range of given frequencies. The Moiré sensor is placed in an acoustic plane wave tube for dynamic calibration. Acoustic plane waves of known frequencies are generated by speaker and controlled by frequency generator. The shear stress sensor is packaged along with the fiber bundle such that the photodiodes can detect the transverse spatial oscillations in the floating element. Microphones are placed with the shear stress sensor to measure the pressure to calculate the shear stress and the frequency response is recorded by a spectrum analyzer. The desired measurements from a dynamic calibration are the resonant frequency and the bandwidth of the shear stress sensor.

The three different types of dynamic shear stress calibration that is performed in the plane-wave-tube are:

- 1) AC sensitivity calibration shear stress only
- 2) Pressure sensitivity only
- 3) Frequency sensitivity

The dynamic calibration consists of the shear stress sensor placed at a quarter-wavelength from a rigid termination so the velocity is at a maximum. The pressure sensitivity calibration tests the shear stress sensor at the half-wavelength. The frequency response of the sensor is determined by using an adjustable rigid termination

to maintain the quarter-wavelength distances for across the testing frequency bandwidth.

7.3.13 Dynamic Calibration Theory

For a dynamic calibration of the shear stress sensor, a Stokes Excitation Technique is used to observe the frequency response of the device [100]. The sensor is mounted in a plane-wave tube and acoustics planes waves generated at known frequencies is compared to the response of the sensor. The key is the no-slip boundary condition, which results in a zero particle velocity for the acoustic waves at the wall (Figure 7-30). This momentum deficient region results in a boundary layer as well as a frequency dependent shear stress. The boundary layer thickness $\delta(\omega)$ is given by,

$$\frac{\delta(\omega)}{b} \approx 6.4 \sqrt{\frac{\nu}{\omega}} \approx \frac{6.4}{\eta}, \quad (7-9)$$

where ω is the angular frequency, b is the length scale and $\eta = \sqrt{\frac{\omega b^2}{\nu}}$ is the non-dimensional Stokes number.

The resulting wall shear stress due to the acoustic pressure is given by,

$$\tau' = \frac{P' \sqrt{j\omega\nu}}{c} e^{j\left(\omega t - kx - \frac{\pi}{2}\right)} \tanh(\eta \sqrt{j}), \quad (7-10)$$

where $\frac{-P' \sqrt{j\omega\nu}}{c} = \frac{\mu}{b} \frac{P'}{\rho c} \eta$, P' is the magnitude of the acoustic pressure fluctuation, b is the half width of the tube, c is the speed of sound, k is the wave number, μ is the dynamic viscosity, and ν is the kinematic velocity.

In the experimental setup for dynamic calibration (Figure 7-31), a speaker is controlled by frequency generator. Traveling acoustic plane waves generated by the

speaker are sent towards a flush mounted shear stress sensor in the plane-wave tube. Microphones are mounted in the plane-wave tube to detect the oscillatory acoustic pressure. The microphone measurements are used to calculate acoustically generated shear stress and these results are compared to the optical output response of the sensor.

7.3.13.1 AC sensitivity calibration

The goal of the dynamic ac shear stress calibration is to obtain a shear stress sensitivity measurement while isolating the contribution from pressure effects. In order to achieve this goal, incident acoustic plane-waves are generated by a speaker (BMS 4590P) in a plane-wave tube (PWT) with a square duct of 1" by 1". A rigid termination placed at the opposite end of the PWT incident to the acoustic plane-waves.

At a quarter-wavelength distance away from the rigid termination, the shear stress sensor is placed along the sidewall of the PWT, where the velocity is at a maximum and the pressure is at a minimum from the phase combination of the incident acoustic plane-wave and reflected plane-wave from the rigid wall.

At a quarter-wavelength distance from the wall, ideally only a shear stress component is present due to the velocity gradient and the pressure component is removed since the pressure is at a minimum. Reference microphones are placed at the rigid termination and at a quarter wavelength distance away from the rigid termination to monitor the pressure.

The combination of the incident and reflected plane wave using a rigid end wall is known as a standing wave. The equation to convert the measured pressure at the end wall to shear stress for a standing wave can be calculated by,

$$\tau = \left(-\frac{1}{c} \sqrt{j\omega\nu} \tanh \left(a \sqrt{\frac{j\omega}{\nu}} \right) \frac{e^{jk d_s} - \text{Re}^{-jk d_s}}{e^{jk(d_s-\delta)} - \text{Re}^{-jk(d_s-\delta)}} \right) p' e^{j\omega t} \quad (7-11)$$

where d_s is the distance from the sensor to the wall and δ is the distance between the microphone and the sensor. For a perfect rigid wall termination, the reflection coefficient is assumed to be 1.

The configuration of the dynamic shear stress calibration is shown in Figure 7-32. The frequency range is limited to 6.6 kHz for this particular PWT duct geometry in air. At higher frequencies, the higher order modes of air cut on and cause the incident acoustic waves to become no longer planar.

7.3.13.2 AC sensitivity results

A 50 Pa, 5 kHz shear stress sensor is tested with a forcing frequency of 1.1 kHz using a rigid termination at the end wall. The sound pressure level (SPL) for the ac sensitivity test ranges from 80 dB to 160 dB, which corresponds to ~2.5 Pa of shear stress at 160 dB. A 1/8" Bruel and Kjaer microphone is placed at the end wall to measure the pressure while the shear stress sensor is placed at a quarter-wavelength from the microphone. The result from the ac sensitivity calibration is illustrated in Figure 7-33 with the theoretical mechanical deflection of the floating element of 13.2 nm/Pa. A line-fit of the predicted deflection from the FFT fringe estimation technique yields a sensitivity of 12.4 nm/Pa. The R^2 value in the FFT technique is 0.998 and is higher than the R^2 value of the static calibration.

Using the same ac sensitivity results, the sensitivity is also observed at the half-wavelength frequency and is shown in Figure 7-34. At the half-wavelength, the velocity is at a minimum and pressure is at a maximum. At 2.2 kHz, significant ac sensitivity is

observed at the half-wavelength. At the half-wavelength, the floating element is deflected ~60 nm at 140 dB SPL, whereas the floating element is deflected only ~30 nm at 160 dB at the quarter-wavelength. The larger sensitivity at the half-wavelength suggests that the shear stress sensor is affected by pressure effects. Although the sensor is ideally placed at a quarter-wavelength distance, the pressure surrounding the pressure-minima node is integrated on the surface of the floating element.

7.3.13.3 Pressure sensitivity calibration

During shear stress measurements, pressure may generate out-of-plane displacement on the floating element. The out-of-plane displacement should be observed to determine the contribution of pressure during shear stress measurements.

In order to observe the out-of-plane displacement, a pressure sensitivity calibration is performed. The Moiré sensor is placed normal to incident acoustic plane-waves for pressure measurement. The Moiré sensor is designed to be a lateral displacement sensor and ideally, incident (normal) forces on the floating element should not cause the Moiré fringe to displace laterally. The configuration for the pressure sensitivity calibration is shown in Figure 7-35.

7.3.13.4 Pressure sensitivity calibration results

The 50 Pa, 5 kHz shear stress sensor is tested at 2.2 kHz. The sound pressure level (SPL) for the ac sensitivity test ranges from 80 dB to 160 dB. At 160 dB, the pressure is 2 kPa rms. The results of the pressure sensitivity calibration are illustrated in Figure 7-36. The various fringe estimation techniques show the sensitivity of the shear stress sensor due to pressure is on the order of 1 μm at 160 dB SPL. The sensitivity due to pressure is 30 dB larger than shear stress. The pressure sensitivity predicted by the FFT technique is 0.48 nm/Pa of pressure.

7.3.13.5 Frequency response calibration

In actual flow applications, the Moiré device is subjected to both shear stress and pressure contributions. To model these conditions, the frequency response of the Moiré device determined using a plane-wave tube with an anechoic termination at the end of the PWT where the incident acoustic plane waves are scattered at the anechoic termination. Since the acoustic plane-waves at the anechoic termination are not reflected in-phase back towards the incident acoustic plane-waves, this results in measurements in the PWT with shear stress and pressure components. However, since a lateral deflection due to pressure sensitivity is observed in the dynamic pressure sensitivity calibration, a shear stress only frequency response calibration is performed instead.

For obtaining a shear stress only frequency response, an adjustable rigid termination is used to maintain a quarter-wavelength distance from the shear stress sensor. The setup for minimizing pressure in a frequency response calibration is shown in Figure 7-37. The shear stress only frequency response calibration is used to minimize the lateral deflections due to pressure sensitivity.

7.3.13.6 Frequency response results

A 50 Pa, 5 kHz sensor is tested from 600 Hz to 6.4 kHz. The sound pressure level for the frequency response test is approximately 150 dB. Several quarter wavelength distances could not be achieved due to the maximum and minimum length of the PWT.

The transfer function of the shear stress sensor is given by,

$$H(f) = \frac{G_{xy}}{G_{yy}}, \quad (7-12)$$

where G_{xy} is the cross spectral density between the shear stress sensor and the microphone at the sound hard boundary and G_{yy} is the auto-spectral density at the wall. A plot of the FRF is shown in Figure 7-38. The frequency range from 1.2 kHz to 1.6 kHz is not recorded because the quarter-wavelength distance at those frequencies exceeded the maximum and minimum adjustable distance of the moveable rigid termination.

The predicted resonance of the 50 Pa, 5 kHz shear stress sensor with trapezoidal tethers is at 4.4 kHz. The various fringe estimation techniques did not observe a resonant peak in the FRF.

Although the shear stress only FRF dynamic calibration attempts to minimize pressure by maintaining a quarter-wavelength between the sensor and the end wall, several physical factors can cause pressure to be measured at the pressure minima node. Both the microphone diaphragm and the floating element have a physical sensing area while the pressure minima node is an infinite point. The integrated area around the pressure minima node is captured by the transducers and results in a pressure measurement. As the forcing frequency increases, the width of the pressure node decreases, which results in more pressure integration. For higher frequencies, the pressure measured increases. Another physical factor is if the pressure node is not perfectly aligned to the center of the floating element, the floating element can tilt and lateral deflections can result due to the imbalance of pressure across the floating element. Also, if trapezoidal tethers are manufactured unevenly such that the moment of inertia is off-centered, then the pressure can cause a lateral deflection. The potential sources for lateral deflection due to pressure is illustrated in Figure 7-39.

A comparison of the lateral deflection due to shear stress and the deflection due to pressure is performed. In the frequency response test, the pressure measured by the microphone at the rigid termination for 1.1 kHz is 893.4 Pa while the microphone at the sensor observed 22.4 Pa of pressure for 1.1 kHz. Although the microphone at the sensor is placed at a quarter-wavelength from the rigid termination, the pressure rejection is only 33 dB as shown in Figure 7-40.

For 1.1 kHz, the shear stress at the quarter-wavelength measured 0.54 Pa of shear stress. Based on the ac calibration, 0.54 Pa of shear stress results in 7.1 nm of lateral deflection while 22.4 Pa of pressure results in 10.8 nm. The larger lateral deflection due to pressure indicates that pressure already dominates at lower testing frequencies. At the higher frequencies, the lateral deflection due to pressure increases and can interfere with the FRF estimation.

In order to verify that the lack of a resonant peak is a mechanical sensor issue and not with the fringe estimation techniques, an alternate approach is used to determine the resonant peak of the sensor using individual optical fibers and the microphone at the rigid termination. When a forcing frequency is applied on the Moiré fringe, each of the individual should observe a local oscillation of the Moiré fringe. Despite the different sensitivities of photodiodes, each of the photodiodes should observe a fringe oscillation based on the forcing frequency. The localized oscillations at each photodiode are individually compared to the oscillatory signal recorded by the microphone at the end wall termination, which should yield a frequency response. The goal for the single optical fiber approach is to remove the potential errors that may occur in the fringe estimation techniques. The ac sensitivities determined from each individual optical

fiber, shown in Figure 7-41, and the resulting FRF is shown in Figure 7-42. Likewise, lateral deflections attributed to pressure sensitivity interfere with the estimation of the FRF using individual fibers.

Although a resonant peak is not observed in the mechanical sensor, the results of the static calibration and dynamic calibration demonstrated a working optical fiber system. Recommendations for improving the sensor and optoelectronics are addressed in the future work chapter.

Table 7-1. Amount of light intensity loss at the various optic fiber interfaces.

Optical Pathway	Measured Light Intensity Levels	Interface Loss (dB)	Total Loss (dB)
LED (19 mW)	0.4 mW	16.8	16.8
LED + Ceramoptec fibers	1.5 μ W	24.3	41.0
LED + Ceramoptec fibers + Romack fibers	0.25 μ W	7.8	48.8
LED + Ceramoptec fibers + Romack fibers + Wafer + Romack Fibers	11.9 nW	13.2	62.0

Table 7-2. Correlation coefficients and slopes for various algorithms.

	Correlation Coefficient	Slope
Least Squares	0.9993	93.053
FFT	0.9972	92.852
Cross-Correlation	0.9824	101.312
Spatial Phase Detection	0.9965	91.097

Table 7-3. Correlation coefficients for simulated photodiode data.

	LSQ	FFT	SPD	XCorr
With dc	1	1	1	---
Without dc	1	1	1	0.994

Table 7-4. Correlation coefficients for simulated photodiode data with static spatial debris.

	LSQ	FFT	SPD	XCorr
With dc	0.989	0.989	0.989	---
Without dc	0.989	0.989	0.989	0.967

Table 7-5. Correlation coefficients for the various fringe estimation techniques using the optical fiber mask simulation.

	Correlation Coefficient
Least Squares	0.996
FFT	0.992
Cross-Correlation	0.977
Spatial Phase Detection	0.932

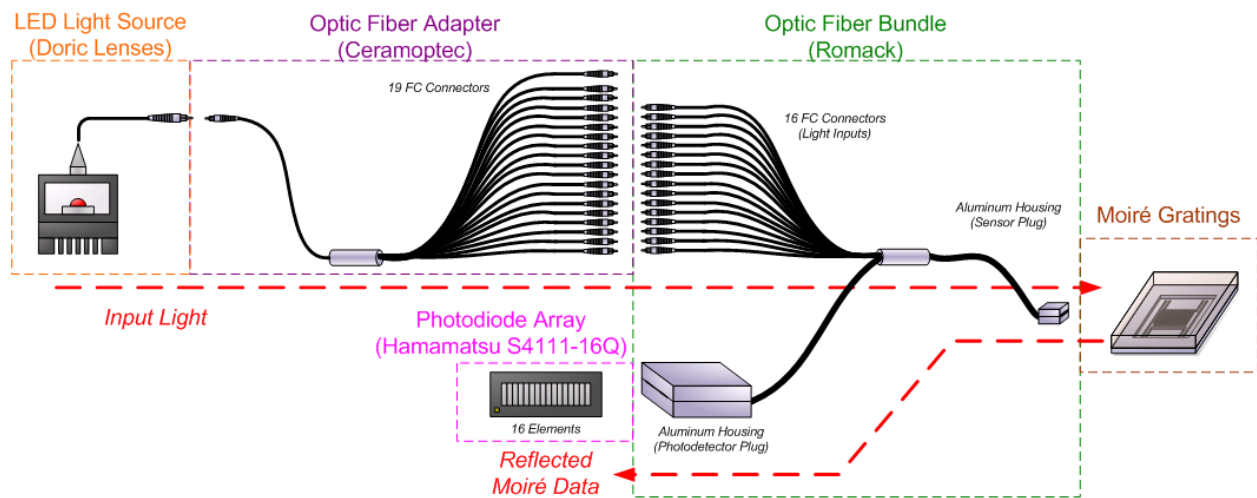


Figure 7-1. Schematic of the optical fiber calibration experimental setup.

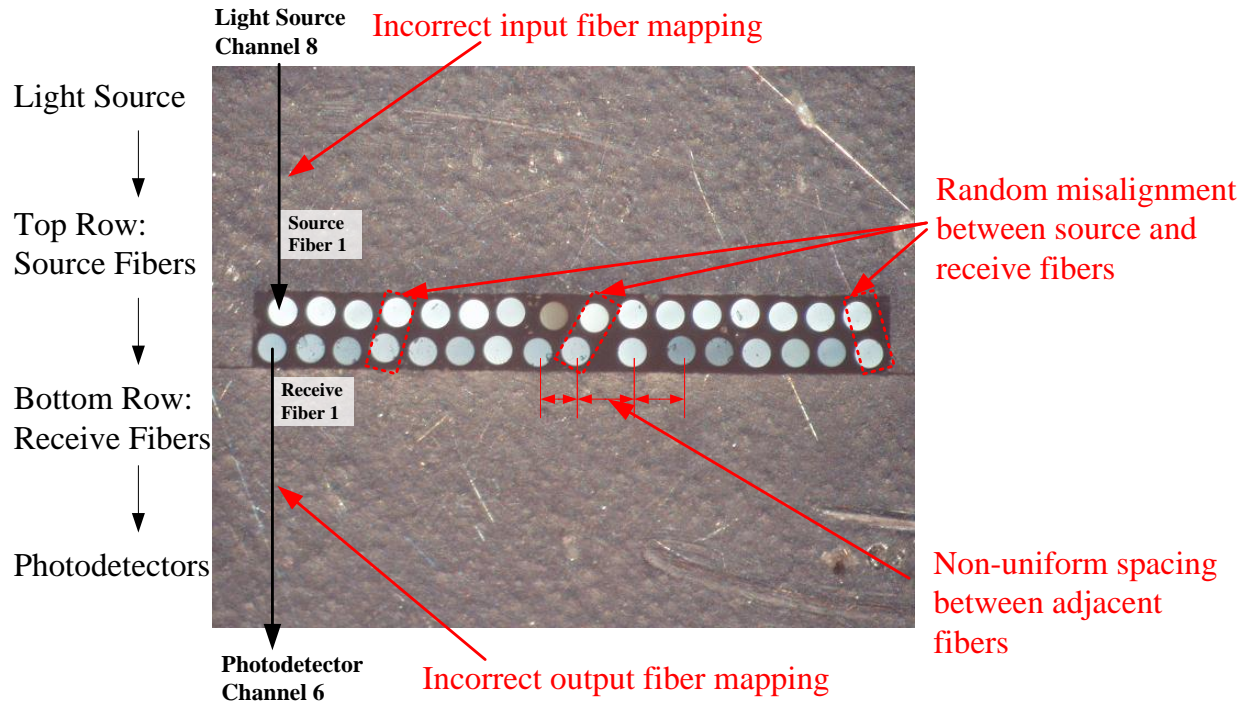


Figure 7-2. Photograph of the sensor plug of the Romack optical fiber bundle illustrating the following: incorrect input/output fiber mapping, random misalignment between source/receive fiber pairs and non-uniform spacing between adjacent optical fibers in the fiber bundle. Photo courtesy of Tai-An Chen.

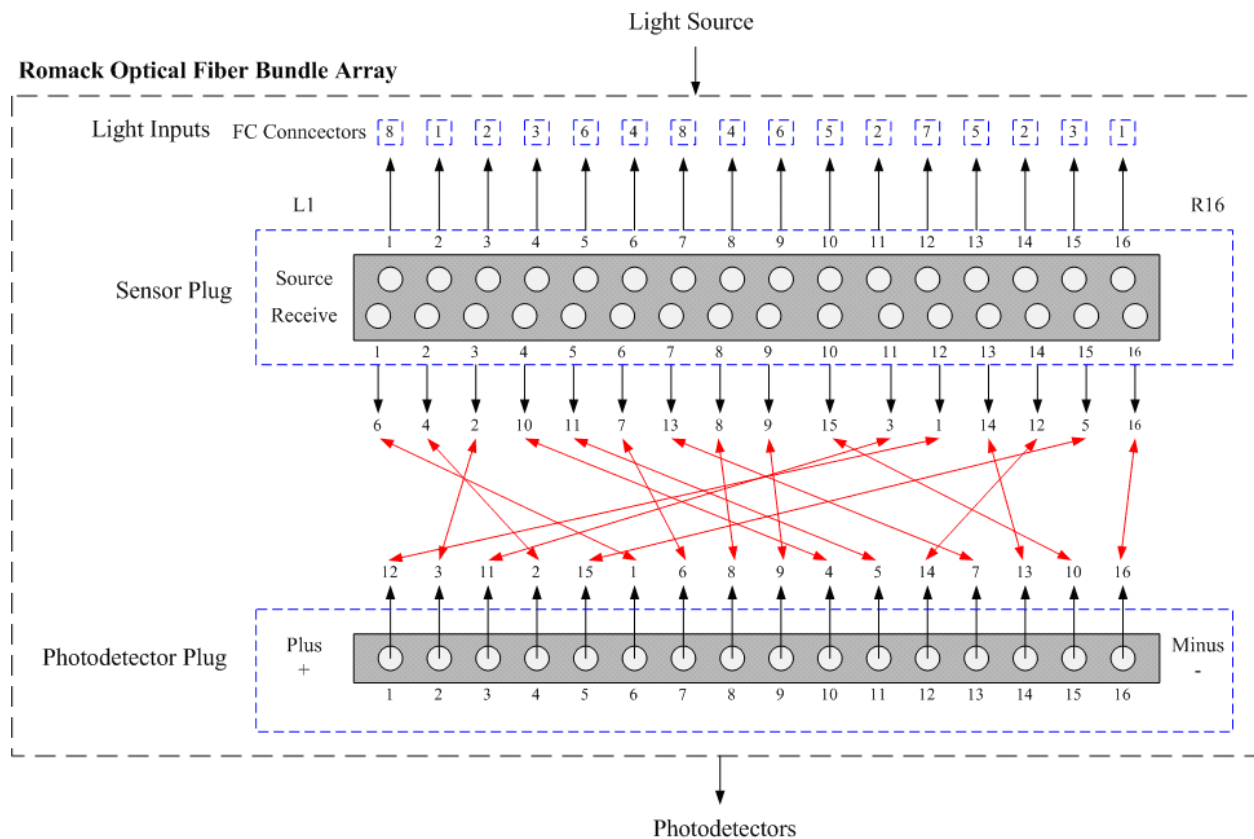


Figure 7-3. Diagram of the optical fiber scrambled mapping between the light source to the source fibers of the sensor plug and the receive fibers to the photodetectors for the Romack fiber bundle.

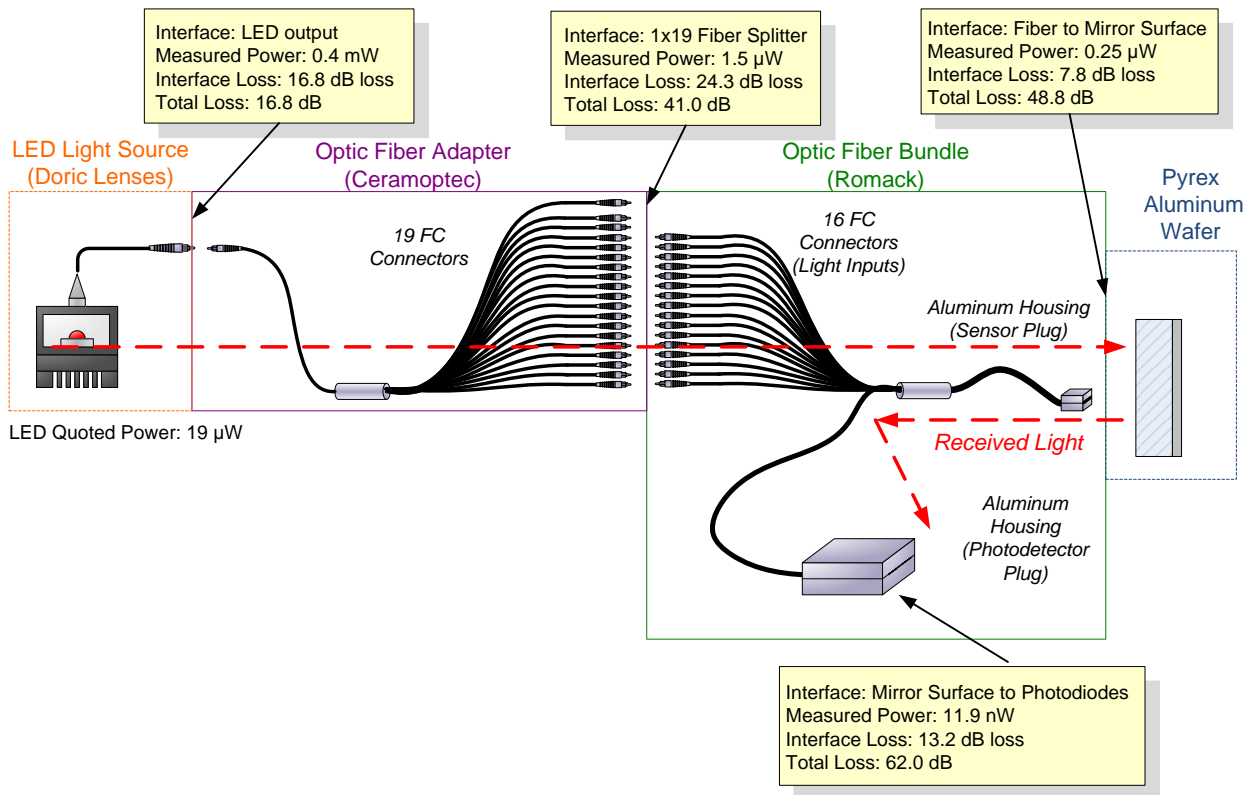


Figure 7-4. Measured light intensity levels indicating light loss from the Doric LED to the Ceramoptec fiber adapter to the Romack fiber bundle to the sensor and back through the Romack fiber bundle and recorded with a photodetector.

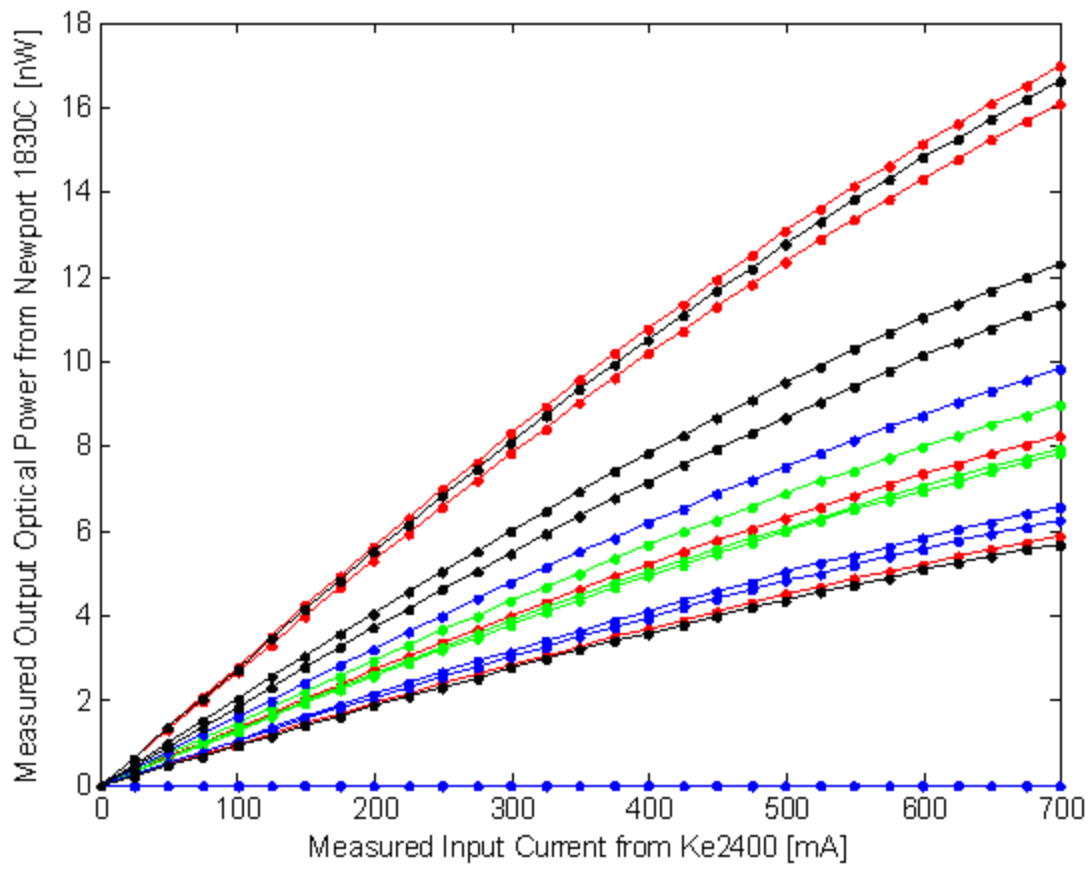


Figure 7-5. Light calibration between each optical pathway from the light source through the various optical fibers channels and to the optical detector.

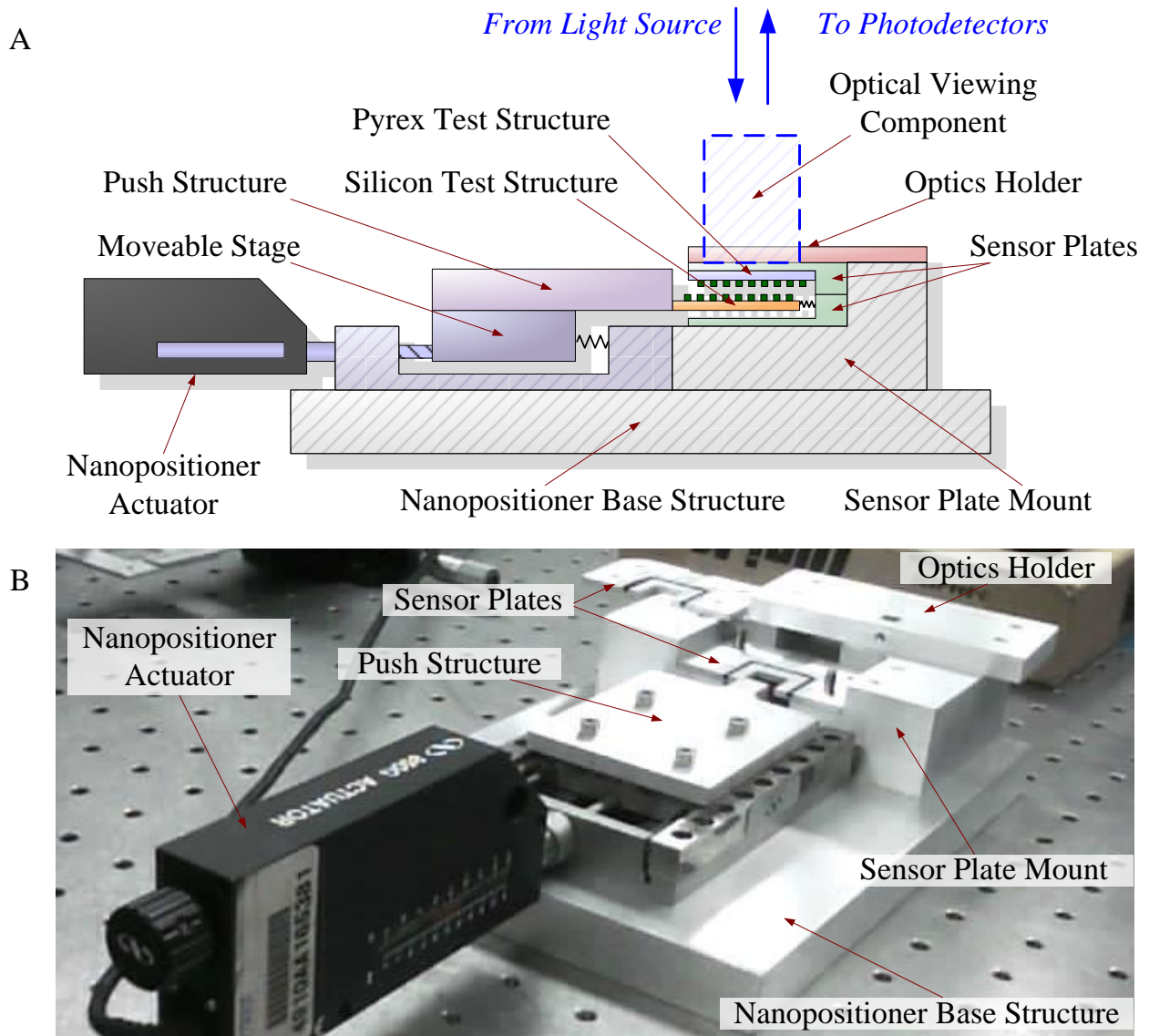


Figure 7-6. Nanopositioner for optical calibration using Moiré test plates. A) Overall schematic of the nanopositioner. B) Photograph of the nanopositioner showing the various optical test-bed components. Photo courtesy of Tai-An Chen.

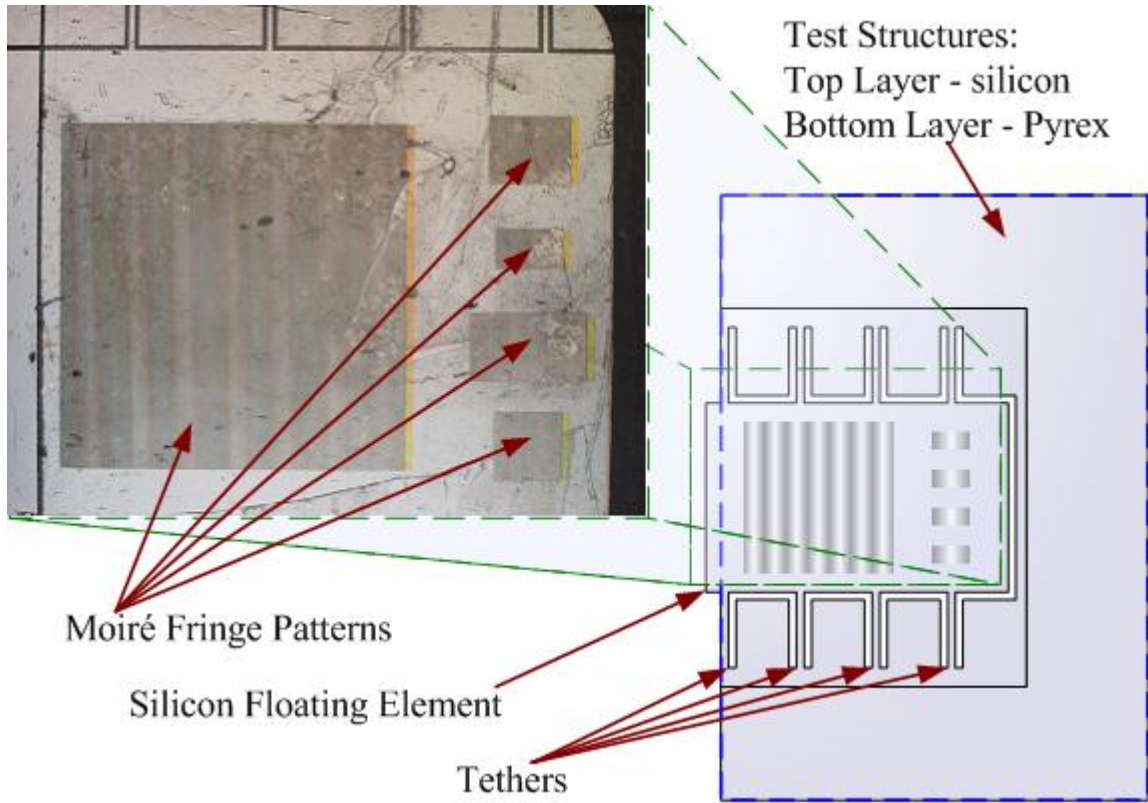


Figure 7-7. Photograph and illustration of the optical test structures. Photo courtesy of Tai-An Chen.

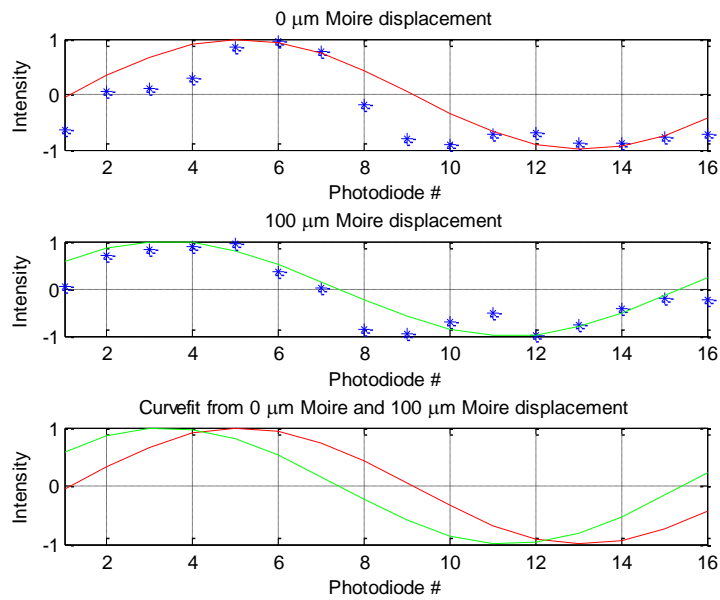


Figure 7-8. Test structure data using the fiber bundle and the nanopositioner along with least squares curvefits.

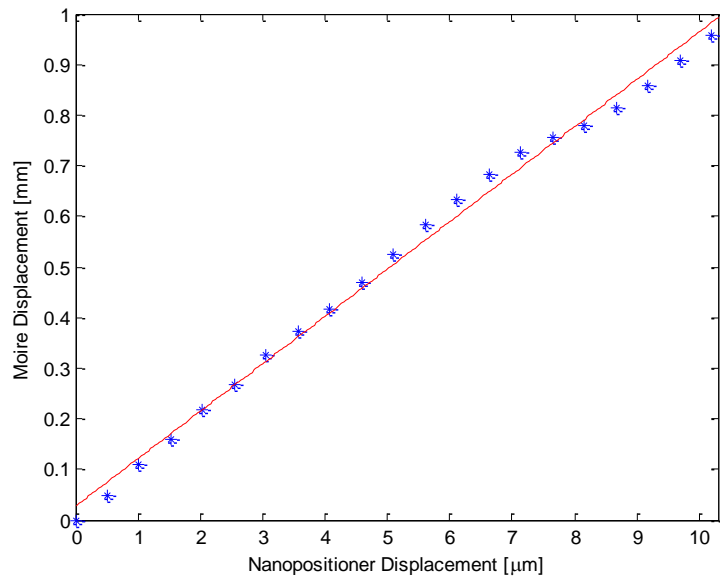


Figure 7-9. Displacement of the Moiré fringe pattern versus the mechanical displacements of the floating element test structures.

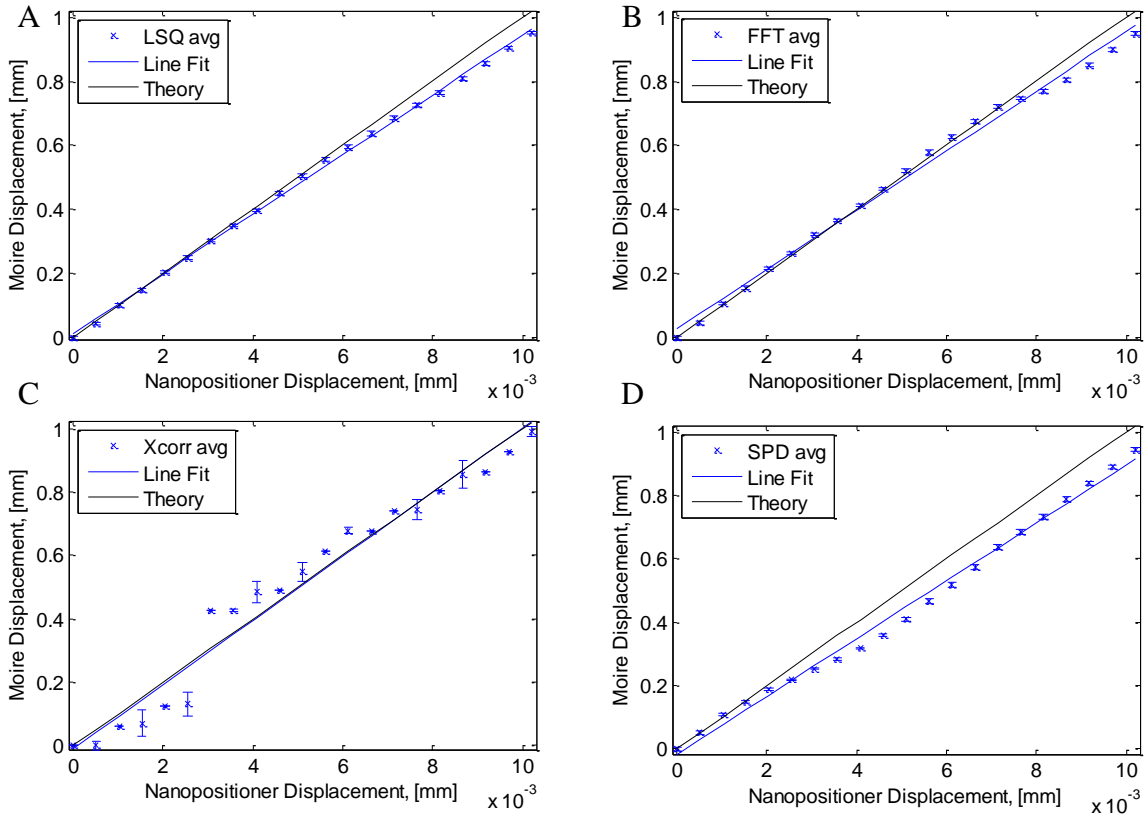


Figure 7-10. The resulting sensitivities and error bars from the nanopositioner using various optical fringe estimation techniques. A) Least squares curvefit. B) Fast Fourier Transform. C) Cross-correlation. D) Spatial phase detection.

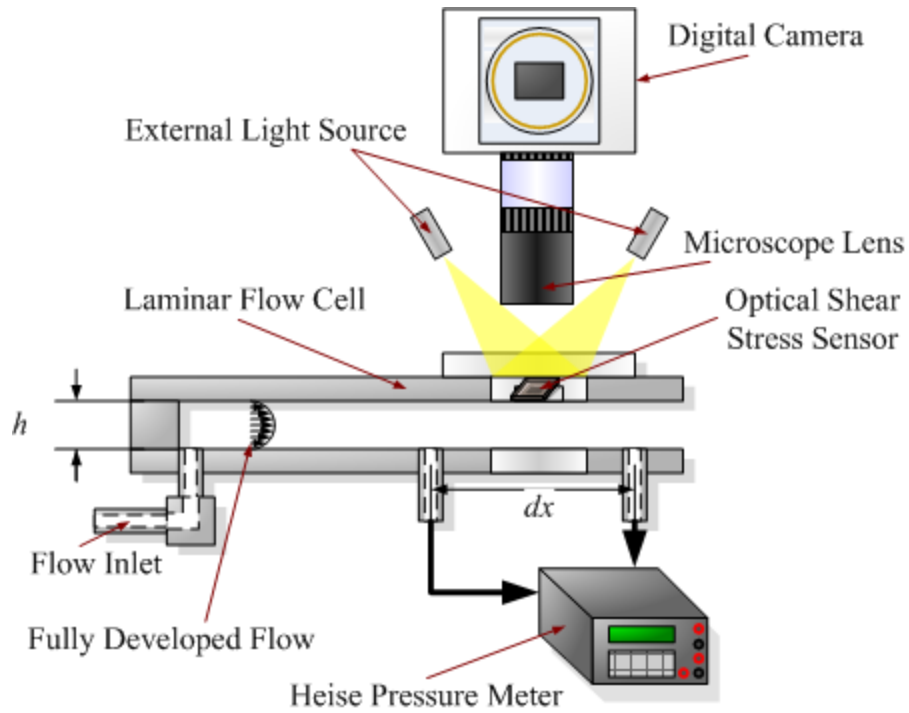


Figure 7-11. Schematic illustrating the experimental setup for statically calibrating the shear stress sensor in a laminar flow cell.

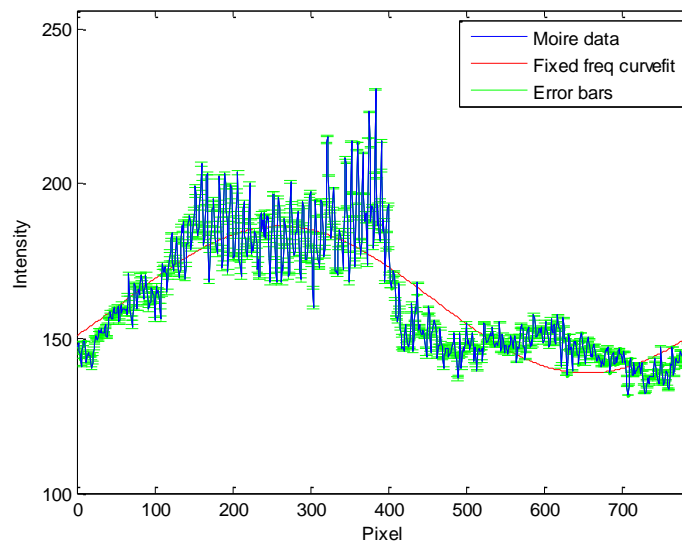


Figure 7-12. A graph of the Moiré fringe pattern with a sinusoidal least-squares curve-fit superimposed.

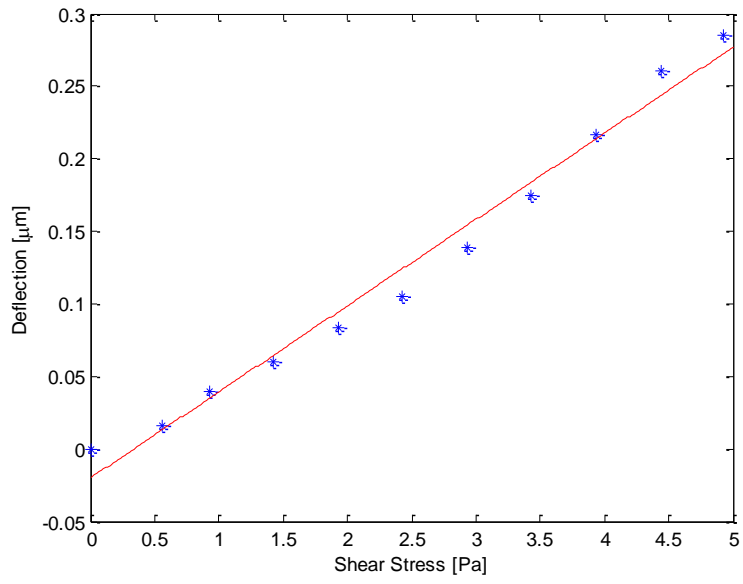


Figure 7-13. The deflection of the 5 Pa, 2 kHz shear stress sensor over a 5 Pa range in a laminar flow cell.

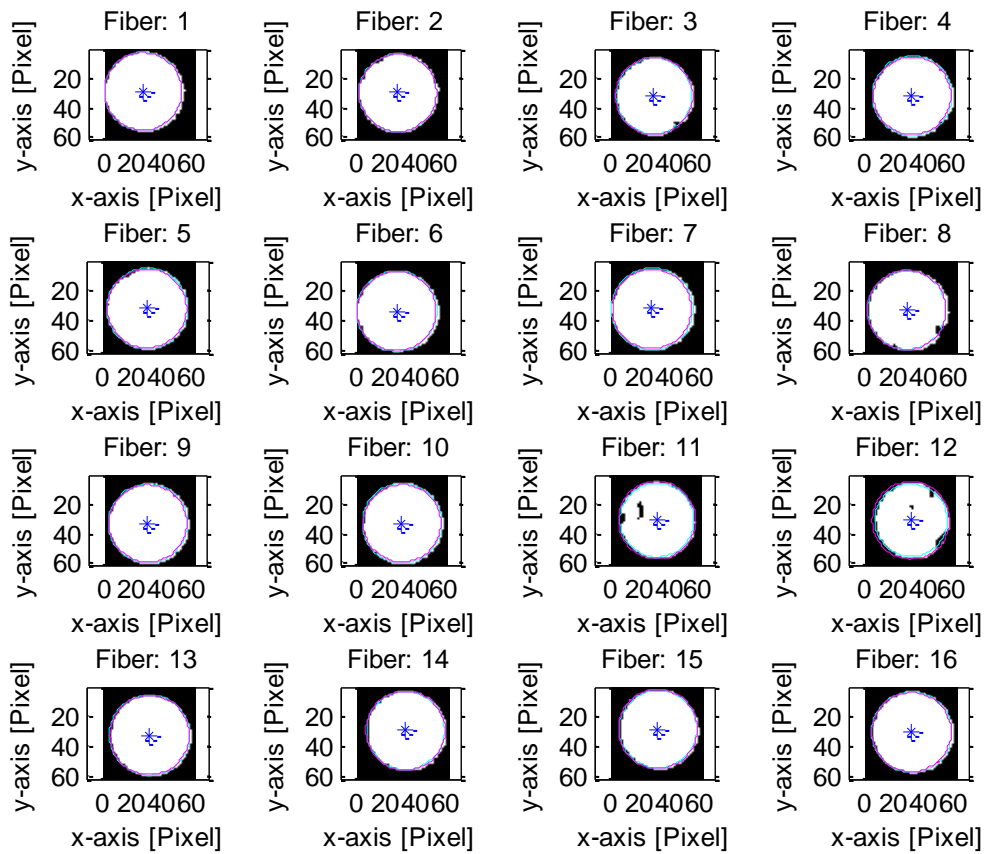


Figure 7-14. Resulting image plots of the optical fiber centroid detection algorithm.

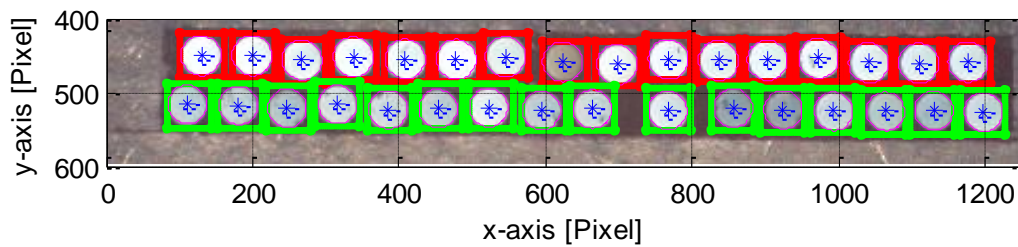


Figure 7-15. The relative fiber centroid locations are mapped to the image of the fiber bundle.

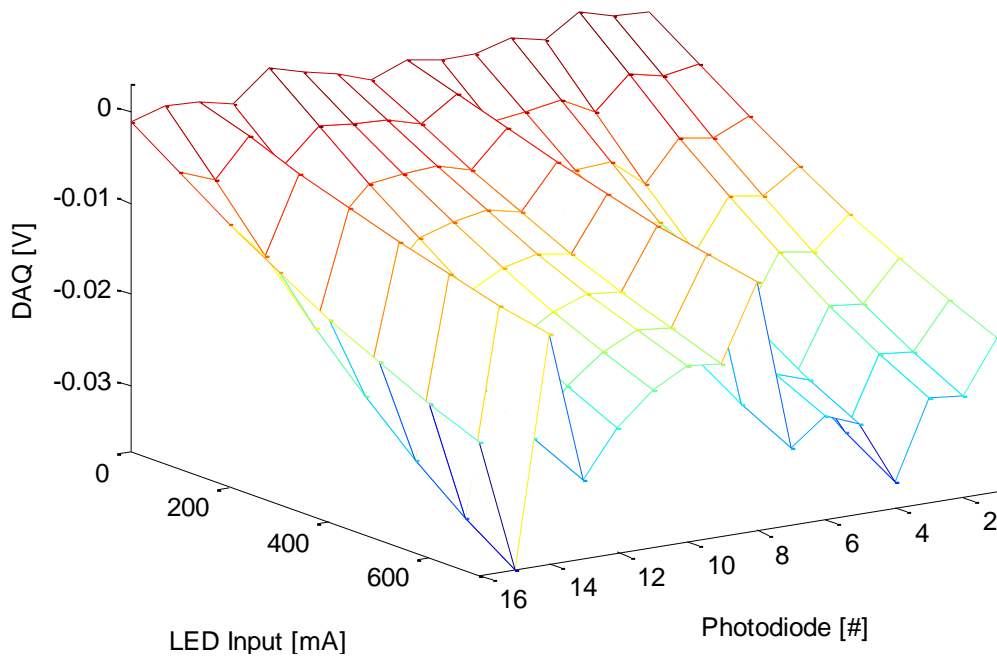


Figure 7-16. A plot showing the recorded photodiode intensities using simultaneous source fiber illumination.

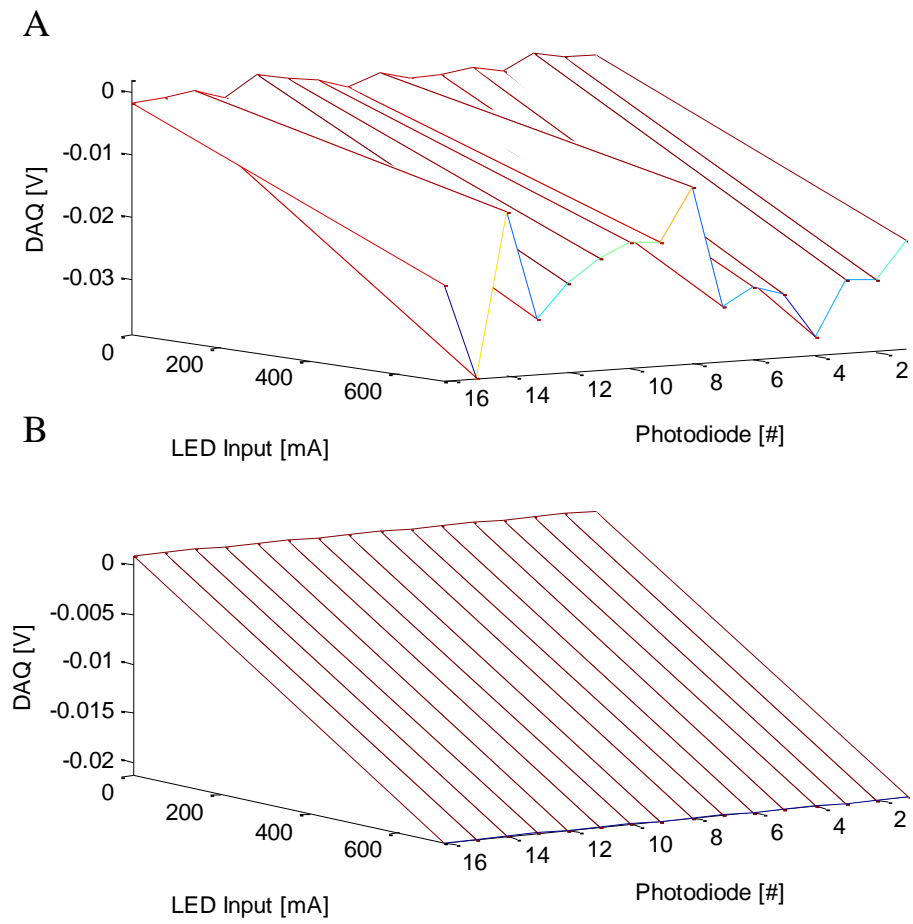


Figure 7-17. Photodiode sensitivity calibration plots. A) Linear sensitivity fit of optical wafer calibration using simultaneous source fiber illumination. B) Adjusted uniform sensitivities of each photodiode channel.

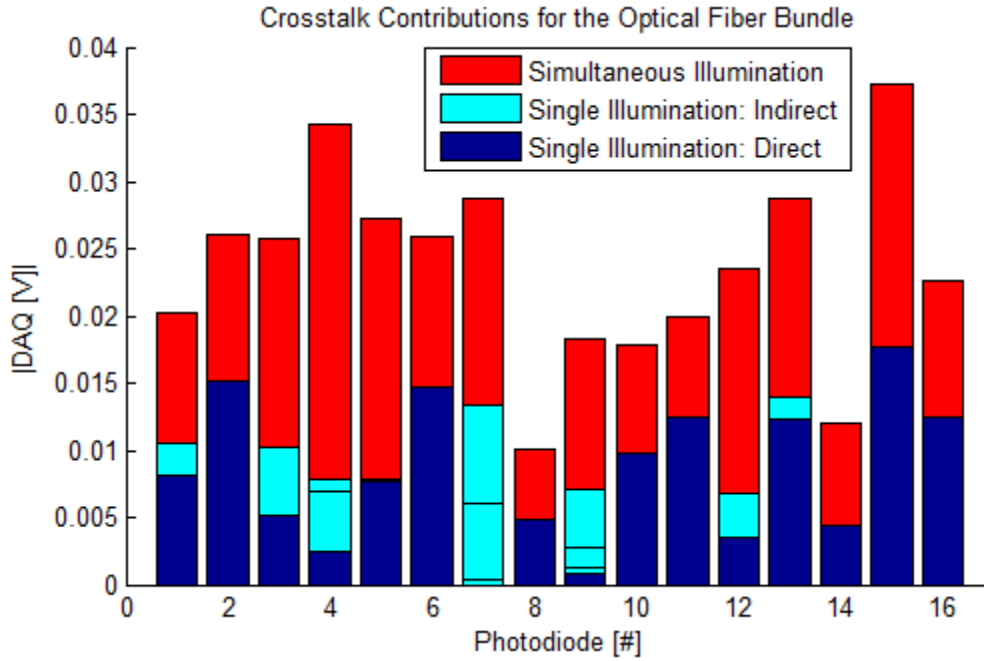


Figure 7-18. Comparison of the simultaneous source fiber illumination calibration vs. individual source fiber illumination calibration technique showing the amount of optical crosstalk.

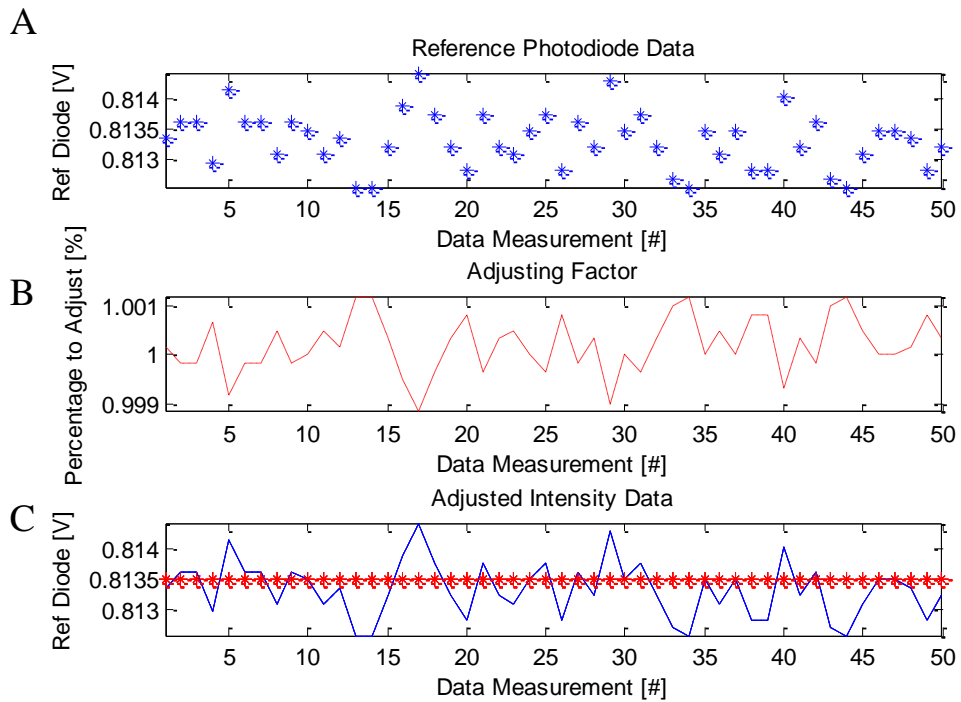


Figure 7-19. Correction plots for light fluctuation compensation using a reference photodiode. A) Direct measurement of the fluctuating light intensity using the reference photodiode. B) Correction factors for each data measurement. C) Comparison of the original reference photodiode measurements and the corrected photodiode data.

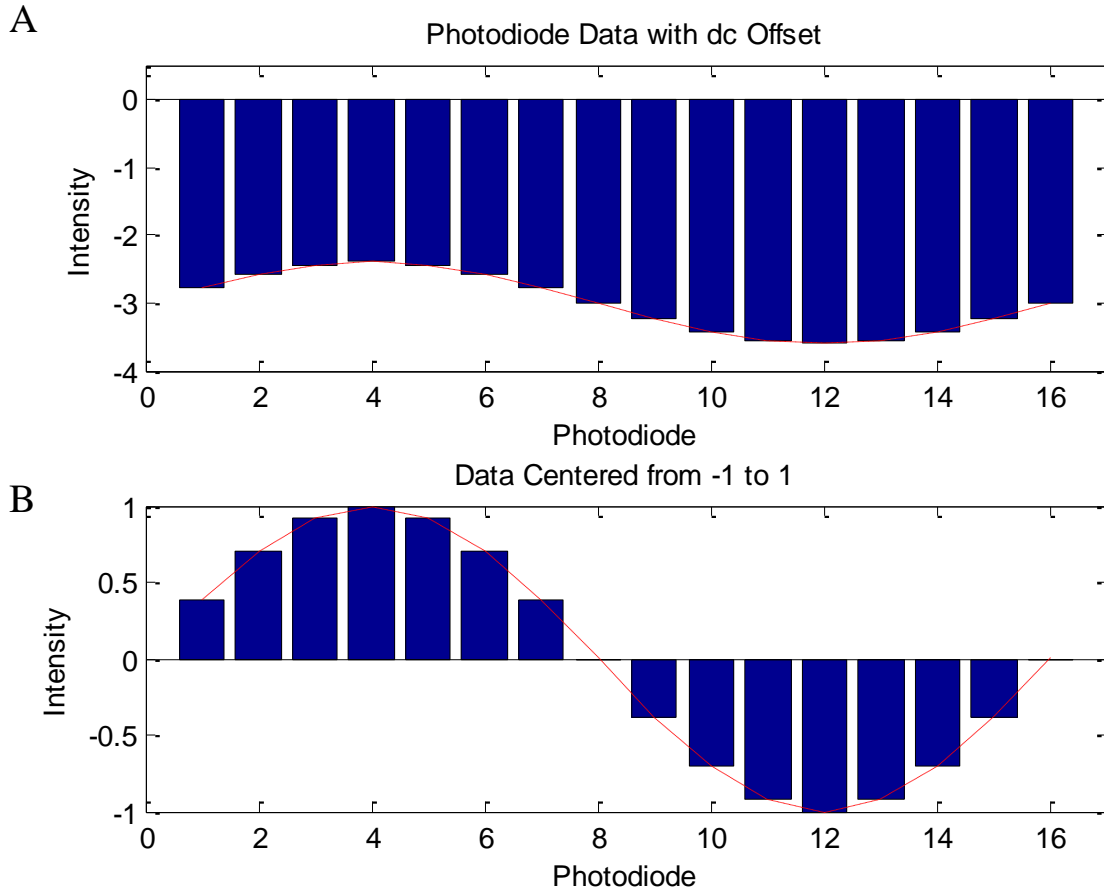


Figure 7-20. Simulated photodiode data for optical fringe estimation. A) Photodiode data with a dc offset. B) Normalized photodiode data without dc offset.

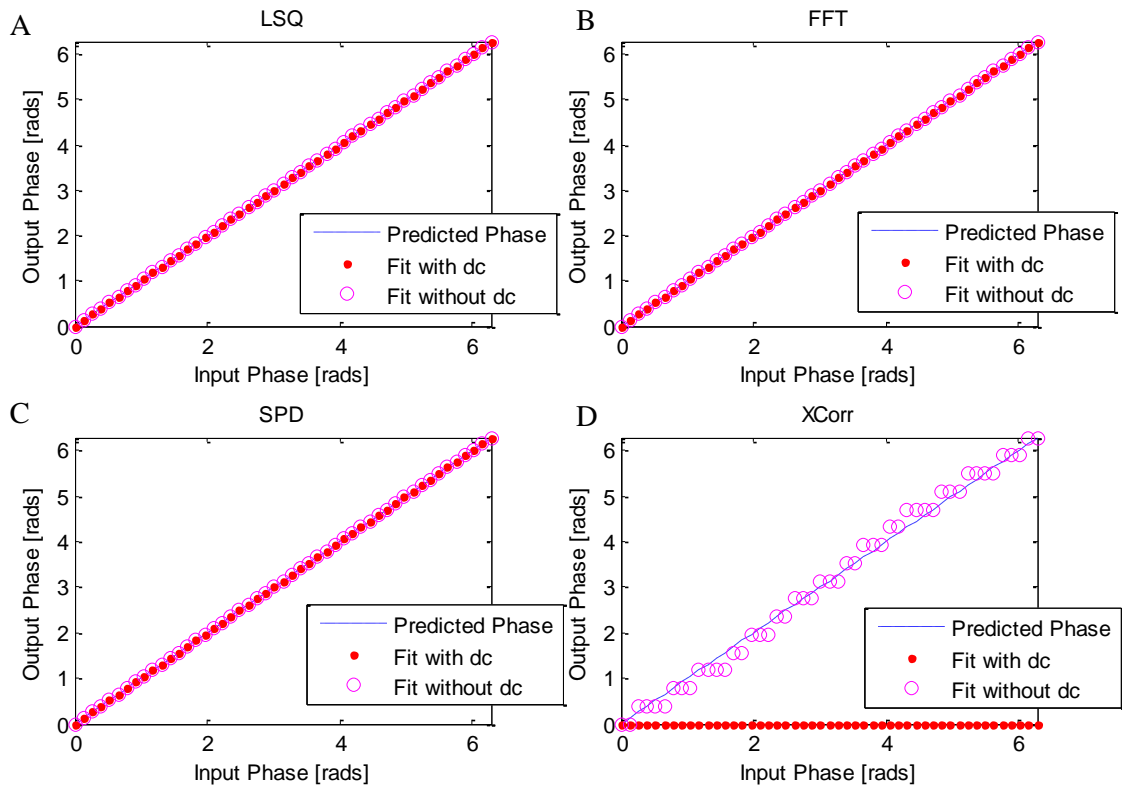
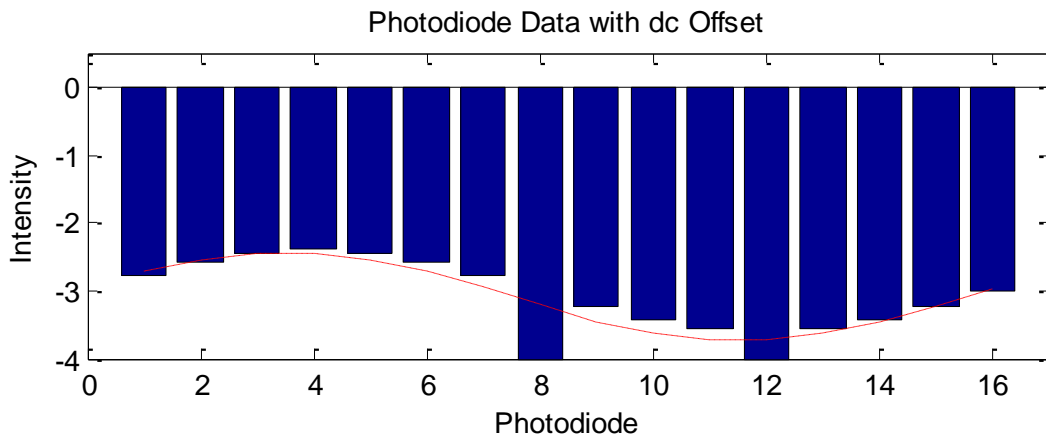


Figure 7-21. Performance of the spatial phase estimation using various fringe estimation techniques. A) Least squares (LSQ). B) Fast Fourier Transform (FFT). C) Spatial phase detection (SPD). D) Cross-correlation (XCorr).

A



B

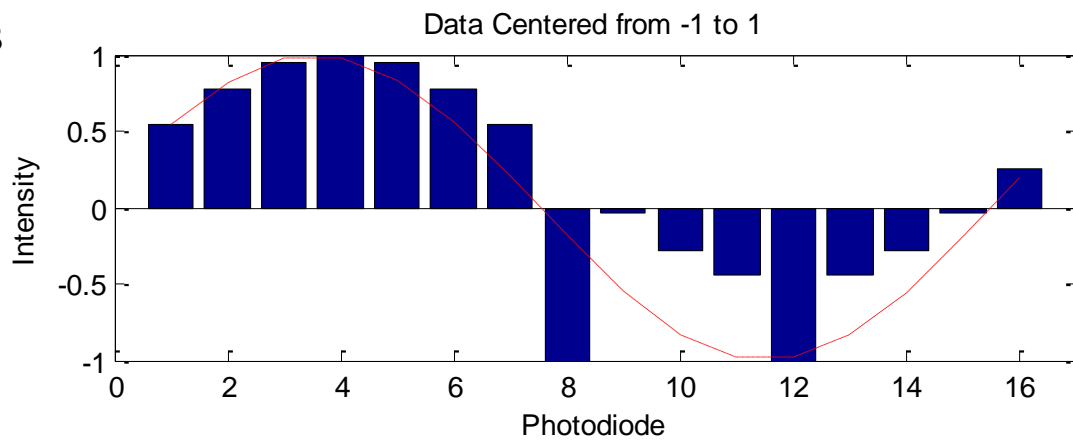


Figure 7-22. Simulated spatial debris superimposed on the simulated photodiode data. A) Photodiode data with dc offset. B) Normalized photodiode data without dc offset.

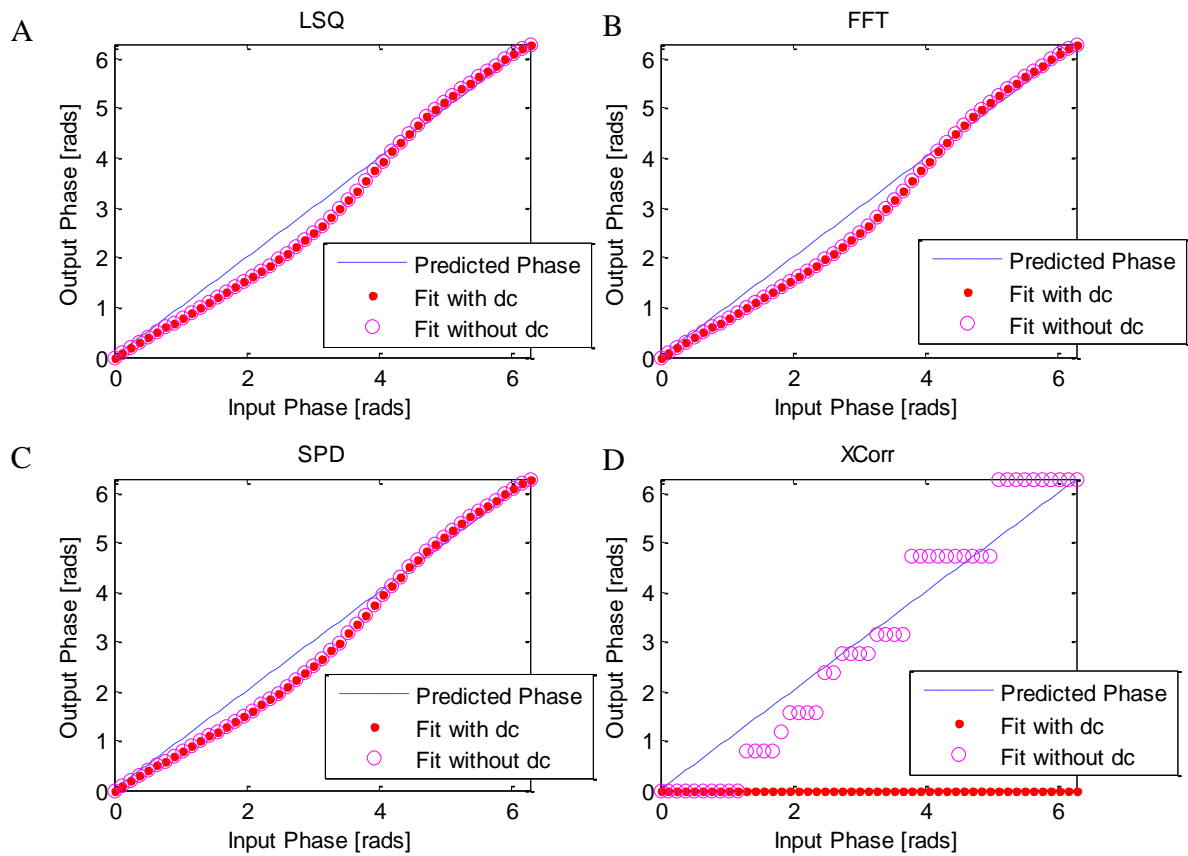


Figure 7-23. Performance of the spatial phase estimation in the presence of spatial debris using various fringe estimation techniques. A) Least squares (LSQ). B) Fast Fourier Transform (FFT). C) Spatial phase detection (SPD). D) Cross-correlation (XCorr).

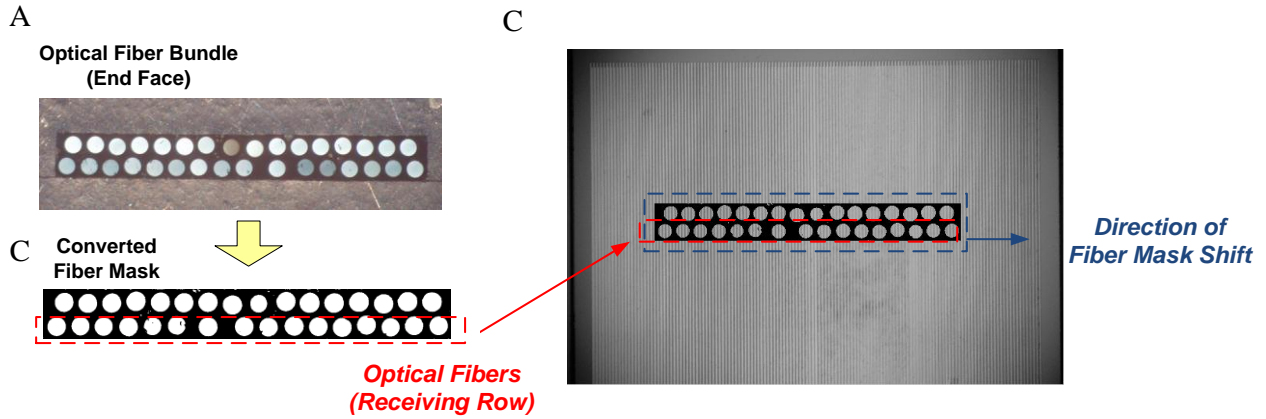


Figure 7-24. A photograph of the fiber mask simulation using a imaged Moiré fringe. A) Photograph of a fiber bundle end-face. B) Converted fiber end-face into an image mask. C) Superimposed fiber mask on the Moiré floating element. Photo courtesy of Tai-An Chen.

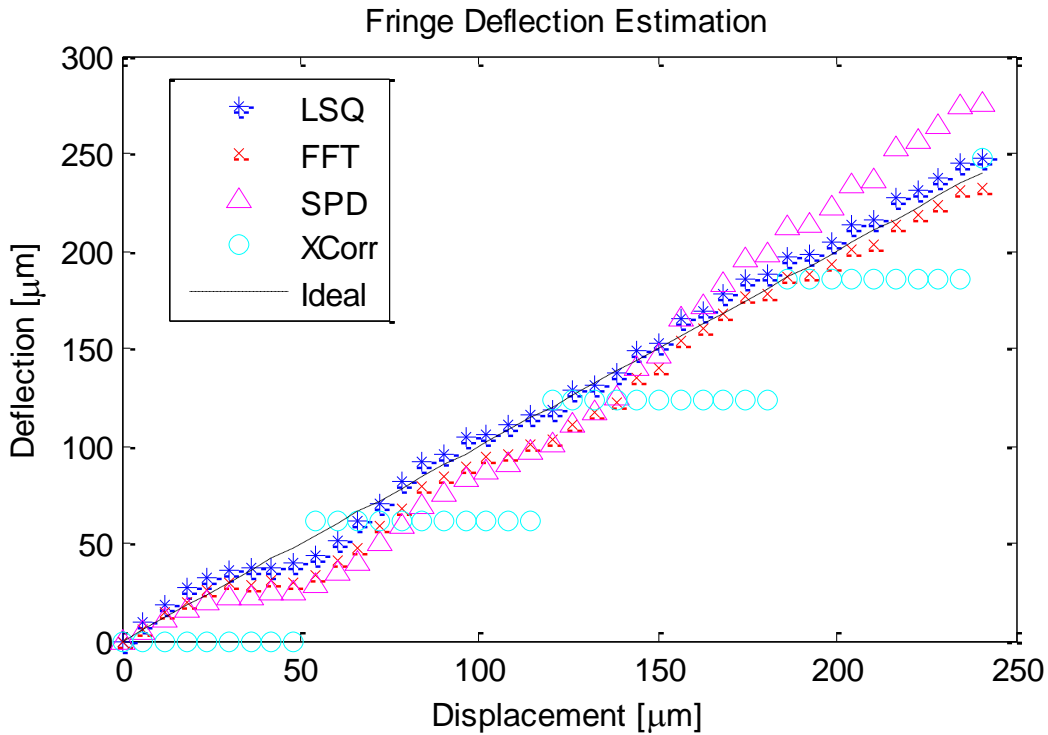


Figure 7-25. Various fringe estimation of simulated optical fringe deflection using a fiber mask.

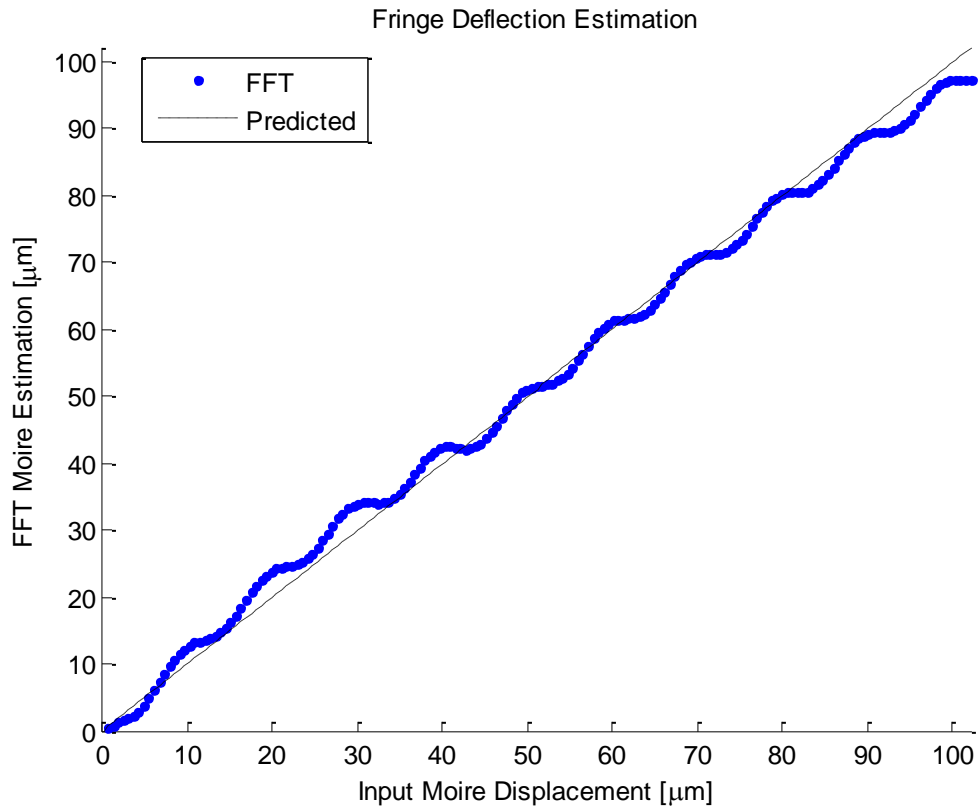


Figure 7-26. FFT fringe estimation of simulated optical fringe deflection using a fiber mask at a pixel deflection resolution.

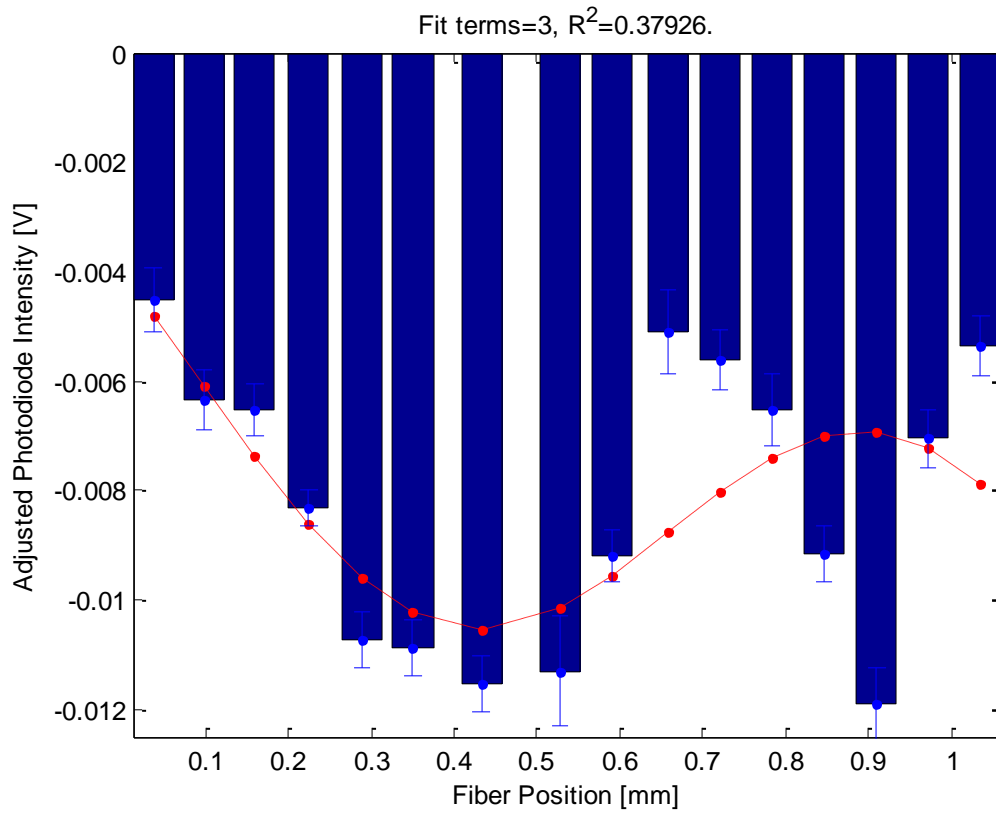


Figure 7-27. Phase estimation on the photodiode data using the n-sines, least-squares curvefit.

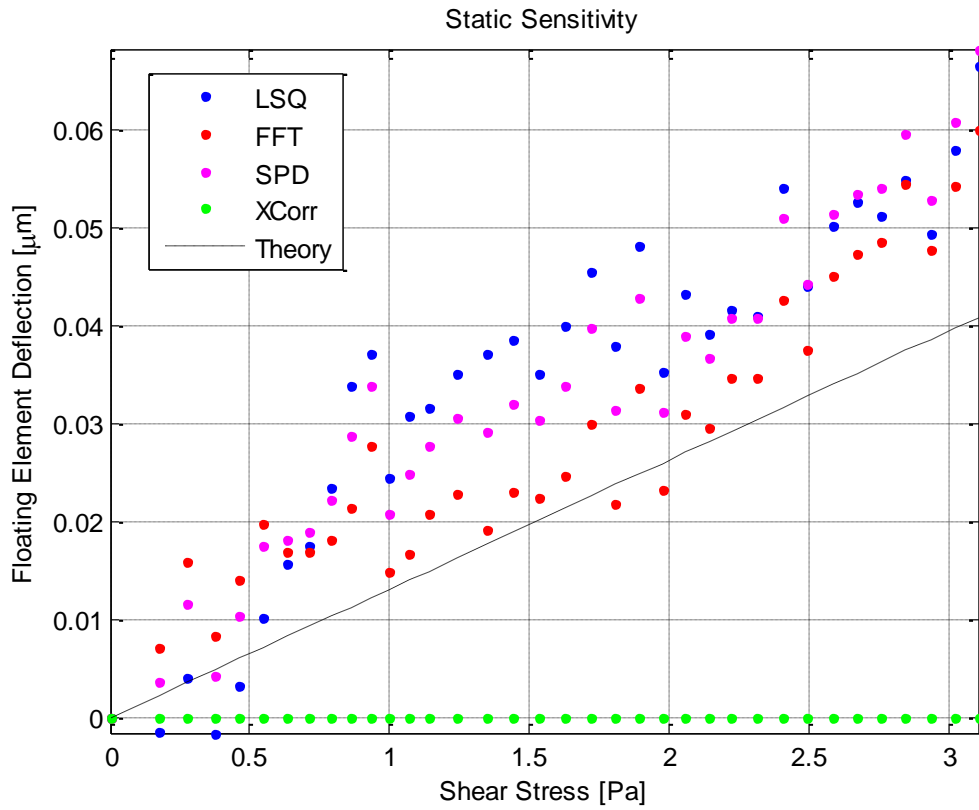


Figure 7-28. Performance of the phase estimation techniques on a 5Pa, 5kHz sensor using the various fringe estimation techniques.

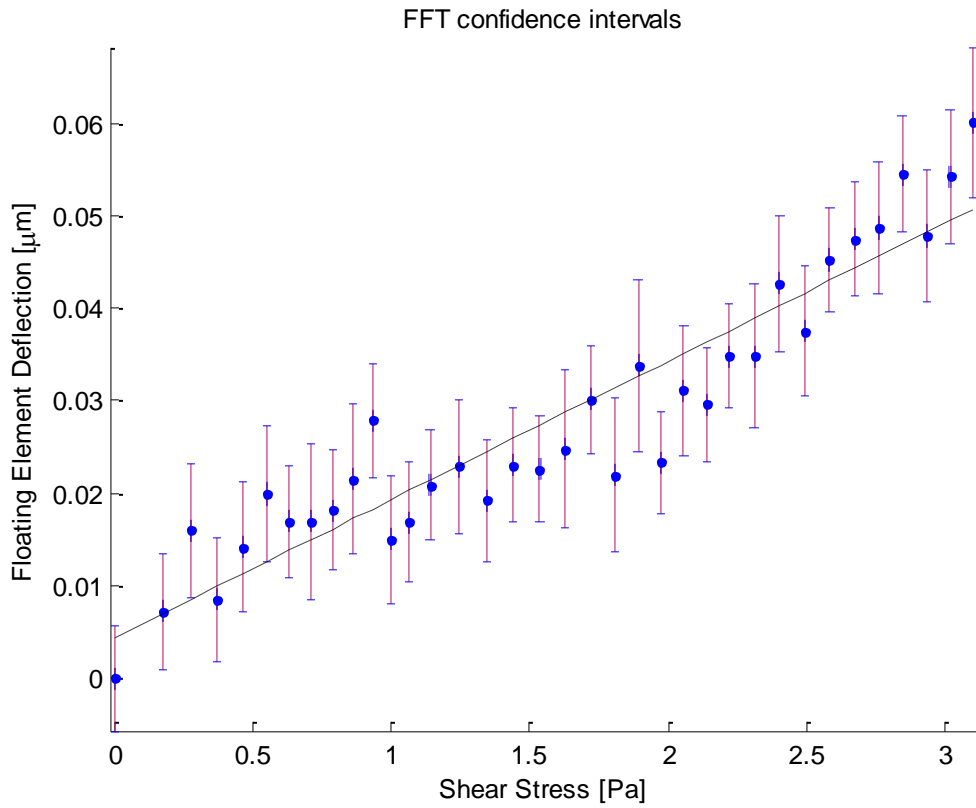


Figure 7-29. Static calibration results with error bounds generated from a Monte Carlo simulation using 95% confidence intervals.

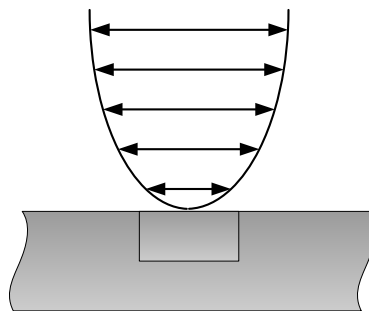


Figure 7-30. Particle velocity profile of the acoustic waves at the wall due to the no-slip boundary condition.

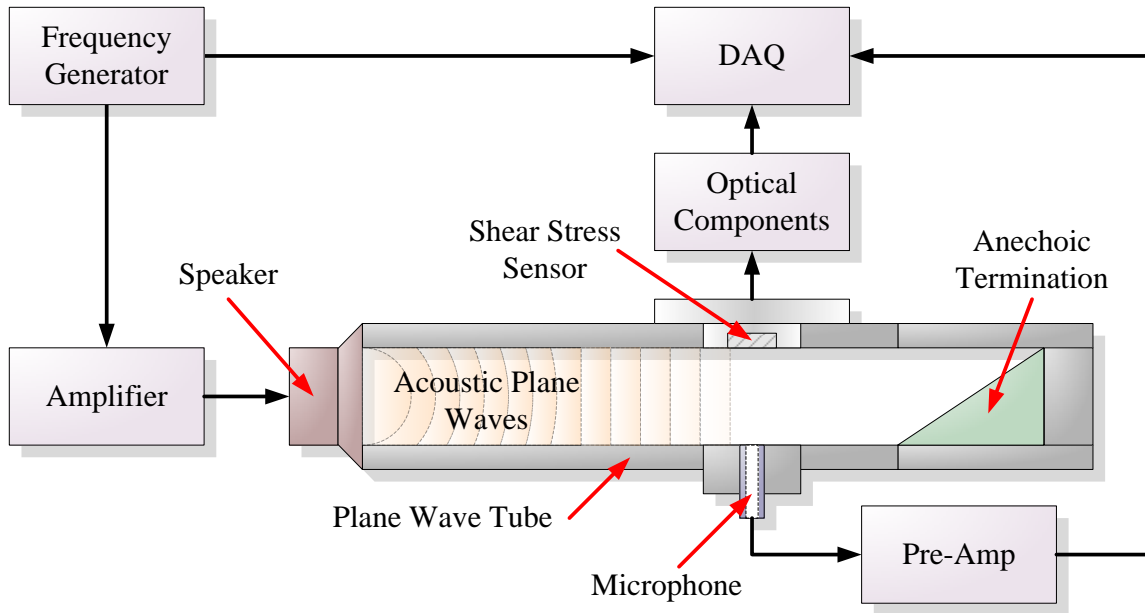


Figure 7-31. Schematic illustrating the experimental setup for dynamically calibrating the shear stress sensor in a plane wave tube.

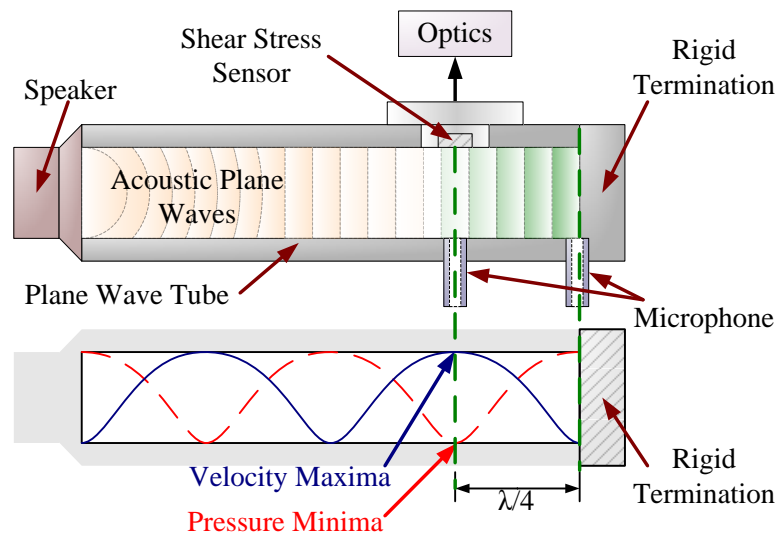


Figure 7-32. Dynamic calibration setup configuration for shear stress only in the PWT.

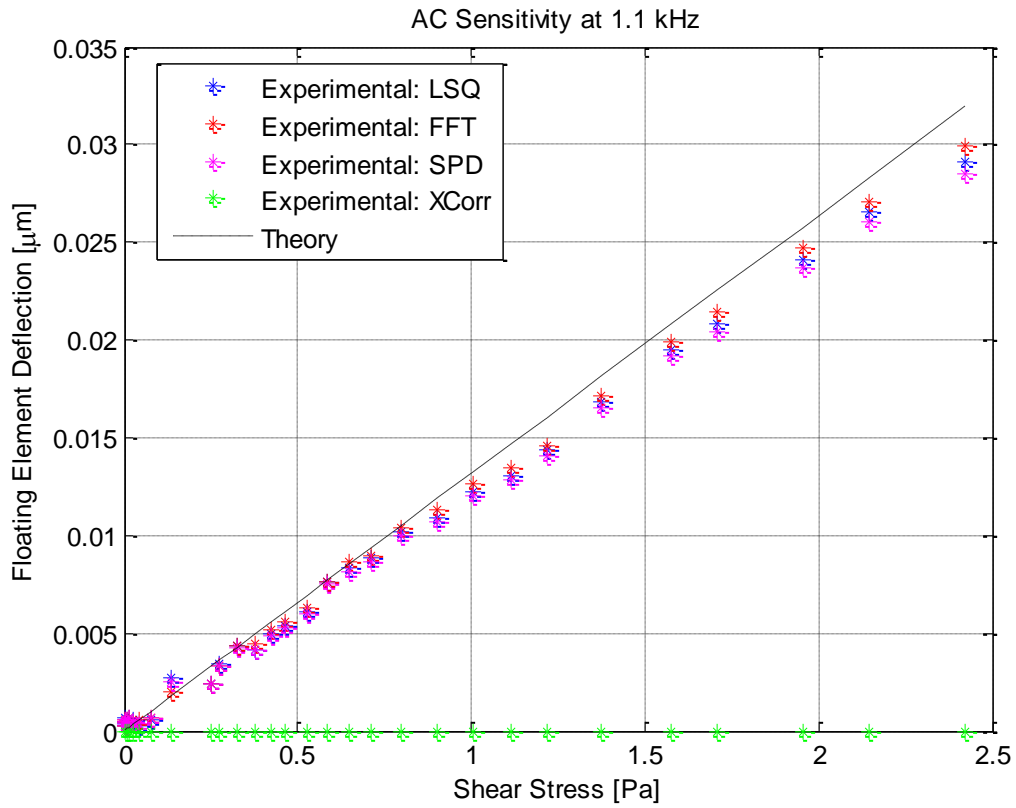


Figure 7-33. Ac sensitivity results of a 50 Pa, 5 kHz sensor placed at quarter-wavelength from a rigid termination at a frequency of 1.1 kHz.

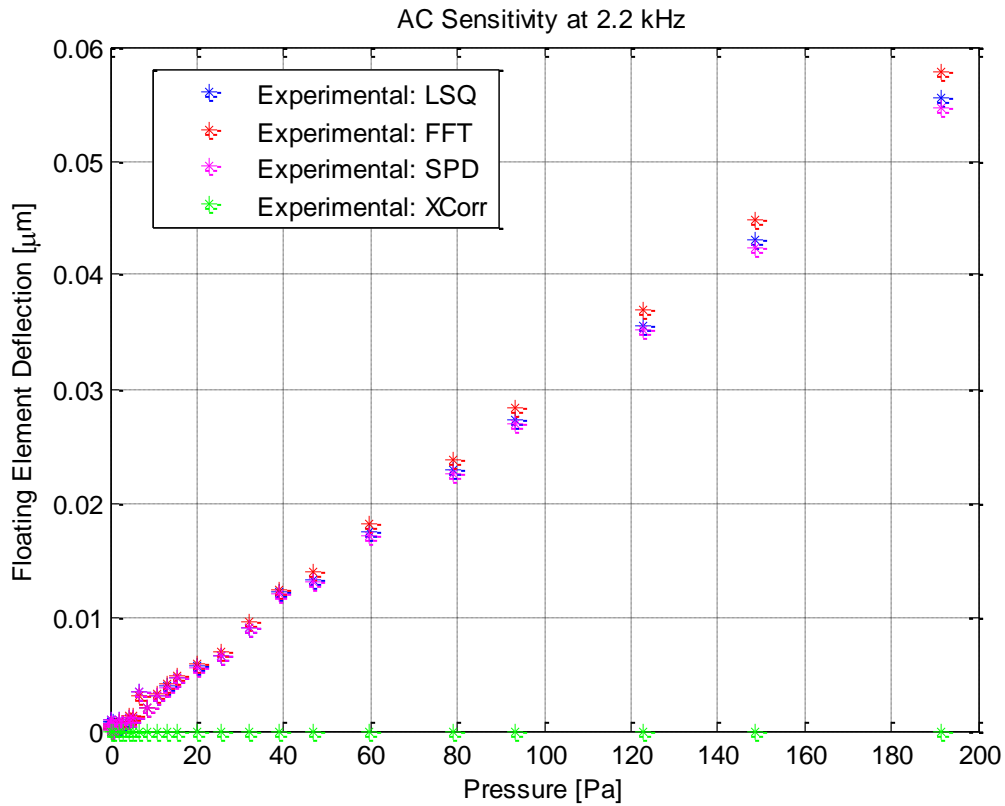


Figure 7-34. Sensitivity due to pressure monitored at 2.2 kHz during the quarter-wavelength ac sensitivity testing at 1.1 kHz.

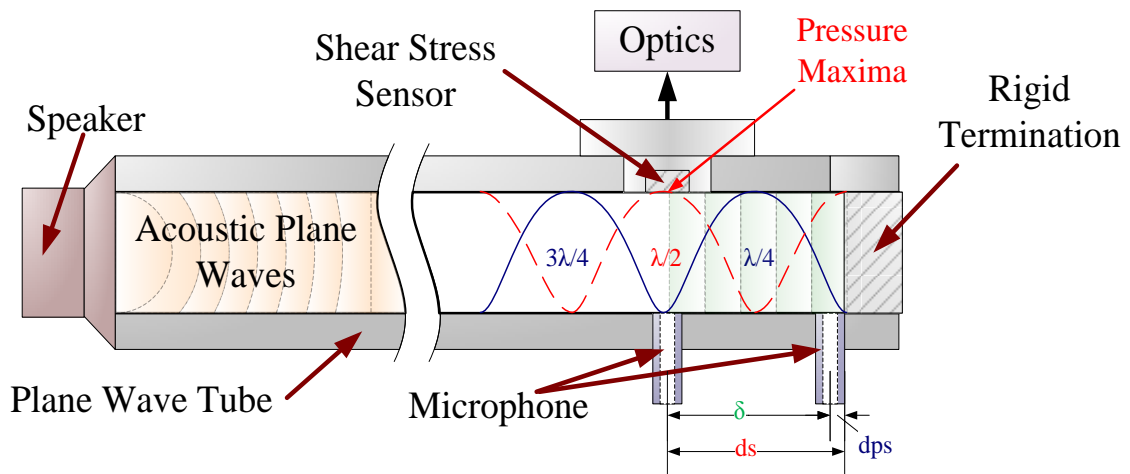


Figure 7-35. Dynamic calibration setup configuration for pressure only in the PWT.

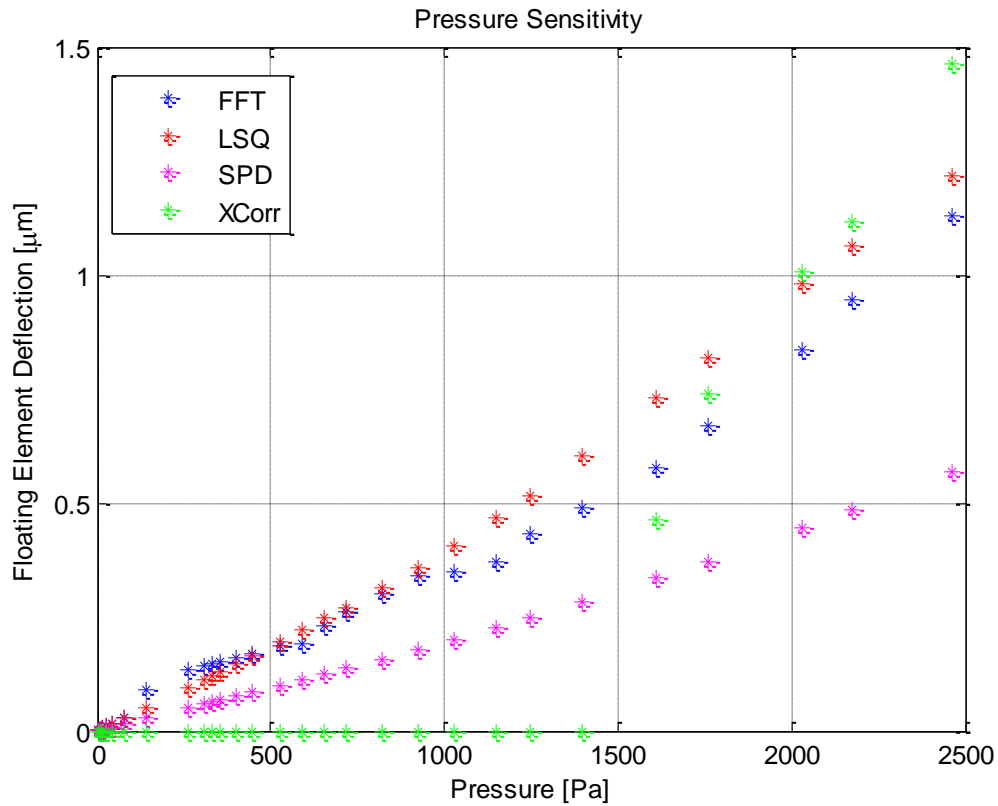


Figure 7-36. The sensitivity of a 50 Pa, 5 kHz due to pressure at a half-wavelength.

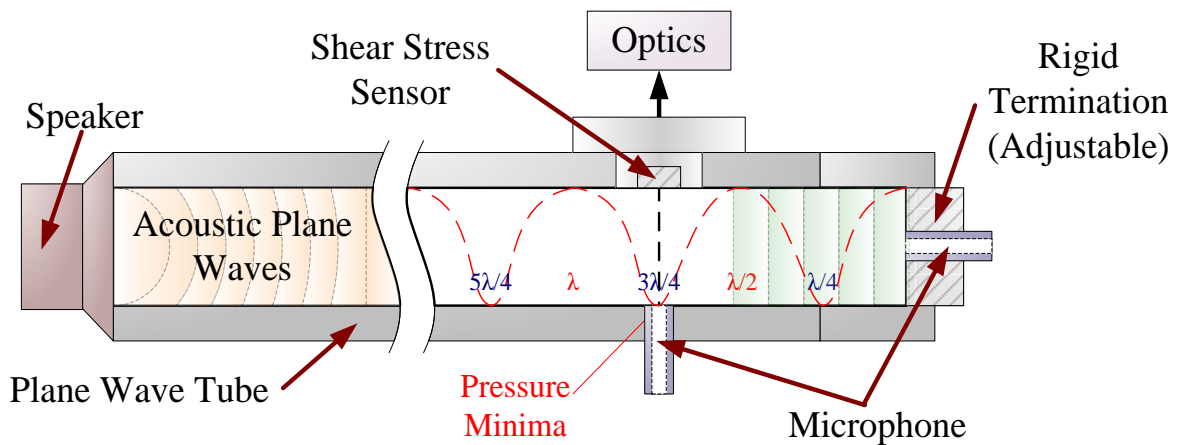


Figure 7-37. Dynamic calibration setup configuration for frequency response calibration in the PWT.

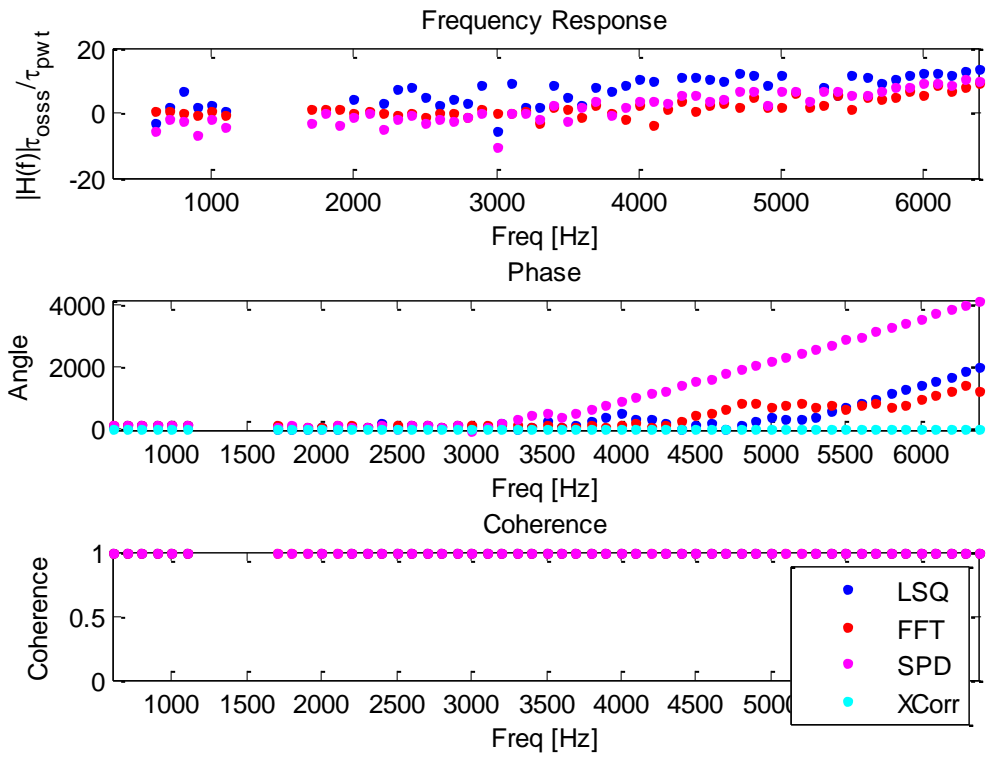


Figure 7-38. Frequency response calibration of 50 Pa, 5 kHz sensor maintained at quarter-wavelength distance from a rigid termination.

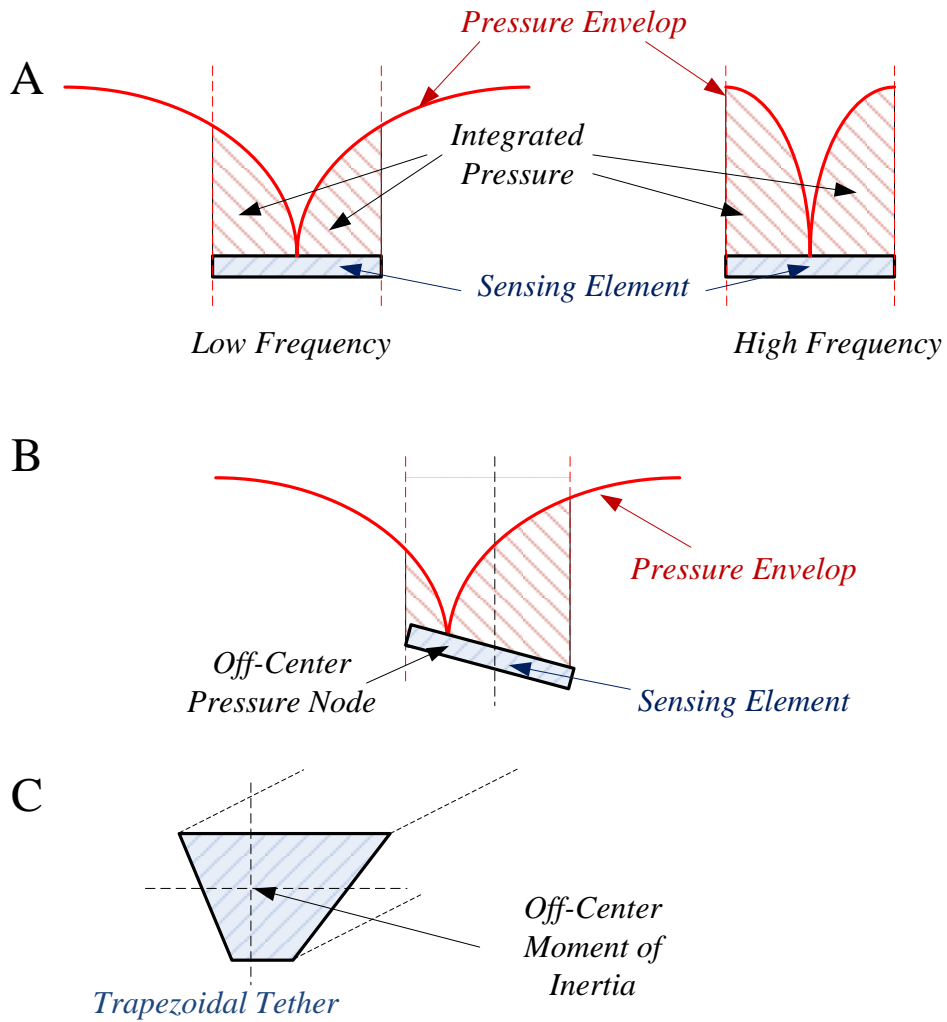


Figure 7-39. Illustration of several potential lateral deflection sources due to pressure. A) Integration of pressure around pressure minima node. B) Off-center pressure minima node. C) Off-center moment of inertia in the tether.

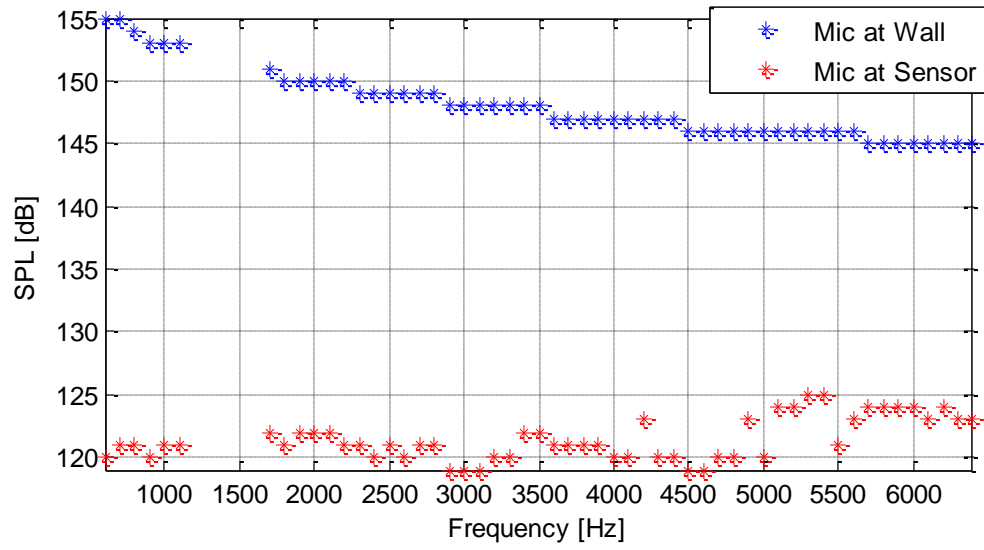


Figure 7-40. The measured sound pressure levels by the microphone at the rigid termination and the microphone at the sensor.

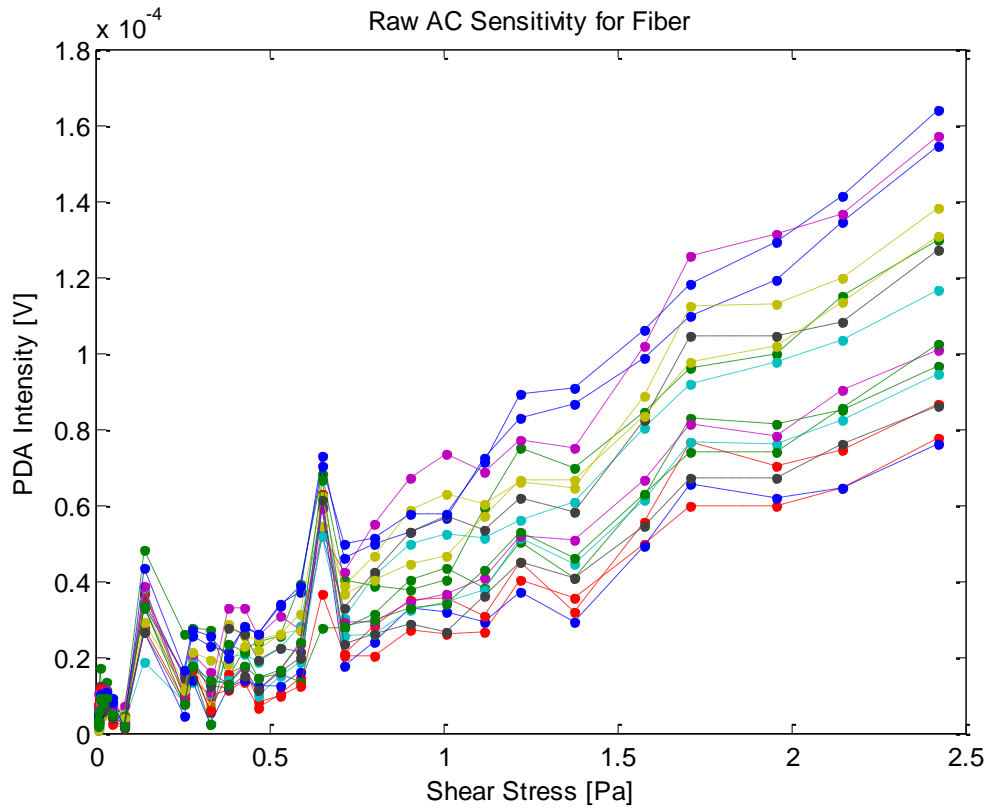


Figure 7-41. Ac sensitivity using individual optical fibers tested at 1.1 kHz.

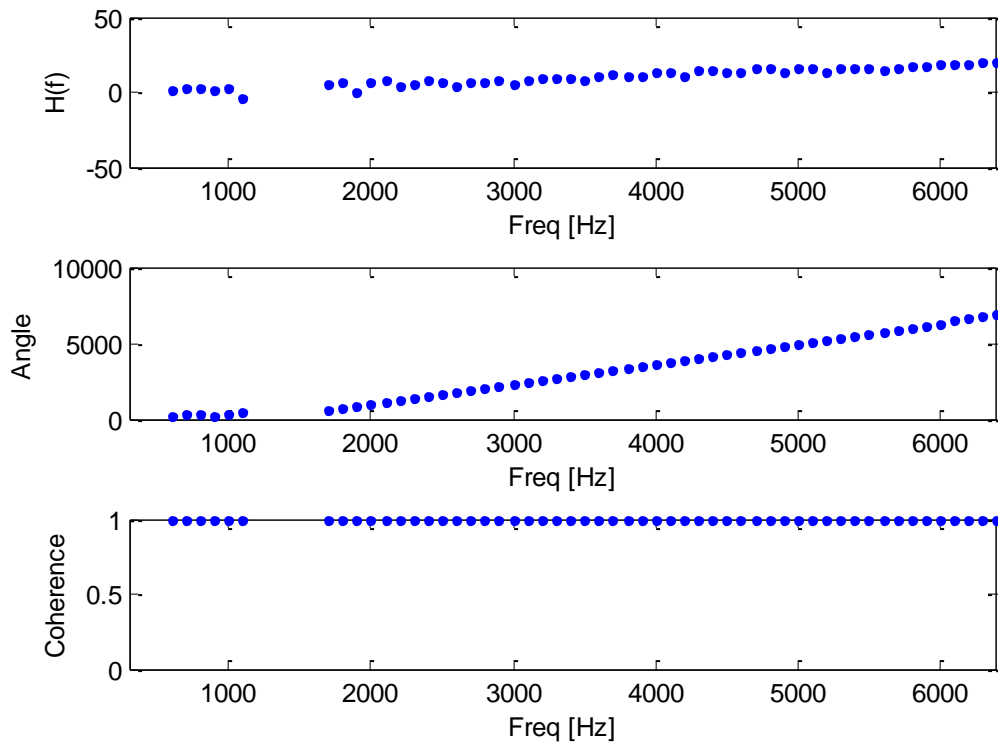


Figure 7-42. FRF estimation using the results of a single optical fiber and the microphone at the wall.

CHAPTER 8 CONCLUSIONS AND FUTURE WORK

This chapter presents the primary research contributions from this project. The limitations encountered in the project are discussed followed by recommendations for future work on this project.

8.1 Conclusions

The ability to measure direct, time-resolved shear stress is important in fluid dynamics but difficult to achieve in a real-world environment. Inhospitable factors such as high-temperature or underwater environments limit the type of transduction techniques available for shear stress detection in these environments. The optical transduction technique outlined in this research offers a potential solution for such environments.

In this research, the conventional optical system for the Moiré shear stress sensor is transitioned into miniaturized optical package system for off the optical benchtop measurements. The optoelectronics, optical fibers and fringe estimation techniques are demonstrated to work with a simulated Moiré fringe pattern that is controlled by a nano-positioner. The result of the nano-positioner tests illustrates the need optical sensitivity calibration in the optoelectronics and ideal optical fringes. Optical calibration techniques for characterizing the optical fiber bundle are developed as well.

The shear stress sensor and the miniaturized optical packaging are tested in a laminar flow cell for mean shear stress measurements up to 3.5 Pa. The resulting sensitivity from the multiple fringe estimation techniques supports the predicted floating element deflection of 13 nm/Pa using trapezoidal tethers. The inaccuracies in the flowcell resulted in large error bars in the fringe estimation.

The sensor, along with the optical fiber bundle system, is tested dynamic shear stress environment. The ac sensitivity shear only test results also matched the theoretical sensitivity model for trapezoidal tethers while the pressure sensitivity test illustrated that the floating element is deflecting laterally despite the removal of shear stress. The inherent mechanical sensitivity in the Moiré sensor towards pressure interferes with the frequency response estimation.

Despite the mechanical issues of the floating element sensor, the optical fiber bundle and optoelectronics are demonstrated to work for mean and dynamic flow calibrations. The miniaturized optic system had to overcome various optical non-idealities involved in the system. Spatial debris on the optical fringe, optical crosstalk between fibers, uneven spacing of fibers, varying sensitivity between photodetectors, scrambled transmit-receive fibers are some of the challenges encountered with the optical-fiber system. Suggestions for improving the performance of the optical detection system and the sensor are highlighted in future work section of this chapter.

8.2 Research Contributions

The primary contributions of this research are discussed in this section. Although previous research efforts for shear stress measurements using optics in Chapter 2, this research represents the development of the first optical-based, micromachined, floating element sensing system suitable for moderately high-temperature environments and water tunnel measurements. Conventional optic approaches restrict the measurements system to an optical test-bench, which is unsuitable for high-temperature or underwater applications. The miniaturization of the optical packaging in this research removes such restrictions. The use of optic fibers in this research enables the optoelectronics to be placed away from the shear stress sensor to further reduce the size of the packaging

and protect the optoelectronics from the harsh environment. The optic fibers can be rigidly attached to the sensor which mitigates vibration and optical pathway obstruction as seen by conventional free space optics.

The small size of the miniaturized optics allows multiple shear stress sensors to be placed in an array for high-resolution and sampling of test surfaces. The miniaturized optic imaging system in this research reduces the number of photodetector channels which increases the bandwidth of this system. With the increased bandwidth, this research has the potential for real-time shear stress measurements instead of post-processing recorded measurements.

This research also benefited from the development of an optical test-bed to mechanically simulate floating-element deflection and optical fringe deflection for calibrating various optical setups. The calibration of the optical fiber using the test-bed demonstrates the potential for Moiré fringe measurement from miniaturized optics.

8.3 Research Limitations

The goal of the optical packaging and sensor redesign is apply the knowledge gained from this research to produce an optimal optoelectronic package for the Moiré shear stress sensor. Manufacturing an optic fiber bundle is costly and having fore-knowledge of which limitations are more critical is useful for time and cost reductions during the design process. These limitations imposed by the optical package influences the design of the Moiré sensor. Some of the issues designing an optical fiber packaging and sensor encountered from this research are addressed in this section.

The light intensity variations experienced between optical fibers due to manufacturing misalignments and multiple fiber coupling resulted in signal intensity reduction and interference. The prototype manufactured optical fiber design (Romack)

included multiple fiber inputs with multiple light sources to illuminate each fiber.

However, light fluctuations between the multiple input light sources and each optical fiber channel was difficult to compensate. The multiple light sources from the prototype setup was replaced with a single, high intensity LED light source and a fiber bundle adapter (Ceramoptec) to couple the single light source to the multiple fiber inputs of the Romack fiber bundle. The addition of the fiber bundle adapter to the existing prototype fiber bundle results in further light intensity losses due to additional fiber interfaces.

The selected optical photodiode array (Hamamatsu S4111-16Q) consists of 16 elements, which is a typical number for a photodiode array that is readily available. The selected photodiode diode array resulted in 16 optical fibers light source transmission and 16 optical fibers for the receiving the encoded Moiré fringe pattern. The optical fibers selected are multimode fibers, which restricts the core size of the optical fiber to 50 μm or greater. The size of the optical fiber core adds limitations to the design of the Moiré period and how much the Moiré pattern should laterally deflect.

Currently, the optical shear stress sensor is designed with a Moiré period width of 1 mm. The width of the Moiré pattern is used to accommodate the 16 optic fibers for imaging. Since the size of the floating element is based on the width of the Moiré fringe, then the performance of the shear stress sensor is also influenced by the optic limitations. As the mass of the floating element is increased, the resonance of the sensor is decreased. Furthermore, the stiffness of the tethers determines the amount lateral deflection in the Moiré pattern. For a large, lateral deflection in the Moiré fringe, the overall compliance is increased which also results in a lower resonance in the

sensor. Microfabrication processes also dictate the minimum width that can be achieved in the Moiré gratings.

8.4 Recommendations for Future Work

The recommended optical fiber bundle configuration is to have a single input fiber connector for the input light source, such as a FC connector with all the fibers bundled together, a custom sensor plug interface housing the transmit-receive optical fiber pairs and a custom photodetector plug for transmitting the encoded Moiré fringe to the photodiodes. The revised optic fiber configuration is shown in Figure 8-1.

The number of optical fibers used in the prototype bundle is dictated by the photodiode array selected for this application. Reducing the number of optical detectors and optical fibers for mapping the Moiré fringe pattern reduces the size and complexity of the overall packaging. However, the signal noise of the Moiré fringe may increase due to the sampling reduction. A quadrature optical fiber approach involving four optical fibers and a Moiré optical fringe may be useful for this research but further studies are needed.

If an appropriate photodiode array is not readily available for this application, such as a 10 element photodiode array, then the photodetector plug can be replaced with multiple fiber outputs for coupling into individual photodiodes. However, the multiple photodiodes may not be advisable since this approach may require some compensation to adjust the gain of each photodetector to match.

A reduced number of fibers can allow for some flexibility in the design of the shear stress sensor. An optimization can be performed based on the new design criteria to reduce the size of the sensor and improve the performance of the device.

8.4.1 Fiber Bundle Redesign

One of the main issues with the current optical fiber configuration is the presence of optical crosstalk between adjacent source-receive fiber pairs. A proposed design is to remove the source-receive fibers and replace the fiber pairs with fiber beam-splitters. Using the fiber beam-splitter, the row of fibers at the optical fringe will serve as both the source and receive fiber. Ideally, the fiber-beam splitter setup can be mounted directly to an optical fringe whereas the source-receive fiber pair requires a finite distance for the light to bounce from the source to the receive fiber. Crosstalk is mitigated by minimizing the gap distance from the end face of an optical fiber to the optical fringe. Alignment of the fibers at the optical fringe can be achieved using a V-groove array for packaging.

Coupling efficiency between the optical fibers and the photodetectors can be improved by replacing the photodiode array with individual photodiodes. Individual photodiodes with FC pigtail fibers can be used to receive the encoded optical fringe from the fiber beam-splitter setup. The FC connectors resolve the need for physical alignment between a fiber bundle and a photodiode array.

8.4.2 Sensor Redesign

Pressure rejection is an issue in the current shear stress sensor. The sensor deflects laterally in the presence of pressure than interferes with shear stress measurements. One possible solution is to increase the tether thickness to width ratio in order to reduce pressure sensitivity. However, the increase in the tether thickness may increase the overall mass of the floating element and reduce the resonant frequency. Thinning the mass of the floating element independent of the tether thickness may have some potential issues. If the mass of the floating element is

decreased on the surface in contact of shear stress, the flushness of the sensor becomes an issue. If the mass of the floating element is decreased from the grating side, the mass reduction will increase the Talbot distance between the two grating sets.

A mechanical optimization can be performed on the dimensions of the floating element to maximize the resonance and lateral sensitivity due to shear stress while rejecting pressure sensitivity. If cross-talk is reduced by replacing the source-receive fiber pair, then the MDS of the sensor should improve and establish the lower bound of the dynamic range. The design of the in-plane response of the sensor can then be designed to filter out the out-of-plane response of the sensor.

The optical contrast of the Moiré fringe can be improved by changing the background surface of the floating element cavity. Currently, the reflectivity of the aluminum gratings and silicon floating element determine the amplitude of the optical fringe. One recommendation is to coat the back surface of the floating element with an alternate material such that the difference in reflectivity between the optical gratings and back surface is increased.

The current shear stress sensor is also limited to a temperature of ~ 350 C, which is the bonding temperature of the shear stress sensor. For high temperature sensing, the shear stress sensor and optical fibers can be transitioned to high temperature materials such as sapphire.

8.5 Summary

A proof-of-concept, optically miniaturized, fiber bundle setup has been demonstrated to have the ability to transmit light and receive an encoded Moiré fringe pattern to the receiving photodetectors for mean and dynamic flow. Some of the challenges with the optical setup include, but are not limited to, multiple input light

sources, poor alignment of optical fibers in the optical bundle due to manufacturing, varying sensitivities of each photodiode element. These issues contribute to the difficulty with the Moiré fringe estimation. However, these non-idealities may be overcome with the suggested alternate fiber bundle packaging. Further improvements can be made to the device by optimizing the mechanical features to accommodate the optic fiber requirements.

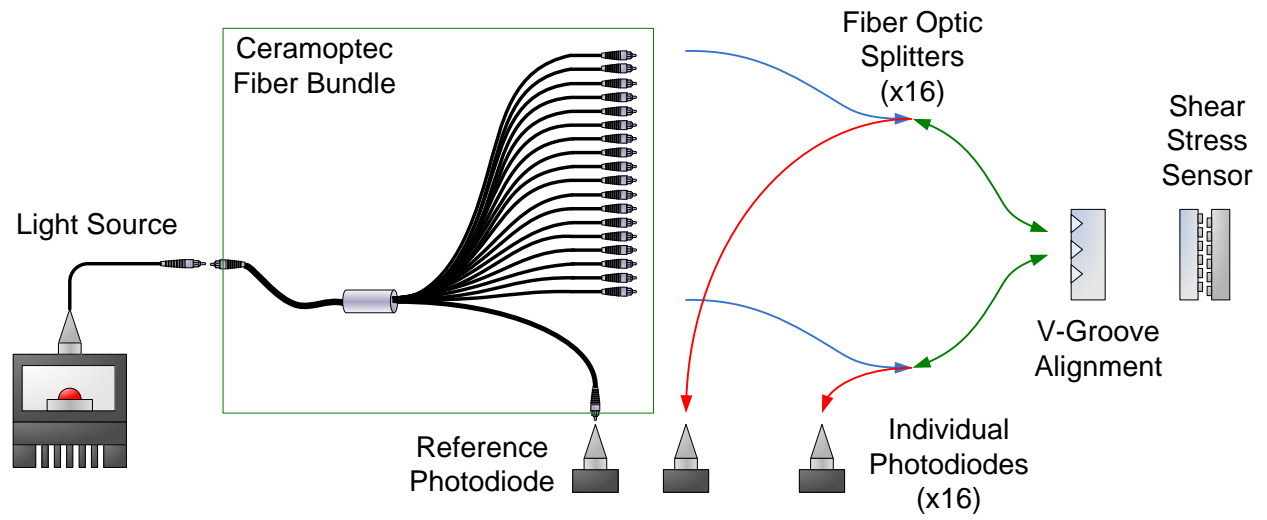


Figure 8-1. Illustration of the proposed optical fiber configuration for future experiments.

APPENDIX A MECHANICAL ANALYSIS

The mechanical equations representing the structure of the floating element sensor is described in more detail in this section. The derivations for the linear deflection, lumped compliance and lumped mass are presented.

A.1 Linear Deflection Analysis

For small, linear deflections of the floating element, the tethers of the floating element can be represented by a pair of clamped-clamped beam. The applied shear stress on the floating element is modeled by a point load at the center of the clamped-clamped beam and the applied shear stress on the tethers is a distributed load on the beam and is shown in Figure A-1. Since the deflection is linear, superposition can be used to sum the point load and distributed load.

A.1.1 Derivation for a Point Load on a Clamped-Clamped Beam

For a point load on a clamped-clamped beam with a length of $2 \cdot L_t$, the sum of the forces from the point load P and the reaction forces at the wall yields, V_{R1} and V_{R2} , the following equation,

$$\sum F_y = -P + V_{R1} + V_{R2} = 0. \quad (\text{A-1})$$

Since the point load is at the center of the beam, the reaction forces are equal to each other such that, $V_{R1} = V_{R2} = V_R$. Using equation (A-1), the point load is found to be, $P = V_R / 2$.

At a given distance x for $0 < x < L_t$, the shear force, V_x is found by summing the forces,

$$\sum F_y = -V_x + V_{R1} = 0. \quad (\text{A-2})$$

Since the reaction force is $V_R = P/2$, the shearing force is also found to be

$$V_x = P/2; \text{ hence } V_R = V_x,$$

The sum of the moments evaluated at $x=0$ is given by,

$$\sum M = 0 = M_R - M_x - V_x x \quad (\text{A-3})$$

where M_R is the moment at the wall and M_x is the moment at the shear force, V_x .

Substituting $V_x = V_R$ yields,

$$M_x = M_R + V_R x. \quad (\text{A-4})$$

The governing second order differential equation for bending beams is given by,

$$EI \cdot \frac{d^2 \delta}{dx^2} = -M_x. \quad (\text{A-5})$$

where E is Young's modulus and I is the moment of inertia. Substituting equation

(A-4) into equation (A-5) results in the following equation (A-6),

$$-EI \cdot \frac{d^2 \delta(x)}{dx^2} = V_R \cdot x + M_R. \quad (\text{A-6})$$

Integrating equation (A-6) yields a slope equation,

$$-EI \cdot \frac{d\delta(x)}{dx} = \frac{1}{2} V_R \cdot x^2 + M_R \cdot x + C_1 \quad (\text{A-7})$$

where C_1 is a constant from the integration. Integrating equation (A-7) yields a

deflection equation for a point load,

$$-EI \cdot \delta(x) = \frac{1}{6} V_R \cdot x^3 + \frac{1}{2} M_R \cdot x^2 + C_1 \cdot x + C_2 \quad (\text{A-8})$$

where C_2 is also a constant. The constants C_1 and C_2 can be solved by applying boundary conditions. For the boundary conditions at the wall, $x = 0$, the deflection is given by,

$$w(0) = 0, \quad (\text{A-9})$$

and the slope is given by,

$$\frac{d\delta(0)}{dx} = 0. \quad (\text{A-10})$$

At the center of the beam, $x = L_t$, where the maximum deflection of the beam occurs, the slope is zero which yields the following boundary condition,

$$\frac{d\delta(L_t)}{dx} = 0. \quad (\text{A-11})$$

Applying the boundary condition (A-9) to equation (A-7) yields $C_1 = 0$. Similarly, applying the boundary condition (A-10) to equation (A-8) results in $C_2 = 0$. Using $V_R = P/2$, $C_1 = 0$ and $C_2 = 0$, the deflection equation for a point load can be simplified to,

$$\delta(x) = \frac{P}{24EI} x^2 (3L_t - 2x). \quad (\text{A-12})$$

At the maximum deflection, $x = L_t$, equation (A-12) can be simplified to,

$$\delta(L_t) = \frac{1}{24} \frac{P}{EI} L_t^3. \quad (\text{A-13})$$

A.1.2 Derivation for a Distributed Load on a Clamped-Clamped Beam

Starting with the second order differential equation (A-5), taking the derivative yields a shear force equation,

$$EI \cdot \frac{d^3\delta(x)}{dx^3} = -V(x). \quad (\text{A-14})$$

Taking the derivative of (A-14), yields the following equation,

$$EI \cdot \frac{d^4 \delta(x)}{dx^4} = Q(x), \quad (\text{A-15})$$

where $q(x)$ is the external load.

Integrating equation (A-15) yields the following equations in terms of $q(x)$.

$$\frac{d^3 \delta(x)}{dx^3} = \frac{1}{EI} Q(x) \cdot x + C_1 \quad (\text{A-16})$$

$$\frac{d^2 \delta(x)}{dx^2} = \frac{1}{2EI} Q(x) \cdot x^2 + C_1 \cdot x + C_2 \quad (\text{A-17})$$

$$\frac{d\delta(x)}{dx} = \frac{1}{6EI} Q(x) \cdot x^3 + \frac{1}{2} C_1 \cdot x^2 + C_2 \cdot x + C_3 \quad (\text{A-18})$$

and,

$$\delta(x) = \frac{1}{24EI} Q(x) \cdot x^4 + \frac{1}{6} C_1 \cdot x^3 + \frac{1}{2} C_2 \cdot x^2 + C_3 \cdot x + C_4. \quad (\text{A-19})$$

In addition to the boundary conditions (A-9) and (A-10) at the wall, $x=0$, two more boundary conditions exist at the other wall, $x=2 \cdot L_t$.

$$\delta(2 \cdot L_t) = 0, \quad (\text{A-20})$$

and,

$$\frac{d\delta(2 \cdot L_t)}{dx} = 0. \quad (\text{A-21})$$

Applying the boundary conditions results in $C_4 = 0$, $C_3 = 0$, $C_2 = Q(x)(2L_t)^2 / (12EI)$ and $C_1 = -Q(x)(2L_t) / (2EI)$. Equation (A-19) simplifies to the slope equation for a distributed load,

$$\delta(x) = \frac{1}{24} \frac{Q(x)}{EI} x^2 (x - 2L_t)^2. \quad (\text{A-22})$$

Using the maximum deflection at the center of the beam $x = L_t$, equation (A-22) further simplifies to,

$$\delta(L_t) = \frac{1}{24} \frac{Q}{EI} L_t^4. \quad (\text{A-23})$$

A.1.3 Euler Bernoulli Equation for Linear Deflections

The deflection equations for a point load (A-12) and distributed load (A-22) across a clamped-clamped beam are linear and superposition may be used. The point load for a pair of clamped-clamped beams can be expressed in terms of shear stress as,

$$P = \frac{\tau_w W_e L_e}{2}. \quad (\text{A-24})$$

Likewise, the distributed load can be expressed in terms of shear stress as,

$$Q = \tau_w W_t. \quad (\text{A-25})$$

The moment of inertia for a rectangle is given by,

$$I = \frac{1}{12} b h^3 = \frac{1}{12} T_t W_t^3. \quad (\text{A-26})$$

where b is considered to be the base and h is the height.

For a deflection equation across the clamped-clamped beam, combining equations (A-12), (A-22), (A-24), (A-25) and (A-26) yields the following equation,

$$\delta(x) = \frac{\tau_w}{4ET_t W_t^3} \left(2W_t \cdot x^4 - (2W_e L_e + 8W_t L_t) \cdot x^3 + L_t (3W_e L_e + 8W_t L_t) \cdot x^2 \right). \quad (\text{A-27})$$

At the maximum deflection of the beam occurs at $x = L_t$. Substituting $x = L_t$ into equation (A-27) yields the Euler Bernoulli equation for small, linear deflections,

$$\delta(L_t) = \tau_w \frac{L_e W_e}{4ET_t} \left(\frac{L_t}{W_t} \right)^3 \left(1 + 2 \frac{L_t W_t}{L_e W_e} \right). \quad (\text{A-28})$$

A.1.4 Effective Compliance

Using work energy equations, the effective compliance can be found by relating the lumped parameters to the potential energy of the system, given by,

$$W_{PE} = \int W_{PE}^* = \int_0^{q_0} e dq = \frac{1}{2} \frac{\delta^2(L_t)}{C_{me}}, \quad (\text{A-29})$$

where e is the effort variable and q is considered to be displacement variable. The contribution of the potential energy for a point load is given by,

$$W_{PE}^* = \int_0^{L_t} \int_0^{\delta(x)} \frac{P}{2} \delta(x - L_t) \cdot d\delta(x) \cdot dx \quad (\text{A-30})$$

The ratio between $\delta(x)$ and $\delta(L_t)$ is given by,

$$\frac{\delta(x)}{\delta(L_t)} = \frac{\tau_w}{4ET_t W_t^3} \left(2W_t \cdot x^4 - (2W_e L_e + 8W_t L_t) \cdot x^3 + L_t (3W_e L_e + 8W_t L_t) \cdot x^2 \right) \cdot \frac{\tau_w \frac{L_e W_e}{4ET_t} \left(\frac{L_t}{W_t} \right)^3 \left(1 + 2 \frac{L_t W_t}{L_e W_e} \right)}{\tau_w \frac{L_e W_e}{4ET_t} \left(\frac{L_t}{W_t} \right)^3 \left(1 + 2 \frac{L_t W_t}{L_e W_e} \right)}. \quad (\text{A-31})$$

Combining equations (A-24) and (A-30) results in the double integral,

$$W_{PE}^* = \int_0^{L_t} \int_0^{\delta(x)} \frac{\delta(x - L_t)}{2} \left(\frac{\tau_w L_e W_e}{\underbrace{2}_P} \right) \cdot \frac{\delta(x)}{\underbrace{\frac{\tau_w}{4ET_t} \frac{1}{W_t^3} \left(\begin{array}{l} (2W_t)x^4 - \\ (2L_e W_e + 8L_t W_t)x^3 + \\ L_t (3L_e W_e + 8L_t W_t)x^2 \end{array} \right)}}_1} \cdot d\delta(x) \cdot dx \quad (\text{A-32})$$

Evaluating the inner integral yields the following equation,

$$W_{PE}^* = \int_0^{L_t} \frac{\left(\frac{\tau_w L_e W_e}{4} \right) \cdot \delta(x - L_t)}{\frac{\tau_w}{4ET_t} \frac{1}{W_t^3} \left(\begin{array}{l} (2W_t)x^4 \\ -(2L_e W_e + 8L_t W_t)x^3 \\ +L_t(3L_e W_e + 8L_t W_t)x^2 \end{array} \right)} \cdot \frac{\delta(x)^2}{2} \cdot dx \quad (A-33)$$

Replacing $\delta(x)$ using (A-31) gives the following equation,

$$W_{PE}^* = \frac{\frac{1}{2} \cdot ET_t \cdot \frac{1}{W_t^3} \cdot \delta(L_t)^2}{(L_e W_e) \left(1 + 2 \frac{L_t W_t}{L_e W_e} \right)^2 \left(\frac{L_t}{W_t} \right)^6} \int_0^{L_t} \left(\begin{array}{l} (2W_t)x^4 \\ -(2L_e W_e + 8L_t W_t)x^3 \\ +L_t(3L_e W_e + 8L_t W_t)x^2 \end{array} \right) \cdot \delta(x - L_t) \cdot dx \quad (A-34)$$

Evaluating the integral results in the contribution of potential energy from a point load given by,

$$W_{PE}^* = \frac{1}{2} \frac{ET_t}{\left(1 + 2 \frac{L_t W_t}{L_e W_e} \right)} \left(\frac{W_t}{L_t} \right)^3 \cdot \delta^2(L_t) \quad (A-35)$$

The contribution of the potential energy for a distributed load is given by,

$$W_{PE}^* = \int_0^{L_t} \int_0^{\delta(x)} Q \cdot d\delta(x) \cdot dx \quad (A-36)$$

Combining equations (A-25) and (A-36) results in the following double integral,

$$W_{PE}^* = \int_0^{L_t} \int_0^{\delta(x)} \tau_w W_t \cdot \left(\frac{\delta(x)}{\frac{\tau_w}{4ET_t} \frac{1}{W_t^3} \left(\begin{array}{l} (2W_t)x^4 \\ -(2L_e W_e + 8L_t W_t)x^3 \\ +L_t(3L_e W_e + 8L_t W_t)x^2 \end{array} \right)} \right) \cdot d\delta(x) \cdot dx. \quad (A-37)$$

This results in

$$W_{PE}^* = \int_0^{L_t} \tau_w W_t \cdot \left(\frac{1}{\frac{\tau_w}{4ET_t} \frac{1}{W_t^3} \left((2W_t)x^4 - (2L_e W_e + 8L_t W_t)x^3 \right) + L_t (3L_e W_e + 8L_t W_t)x^2} \right) \cdot \frac{\delta(x)^2}{2} \cdot dx. \quad (A-38)$$

Replacing $\delta(x)$ using (A-31) gives the following equation,

$$W_{PE}^* = \int_0^{L_t} \tau_w W_t \cdot \left(\frac{\frac{\tau_w}{4ET_t} \frac{1}{W_t^3} \left((2L_t W_t) \cdot x^4 - (2L_e W_e + 8L_t W_t) \cdot x^3 + L_t (3L_e W_e + 8L_t W_t) \cdot x^2 \right)}{\left(\frac{\tau_w L_e W_e}{4ET_t} \left(\frac{L_t}{W_t} \right)^3 \left(1 + 2 \frac{L_t W_t}{L_e W_e} \right) \right)^2} \right) \cdot \frac{\delta(L_t)^2}{2} \cdot dx \quad (A-39)$$

Evaluating the integral results in the contribution of potential energy from a distributed load given by,

$$W_{PE}^* = \frac{ET_t}{W_e L_e} \left(\frac{W_t^2}{L_t} \right)^2 \frac{\left(1 + \frac{32}{15} \frac{L_t W_t}{L_e W_e} \right)}{\left(1 + 2 \frac{L_t W_t}{L_e W_e} \right)^2} \cdot \delta^2(L_t). \quad (A-40)$$

Summing equations (A-35) and (A-40) results in the potential energy for a single tether,

$$W_{PE}^* = \frac{1}{2} ET_t \left(\frac{W_t}{L_t} \right)^3 \frac{\left(1 + 4 \frac{L_t W_t}{L_e W_e} + \frac{64}{15} \left(\frac{L_t W_t}{L_e W_e} \right)^2 \right)}{\left(1 + 2 \frac{L_t W_t}{L_e W_e} \right)^2} \cdot \delta^2(L_t). \quad (A-41)$$

For four tethers, the result is multiplied by 4,

$$W_{PE}^* = 2ET_t \left(\frac{W_t}{L_t} \right)^3 \frac{\left(1 + 4 \frac{L_t W_t}{L_e W_e} + \frac{64}{15} \left(\frac{L_t W_t}{L_e W_e} \right)^2 \right)}{\left(1 + 2 \frac{L_t W_t}{L_e W_e} \right)^2} \cdot \delta^2(L_t) \quad (A-42)$$

The potential energy of the system is set to the potential energy of the spring,

$$W_{PE_{actual}} = W_{PE_{spring}} \quad (A-43)$$

This results in the following equation,

$$2ET_t \left(\frac{W_t}{L_t} \right)^3 \frac{\left(1 + 4 \frac{L_t W_t}{L_e W_e} + \frac{64}{15} \left(\frac{L_t W_t}{L_e W_e} \right)^2 \right)}{\left(1 + 2 \frac{L_t W_t}{L_e W_e} \right)^2} \cdot \delta^2(L_t) = \frac{1}{2} \frac{1}{C_{me}} \cdot \delta^2(L_t) \quad (A-44)$$

The effective compliance is found to be,

$$C_{me} = \frac{1}{4ET_t} \left(\frac{L_t}{W_t} \right)^3 \frac{\left(1 + 2 \cdot \left(\frac{L_t W_t}{L_e W_e} \right) \right)^2}{\left(1 + 4 \left(\frac{L_t W_t}{L_e W_e} \right) + \frac{64}{15} \left(\frac{L_t W_t}{L_e W_e} \right)^2 \right)} \quad (A-45)$$

A.1.5 Effective Mass

The effective mass of the system is found by relating the kinetic co-energy of the beam to the kinetic co-energy of the lumped system given by,

$$W_{KE}^* = \int dW_{KE}^* = \int_0^f p df = \frac{1}{2} M_{me} f^2, \quad (A-46)$$

where p is momentum and f is a flow variable. The velocity, $u(x)$ is given by the derivative of the distance,

$$u(x) = j\omega \cdot \delta(x) \quad (A-47)$$

At the position of maximum deflection, $x = L_t$, the previous equation can be written as,

$$u(L_t) = j\omega \cdot \delta(L_t). \quad (\text{A-48})$$

The relation between $u(x)$ and $u(L_t)$ is given by,

$$u(x) = \frac{\delta(x)}{\delta(L_t)} u(L_t). \quad (\text{A-49})$$

Momentum is given by,

$$p = dm \cdot u(x) = \underbrace{\rho T_t W_t dx}_{dm} \cdot u(x). \quad (\text{A-50})$$

Hence, the derivative of momentum is given by,

$$dW_{KE}^* = \underbrace{\rho T_t W_t dx}_{dm} \cdot u(x) du(x). \quad (\text{A-51})$$

Substituting equation (A-51) into equation (A-46) yields

$$W_{KE}^* = \int dW_{KE}^* = \int_0^{L_t} \int_0^{u(x)} \rho T_t W_t u(x) du(x) dx. \quad (\text{A-52})$$

Integrate with respect to du to obtain,

$$W_{KE} = \int_0^{L_t} \underbrace{\rho T_t W_t}_{\int_0^{u(x)} \rho T_t W_t u(x) du(x)} \frac{u(x)^2}{2} dx \quad (\text{A-53})$$

Substitute equation (A-49) into equation (A-53) yields the following relation,

$$W_{KE} = \int_0^{L_t} \rho T_t W_t \frac{1}{2} \underbrace{\left(\frac{\delta(x)}{\delta(L_t)} u(L_t) \right)^2}_{u(x)} dx. \quad (\text{A-54})$$

The effective mass of a single tether M_{me}^* can be equated to equation

$$W_{KE} = \frac{1}{2} \rho T_t W_t \frac{u^2(L_t)}{\delta^2(L_t)} \int_0^{L_t} \delta^2(x) dx = \frac{1}{2} M_{me}^* \cdot u^2(L_t). \quad (A-55)$$

Simplifying the equation yields the effective mass for a single tether M_{me}^* ,

$$M_{me}^* = \frac{\rho T_t W_t}{\delta^2(L_t)} \int_0^{L_t} \delta^2(x) dx. \quad (A-56)$$

For 4 tethers, the effective mass for the total number of tethers M_{me} is found to be

$$M_{me} = 4M_{me}^* = 4 \underbrace{\frac{\rho W_t T_t}{\delta^2(L_t)} \int_0^{L_t} \delta^2(x) dx}_{M_{me1}}. \quad (A-57)$$

Using equation (A-27) and (A-28), substituting $\delta(x)$ and $\delta(L_t)$ respectively into equation (A-57) results in,

$$M_{me} = \frac{4\rho T_t W_t}{\left(\frac{\tau_w L_e W_e}{4ET_t W_t^3} \left(1 + 2 \frac{W_e L_e}{W_t L_t} \right) \right)^2} \int_0^{L_t} \underbrace{\left(\frac{\tau_w}{4ET_t W_t^3} \left((2W_t)x^4 - (2W_e L_e)x^3 \right) + (3W_e L_e + 8W_t L_t)x^2 \right)}_{\delta(x)} dx. \quad (A-58)$$

Evaluating the integral results in

$$M_{me} = \frac{4\rho T_t W_t}{\left(\frac{\tau_w L_e W_e}{4ET_t W_t^3} \left(1 + 2 \frac{W_e L_e}{W_t L_t} \right) \right)^2} \cdot \underbrace{\left(\frac{1}{5040} \frac{\tau_w^2 L_t^7}{E^2 T_t^2} \frac{(W_e L_e)^2}{W_t^6} \left(117 + 489 \left(\frac{W_t L_t}{W_e L_e} \right) \right) + 512 \left(\frac{W_t L_t}{W_e L_e} \right)^2 \right)}_{\int_0^{L_t} \left(\frac{\tau_w}{4ET_t W_t^3} \left((2W_t)x^4 - (2W_e L_e)x^3 \right) + (3W_e L_e + 8W_t L_t)x^2 \right) dx}. \quad (A-59)$$

Simplifying the equation results in the effective mass for all four tethers,

$$M_{me} = \frac{4}{315} \frac{\rho T_t W_t L_t}{\left(1 + 2 \frac{W_t L_t}{W_e L_e} \right)^2} \left(117 + 489 \left(\frac{W_t L_t}{W_e L_e} \right) + 512 \left(\frac{W_t L_t}{W_e L_e} \right)^2 \right). \quad (A-60)$$

The total effective mass M_{me} is equal to the sum of the effective mass of the tethers and the mass of the floating element and is given by,

$$M_{me} = \underbrace{\frac{4}{315} \frac{\rho T_t W_t L_t}{\left(1 + 2 \frac{W_t L_t}{W_e L_e}\right)^2} \left(117 + 489 \left(\frac{W_t L_t}{W_e L_e}\right) + 512 \left(\frac{W_t L_t}{W_e L_e}\right)^2\right)}_{M_{me}} + \underbrace{\rho T_e W_e L_e}_{M_{element}}. \quad (\text{A-61})$$

If the thickness of the tethers is equal to the thickness of the floating element, the total effective mass M_{me} is given by,

$$M_{me} = \frac{\rho \cdot T}{(W_e L_e + 2W_t L_t)^2} \left[\begin{aligned} & (W_e L_e)^3 + \frac{192}{35} (W_e L_e)^2 (W_t L_t) \\ & + \frac{1072}{105} (W_t L_t)^2 (W_e L_e) + \frac{2048}{315} (W_t L_t)^3 \end{aligned} \right]. \quad (\text{A-62})$$

A.2 Deflection Analysis for Trapezoidal Tethers

For the case where the tethers are trapezoidal and not rectangular such that the width of the tether on the top is not equal to the width of the tethers on the bottom ($W_t \neq W_b$), a set of equations for the linear deflection, effective compliance and effective mass are derived similarly to the rectangular tether case. The moment of inertia of a rectangle is replaced by the moment of inertia for a trapezoid and is given by,

$$I_{yc} = \frac{h(a+b)(a^2 + b^2)}{48} = \frac{T_t (W_b + W_t)(W_b^2 + W_t^2)}{48}. \quad (\text{A-63})$$

The deflection equation (A-27) derived for a generalized moment of inertia is given by,

$$\delta(x) = \frac{\tau_w}{24EI_{yc}} \left(\frac{x^2}{2} \right) \left(2W_t \cdot x^2 - (8W_t L_t + 2W_e L_e) \cdot x + (8W_t L_t + 3W_e L_e) L_t \right), \quad (\text{A-64})$$

where I_{yc} is the generalized moment of inertia. Likewise, the the Euler-Bernoulli equation for a generalized moment of inertia is,

$$\delta = \tau_w \frac{L_e W_e L_t^3}{48 E_t \cdot I_{yc}} \left(1 + 2 \frac{L_t W_t}{L_e W_e} \right) \quad (A-65)$$

Combining equations (A-63) and (A-65) yields a deflection equation for trapezoidal tethers and is given by,

$$\delta(L_t) = \frac{\tau_w}{E} \frac{L_t^3 W_e L_e \left(1 + 2 \frac{W_t L_t}{W_e L_e} \right)}{T_t (W_b + W_t) (W_b^2 + W_t^2)}. \quad (A-66)$$

A similar analysis is performed to obtain the effective compliance and effective mass for a generalized moment of inertia. The effective compliance and mass are given by,

$$C_{me} = \frac{L_t^3}{48 E_t \cdot I_{yc}} \frac{\left(1 + 2 \cdot \left(\frac{W_t L_t}{W_e L_e} \right) \right)^2}{\left(1 + 4 \left(\frac{W_t L_t}{W_e L_e} \right) + \frac{64}{15} \left(\frac{W_t L_t}{W_e L_e} \right)^2 \right)} \quad (A-67)$$

and

$$M_{me \text{ Trapezoid}} = \underbrace{\rho T_e (W_e L_e)}_{M_{\text{element}}} + I_{yc} \underbrace{12 \rho (W_e L_e) \frac{\left(\frac{2048}{315} \left(\frac{L_t}{W_e L_e} \right)^3 + \frac{652}{105} \frac{1}{W_t} \left(\frac{L_t}{W_e L_e} \right)^2 + \frac{52}{35} \frac{1}{W_t^2} \left(\frac{L_t}{W_e L_e} \right) \right)}_{M_{\text{tethers_effective}} \left(1 + 2 \frac{W_t L_t}{W_e L_e} \right)^2}. \quad (A-68)$$

Equations (A-63), (A-67) and (A-68) are combined to obtain the effective compliance mass and compliance for a trapezoid.

A.3 Equations for Out of Plane Deflection

Performing a similar analysis, the deflection equation, effective mass and effective compliance of the floating element and tethers due to the out-of-plane loading pressure are derived and is illustrated in Figure A-2.

The point load due to pressure is given by,

$$P_p = \frac{PL_e T_e}{2}, \quad (\text{A-69})$$

and the distributed load due to pressure is given by,

$$Q_p = PT_t. \quad (\text{A-70})$$

The combined point load and distributed load due to pressure is given by,

$$\delta(x) = \underbrace{\frac{P}{24EI} x^2 (3L_t - 2x)}_{\text{point load}} + \underbrace{\frac{1}{24} \frac{Q(x)}{EI} x^2 (x - 2L_t)^2}_{\text{distributed load}}. \quad (\text{A-71})$$

The moment of inertia for rectangular tethers in the pressure direction is,

$$I = \frac{1}{12} bh^3 = \frac{1}{12} W_t T_t^3, \quad (\text{A-72})$$

whereas the moment of inertia for trapezoidal tethers is,

$$I_{xc} = \frac{h^3 (a^2 + 4ab + b^2)}{36(ab)} = \frac{(T_t)^3 (W_b^2 + 4W_b W_t + W_t^2)}{36W_b W_t}. \quad (\text{A-73})$$

A generalized effective compliance due to pressure is given by,

$$C_{me} = \frac{5L_t^3 (2L_t + L_e)^2}{8EI_{xc} (15L_e^2 + 60L_e L_t + 16L_t^2)}, \quad (\text{A-74})$$

and a generalized effective mass due to pressure is given by,

$$M_{me} = \rho T_t \left(\frac{4}{315} \frac{(512L_t^2 + 489L_eL_t + 117L_e^2)}{(2L_t + L_e)^2} W_t L_t + W_e L_e \right). \quad (\text{A-75})$$

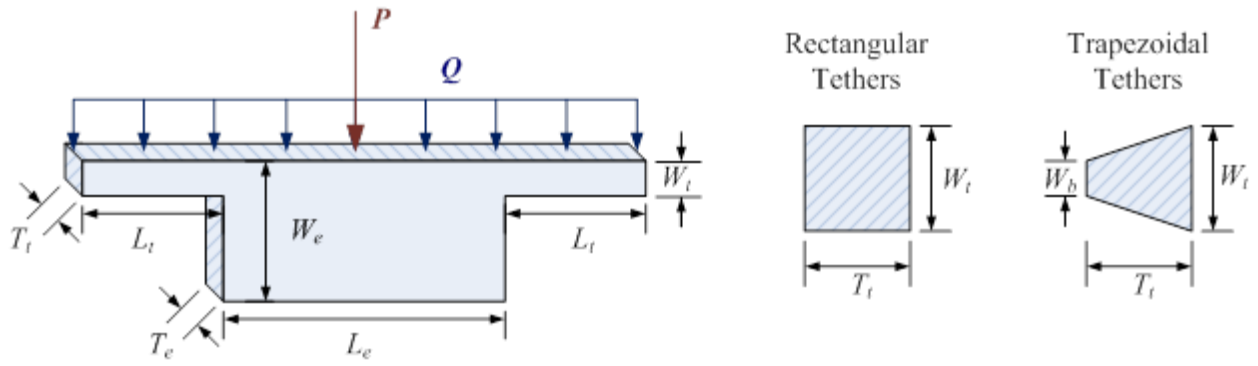


Figure A-1. Illustration of point and distributed forces for in-plane (shear stress) deflection.

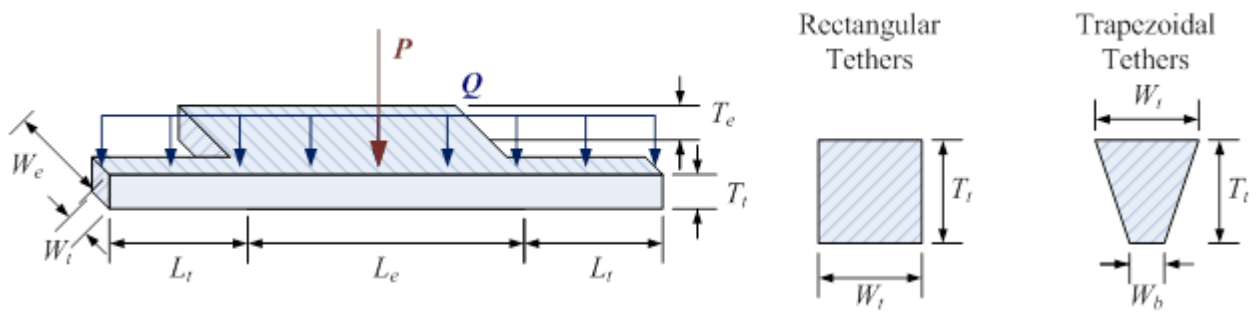


Figure A-2. Illustration of point and distributed forces for out-of-plane (pressure) deflection.

APPENDIX B MICROFABRICATION PROCESS TRAVELER

Wafers

- 1) SOI wafer diameter of 100 ± 0.1 mm, p-type $\langle 1-0-0 \rangle$, 100 ± 0.1 μm thick device layer with resistivity of $0.01-0.02$ $\Omega\text{-cm}$, 1 μm BOX layer, and a 500 ± 0.1 μm thick handle layer resistivity of $1-20$ $\Omega\text{-cm}$.
- 2) Corning 7740 Pyrex wafer of 100 mm, 500 μm thickness.

Masks

- 1) Cavity Mask
- 2) SOI Gratings Mask
- 3) Pyrex Gratings Mask
- 4) Tethers and Floating Element Release Mask

Microfabrication Steps

- 1) Cavity Etch
 - a. Photoresist on device layer of SOI
 - i. Equipment: Karl Suss RC8
 - ii. Materials: Shipley 1813
 - iii. Recipe: Ramp 1000 rpm/s, Spin 4000 rpm, Duration 50 s
 - b. Soft Bake
 - i. Equipment: Hotplate
 - c. Expose Cavity Etch Mask
 - i. Equipment: Karl Suss MA6 TSA
 - ii. Recipe: Intensity 10 mW/cm², wavelength 365 nm, expose time 2 s, vacuum Contact
 - d. Develop photoresist
 - i. Materials: AZ MF300
 - ii. Recipe: Develop for 55 seconds
 - e. Hard Bake
 - i. Equipment: Hotplate
 - ii. Recipe: Duration 90 seconds
 - f. DRIE etch 2 μm on device layer of SOI
 - i. Equipment: STS AOE
 - ii. Default STS etch recipe at the Georgia Institute of Technology
- 2) Gratings Deposition on SOI device layer
 - a. Sputter 0.25 μm Aluminum on SOI
 - i. Equipment: PVD75 RF Sputterer
 - ii. Material: Aluminum
 - iii. Default sputter recipe at the Georgia Institute of Technology
 - b. Photoresist on device layer of SOI
 - i. Equipment: Karl Suss RC8
 - ii. Materials: Shipley 1813
 - iii. Recipe: Ramp 1000 rpm/s, Spin 4000 rpm, Duration 50 s

- c. Soft Bake
 - i. Equipment: Hotplate
 - d. Expose SOI Gratings Mask
 - i. Equipment: Karl Suss MA6 TSA
 - ii. Recipe: Intensity 10 mW/cm², wavelength 365 nm, expose time 6 s, vacuum Contact
 - e. Develop photoresist
 - i. Materials: AZ MF300
 - ii. Recipe: Develop for 55 seconds
 - f. Hard Bake
 - i. Equipment: Hotplate
 - g. Aluminum Etch
 - i. Materials: Transene Type A
 - ii. Recipe: Temperature 45~60C, Duration 10 seconds
- 3) Gratings Deposition on Pyrex
- a. Sputter 0.25 μ m Aluminum on Pyrex
 - i. Equipment: PVD75 RF Sputterer
 - ii. Material: Aluminum
 - iii. Default sputter recipe at the Georgia Institute of Technology
 - b. Photoresist on Pyrex
 - i. Equipment: Karl Suss RC8
 - ii. Materials: Shipley 1813
 - iii. Recipe: Ramp 1000 rpm/s, Spin 4000 rpm, Duration 50 s
 - c. Soft Bake
 - i. Equipment: Hotplate
 - d. Expose SOI Gratings Mask
 - i. Equipment: Karl Suss MA6 TSA
 - ii. Recipe: Intensity 10 mW/cm², wavelength 365 nm, expose time 2 s, vacuum Contact
 - e. Develop photoresist
 - i. Materials: AZ MF300
 - ii. Recipe: Develop for 55 seconds
 - f. Hard Bake
 - i. Equipment: Hotplate
 - g. Aluminum Etch
 - i. Materials: Transene Type A
 - ii. Recipe: Temperature 45~60C, Duration 10 seconds
- 4) Anodic Bond
- a. SOI to Pyrex alignment
 - i. Equipment: Karl Suss Front-to-Back Mask Aligner
 - b. Anodic Bond
 - i. Equipment: Karl Suss SB6 Substrate/Wafer Bonder

- ii. Recipe: Temperature 400C, force 1837 mbar, apply -750V for 4 minutes, apply -1500V for 15 minutes, no vacuum.
- 5) SOI Handle Wafer KOH Etch
 - a. Protect Pyrex wafer
 - i. Equipment: Hotplate
 - ii. Material: Carnauba Wax, Strahl & Pitsch Inc., SP 200, Batch #22903
 - iii. Recipe: Minimum temperature of 85C
 - b. KOH Etch
 - i. Equipment: Microtemp Model C15 Modutek Corp, waferboat
 - ii. Material: J. T. Baker KOH 45% solution
 - iii. Recipe: Temperature 70C, Si etch rate ~ 31 $\mu\text{m/hr}$ (predicted)
 - c. Piranha Etch
 - d. Etch Stop Removal
 - i. Materials: BOE
- 6) Front-to-Back Alignment
 - a. Photoresist on device layer of SOI
 - i. Equipment: Karl Suss RC8
 - ii. Materials: Shipley 1827
 - iii. Recipe: Ramp 500 rpm/s, Spin 4000 rpm, Duration 30 s
 - b. Soft Bake
 - i. Equipment: Hotplate
 - ii. Recipe: Temperature 115C, duration 90 s
 - c. Expose Cavity Etch Mask
 - i. Equipment: Karl Suss MA6 BSA backside aligner
 - ii. Recipe: Intensity 20 mW/cm², expose time 18 s
 - d. Develop photoresist
 - i. Materials: AZ MF319
 - ii. Recipe: Develop for 60 seconds
 - e. Hard Bake
 - i. Equipment: Hotplate
 - ii. Recipe: Duration 5 seconds
- 7) Tethers and Floating Element Release
 - a. DRIE
 - i. Equipment: Deep RIE STS
 - ii. Recipe: Etch Cycle 12 s, Passivation Cycle 7 s
 - b. Dry photoresist removal
 - i. Equipment: Plasma Asher Anatech Barrel SCE600
 - ii. Recipe: Duration 25 min
- 8) Device release
 - a. Dice wafer
 - i. Equipment: Dicing Saw

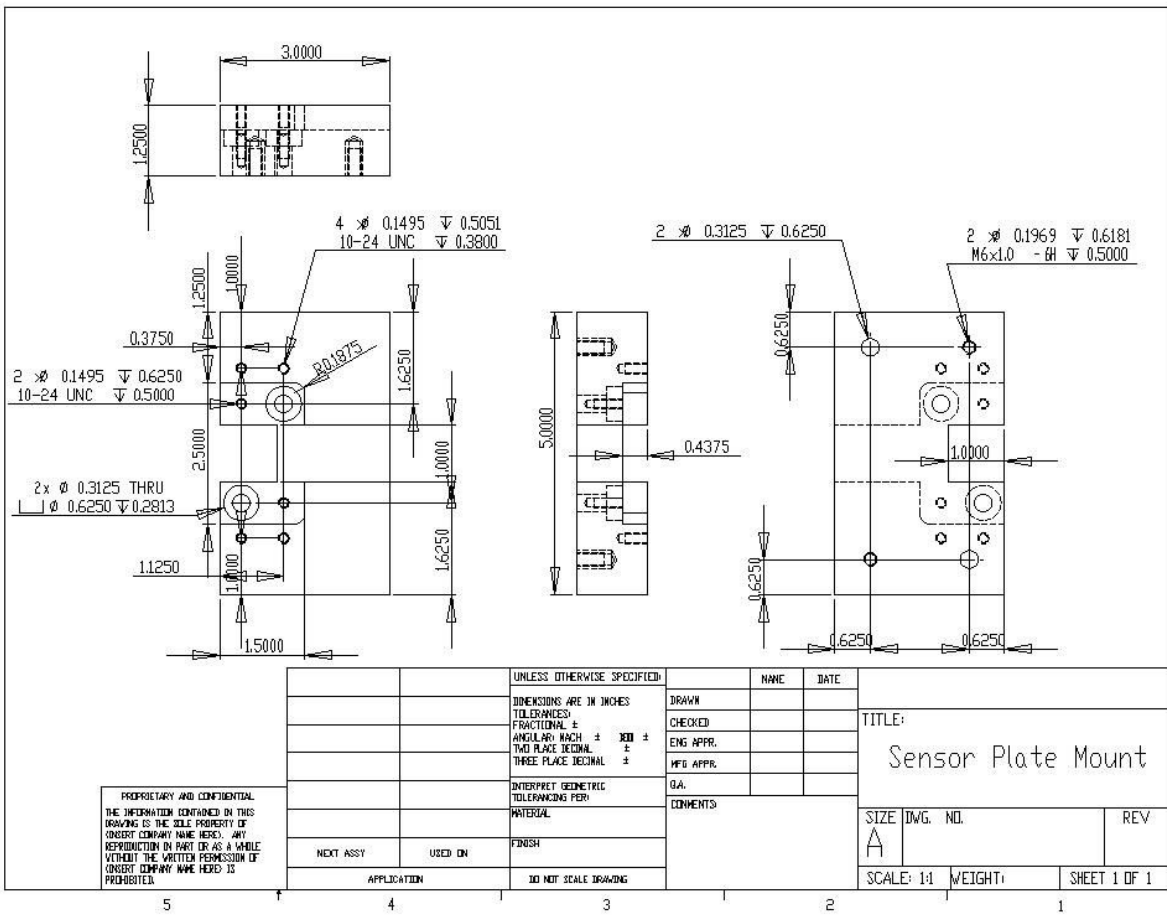


Figure C-2. Schematic of the mount for securing the sensor plates of the optical testbed.

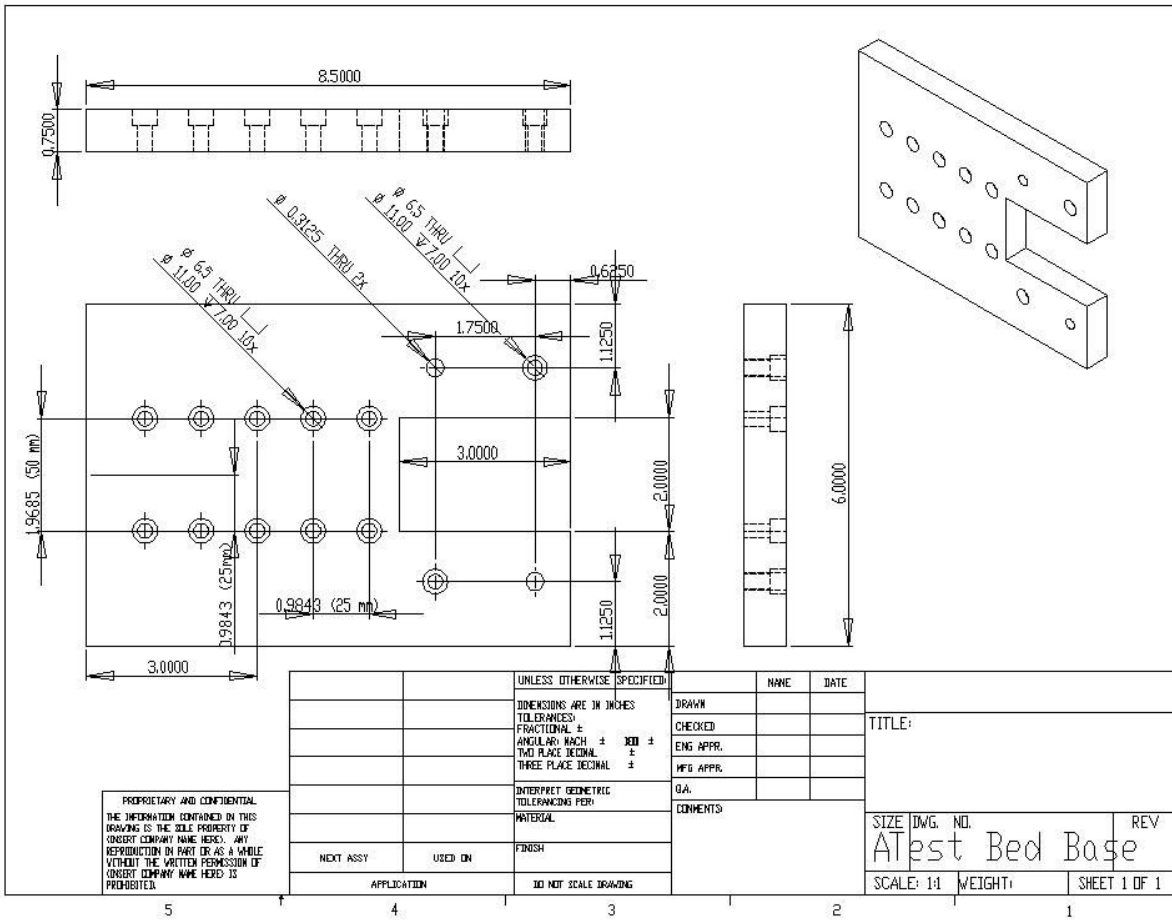


Figure C-3. Schematic of the base structure of the optical testbed.

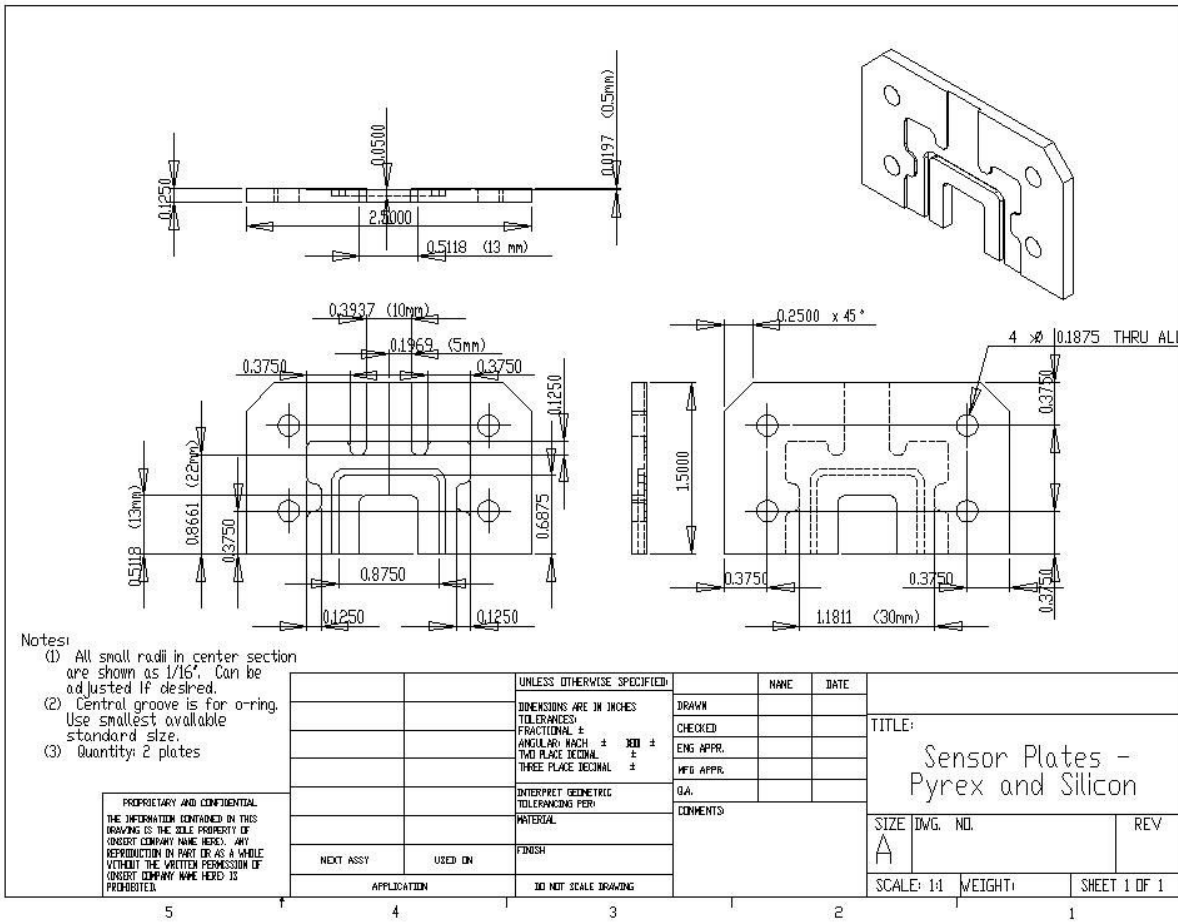


Figure C-4. Schematic of the sensor plates for securing the silicon and Pyrex test structures.

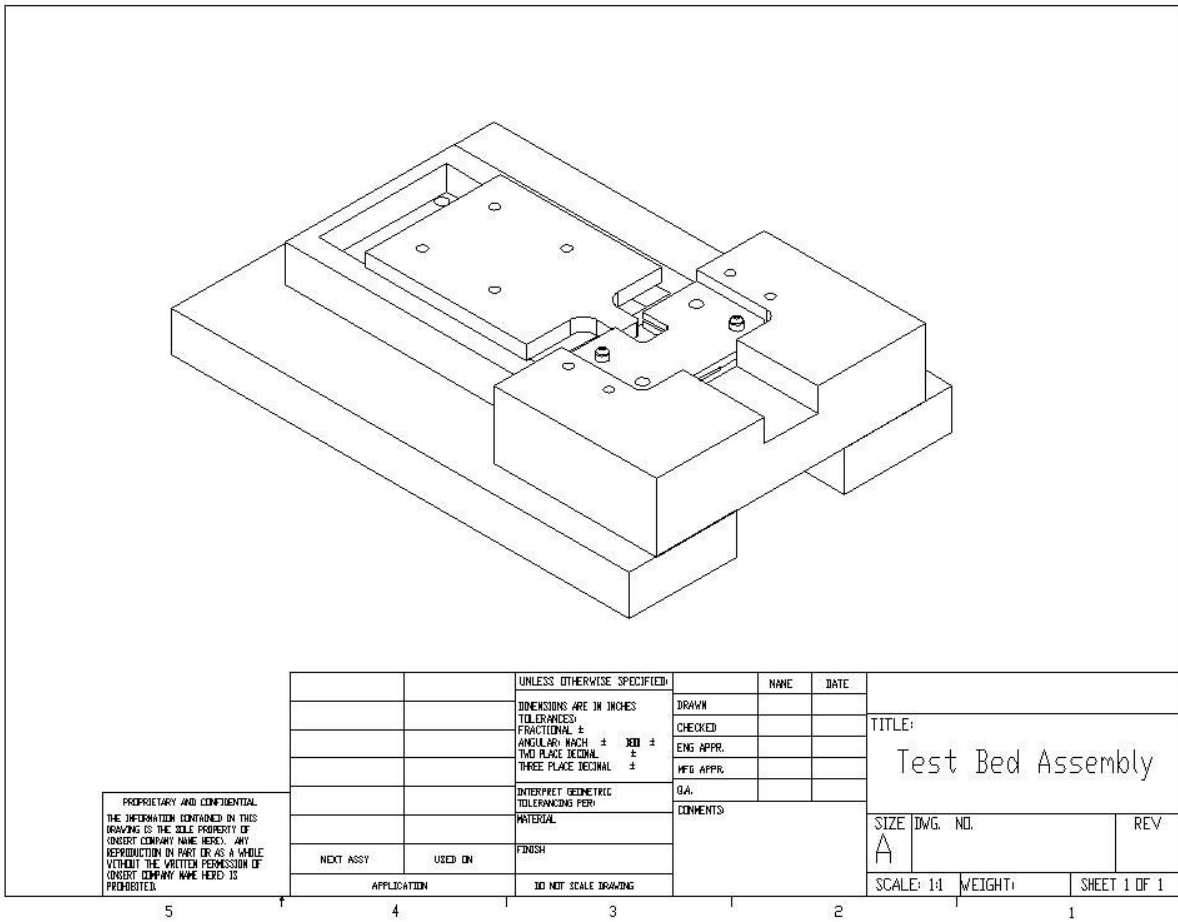


Figure C-5. Overall schematic for the optical testbed.

LIST OF REFERENCES

- [1] S. B. Horowitz et al., "A micromachined geometric Moire interferometric floating-element shear stress sensor," *AIAA Aerospace Sciences Meeting*, no. 42nd. Reno, NV, 2004.
- [2] D. Bushnell, "Turbulent drag reduction for external flows," in *21st AIAA Aerospace Sciences Meeting*, 1983.
- [3] J. Naughton and M. Sheplak, "Modern Developments in Shear-Stress Measurement," *Progress in Aerospace Sciences*, vol. 38, no. 6–7, pp. 515-570, 2002.
- [4] M. Gad-el-Hak, *Flow control: passive, active, and reactive flow management*, 1st ed. Cambridge University Press, 2000, p. 421.
- [5] L. Lofdahl and M. Gad-el-Hak, "MEMS-based pressure and shear stress sensors for turbulent flows," *Measurement Science and Technology*, vol. 10, pp. 665-686, 1999.
- [6] S. Zhong, "Detection of flow separation and reattachment using shear-sensitive liquid crystals," *Experiments in Fluids*, vol. 32, no. 6, pp. 667–673, 2002.
- [7] X.-Q. Wang et al., "A fully integrated shear-stress sensor," in *Proc. of Transducers 99*, 1999, pp. 1074–7.
- [8] F. Jiang, G.-B. Lee, Y.-C. Tai, and C.-M. Ho, "A flexible micromachine-based shear-stress sensor array and its application to separation-point detection," *Sensors and Actuators*, vol. 79, no. 3, pp. 194–203, 2000.
- [9] C. Cheng et al., "The role of shear stress in atherosclerosis," *Cell Biochemistry and Biophysics*, vol. 41, no. 2, pp. 279-294, 2004.
- [10] M. Grigoni, C. Daniele, G. D'Avenio, and G. Pontrelli, "The role of wall shear stress in unsteady vascular dynamics," *Progress in Biomedical Research*, vol. 7, no. 3, pp. 204-212, 2002.
- [11] A. Etebari, "Recent Innovations in Wall Shear Stress Sensor Technologies," *Recent Patents on Mechanical Engineering*, vol. 1. Bentham Science Publishers Ltd., pp. 22-28, 2008.
- [12] J. A. Schetz, "Direct measurement of skin friction in complex flows," *48th AIAA Aerospace Sciences Meeting Including the New Horizons Forum and Aerospace Exposition*. Orlando, FL, 2010.

- [13] J. Wilson and J. Hawkes, *Optoelectronics, an introduction*, 3rd ed. London: Prentice Hall Europe, 1998, pp. 293-395.
- [14] R. Ramaswami, "Optical fiber communication: from transmission to networking," *IEEE Communications Magazine*, pp. 138-147, 2002.
- [15] E. Udd, *Fiber optic sensors: an introduction for engineers and scientists*. New Jersey: Wiley-Interscience, 2006, pp. 1-24,69-97.
- [16] C. Podmore and D. Faguy, "The challenge of optical fibres," *Telecommunications Policy*, vol. 10, no. 4, pp. 341-351, 1986.
- [17] D. Grobncic, S. J. Mihailov, C. W. Smelser, and H. Ding, "Sapphire Fiber Bragg Grating Sensor Made Using Femtosecond Laser Radiation for Ultrahigh Temperature Applications," *IEEE Photonics Technology Letters*, vol. 16, no. 11, pp. 2505-2507, Nov. 2004.
- [18] S. Khaliq, S. W. James, and R. P. Tatam, "Fiber-optic liquid-level sensor using a long-period grating," *Optics Letters*, vol. 26, no. 16, pp. 1224-1226, 2001.
- [19] R. Zhang and F. G. Shi, "A Novel Algorithm for Fiber-Optic Alignment Automation," *IEEE Transactions on Advanced Packaging*, vol. 27, no. 1, pp. 173-178, Feb. 2004.
- [20] K. V. S. S. Sairam, *Optical Communications*. Laxmi Publications, 2008, p. 10.
- [21] R. W. Fox and A. T. McDonald, *Introduction to Fluid Mechanics Fifth Edition*. John Wiley & Sons, Inc, 1998, pp. 26,345-354.
- [22] D. Halliday, R. Resnick, and J. Walker, *Fundamentals of physics: extended*, 5th ed. John Wiley & Sons, 1996, pp. 309-311.
- [23] R. L. Panton, *Incompressible Flow*, 2nd ed. New York: John Wiley & Sons, 1996.
- [24] F. M. White, *Viscous fluid flow*, 2nd ed. New York: McGraw-Hill, 1991.
- [25] H. Tennekes and J. L. Lumley, *A first course in turbulence*. Cambridge, MA: MIT Press, 1972, pp. 17,22,158-160.
- [26] N. Hutchins, T. B. Nickels, I. Marusic, and M. S. Chong, "Hot-wire spatial resolution issues in wall-bounded turbulence," *Journal of Fluid Mechanics*, vol. 635, no. 2009, pp. 103-136, Sep. 2009.
- [27] R. W. Johnson, *The handbook of fluid dynamics*. Boca Raton, FL: Springer-Verlag, 1998.

- [28] J. H. Haritonidis, "The measurement of wall shear stress," *Advances in fluid mechanics measurements*, pp. 229-261, 1989.
- [29] M. Gad-el-Hak, "Compliant coatings: a decade of progress," *Applied Mechanics Reviews*, vol. 49, no. 10S, p. 11, 1996.
- [30] Z. W. Hu, C. L. Morfey, and N. D. Sandham, "Wall pressure and shear stress spectra from direct simulations of channel flow," *AIAA*, vol. 44, no. 7, pp. 1541-1549, 2006.
- [31] H. Schlichting, K. Gersten, and K. Gersten, *Boundary-layer theory 8th edition*. Berlin: Springer, 2000, p. 801.
- [32] M. Sheplak, L. Cattafesta, T. Nishida, and C. B. McGinley, "MEMS Shear Stress Sensors: Promise and Progress," in *AIAA*, 2004.
- [33] K. G. Winter, "An outline of the techniques available for the measurements of skin friction in turbulent boundary layers," *Progress in Aerospace Sciences*, vol. 18, no. 1, pp. 1-57, 1977.
- [34] M. Schrober, E. Obermeier, S. Pirskawetz, and H.-H. Fernholz, "A MEMS skin-friction sensor for time resolved measurements in separated flows," *Experiments in Fluids*, vol. 36, no. 4, pp. 593-599, 2004.
- [35] B. W. Van Oudheusden, "Silicon thermal flow sensors," *Sensors and Actuators*, vol. 30, pp. 5-26, 1992.
- [36] B. W. Van Oudheusden and J. H. Huijsing, "Integrated flow friction sensor," *Sensors and Actuators*, vol. 15, no. 2, pp. 135-144, 1988.
- [37] F. K. Jiang et al., "A surface-micromachined shear-stress imager," in *IEEE MEMS Workshop (MEMS '96)*, 1996, pp. 110-115.
- [38] E. Kalvesten, C. Vieider, L. Lofdahl, and G. Stemme, "An integrated pressure-flow sensor for correlation measurements in turbulent gas flows," in *Sensors and Actuators A*, 1996, vol. 52, pp. 51-58.
- [39] M. Sheplak, V. Chandrasekaran, A. Cain, T. Nishida, and L. Cattafesta, "Characterization of a Micromachined Thermal Shear Stress Sensor," *AIAA J.*, vol. 40, no. 6, pp. 1099-1104, 2002.
- [40] A. A. Naqwi, W. C. Reynolds, and L. W. Carr, "Dual cylindrical wave laser-Doppler method for measurement of wall shear stress," in *Laser Anemometry in Fluid Mechanics*, D. F. G. Durão, F. Durst, H. Mishima, and J. H. Whitelaw, Eds. Lisbon, Portugal: LADOAN—Instituto Superior Técnico, 1984, pp. 105–122.

- [41] D. Fourquette, D. Modarress, D. Wilson, M. Koochesfahani, and M. Gharib, "An optical MEMS-based shear stress sensor for high reynolds number applications," in *41st AIAA Aerospace Sciences Meeting & Exhibit*, 2003.
- [42] S. Große and W. Schröder, "Mean wall-shear stress measurements using the micro-pillar shear-stress sensor MPS3," *Measurement Science and Technology*, vol. 19, no. 1, 2008.
- [43] J. W. Crafton, S. D. Fonov, E. G. Jones, L. P. Goss, R. A. Forlines, and A. Fontaine, "Measurements of skin friction in water using surface stress sensitive films," *Measurement Science and Technology*, vol. 19, no. 7, p. 10, 2008.
- [44] A. Etebari, B. Akle, K. Farinholt, M. Bennett, D. J. Leo, and P. P. Vlachos, "The use of active ionic polymers in dynamic skin friction measurements," in *ASME Heat Transfer/Fluids Engineering Summer Conference*, 2004, vol. 1, pp. 667-675.
- [45] J. M. Allen, "Improved sensing element for skin-friction balance measurements," *AIAA*, vol. 18, no. 11, pp. 1342-1345, 1980.
- [46] M. A. Schmidt, R. T. Howe, S. D. Senturia, and J. H. Haritonidis, "Design and calibration of a microfabricated floating-element shear-stress sensor," *IEEE Tr. on Elect. Dev.*, vol. 35, no. 6, pp. 750-757, 1988.
- [47] W. J. Pulliam, J. A. Schetz, M. E. Jones, and K. A. Murphy, "Fiber optic pressure/skin friction gage for supersonic flow applications," *IEEE*, pp. 355-361, 2002.
- [48] D. J. DeTurris, J. A. Schetz, and R. F. Hellbaum, "Direct measurement of skin friction in a scramjet combustor," *AIAA*. Orlando, FL, 1990.
- [49] M. A. Schmidt, "Microsensors for the measurement shear forces in turbulent boundary layers," MIT, 1988.
- [50] T. Pan, D. Hyman, M. Mehregany, E. Reshotko, and S. Garverick, "Microfabricated shear stress sensors, Part 1: Design and fabrication," *AIAA J.*, vol. 37, pp. 66-72, 1999.
- [51] D. Hyman, T. Pan, E. Reshotko, and M. Mehregany, "Microfabricated shear stress sensors, Part 2: Testing and calibration," *AIAA J.*, vol. 37, no. 1, pp. 73-8, 1999.
- [52] J. Zhe, V. Modi, and K. R. Farmer Jr., "A microfabricated wall shear-stress sensor with capacitive sensing," *J. Microelectromech. Syst.*, vol. 14, pp. 167-175, 2005.

- [53] V. Chandrasekharan, J. Sells, D. P. Arnold, and M. Sheplak, "Characterization of a MEMS-based floating element shear stress sensor," in *47th AIAA Aerospace Sciences Meeting and Exhibit*, 2009.
- [54] V. Chandrasekharan, J. Sells, J. Meloy, D. P. Arnold, and M. Sheplak, "A metal-on-silicon differential capacitive shear stress sensor," in *Transducers*, 2009, pp. 1537-1540.
- [55] J. Sells, V. Chandrasekharan, J. Meloy, M. Sheplak, H. Zmuda, and D. P. Arnold, "Microfabricated silicon-on-Pyrex passive wireless wall shear stress sensor," in *2011 IEEE SENSORS Proceedings*, 2011, pp. 77-80.
- [56] J. Meloy, J. Griffin, J. Sells, V. Chandrasekharan, L. N. Cattafesta, and M. Sheplak, "Experimental Verification of a MEMS Based Skin Friction Sensor for Quantitative Wall Shear Stress Measurement," in *41st AIAA Fluid Dynamics Conference and Exhibit*, 2011, no. June, pp. 1-18.
- [57] K. Ng, J. Shajii, and M. A. Schmidt, "A liquid shear-stress sensor fabricated using wafer-bonding technology," *IEEE Transducers '91*. San Francisco, CA, pp. 931-934, 1991.
- [58] H. D. Goldberg, K. S. Breuer, and M. A. Schmidt, "A Silicon Wafer-Bonding Technology for Microfabricated Shear-Stress Sensors with Backside Contacts," in *Solid-State Sensor and Actuator Workshop*, 1994, pp. 111-115.
- [59] A. Barlian, S. J. Park, V. Mukundan, and B. Pruitt, "Design and characterization of microfabricated piezoelectric floating element-based shear stress sensors," in *Sensors Actuators*, 2007, vol. 134, pp. 77-87.
- [60] Y. Li, V. Chandrasekharan, B. Bertolucci, T. Nishida, L. Cattafesta, and M. Sheplak, "A MEMS shear stress sensor for turbulence measurements," *46th AIAA Aerospace Sciences Meeting and Exhibit*. Reno, NV, 2008.
- [61] A. Padmanabhan, H. D. Goldberg, M. A. Schmidt, and K. S. Breuer, "A Wafer-Bonded Floating-Element Shear-Stress Microsensor with Optical Position Sensing by Photodiodes," *Journal of Microelectromechanical Systems*, vol. 5, no. 4, pp. 307-315, 1996.
- [62] F.-G. Tseng and C.-J. Lin, "Polymer MEMS-based Fabry-Perot shear stress sensor," *IEEE Sensors Journal*, vol. 3, no. 6, pp. 812-817, 2003.
- [63] S. Horowitz et al., "A wafer-bonded, floating element shear-stress sensor using a geometric Moiré optical transduction technique," in *Transducers 2004*, 2004, pp. 13-18.

- [64] U. K. Ayaz, T. Ioppolo, and M. V. Ötügen, "Wall shear stress sensor based on the optical resonances of dielectric microspheres," *Measurement Science and Technology*, vol. 22, no. 7, p. 075203, Jul. 2011.
- [65] C. Liu et al., "A micromachined flow shear-stress sensor based on thermal transfer principles," *J.MEMS*, vol. 8, pp. 90-99, 1999.
- [66] E. Kalvesten, "Pressure and Wall Shear Stress Sensors for Turbulence Measurements," Royal Institute of Technology, 1996.
- [67] D. Modarress, D. Fourquette, F. Taugwalder, M. Koochesfahani, M. Gharib, and D. W. Wilson, "Diffractive optic fluid shear stress sensor," *Diffractive Optics and Micro-Optics Topical Meeting*. Quebec City, Quebec, Canada , p. 2, 2000.
- [68] J. Sells, "Passive Wireless Wall Shear Stress Sensors," University of Florida, 2011.
- [69] Y. Li, M. Papila, T. Nishida, L. Cattafesta, and M. Sheplak, "Modeling and optimization of a side-implanted piezoresistive shear stress sensor," in *SPIE*, 2006.
- [70] V. Chandrasekharan, J. Sells, D. P. Arnold, and M. Sheplak, "Effect of dynamic pressure on direct shear stress sensor design," *AIAA Aerospace Sciences Meeting Including the New Horizons Forum and Aerospace Exposition*. Orlando, FL, 2010.
- [71] S. D. Senturia, *Microsystems Design*. Springer, 2001, pp. 191-196,364.
- [72] W. A. Brantley, "Calculated elastic constants for stress problems associated with semiconductor devices," *Journal of Applied Physics*, vol. 44, pp. 534-535, 1973.
- [73] J. Meloy, "An Instrumentation-Grade Differential Capacitive MEMS Shear Stress Sensor System for Wind Tunnel Applications," University of Florida, 2012.
- [74] N. Bilaniuk, "Optical microphone transduction techniques," *Applied Acoustics*, vol. 50, no. 1, pp. 35-63, 1997.
- [75] S. Arnold, M. Khoshsima, I. Teraoka, S. Holler, and F. Vollmer, "Shift of whispering-gallery modes in microspheres by protein adsorption.," *Optics letters*, vol. 28, no. 4, pp. 272-4, Feb. 2003.
- [76] M. D. Todd Johnson, G. A., and Chang, C. C., "Passive, light intensity-independent interferometric method for fibre Bragg grating interrogation," *Electronics Letters*, vol. 35, no. 22, pp. 1970-1971, 1999.
- [77] D. Post, B. Han, and P. Ifju, *High Sensitivity Moiré*. NY: Springer, 1994.

- [78] J. T. M. Stevenson and J. R. Jordan, "Metrological gratings and moiré fringe detection methods for displacement transducers," *Physical Science, Measurement and Instrumentation, Management and Education, IEE Proceedings A*, vol. 136, no. 5, pp. 243–253, 1989.
- [79] I. Amidror, *The Theory of the Moiré Phenomenon*, 2nd ed., no. 38. Kluwer, Dordrecht, The Netherlands: Springer, 2009, pp. 21-23.
- [80] K. Creath and J. C. Wyant, "Moiré and fringe projection techniques," in *Optical Shop Testing*, D. Malacara, Ed. Wiley, 1992, pp. 653-686.
- [81] "Optical Properties of Silicon,
<http://www.virginiasemi.com/pdf/Optical%20Properties%20of%20Silicon71502.pdf>
." [Online]. Available: <http://www.virginiasemi.com/pdf/Optical Properties of Silicon71502.pdf>.
- [82] J. Bartl and M. Baranek, "Emissivity of aluminium and its importance for radiometric measurement, measurement of physical quantities," *Journal of the Institute of Measurement Science SAS*, vol. 4, no. 3, 2004.
- [83] "Properties of PYREX®, PYREXPLUS® and Low Actinic PYREX Code 7740 Glasses,
http://catalog2.corning.com/lifesciences/media/pdf/description_of_7740_glasses.pdf.
" [Online]. Available:
http://catalog2.corning.com/lifesciences/media/pdf/description_of_7740_glasses.pdf.
- [84] M. R. Sajan, C. J. Tay, H. M. Shang, and A. Asundi, "Improved spatial phase detection for profilometry using a TDI imager," *Optics Communications*, vol. 50, no. 1, pp. 66-70, 1998.
- [85] S. C. Chapra, *Applied numerical methods with MATLAB for engineers and scientists*, 2nd ed. McGraw-Hill, 2006, pp. 322-329.
- [86] J. S. Bendat and A. G. Piersol, *Random data: analysis and measurement procedure*. New York: John Wiley & Sons, 2000.
- [87] S. Toyooka and Y. Iwaasa, "Automatic profilometry of 3-D diffuse objects by spatial phase detection," *Applied Optics*, vol. 25, no. 10, pp. 1630-1633, 1986.
- [88] E. Hecht, *Optics*, 4th ed. Addison-Wesley, 2002, p. 698.
- [89] P. Puangmali, K. Althoefer, and L. D. Seneviratne, "Mathematical Modeling of Intensity-Modulated Bent-Tip Optical Fiber Displacement Sensors," *IEEE Transactions on Instrumentation and Measurement*, vol. 59, no. 2, pp. 283-291, Feb. 2010.

- [90] W. Kester, S. Wurcer, and C. Kitchin, "Analog Devices Op Amp Applications," in *Op Amp Applications Handbook*, W. Jung, Ed. Newnes, 2004, p. 896.
- [91] C. D. Motchenbacher and J. A. Connelly, *Low-noise electronic system design*. New York: Wiley, 1993, pp. 191-192.
- [92] "Si Photodiode Array S4111/S4114 series, http://sales.hamamatsu.com/assets/pdf/parts_S/s4111-16q_etc_kmpd1002e06.pdf." [Online]. Available: http://sales.hamamatsu.com/assets/pdf/parts_S/s4111-16q_etc_kmpd1002e06.pdf.
- [93] J. G. Graeme, *Photodiode amplifiers: op amp solutions*. New York: McGraw-Hill Professional, 1996, p. 292.
- [94] E. Palik, *Handbook of optical constants of solids*, vol. 1. New York: Academic Press, 1985, p. 389.
- [95] P. Walker and W. H. Tarn, *CRC handbook of metal etchants*. Boca Raton: CRC Press, Inc, 1991, p. 80.
- [96] M. Despont, H. Gross, F. Arrouy, C. Stebler, and U. Staufer, "Fabrication of a silicon-Pyrex-silicon stack by a.c. anodic bonding," *Sensors and Actuators A*, vol. 55, pp. 219-224, 1996.
- [97] H. Seidel, "Anisotropic etching of crystalline silicon in alkaline solutions," *J. Electrochem. Soc.*, vol. 137, no. 11, pp. 3612-3632, 1990.
- [98] Y. Miyagawa, T. Okabe, Y. Yamaguchi, and E. Al., "Controlled release of diclofenac sodium from wax matrix granule," *International Journal of Pharmaceutics*, vol. 138, no. 2, pp. 215-224, 1996.
- [99] V. Chandrasekharan, "A Microscale Differential Capacitive Direct Wall Shear Stress Sensor," University of Florida, 2009.
- [100] V. Chandrasekaran, A. Cain, T. Nishida, L. N. Cattafesta, and M. Sheplak, "Dynamic calibration technique for thermal shear-stress sensors with mean flow," *Experiments in Fluids*, vol. 39, no. 1, pp. 56-65, 2005.

BIOGRAPHICAL SKETCH

Tai-An Chen was born in Ciaotou, Taiwan and was raised in Beavercreek, Ohio. He became a U.S. citizen in 1992 and graduated from Beavercreek High School in 1997. Tai-An majored in electrical and computer engineering while attending the Ohio State University and received his bachelor's degree in 2002. Upon graduation, Tai-An worked at Taitech, Inc. developing post-processing software for aero-acoustic applications and financial software. In 2004, Tai-An attended graduate school at the University of Florida and graduated with a master's degree in electrical and computer engineering in 2008 and completed his doctoral degree in 2012. His research focuses on shear stress sensors using MEMS technology and optics.